Electron Diffraction Studies of Unsupported Clusters

A thesis
submitted in partial fulfilment
of the requirements for the Degree
of
Doctor of Philosophy in Physics
in the
University of Canterbury

by

Michael Hyslop

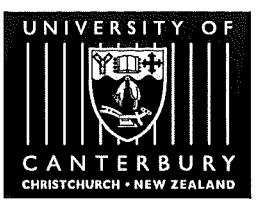

University of Canterbury
2002

Abstract

The motivation to study the structure of clusters is the possible observation of unusual structures for small cluster sizes. The presence of such structural size effects is generally associated with the optimization of surface energy in clusters. For metals that have face centred cubic (FCC) structure in the bulk, optimization of the surface energy typically results in icosahedral or decahedral structures being preferred for nanometre sized clusters.

The inert gas aggregation (IGA) technique has been used to produce a beam of clusters (diameter $\lesssim$10 nm) for structural studies using electron diffraction. Studying the clusters while in a molecular beam, as opposed to on a substrate, means that the clusters are unsupported and thus free of any perturbing effects due to a substrate. The use of a beam also means each cluster is subjected to only a brief exposure to the electron beam, minimizing effects due to the electron beam. Attempts to obtain diffraction patterns from Zn clusters were unsuccessful, however using Pb it was possible to obtain diffraction patterns from clusters using a wide range of parameters in the IGA source.

The experimental diffraction patterns result from the range of different sized and structured clusters produced by the source. The analysis reflects the distribution of cluster sizes and structures by combining diffraction patterns from model clusters with a range of sizes and structures to produce a best fit to the experimental pattern. In general, two sets of model clusters are used: the first set contains models with up to ~6500 atoms, created using bulk and symmetry properties for clusters with FCC, decahedral and icosahedral structure. The second set contains the same sizes and structures as the first, however each model has been relaxed using molecular dynamics (MD) simulations. In the analysis of several experimental diffraction patterns, models with twinned FCC, liquid, anti–Mackay icosahedral and shaved icosahedral[1] structures are also considered. Domain size estimates are obtained using the fit results; cluster size estimates are made from samples collected from the beam and observed in a TEM. Size estimates are also made using the Scherrer formula and the Fourier inversion method[2].

Analysis of diffraction patterns from Pb clusters shows that changing the type of inert gas produces the greatest variation in the size and structure of the clusters. The small clusters produced using He are found to be based on icosahedral structures. The clusters produced using Ar are larger than those produced using He and the diffraction patterns are difficult to interpret. The patterns bear a strong resemblance to those from decahedra, but diffraction patterns from decahedra are similar to those from twinned FCC structures, and from a combination of shaved icosahedra and FCC structures. FCC structure is not observed, which is both interesting and surprising.

[1] S. Hendy and B. D. Hall, *Phys. Rev. B* **64** (2001) 085425.
[2] B. D. Hall, *J. Appl. Cryst.* **33** (2000) 1335.

Contents

Figures

Tables

Chapter 1

Introduction

Clusters are neither new nor rare, in the atmosphere they are the precursors to rain and hail, they are the cause of colouring in stained glass and are now the topic of many scientific and industrial studies. A cluster is a very small particle containing upwards of a few atoms or molecules, however their properties can be so different to atoms or the bulk material that Stein [1] proposed them to be the fifth state of matter.

Several well known examples of the differences between clusters and bulk material are given below.

- **Melting Temperature**
  The melting temperature of clusters is predicted [2,3] and observed [4–6] to decrease with size. For clusters $\sim$10 nm in diameter the melting temperature is typically $\sim$90% of the bulk value. Further reductions of the cluster size cause the melting temperature to drop rapidly. Pb clusters with diameter $\sim$3 nm have been observed to be liquid at room temperature [7]. Very small clusters may not follow this trend, a recent experiment [8] observed that Sn clusters with between 10 and 30 atoms (diameter $\sim$1 nm) have a melting temperature *above* the bulk melting temperature. Note that Sn clusters with diameter $\gtrsim$3 nm have the typical size–melting temperature dependence initially described [9, 10][1].

- **Lattice Contractions**
  The surface tension of a cluster creates a compressive pressure on the cluster. This compression is expected to cause a lattice contraction [11, 12] that increases as the cluster size reduces. The observed contraction is reported to be the order of $\sim$1% for clusters a few nanometres [13–20] in diameter, but depends on the material the cluster is made from. However, the determination of the lattice constant in clusters is difficult and the measurement can be influenced by surface and structural effects [21,22]. The surface atoms are expected to reduce their interatomic distances to compensate for having fewer neighbouring atoms [23, 24].

[1]The melting temperature of Sn clusters in the size range $\sim$1 to $\sim$3 nm has not been examined

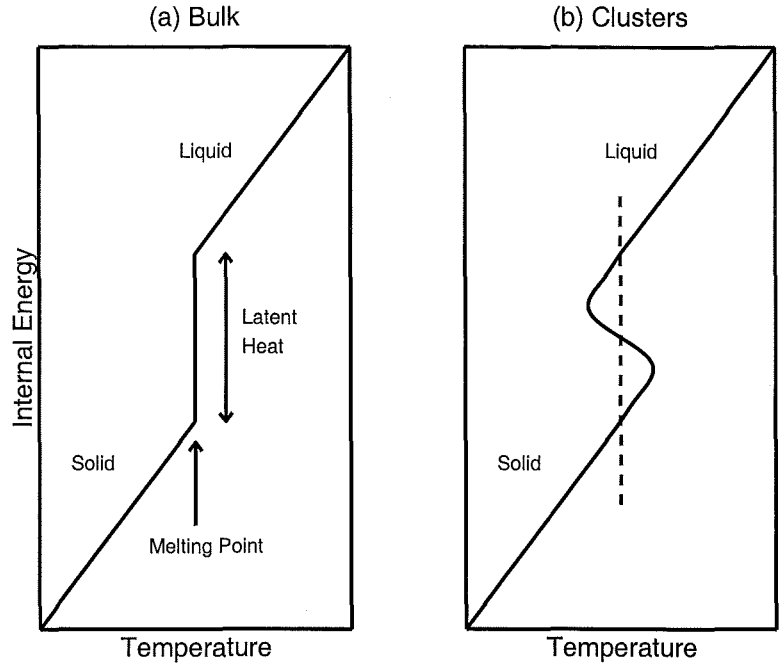

Figure 1.1: Schematic caloric curves for (a) bulk material and (b) 147 atom Na clusters. The 's' bend in the curve for clusters indicates the negative heat capacity. After Jarrold [28].

- **Catalysis**

  For certain chemical reactions the catalytic activity of clusters is often much higher than that of macroscopic particles [25]. Perhaps most interesting is bulk materials that are inert can show catalytic behaviour as clusters. Small Au cluster with 8 to 20 atoms deposited on MgO have been observed to be effective catalysts of CO [26]. Clusters smaller than 8 atoms were inert, indicating that catalytic activity can be very sensitive to size.

- **Heat Capacity**

  The heat capacity of 147 atom Na clusters has been observed to be negative near the melting point [27,28]. A negative heat capacity means that as more energy is added to a cluster the temperature of the cluster decreases. Schematic caloric curves for clusters and the bulk material are shown in Fig. 1.1. During melting the temperature of the Na clusters was estimated to decrease by about 10 K. This behaviour is due to the melting process in the Na clusters, the clusters do not partially (surface) melt and hence are either entirely liquid or solid. When melting occurs the required latent heat is that to melt the whole cluster, some of which comes from the kinetic (thermal) energy of the cluster, causing a reduction of the temperature.

- **Structure**

  The structure of clusters is often observed to be different to the structure of the bulk material [29–38]. For some materials the structure adopted by clusters contains fivefold symmetry, which is not observed in bulk materials. Fivefold symmetric clusters were almost simultaneously discovered by Ino [29], and Allpress and Sanders [30]. These fivefold symmetric clusters are collectively called Multiply Twinned Particles (MTPs) as they can be thought of as an assembly of smaller crystals joined by twin planes. The size and surface properties are generally considered to be dominant factors in determining the structure of clusters, however the conditions used to produce the clusters can also be very important [39–42].

The goal of this thesis is to examine this last point, the structure, and how it is influenced by size and the conditions used to produce the clusters. To study the structure a high energy electron diffractometer specifically designed to obtain diffraction patterns from a beam of clusters is used. The clusters are produced using an inert gas aggregation (IGA) source. The details of this source are given in chapter 3, though briefly, in the IGA source used, a metal is evaporated from a crucible into a flow of inert gas, cooling from the inert gas causes the metal vapour to supersaturate and condense into nanometre–sized clusters. Changing the crucible temperature, inert gas flow rate and pressure, and the type of inert gas all affect the conditions in which the clusters are produced. The mixture of inert gas and clusters passes through a series of nozzles to form a cluster beam. Shortly after exiting the final nozzle the cluster beam is crossed by a high energy electron beam.

In many experiments structural measurements of clusters are made by diffraction or high resolution transmission electron microscope (HRTEM) observation of *supported* clusters. The energy difference between possible structures for a cluster is often very small and any external interaction, such as a support, may have sufficient effect to change the structure of the cluster. In addition, the electron flux that clusters are exposed to during HRTEM studies has been observed to cause structural fluctuations [43–46] in some clusters. Both these problems are effectively solved by the diffractometer used in the present study. The clusters are probed while they are unsupported in the beam, hence there is no effect due to a substrate and the electron flux the clusters are exposed to as they pass through the electron beam is very small in comparison to HRTEM observations. The history and previous results obtained with this equipment are discussed in the next section. Then the work completed for this thesis is summarized. The final section outlines the content of the following chapters in this thesis.

1.1 History and Previous Studies

The origin of the equipment was through a collaboration between the Ecole Polytechnique Fédérale de Lausanne, Switzerland and Professor G. Stein of Northwestern University, USA. Built in Lausanne, the equipment was designed to be an advancement of the diffractometer in use by Yokozeki and Stein [31], providing a more controlled cluster source and better detection of the diffraction patterns. Much of the actual construction was by Ph.D. students Flüeli and Hall as partial fulfillment of their theses [47, 48].

The equipment was used by Hall to study the structure of Ag clusters. Hall found that in the size range examined (up to ~5 nm) the conditions used to produce the clusters were more important than their size in determining their structure [48, 49]. The success of experiments with Ag meant the later part of Hall's thesis work was involved with further improvements to the equipment. The original single channel electron detector used to measure diffraction patterns was replaced by linear CCDs (essentially multi–channel detectors) significantly reducing the time required to obtain diffraction patterns and a higher energy electron beam was installed. Once these improvements were completed the equipment was used by Reinhard [35, 40, 50] for further studies of Ag clusters, and studies of Cu and Ge clusters. Reinhard's work with Ag further reinforced the findings of Hall that the conditions used to produce Ag clusters were more important than the size and for some source conditions very large (~10 nm) icosahedra were observed. In contrast, for Cu Reinhard found that the structure was primarily dependent on the size of the clusters. Only preliminary measurements were made on Ge clusters and relationships between size, structure and source conditions were not determined.

Following the completion of Reinhard's experiments the equipment was relocated to Massey University, New Zealand by Hall where it resided briefly before being relocated again, this time to its present location, the University of Canterbury, New Zealand.

1.2 Review of Thesis Work

The initial tasks of this thesis involved the reconstruction of the equipment shipped from Massey University. Essentially all the equipment necessary for the experiments (except for a crucible) came from Massey and reconstruction proceeded reasonably smoothly, although several leaks in the vacuum system took some time to be identified.

The first metal tried in experiments was Zn. Zn was chosen as it was estimated it would only require heating to about 500°C to produce clusters. The low temperature (compared to $\gtrsim$1200°C required for Ag, Cu and Ge) meant designing a crucible for Zn would be relatively easy. Unfortunately, Zn clusters were difficult to produce and no

diffraction patterns were obtained. A weak cluster beam was occasionally detected by a quartz crystal deposition monitor, but this was not consistently reproducible between experiments. The observation that diffraction patterns from Bi clusters were only observed with much higher deposition rates [51] prompted a change of material[2].

The next metal tried in experiments was Pb, and diffraction patterns were obtained during the very first experiment. Many different conditions were used to produce Pb clusters. The most influential factor when producing Pb clusters was found to be the type of inert gas used. MTPs were typically produced when using He as the inert gas. Using Ar tended to increase the cluster size, however the diffraction patterns obtained were difficult to interpret, but suggested that clusters with faulted structures were being produced. Factors such as crucible temperature, inert gas flow rate and pressure changed the number of clusters produced, but had a lesser effect on the size and structure.

1.3 Outline of the Following Chapters

An outline of the following chapters is given below. Due to the lack of experimental results for Zn clusters there is a bias in many chapters, especially chapters 2 and 5, towards topics relating to Pb clusters.

Chapter 2 examines how the structure of clusters can be predicted. The influence of the surface on the structure is investigated and the shape and structure of the MTPs are introduced. Two methods used to determine the energy of clusters with different structures are reviewed. Then simulations of cluster growth are examined showing surface diffusion, growth rate and cluster temperature are also important in determining the shape and structure of clusters.

Chapter 3 describes the experimental equipment. Overall the equipment has not changed significantly from that used by Hall and Reinhard and consists of the cluster source, the electron beam, the detection system and beam sampling devices. The design and operation of each part is described. For the cluster source and detection system an outline of the theory behind their operation is also given.

In chapter 4 the Debye equation, used to calculate diffraction patterns for clusters, is introduced. Examples of diffraction patterns from a variety of different Pb and Zn clusters are given. For Pb diffraction patterns from clusters with different sizes and structures are shown. The range of sizes and structures corresponds to the sizes and structures considered in the analysis of diffraction patterns obtained from Pb clusters. For Zn the diffraction patterns shown are mostly from different shapes of cluster. The

[2]A. Wurl is concurrently using the same equipment to examine the structure of Bi clusters.

shapes correspond to those observed in an earlier study [52] of Zn clusters.

Chapter 5 describes the procedure followed during experiments and the methods used to analyse the diffraction patterns obtained. The analysis of the data is primarily based on reproducing the experimental diffraction pattern using a combination of patterns calculated from model clusters. The diffraction pattern is also used to obtain estimates of the cluster size by applying the Scherrer formula and using Fourier inversion. Another measurement of cluster size, independent of the diffraction pattern, is made by observing a sample of clusters collected from the cluster beam in a transmission electron microscope (TEM).

Chapter 6 presents the results obtained from experiments on Pb clusters. The chapter begins by reviewing previous studies of Pb clusters to provide several background details. Then the results from experiments with Pb clusters are displayed and analysed. The diffraction patterns presented have been grouped to show the effect of one source parameter on the production of clusters. Results are discussed with reference to other diffraction experiments, and theories and observations of cluster formation.

Chapter 7 begins by reviewing several theoretical studies of Zn clusters. The studies show that non–bulk structures are expected for very small clusters. The production of Zn clusters in previous studies is examined before describing the attempts to observe diffraction patterns from Zn clusters. The chapter closes with a discussion on the possible reasons for the difficulties encountered using Zn.

In chapter 8 the main conclusions from chapters 6 & 7 are reviewed. The outlook for this experiment and possible future work is discussed.

Chapter 2

Predicting the Structure of Clusters

This chapter reviews the methods and results of predicting the structure of metal clusters. Throughout the chapter, structure is meant to indicate the arrangement of atoms in the cluster (e.g. face centred cubic), and shape is used to define the external geometry of the cluster (e.g. spherical). Minimization of surface free energy is introduced as an important factor in determining the shape and structure of a cluster. For the bulk structure a shape which minimizes the surface free energy of the cluster can be found, however non–bulk structures that reduce the surface free energy further may exist, and two candidate structures are introduced. To determine the lowest energy structure common methods involve either a calculation based on macroscopic (bulk) properties or a simulation by molecular dynamics (MD). Recent MD simulations of cluster formation are reviewed. The simulations show that surface diffusion, growth rate and cluster temperature are also important in determining the shape and structure of the cluster.

2.1 Surface Energy

The structure a macroscopic crystal adopts is generally the structure that allows the bulk atoms to have the lowest possible energy. This structure may not be ideal for the surface atoms and their arrangement may not reproduce the underlying bulk structure. In a macroscopic crystal the proportion of surface atoms is small and the contribution from surface energy to the total energy of the crystal is negligible. However, as the crystal size is decreased the proportion of surface atoms increases. The fraction, F_s, of surface atoms can be approximated by [53]

$$F_s(N) = 4N^{-\frac{1}{3}}, \tag{2.1}$$

where N is the number of atoms in the cluster. For example, a 64000 atom cluster ($\sim$12 nm diameter) has 10% of its atoms at the surface. The high proportion of surface atoms means the surface energy must be considered when determining the lowest energy shape and structure for a cluster. The surface energy can be reduced by adopting a compact shape, thus minimizing the total surface area, and by having facets with low surface energy.

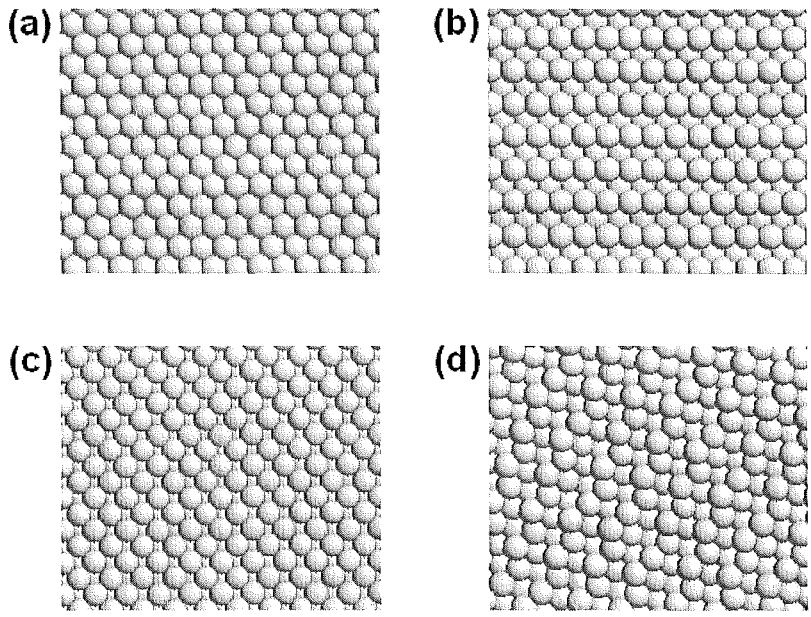

Figure 2.1: The packing of atoms on different facets of a crystal. All the facets shown are from a face centred cubic (FCC) crystal, (a) (111), (b) (110), (c) (100) and (d) randomly created (926).

To first order the energy of a surface facet depends on how tightly packed the atoms are, tighter packing tends to reduce the surface energy. It is unlikely that for a randomly oriented facet the atoms will be tightly packed, however for some specific facets the atoms are tightly packed.

Fig. 2.1 shows the packing in four different facets of a face centred cubic (FCC) crystal, facet (a) is the (111) plane and generally has the lowest surface energy, (b) and (c) are two ((110) and (100) respectively) other low energy facets. Facet (d) is an example of a randomly chosen facet (926), note the loose packing in this surface compared with the others.

To determine the lowest energy shape from the surface energies of different facets, Wulff [54] proposed a geometric method which is discussed in the next section.

2.2 Wulff Shapes

Minimization of surface free energy requires minimizing the expression

$$\int \gamma \, dA, \tag{2.2}$$

where γ is the surface free energy and dA the surface area. Wulff's solution to Eqn. 2.2 involves a geometrical construction where vectors are drawn from an origin in directions

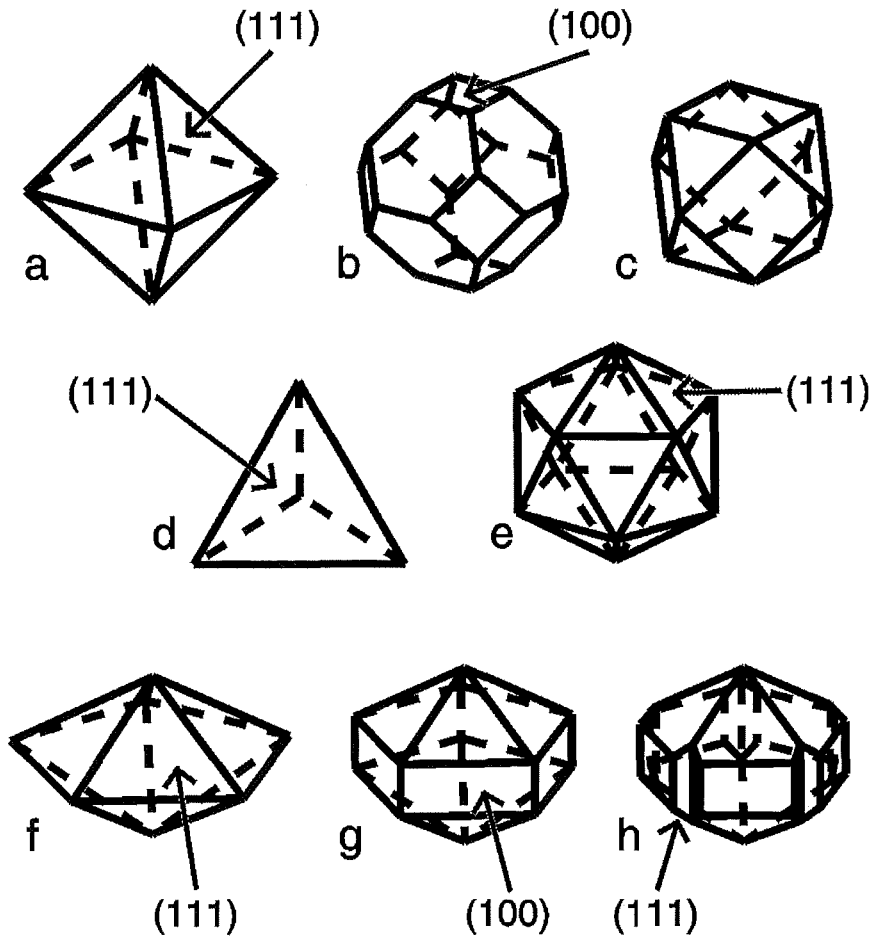

Figure 2.2: Examples of cluster shapes. (a) octahedron, (b) cuboctahedron (hexagonal facets), (c) cuboctahedron (triangular facets), (d) tetrahedron, (e) icosahedron, (f) decahedron, (g) truncated decahedron and (h) Mark's decahedron.

corresponding to crystallographic planes. The vector lengths are proportional to the surface free energy of the crystallographic plane. At the termination of each vector a normal plane is constructed; the internal most polyhedron described by these planes is then geometrically similar to the polyhedron that minimizes Eqn. 2.2. This shape is called the Wulff shape for the cluster.

For a metal with FCC structure the Wulff shape is generally similar to the cuboctahedron (Fig. 2.2(b) & (c)), only the (111) and (100) facets are exposed. Although the octahedron (Fig. 2.2(a)) exposes only (111) facets it is not the Wulff shape as it is a less compact shape. Two alternative structures, icosahedral (Fig. 2.2(e)) [55] and decahedral (Fig. 2.2(f)) [56], produce clusters that can expose solely (111) facets, and therefore can minimize the surface free energy well.

2.3 Multiply Twinned Particles

Both the decahedron and icosahedron are comprised of multiple tetrahedra (Fig. 2.2(d)) based on the FCC lattice. The join between tetrahedra is a twin plane and hence clusters with these structures are referred to as Multiply Twinned Particles (MTPs). The decahedron (Fig. 2.2(f)) contains five tetrahedra sharing a common edge and the icosahedron (Fig. 2.2(e)) contains twenty tetrahedra sharing a common vertex. Tetrahedra only expose (111) facets, and thus the decahedron and icosahedron also have only (111) facets. However, if the MTPs are created using perfect FCC tetrahedra there are small gaps in the structures. To fill the gaps (become space filling) the tetrahedra must be deformed, introducing an internal strain to the cluster. The total strain energy increases with size and means MTPs will only exist at small sizes where the improved arrangement of surface atoms can compensate for the strain.

Assuming that MTPs become space filling by homogeneous elastic strain[1], Ino [57] calculated the total energy for decahedral and icosahedral structures. Ino truncated the outer edges of the decahedron to expose (100) facets (Fig. 2.2(g)), this gave approximately the Wulff shape for the decahedron.[2] The results were compared to the energy of a Wulff FCC cluster. For a FCC cluster the total energy, U, is given by

$$U_{FCC} = -U_c + U_s, \tag{2.3}$$

where U_c is the cohesive energy and U_s the surface energy. For the decahedron and icosahedron the total energy is given by

$$U_{MTPs} = -U_c + U_s + U_e + U_t, \tag{2.4}$$

where the extra terms U_e and U_t are the elastic strain and twin boundary energies respectively. Fig. 2.3 reproduces the stability curves calculated by Ino for the cuboctahedra, decahedra and icosahedra. Ino's results show icosahedra as most stable for small sizes, FCC as most stable at large sizes, while decahedra are never predicted as the most stable.

A modification to the Wulff construction by Marks [58] allowed the derivation of shapes for twinned particles. The modification showed that twinned FCC particles could exist as metastable structures with respect to single crystals and that Ino's decahedra should be modified to include re–entrant faces (Fig. 2.2(h)) between the twin planes, producing the

[1]The atoms are uniformly displaced and the tetrahedra have flat faces, c.f. inhomogeneous strain where the displacement is non–uniform and the faces of the tetrahedra may bulge.

[2]At the time of Ino's calculations the true Wulff shape for decahedra and other twinned particles had not been determined. For decahedral structures the Marks' decahedra (fig.2.2(h)) is the Wulff shape.

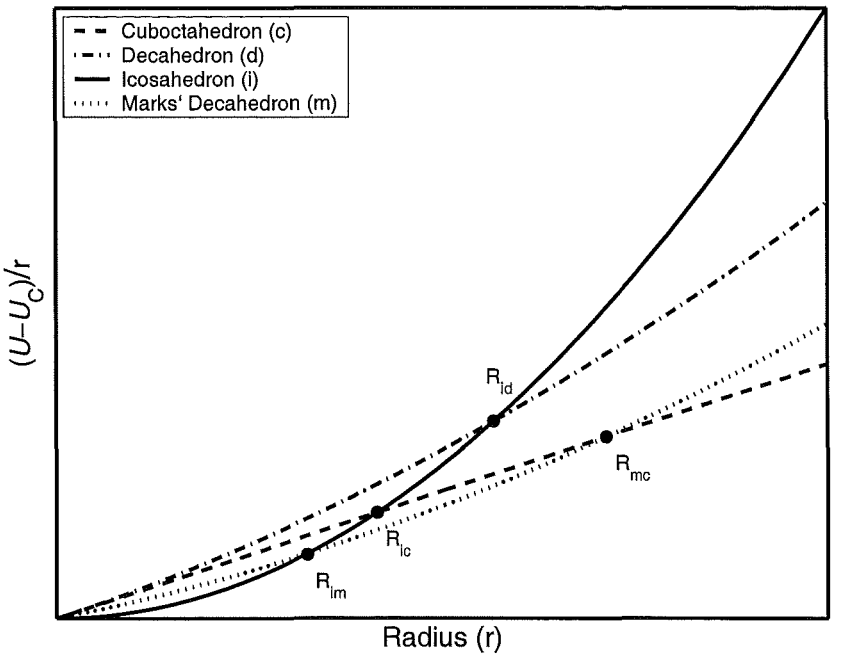

Figure 2.3: Schematic energy comparison between cuboctahedral, truncated decahedral, icosahedral and Marks' decahedral structures. The point R_{AB} indicates the size where structure B becomes more favourable than structure A.

Marks' decahedra. The inclusion of re–entrant faces on the decahedra reduced its energy such that the Marks' decahedra is stable in an intermediate size range (see Fig. 2.3) [59].

The internal strain of the decahedra and icosahedra may result in defects. HRTEM observation of Au and Ag decahedral and icosahedral clusters by Marks [60] showed the presence of dislocations in icosahedral clusters larger than 15 nm. Marks concluded that the smaller clusters were able to distort sufficiently using only inhomogeneous strain, however larger clusters required dislocations to relieve the strain. Decahedral particles have less strain than icosahedral particles and no defects were observed up to a size of 30 nm. In larger decahedral clusters Marks observed defects including stacking faults running parallel to twin boundaries and migration of twin boundaries.

2.4 Magic Numbers

The fixed ratios of edge lengths for Wulff structures and MTPs mean that the correct shape can only be created with certain numbers of atoms. The sets of numbers that fulfill the criteria are known as magic numbers. For cuboctahedra (triangular facets) and

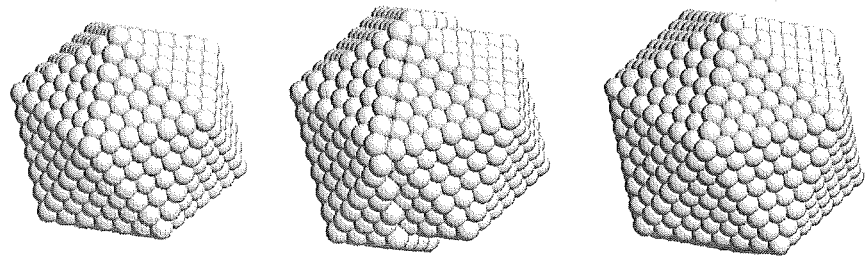

Figure 2.4: The shell like construction of magic number clusters. Left: a completed 923 atom icosahedron, middle: a partially completed shell on the 923 atom icosahedron and right: a complete shell on the 923 atom icosahedron resulting in a 1415 atom icosahedron.

icosahedra the set is given by [61]

$$\begin{aligned} n_{icos,cubo} &= \frac{10}{3}K^3 - 5K^2 + \frac{11}{3}K - 1 \\ &= [13, 55, 147, 309, 561, 923, 1415, 2057, 2869, 3871, 5083, 6525, ...], \end{aligned} \tag{2.5}$$

where K is a positive integer. For truncated decahedra with square truncated faces the magic numbers are also given by Eqn. 2.5, however the truncation rule used by Ino [57] to create the approximate Wulff shape for decahedral clusters produces the set

$$n_{deca} = [39, 116, 258, 605, 992, 1514, 2491, 3428, 4570, 6497, ...].$$

Each number in the set corresponds to a new shell surrounding the previous structure (see Fig. 2.4), and hence the magic numbers are often referred to as shell structures. Magic numbers are observed as peaks or dips (depending on the experiment) in mass spectra for many materials [61]. The position of the peaks or dips in the mass spectra can sometimes be used to determine cluster structure, though this is often limited as, for example, it is difficult to distinguish between icosahedra and cuboctahedra because they both contain the same number of atoms per shell.

A different type of shell structure can be created by the electron energy levels within a cluster. In bulk material electron energy levels are quasi–continuous, however in clusters the energy levels are discrete [53] (due to confinement in a potential well). For a spherical cluster the energy levels are characterized by the radial quantum number n and the angular momentum quantum number l. Each energy level has a degeneracy of $2(2l+1)$ [62]. A shell is completed if the valence electrons of the cluster fill all the degenerate energy levels in the highest occupied energy level. This type of shell structure was first observed by Knight [62] in mass spectra from Na clusters. Strong peaks in the mass spectra were

observed for $N = 8$, 20, 40, 58, and 92 atoms, and, as Na has one valence electron, the numbers also correspond to the number of valence electrons required to close the electronic shells.

In general, electronic and geometric magic numbers are not expected to coincide and typically the electronic shell structure is exhibited by liquid clusters, whereas geometric shells are exhibited by solid clusters [53]. A transition from electronic to geometric shell structure was observed by Martin *et al.* [63] in the mass spectra of Na clusters. For clusters with up to ~1500 atoms the observed shell sizes agreed well with predicted electronic shell sizes, while for above ~1500 atoms the observed shell sizes were more consistent with geometric shell sizes. This transition is thought to indicate that the Na clusters solidified at ~1500 atoms.

2.5 Molecular Dynamics

The simulation of the movement and interaction of atoms is known as Molecular Dynamics (MD). In general, MD simulations use numerical methods to solve the equations of motion for each atom. The simulation requires an accurate model of the potential that describes the interaction between atoms and is often computationally intensive. In this section a brief review of MD simulations on metallic clusters is given.

2.5.1 Relaxation of Model Clusters

The energy of a cluster can be calculated using the potential and a model cluster that defines the atomic positions. However, depending on how the model was created, the position of atoms may not be ideal, for example a cuboctahedron cut from an infinite FCC lattice has the ideal atomic positions for atoms in the infinite lattice not for atoms near the surface of a cluster. The relaxation process allows the atoms to move to positions corresponding to local energy minima, thus reducing the energy while preserving the general structure. Repeating the process for clusters with different structures allows the structures to be ranked according to energy.

Cleveland and Landman [64] compared the predictions of relaxation and Eqns. 2.3 & 2.4 for Ni clusters and found that similar results were obtained for both methods. Cleveland's relaxation results showed icosahedral clusters were preferred for clusters up to ~2300 atoms, Mark's decahedra in the range ~2300 to ~17000 atoms and FCC clusters at larger sizes. Other authors [65–68] studying clusters of FCC materials also predict a transition from icosahedra (to decahedra) to FCC as cluster size increases, their results are summarized in Table 2.1. Pb appears to be an exception to this pattern: using relaxation

of model clusters Lim *et al.* [69] predicted that FCC structure is more favourable than icosahedral for all sizes. Hendy and Hall [70,71] have extended Lim *et al.*'s work to include decahedra and anti–Mackay icosahedra (the outer layer of these icosahedra has hexagonal close–packed (HCP) stacking instead of FCC). The energy of both structures is lower than the normal icosahedra but still higher than FCC clusters.

Table 2.1: Structural transition sizes (in atoms) predicted by MD relaxation of model clusters.

Author	Element	Icosahedra	Decahedra	Cuboctahedra
Cleveland and Landman [64]	Ni	<2300	2300 → 17000	>17000
Hearn and Johnston [65]	Sr	<128000	-	>128000
	Ca	<32000	-	>32000
Valkealahti and Manninen [66]	Cu	<2500	-	>2500
Uppenbrink and Wales [67]	Ag	<3739	3739 → 83905	>83905
	Pd	<1388	1388 → 19022	>19022
	Ni	<7382	7382 → 121371	>121371
	Au	<393	393 → 704	>704
Yi *et al.* [68]	Al	$\lesssim$100	-	$\gtrsim$100
Lim *et al.* [69]	Pb	-	-	all sizes
Hendy and Hall [70]	Pb	-	-	all sizes

Often only the energy of magic number clusters is calculated and the results interpolated using an equation of the form [69]

$$E_N = A + BN^{1/3} + CN^{2/3}, \tag{2.6}$$

where A,B and C are fitted parameters, to predict the relative stability of structures with N atoms. While Eqn. 2.6 may provide an estimate of when structures are favourable, the energy–structure relationship between magic numbers can, especially for small clusters, be complicated [42, 72, 73]. For example Baletto *et al.* [42] find that for 309 atoms the icosahedron is the most stable structure for Ag, but for clusters with ± 1 atom imperfect decahedra are more stable.

2.5.2 Structural Changes and the Lowest Energy Structure

Relaxation of model clusters is generally limited to comparing the energy of several ideal structures. Of these structures there is no guarantee that the one with the least energy has the lowest energy of all possible structures. To allow MD to predict new structures generally requires the melting then freezing and cooling of the cluster to be simulated. In some

cases the structures found may have a lower energy than previously considered structures, while in others nucleation and growth effects may create unfavourable structures.

The simulated melting and freezing of Ni clusters with 336 and 736 atoms by Qi *et al.* [74] found that neither cluster froze with the original FCC structure. The larger cluster did consist mostly of FCC structure but also contained two small disordered regions, while the 336 atom cluster had a slightly deformed icosahedral structure that was more stable than the original FCC structure.

To find the lowest energy structure for small Au clusters (N=38, 55, 75) Garzón *et al.* [75–77] repeatedly simulated the freezing and further cooling of liquid clusters. The total energy of each cluster was recorded once the temperature was close to 0 K. For each cluster size the structures obtained were ranked in order of energy. It was found that many different structures, mostly amorphous, had close to the minimum energy. For 38 and 55 atom clusters amorphous structures were found to have the lowest energy, while the lowest energy non–amorphous structures for each size were FCC and icosahedral respectively. For 75 atoms the Marks' decahedra was found to be the lowest energy structure.

A structural transition prior to melting was observed during the simulated heating of FCC and decahedral Au clusters by Cleveland *et al.* [78, 79]. The original clusters, a 75 atom decahedron, a 146 atom decahedron and a 459 FCC cluster, all transformed to icosahedra at elevated temperature. During the heating, but prior to fully transforming, the 146 atom decahedra was observed to become a polyparticle containing a region of decahedral structure and another region of icosahedral structure.

The simulated melting and freezing of larger Au clusters (459, 1157 and 3943 atoms) has been performed by Chushak and Bartell [80,81]. Spherical FCC clusters were heated to 200 K above their melting point. As in the simulations by Cleveland *et al.* the structure of the 459 atom clusters was observed to reorganize before melting (the new structure was not specified by Chushak and Bartell). To refreeze the clusters they were cooled to a temperature of 700, 720 or 740 K. For each size and final temperature up to 20 clusters were frozen. Icosahedral structures were typically obtained, although decahedral, FCC and HCP structures were also observed. The dominance of the icosahedral structure is interesting, for Au icosahedra are considered unfavourable, however the energy of each structure obtained is very similar, indicating that nucleation and growth are probably influential in determining the structure of the clusters.

In some cases structures are unstable and can undergo structural transformations at very low temperatures. Valkealahti and Manninen [66, 82] observed a diffusionless transformation in copper clusters from closed shell cuboctahedra (triangular facets) to icosahedra for clusters with 13, 55 and 147 atoms at a simulated temperature of 0 K; they

expect the transition would occur at 0 K for clusters with up to ~2000 atoms. The lack of an activation barrier for the transition means that for small Cu clusters cuboctahedra (triangular facets) are a saddle point in the multidimensional configuration space. The simplicity of the icosahedra↔cuboctahedra (triangular facets) transformation has been described by Mackay [55]. However, Valkealahti and Manninen also report [66] that a 219 atom FCC cluster (non–magic number) did not change structure at temperatures up to its melting temperature. They suggest that FCC clusters that would require diffusion to become icosahedral are more stable against a transformation to icosahedral structure. Interestingly, later studies [83] showed that when liquid drops are crystallized only those drops with magic numbers of atoms for icosahedra crystallized as icosahedra, other sizes crystallized as twinned FCC clusters.

For Pb, Hendy and Hall [70] have performed melting and freezing simulations of FCC clusters up to 6525 atoms. For clusters with between ~500 and ~5000 atoms the frozen clusters had a structure that is described as a surface reconstructed or 'shaved' icosahedron. In comparison to a normal icosahedron the shaved icosahedron has the atoms on the apexes and (111)/(111) facet edges of the outer shell redistributed within the cluster, and the surface (111) layers moved to form stacking faults with respect to the internal FCC tetrahedra. There are also stacking faults and disorder within the shaved icosahedra. Throughout this thesis clusters with this new structure are referred to as 'shaved icosahedra' to prevent confusion with other types of icosahedra. Shaved icosahedra were also obtained, without melting, by heating icosahedral clusters, presumably this was possible because of the similarity between the two structures.

2.6 Cluster Growth

The previous sections have only considered the clusters at their final size, however to achieve these sizes the clusters must, in general, grow from smaller sizes either by addition of single atoms or coalescence. Given that different structures may be preferable at different sizes and that energy barriers may prevent a structural transformation, it is desirable to examine the growth process in detail. During growth, if the cluster is able to transform to the most favourable structure the process is referred to as *thermodynamic*, however if the cluster is prevented from having the most favourable structure due to the growth conditions, then the process is referred to as *kinetic*.

Using the lattice gas model for cluster growth, where Monte Carlo techniques simulate atoms being absorbed onto, evaporating from or diffusing around discrete predetermined lattice sites, Valkealahti *et al.* [84, 85] examined the effect of growth rate and diffusion on

the cluster shape. Absorbed atoms were assumed to stick to a cluster if the absorption site had three or more nearest neighbours (atoms that did not stick were assumed to immediately evaporate). Varying the rates of adsorption and diffusion showed that low adsorption and high diffusion rates allowed the clusters to grow with an approximately compact shape. Using low adsorption and high diffusion rates, the (100) facets of the cuboctahedral clusters would be filled first leaving only (111) facets, growth would then occur on only one (111) facet at a time. The probability of growth occurring on a (111) facet was independent of previous growth and meant that the cluster did not necessarily make perfect octahedral shells as it grew. In contrast, icosahedral clusters would complete an entire shell before starting a new shell because growth of one facet would promote growth on neighbouring facets.

For cuboctahedra, reducing the probability of absorbed atoms sticking to sites with three nearest neighbours to very small values and limiting diffusion also produced approximately compact growth. This meant any (100) facets and any unfinished (111) facets were quickly filled as these facets contain sites with four nearest neighbours. Initiating growth on a clean (111) facet would take a long time (as the sticking probability was very low), though once started the facet would grow easily.

More recent simulations, similar to those above, have been performed by Valkealahti and Manninen [86] for Al clusters and by Baletto *et al.* [87] for Ag and Au clusters using MD rather than the lattice gas method. The growth simulations studied the transition of cluster shape from cuboctahedral (hexagonal facets) to octahedral. The shape transition was found to be dependent on the temperature. At low temperatures only diffusion around (111) facets was possible and meant each (111) facet grew individually. Increasing the temperature allowed diffusion between (111) facets and providing the growth rate was slow enough a single (111) facet would grow at a time. Further temperature increases allowed diffusion from (111) to (100) facets, but the reverse required still higher temperatures. The activation of the (111) to (100) process meant the (100) facets disappeared and the shape tended to become octahedral. The temperatures at which the various diffusion processes are allowed varies between the metals, for Au diffusion from (111) to (100) occurs at lower temperatures than for Ag and hence Au clusters tended to transform to octahedral shape more readily than Ag clusters.

In the above growth simulations the octahedron is not predicted as the shape with the lowest energy for FCC clusters, however the octahedron appears due to kinetic effects.

More extensive growth simulations of Ag clusters have been performed by Baletto *et al.* [41,42] in an attempt to explain the observations made by Reinhard *et al.* [40] of very large ($\sim 10\,\mathrm{nm}$) icosahedral clusters. Starting from a 7 atom Ag cluster at a temperature

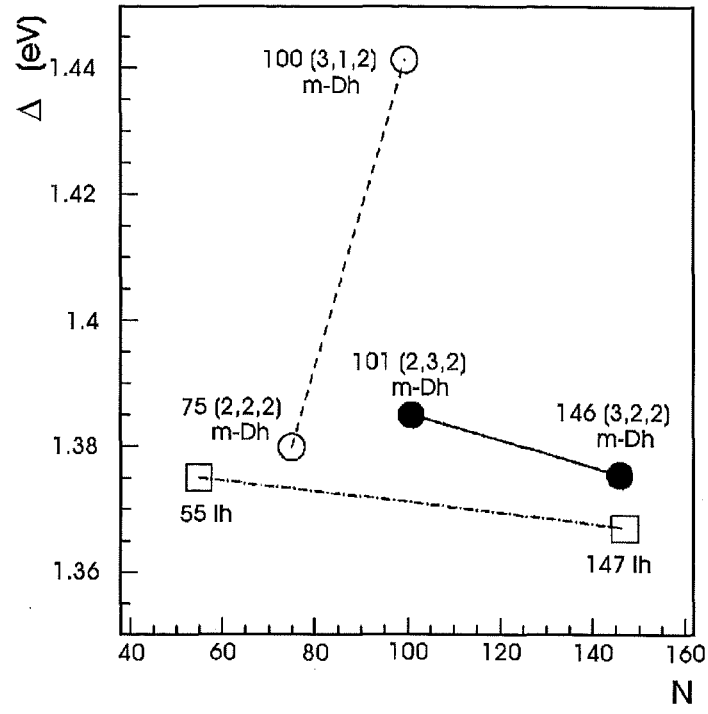

Figure 2.5: Comparison of energy for several Ag clusters with magic numbers of atoms. The squares correspond to icosahedral structures, the open circles are Marks' decahedra with 5 atoms along the axis of symmetry and the closed circles are Marks' decahedra with 6 atoms along the axis of symmetry. The lines are only intended as a guide to the eyes. After Baletto [41].

between 300 and 600 K the cluster was allowed to evolve and periodically atoms were added to the cluster. The temperatures and growth rates used in the simulations were similar to those expected in an inert gas aggregation source.

Fig. 2.5 shows the relative energy of several clusters observed during the growth simulations. For the Mark's decahedra the bracketed numbers describe the external shape of the cluster, the first two numbers are the width and height (in atoms) respectively of the (100) facet. The third number is the length (in atoms) of the re–entrant (111) facet.

The temperature and growth rate were found to influence whether a cluster would grow thermodynamically or kinematically. For higher temperatures the growth is close to thermodynamic as the cluster has sufficient energy to change structure, lowering the temperature introduces kinetic effects as activation barriers become impassable. The growth rate influences the temperature at which the kinetic effects arise, lower growth rate allows the cluster more time to make a transformation and hence thermodynamic growth occurs at lower temperatures.

For a growth rate of $\sim$0.14 atoms/ns the following temperature dependent growth sequences were observed:

- **Low temperatures 350→400K**
  At 55 atoms an icosahedron was observed, this transformed during growth to form a 75 atom (2,2,2) decahedron. Further growth of the cluster resulted in the 100 atom (3,1,2) decahedron. Another 100 atom decahedron, the (2,3,2) decahedron with 1 atom missing, has lower energy than the (3,1,2) decahedron, but due to the low temperature the (2,3,2) decahedron did not form. Additional atoms produced a new layer with HCP stacking relative to the underlying layers on a (111) facet of the (3,1,2) decahedron. The new layer initiated a transformation to icosahedral structure that, due to the low temperature, is expected to be preserved at larger sizes resulting in a large metastable icosahedron.

- **Mid temperatures 450→550K**
  Again the 55 atom icosahedron and 75 atom decahedron were observed. The 75 atom (2,2,2) decahedron grew to become the metastable 100 atom (3,1,2) decahedron. At this temperature the (3,1,2) decahedron was able to change shape and become the (2,3,2) decahedron. The decahedral structure was still observed at ~150 atoms even though an icosahedral structure is more favourable. Further growth of the decahedron resulted in a HCP layer that eventually transformed the cluster to icosahedral structure. This icosahedron is also expected to grow to large sizes.

- **High temperatures >550K**
  At high temperatures the cluster was melted up to ~130 atoms, at 147 atoms an icosahedron was obtained. The icosahedron transformed via a quasi–melted structure to a decahedron with ~170 atoms. At larger sizes FCC and decahedral structures are close in energy, and the high temperature meant that the cluster alternated between these structures.

The growth simulations provide surprising results: for Ag icosahedral structures are never the most favourable above a few hundred atoms, yet the simulations predict that metastable icosahedra can grow to much larger sizes.

2.7 The van de Waal Structure

When a structural transition occurs in a cluster it is often assumed the cluster retains none of the original structure, however a structure predicted by van de Waal [88] shows this assumption is not necessarily required. The structure, developed by van de Waal in response to the inability to correctly explain the structural transition observed in Ar clusters (see Appendix A), is pictured in Fig. 2.6 and transforms during growth from

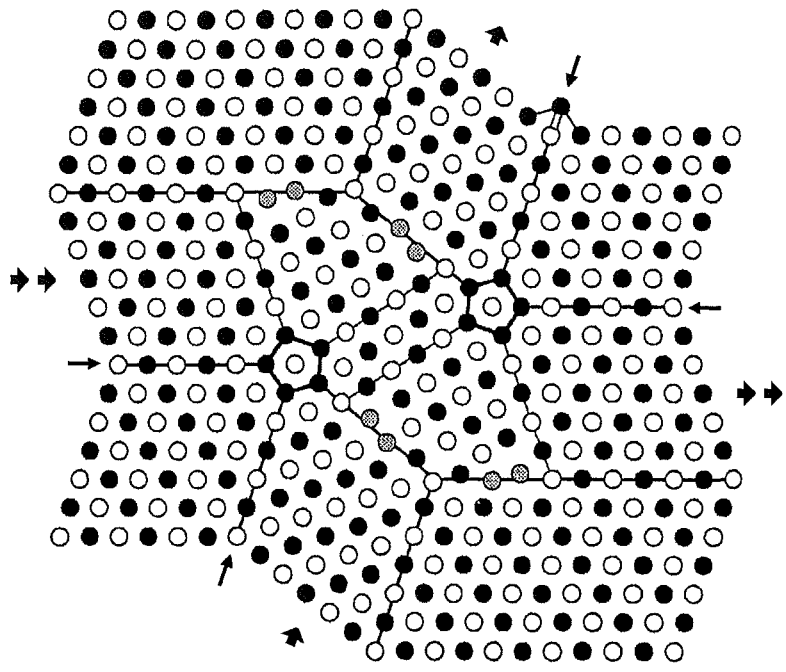

Figure 2.6: [110] view of atoms in the van de Waal structure. Atoms are positioned at z=0 (plane of the page), ±1, etc (black dots) and at z=$\pm\frac{1}{2}$,$\pm\frac{3}{2}$, etc (white dots). Shading denotes uncertain positions near incoherent domain boundaries. Thin arrows mark re–entrant grooves with preferred nucleation sites where new atoms can make four bonds, rather than three (upper thin arrow; the "double" bond denotes two single bonds to atoms at z=$\pm\frac{1}{2}$; new atom is at z=0). Local fivefold symmetry is highlighted by bold pentagons; domain boundaries are shown by thin lines. After van de Waal [88].

dominantly MTP to dominantly FCC. The important features of this structure are the two local fivefold axes of symmetry, the regions of FCC structure and the two crossing twin lamellae (indicated by the heavy arrows in Fig. 2.6) that extend to the surface of the cluster. At small sizes the structure is dominated by the fivefold symmetry, however the twin lamellae create preferred nucleation sites (indicated by thin arrows in Fig. 2.6) at the surface of the cluster. These sites are always in positions that create FCC structure and are self replicating, i.e. filling one site creates a new preferred nucleation site that creates more FCC structure. Hence, as the cluster grows it becomes increasingly dominated by FCC structure, but as the cross twinning is energetically unfavourable the origin of the FCC structure is kinetic.

Although the model described is based on decahedral cores, van de Waal suggests including a third lamella, not parallel to the two already present, could conceivably result in a structure based on icosahedral rather than decahedral cores.

2.8 Summary

Several techniques for predicting the structure of clusters have been examined. Ino's equations, assuming bulk values, calculate the total energy of clusters with different structures. The results from these calculations typically result in icosahedra being predicted at small sizes and a transition to FCC at larger sizes. The relaxation of model clusters also allows the energy of clusters to be calculated. Comparing the energy of relaxed FCC, decahedral and icosahedral clusters typically shows icosahedral structure is favoured in small clusters and FCC structure is favoured in larger clusters. Using MD to simulate the melting and freezing of clusters may result in lower energy structures being found, however kinetic effects during freezing can also influence the structure.

Simulations of cluster growth showed that diffusion, cluster temperature and growth rate can be important in determining the shape and structure of clusters. The van de Waal structure suggested a method for structural transitions to occur without the complete rearrangement of the atoms within the cluster.

Chapter 3

Experimental Equipment

This chapter reviews the experimental equipment used during this study. Section 3.1 briefly summarizes the equipment and gives a general overview of operation. Later sections cover the details and theory of individual sections of the equipment.

3.1 General Overview

A schematic of the experimental equipment is shown in Fig. 3.1. The equipment is a high energy electron diffractometer specifically designed to study the structure of unsupported clusters. The equipment consists of: the cluster source, the electron beam, the detection system and the beam sampling devices.

The clusters are produced in the source chamber (RHS in Fig. 3.1) using the inert gas aggregation (IGA) technique. A description of the source, its operation and theory is given in section 3.2. The clusters exit from the source chamber, pass through a series a nozzles and then enter the diffraction chamber (centre of Fig. 3.1) as a cluster beam. Above the diffraction chamber are the gun and condenser sections from an electron microscope. Details of the microscope and electron beam produced are given in section 3.3.1. As the clusters enter the diffraction chamber they intersect the electron beam, this point is called the diffraction point. The random orientation of the clusters produces a Debye–Scherrer (powder) pattern of diffraction rings that is measured by a pair of linear CCD detectors positioned $\sim$0.5 m below the diffraction point. The type and operation of the CCDs is discussed in section 3.3.2. Towards the rear of the diffraction chamber (LHS in Fig. 3.1) are two beam sampling devices: a quartz crystal deposition rate meter (not shown) and a transmission electron microscope (TEM) grid holder. The use of both devices is described in section 3.4.

3.2 The Cluster Source

The general principle in an IGA source is to heat bulk material to produce a hot vapour; the vapour is cooled through contact with a flowing (in this source) inert gas causing the

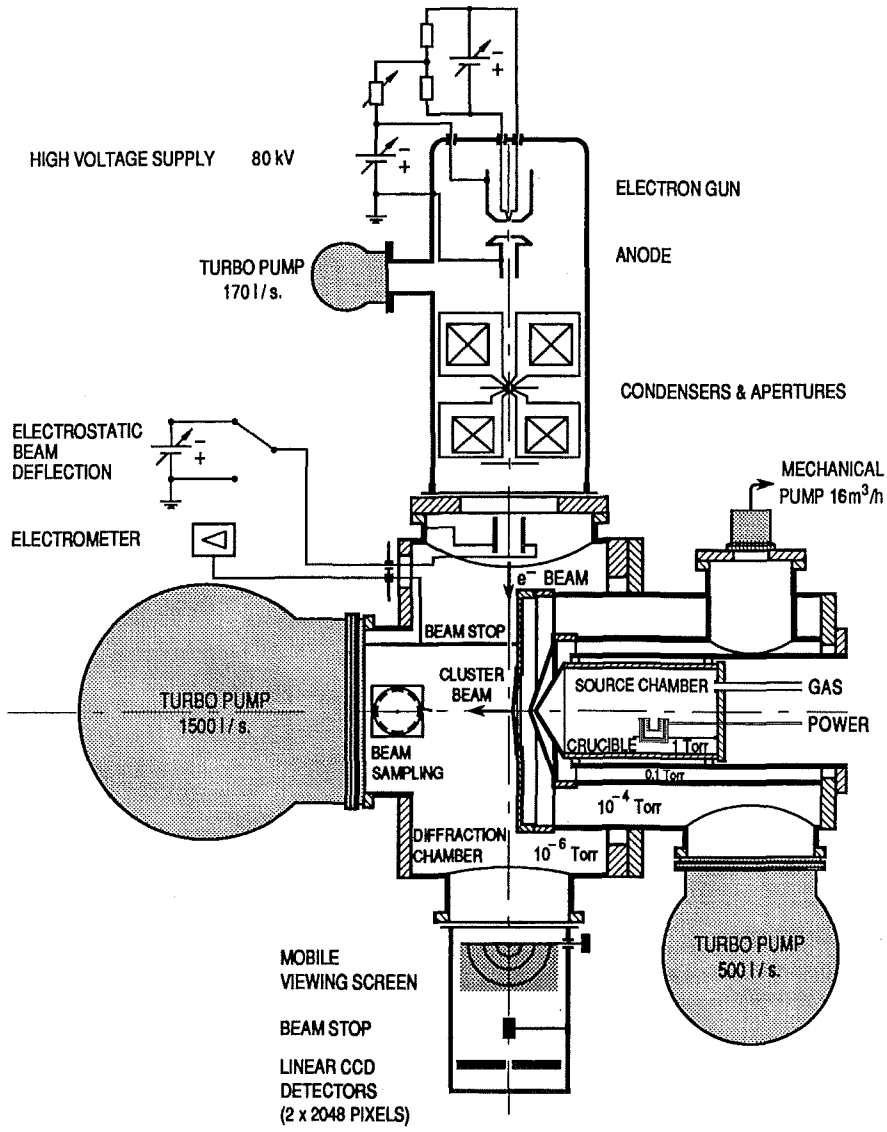

Figure 3.1: Schematic of the experimental equipment. After Hall [89].

vapour to supersaturate. In the supersaturated vapour clusters are formed by homogeneous nucleation. The clusters become entrained in the flowing inert gas and carried out of the source chamber. In this source a resistively heated crucible to used to evaporate the metal and either argon, helium, or a mixture of both is used as inert gas. The pressure of the inert gas is typically between 1 and 20 mbar. The metal vapour pressure is typically between 0.1 and 1 mbar.

Although essential for the production of the clusters, the inert gas contributes to a background signal in the diffraction patterns. To remove a large proportion of the inert gas the mixture of gas and clusters is pumped through a series of nozzles separating differential pumping chambers before entering the diffraction chamber. The series of

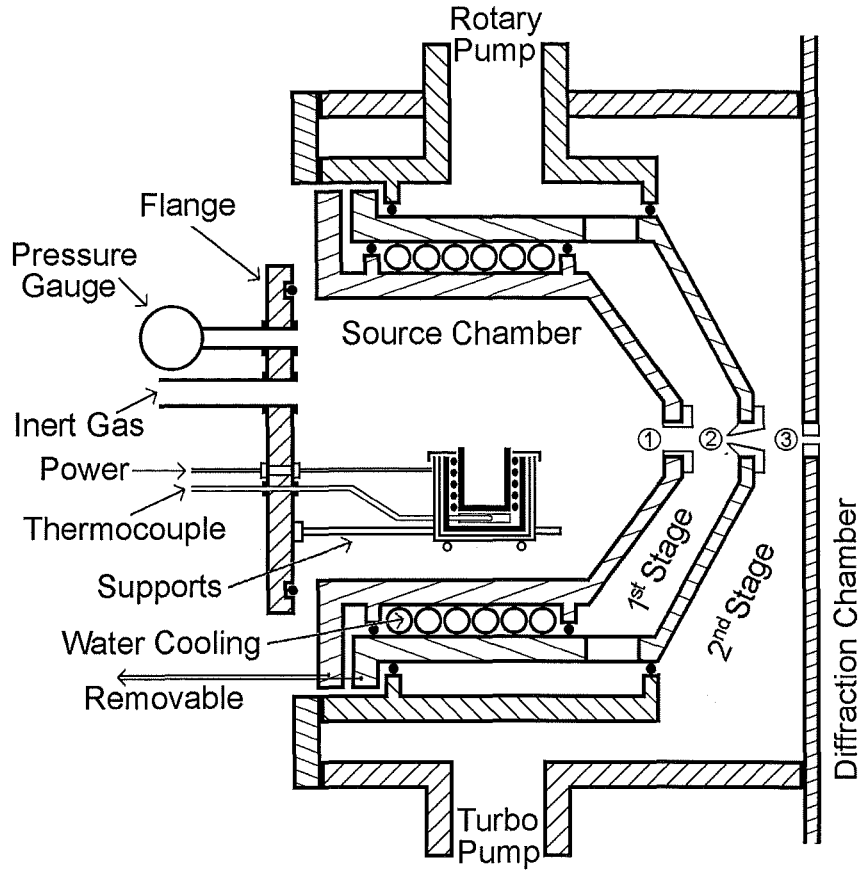

Figure 3.2: Schematic of the source chamber and differential pumping stages. The circled numbers identify the nozzles described in Table 3.1.

nozzles also act as collimators to create a well directed cluster beam.

The next section provides technical details regarding the differential pumping stages, source chamber, crucible and the control of source parameters (crucible temperature and inert gas composition and pressure). This is followed by a review of homogeneous nucleation theory and a summary of observations made on IGA sources.

3.2.1 Source Chamber and Differential Pumping Stages

Fig. 3.2 shows schematically the source chamber and differential pumping stages. The source chamber has an internal diameter of 87 mm and length of 110 mm. The flange fitted to the source chamber holds the crucible arrangement and has feedthroughs for an inert gas inlet, thermocouple, filament power and source pressure gauge. The flange and source chamber are water–cooled to keep the source chamber walls at approximately room temperature during an experiment. Details of the nozzles separating the source chamber, 1 st stage, 2 nd stage and diffraction chamber are given in Table 3.1. The source chamber

has no direct pumping, the 1 st stage is pumped by a 16 m^3/h rotary pump and the 2 nd stage is pumped by a 500 l/s turbo pump.

Table 3.1: Properties of the nozzles used to separate the source chamber, 1 st stage, 2 nd stage and diffraction chamber. Positions of the nozzles are shown in Fig. 3.2. For nozzle 1 the range of diameters listed corresponds to the range of sizes used during experiments. All nozzles are constructed from graphite.

Nozzle	Type	Dimensions
1	Tube	length: 6 mm, diameter: 1–6 mm
2	Skimmer like	length: 4 mm, diameter: 1.5 mm
3	Orifice	length: 2 mm, diameter: 1.5 mm

As indicated in Fig. 3.2 the flange, source chamber and 1 st stage chamber can be removed from the rest of the system. This allows unobstructed access to the nozzles and source chamber for maintenance and cleaning. Throughout this thesis the flange, source chamber and 1 st stage chamber are collectively referred to as 'the source'.

3.2.1.1 Crucible Design

The crucible used during Pb experiments is pictured disassembled in Fig. 3.3. In Fig. 3.4 the crucible is shown assembled and mounted on the flange. The alumina crucible (25 mm high, 20 mm outside diameter, 16 mm internal diameter) holds the Pb to be evaporated. The crucible sits on a thin (3 mm high, 20 mm diameter) boron nitride disc (not visible) that has a 2.5 mm diameter hole for the thermocouple (type K, max. temp. 1200°C). A tungsten filament is wound to wrap around the disc and crucible. The windings of the filament are created so the current in neighbouring wires travels in opposite directions minimizing the magnetic field produced. The insulator (made of alumina) encloses the filament, crucible and disc and prevents electrical shorting between the filament and heat shields. Slots are cut in the insulator for the thermocouple and filament to pass through. A double layer of tantalum heat shielding surrounds the base and sides of the insulator. The top of the arrangement is fitted with a tantalum cap having a hole for the crucible. The hole in the cap has a diameter ~2 mm larger than the smaller crucible allowing some flexibility in the position of the crucible. The top of the crucible protrudes ~2 mm above the tantalum cap. Finally a thinner tantalum cover sheet with a tight fitting hole is positioned over the smaller crucible. Over several experiments a significant amounts of Pb condenses on the cover sheet and it has to be replaced periodically. The tight fit between the crucible and cover sheet prevents the condensed Pb from entering the interior of the crucible arrangement.

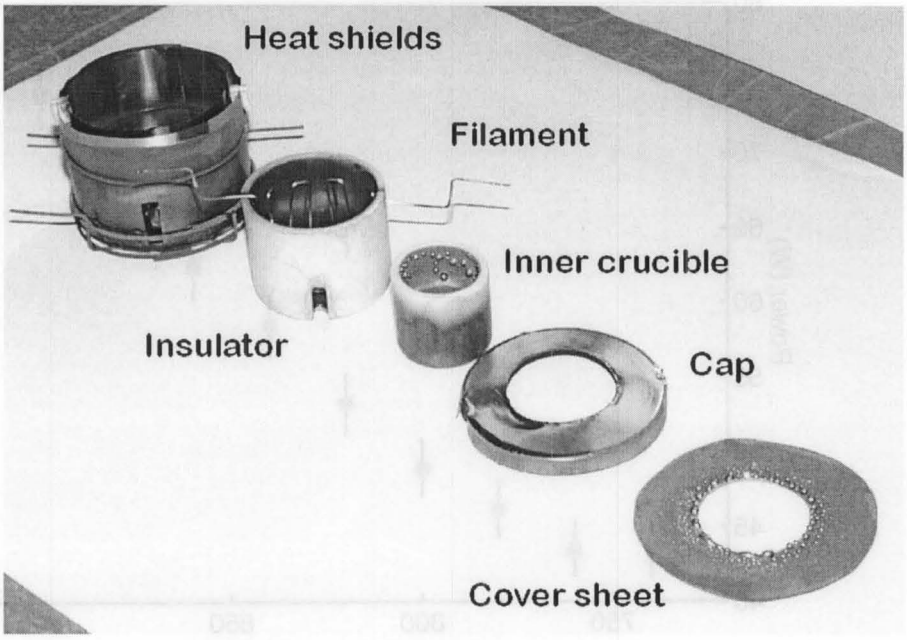

Figure 3.3: Disassembled view of the crucible arrangement.

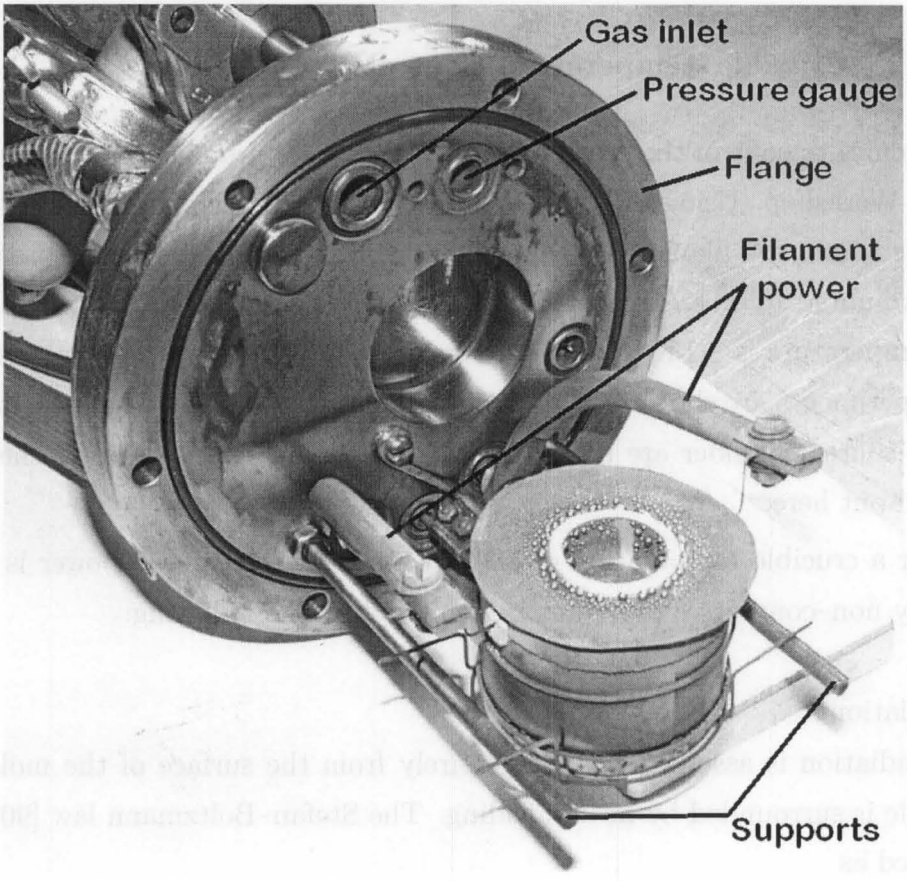

Figure 3.4: The crucible assembled and mounted on the flange.

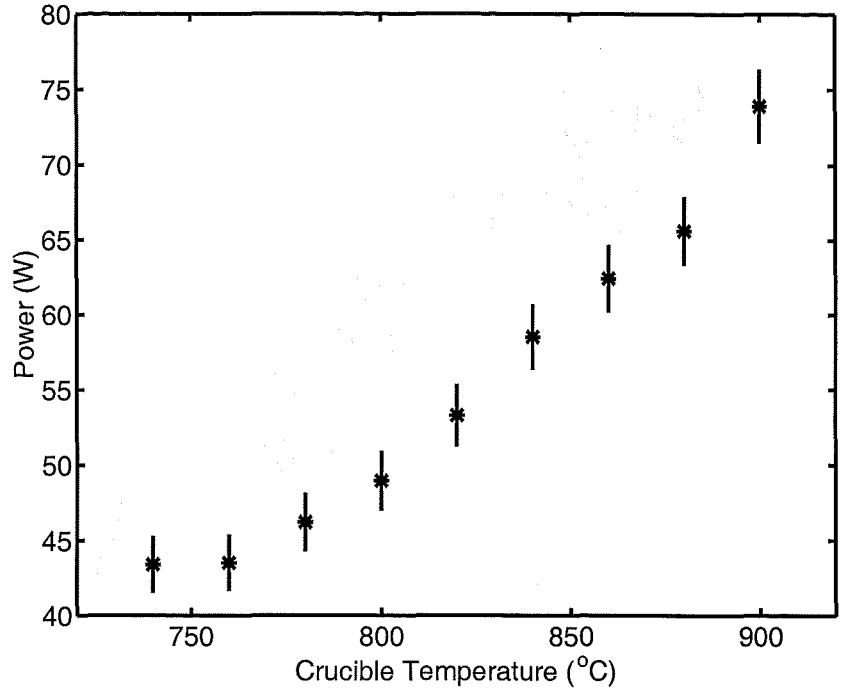

Figure 3.5: Power usage of the crucible during Pb experiments.

3.2.1.2 Crucible Temperature Control

Electronics to control the crucible temperature were produced by the Department's Electronic Workshop. Using the thermocouple readings the temperature controller adjusts the voltage across the filament to change or stabilize the crucible temperature. The heating rate is limited to 20 K/min to prevent thermal shock to the crucible and the stability of the temperature is ±1 K. Crucible temperature *vs.* filament power measurements during Pb experiments are shown in Fig. 3.5. Calculations by Hall [48] on the dissipation of heat in the source chamber are reproduced below for the special case of the Pb experiments carried out here.

For a crucible temperature of 880°C (1153 K) the required power is ~65 W. Dissipation by non–convective processes is estimated by the following:

- Radiation

The radiation is assumed to come entirely from the surface of the molten metal as the crucible is surrounded by heat shielding. The Stefan–Boltzmann law [90] gives the power radiated as

$$Q_{Rad} = Ae\sigma T^4, \tag{3.1}$$

where A is the surface area of the metal, e is the emissivity, σ is the Stefan–Boltzmann

constant ($5.6699 \times 10^{-8}\mathrm{Wm^{-2}K^{-4}}$) and T is the temperature of the metal. Assuming a perfect emitter, $e = 1$, gives $Q_{rad} \approx 20\,\mathrm{W}$.

• Gas flow

By converting the gas flow rate in the source into a mass flow rate and using the heat capacities for He or Ar gases the heat removed by the gas can be estimated using

$$Q_{Flow} \approx 10\,m\mathrm{WK^{-1}}. \tag{3.2}$$

This requires knowledge of the temperature difference between the gas entering and leaving the source chamber, but cannot be more than a few watts.

• Conduction (Without convection)

To estimate the heat flow by conduction a spherical geometry and no gas flow are assumed. The heat flow is then given by [90]

$$Q_{Cond} = \frac{4\pi k r_e r_i}{r_e - r_i}\Delta T, \tag{3.3}$$

where k is the coefficient of thermal conductivity for the gas, r_e is the radius of the external wall, r_i is the radius of the heat source and ΔT the temperature difference between the source and wall. Using the following values

$$\begin{aligned} k_{He} &= 0.14\,\mathrm{Js^{-1}m^{-1}K^{-1}}, \\ k_{Ar} &= 0.016\,\mathrm{Js^{-1}m^{-1}K^{-1}}, \\ r_e &= 4.35 \times 10^{-2}\,\mathrm{m}, \\ r_i &= 1.0 \times 10^{-2}\,\mathrm{m}, \\ \Delta T &= 860\,\mathrm{K}, \end{aligned}$$

gives $Q_{Cond} \approx 20\,\mathrm{W}$ using He and $Q_{Cond} \approx 2\,\mathrm{W}$ using Ar.

The total heat dissipated by convection is estimated at ~25 W using He and ~40 W using Ar. For comparison, the heat dissipated by convection during Hall's experiments on Ag was estimated at ~70 W (these experiments used He as the inert gas and a crucible temperature of ~1500 K, which required a power of ~150 W). Hall suggested that convection caused instability of the cluster beam during his experiments. During experiments performed with Pb, using either He or Ar, no instability of the cluster beam was observed. The reduced convection is possibly a reason for the stability of the beam.

3.2.1.3 Inert Gas Flow Control

The inert gas flow is regulated by a pair of MKS Instruments flow meters (one for Ar and one for He). Electronics to control the flow meters were produced by the Department's Electronics Workshop and allow the user to set the ratio of He to Ar and the total inert gas flow rate. Changing flow rate has an almost immediate effect on the pressure in the source chamber and setting a desired pressure in the source chamber is easily accomplished. The pressure–flow rate relationship in the source chamber is governed by the nozzle separating the source and 1 st stage chambers, as it effectively controls the pumping on the source chamber. Pressure *vs.* flow rate measurements are shown in Fig. 3.6.

3.2.2 Homogeneous Nucleation Theory

In an IGA source the clusters are formed by homogeneous nucleation, that is, the clusters nucleate in the absence of foreign matter that might act as seeds for the condensation of the vapour. The initial condensation of the vapour will result in a liquid drop, however in homogeneous nucleation there is an energy barrier to the formation of a liquid drop that is due to the creation of a new surface when the drop forms. For a droplet with radius r, density ρ and temperature T, the difference in Gibbs free energy between the droplet and the surrounding vapour is given by [91]

$$\Delta F = 4\pi r^2\gamma - \frac{4}{3}\pi r^3 \rho RT \ln S, \tag{3.4}$$

where γ is the surface tension, R the molar gas constant and S the supersaturation ratio (The ratio of actual vapour pressure to the saturated vapour pressure at temperature T) of the surrounding vapour. The first term represents the free energy required to form the surface and the second term represents the change in bulk free energy. Fig. 3.7 shows the Gibbs free energy for the cases of unsaturated (S<1), saturated (S=1) and supersaturated (S>1) vapours.

The maximum of ΔF corresponds to the height of the energy barrier to the formation of the droplets. Only in the case of a supersaturated vapour is height of the barrier finite. The position, called the critical radius (r^*), and height (ΔF^*) of the energy barrier in a supersaturated vapour can be calculated from Eqn. 3.4 by differentiation:

$$r^* = \frac{2\gamma}{\rho RT \ln S}. \tag{3.5}$$

and

$$\Delta F^* = \frac{16\pi\gamma^3}{3(\rho RT \ln S)^2} = \frac{4\pi\gamma}{3}(r^*)^2. \tag{3.6}$$

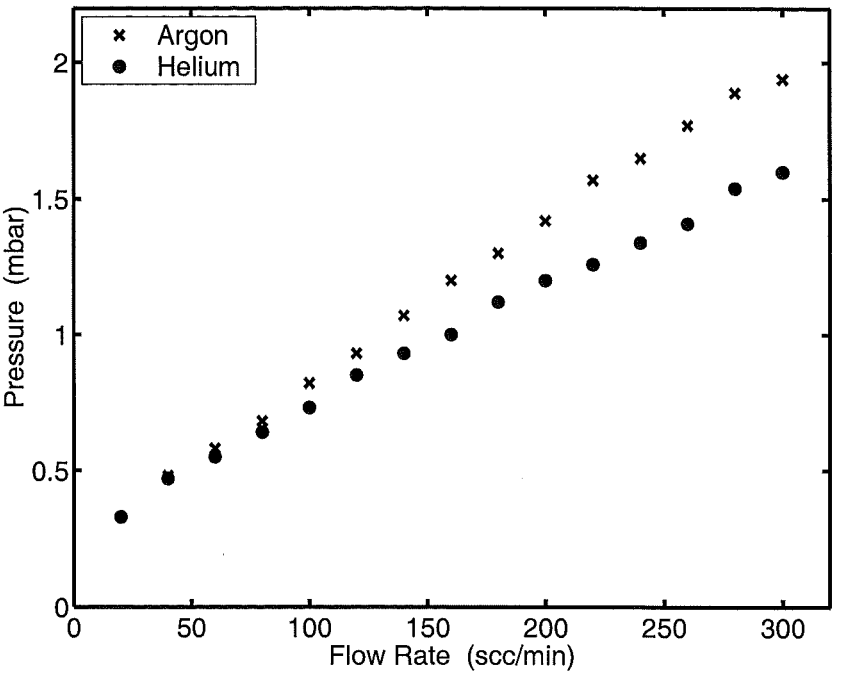

Figure 3.6: The dependence of the pressure in the source chamber on type and flow rate of the inert gas. The nozzle separating the source and 1 st stage is 6 mm in diameter.

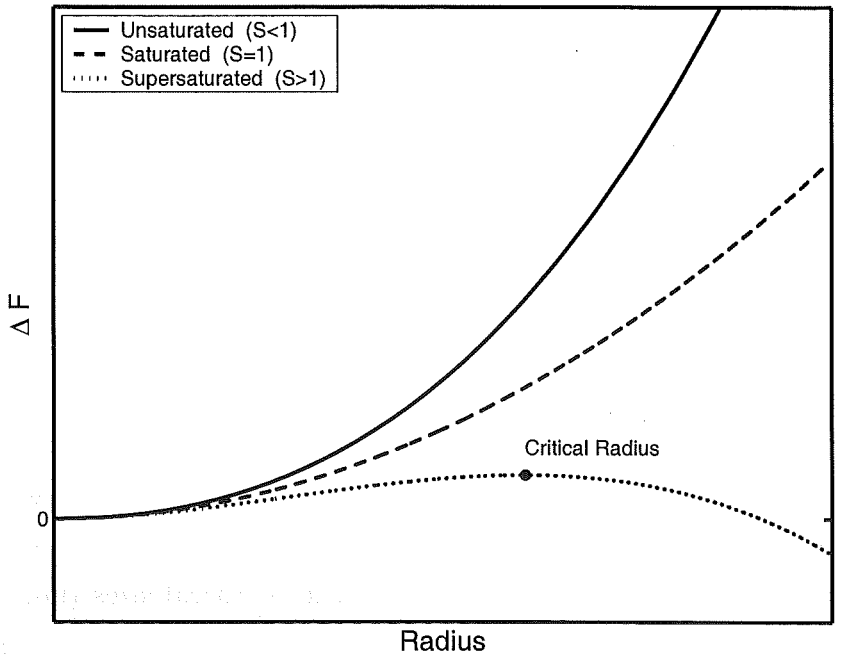

Figure 3.7: ΔF for an unsaturated, saturated and supersaturated vapour. Only the supersaturated vapour has a maximum in ΔF and corresponding critical radius. For clusters larger than the critical radius growth is energetically favourable.

It is energetically favourable for a droplet to grow only when growth decreases the free energy. Droplets larger than the critical radius should therefore grow without limit, while droplets smaller than the critical radius should shrink and evaporate. There is now a clear problem: how do droplets larger than the critical radius form?

The problem is answered by noting that even in an unsaturated vapour there will be a distribution of droplets, which are formed by random processes, that follows a Boltzmann type relation,

$$N_a = N_1 e^{-\Delta F/kT}, \tag{3.7}$$

where N_a is the number density of droplets with a atoms. In an unsaturated vapour these droplets are destined to evaporate. In a supersaturated vapour, the distribution will be different to Eqn. 3.7, but a population of small droplets will still exist. From this population droplets larger than the critical radius will continue to grow.

The nucleation rate, I, at which droplets of size r^* are formed can be calculated using [92]

$$I = \left(\frac{n^2}{\rho}\right)\left(\frac{2m\gamma}{\pi}\right)^{\frac{1}{2}} e^{-\Delta F^*/kT}, \tag{3.8}$$

where n is the number of molecules per unit volume. To create an intense cluster beam it is important to increase the supersaturation ratio as this reduces r^* and ΔF^*, and improves the probability of the small randomly formed droplets growing larger than the critical size.

To complete this section the results of calculating the critical radius (Eqn. 3.5) for several metals and a range of supersaturation ratios are shown. The critical radii were calculated assuming a vapour pressure of one Torr and corresponding temperature. Other values, γ, ρ and saturated vapour pressure for a given temperature, were taken from Ref. [93]. Fig. 3.8(A) shows the critical radii for Ag, Cu, Pb and Zn and indicates that the critical radius becomes extremely small once the supersaturation ratio is several orders of magnitude (which requires cooling the vapour several hundred degrees). In Fig. 3.8(A) the difference in critical radii between the metals does not appear very large, however in (B) the critical radii have been converted into critical sizes (number of atoms) using atomic radii and assuming equal packing factors. There is now a clear difference between Zn and the other metals. The large critical size suggests it may be difficult to produce Zn clusters, this is discussed further in chapter 7.

The supersaturation reached within the source chamber is unknown and undoubtedly has some spatial variation. A minimum supersaturation ratio of $\sim$50 for the nucleation

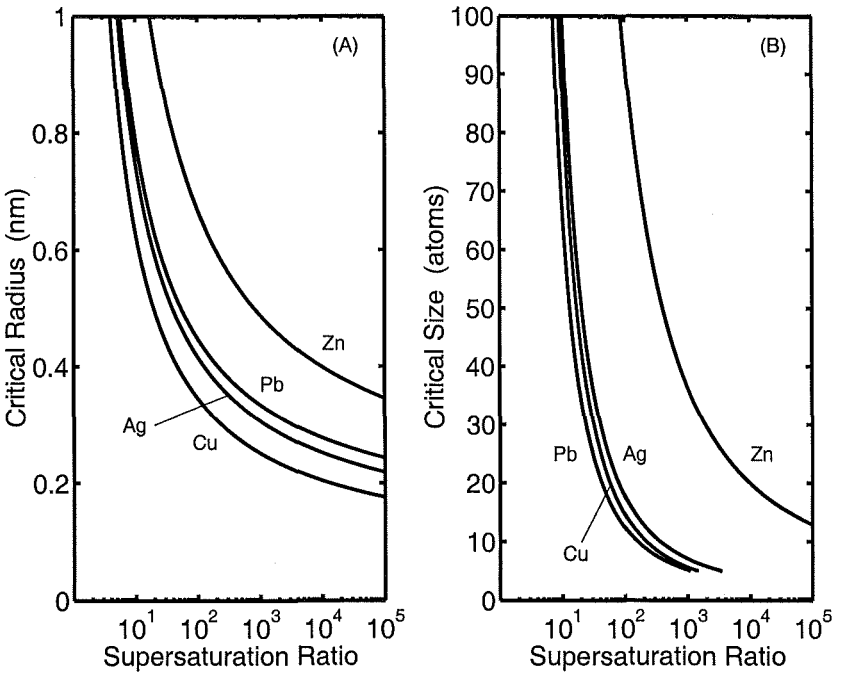

Figure 3.8: (A) The critical radii as a function of supersaturation for Ag, Cu, Pb and Zn. (B) Estimated critical cluster sizes as a function of supersaturation. The curves were all calculated assuming a supersaturation ratio of 100 and vapour pressure of 1 Torr.

of Pb vapour at 1000 K was obtained by Homer and Hurle [94], however their method involved the decomposition of tetramethyl–lead by shock heating so the values may not be directly applicable to an IGA source. An estimate for the supersaturation can be made using temperature measurements from IGA sources: for a crucible at 1400 K Hall [48] measured the temperature above the crucible to be 570 K. A similar measurement by Nishida and Kimoto [95] gave 430 K for a crucible at 1170 K. From these measurements, assuming isobaric cooling, supersaturations greater than 10^{10} could be expected. Such supersaturation ratios would presumably never be reached as diffusion and nucleation would reduce the vapour pressure and hence supersaturation ratio.

3.2.3 Observations on Cluster Production in an IGA Source

A review by Hall, using the observations of Yokozeki and Stein [31], Sattler *et al.* [96], Schulze *et al.* [97, 98] and the theoretical predictions of Kawamura [99], summarized and attempted to explain observations regarding the effect of source conditions on the average cluster size. The important points of the review are listed below. In the explanations for each point Hall neglected any possible effects due to coalescence, however observations by Kasukabe *et al.* [100] and models by Granqvist and Burhman [101, 102], which fit experimental data well, indicate that coalescence could be very important in the growth

of clusters in an IGA source. Hence, where appropriate, the suggested effects [101] of coalescence have been included in the explanations below.

- An increase in crucible temperature increases the mean cluster size.
  Increasing the source temperature produces more vapour. Providing the vapour is still efficiently cooled more clusters will nucleate. The increased number of clusters means more coalescence occurs which results in a larger average cluster size.

  Increasing the crucible temperature may reduce the cooling of the vapour, lowering the supersaturation ratio and thus nucleation rate. In this case, clusters that do form grow in a richer vapour and can grow larger.

- An increase in inert gas pressure increases the mean cluster size.
  Increasing the inert gas pressure limits the vapour diffusion and provides better cooling. This results in a cooler, denser vapour and a higher nucleation rate. The increased number of clusters results in more coalescence and larger clusters.

- A decrease in the inert gas temperature increases the mean cluster size.
  Decreasing the inert gas temperature improves the cooling of the vapour and increases the supersaturation. Thus growth occurs earlier and in a more concentrated vapour (diffusion has less time to disperse the vapour). This leads to larger particles as above.

- An increase in the molecular weight of the inert gas increases the mean cluster size.
  The ability of the inert gas atoms to cool the vapour has been suggested to depend on the amount of energy exchanged during collisions between inert gas and vapour atoms [103]. For hard sphere elastic collisions, with one atom at rest, the ratio of energy exchanged to initial energy is given by

$$\frac{\Delta E}{E} = \frac{4m_1 m_2}{(m_1 + m_2)^2}, \tag{3.9}$$

  where m_1 and m_2 are the respective atomic masses. The ratio is a maximum when the two masses are equal. Hence as the mass of the inert gas atoms is increased up to the mass of the vapour atoms the cooling of the vapour improves. An increase in the mass of the inert gas atoms is also expected to reduce the diffusion of the vapour [103,104]. The improved cooling and reduced diffusion lead to larger clusters as above.

- An increase in the flow rate of the inert gas decreases the mean cluster size.
  Increasing the flow rate of the inert gas reduces the time clusters spend in vapour

rich regions. An increased flow rate will also tend to reduce the concentration of clusters resulting in less coalescence. Both effects will reduce the size of the clusters produced.

3.3 Detection System

Components of the equipment related to the production and detection of the diffraction patterns are now reviewed. The production and control of the electron beam is described in section 3.3.1. This is followed by a description of the type and operation of the CCD detectors in section 3.3.2 and a statistical analysis of the counting system employed by CCDs in section 3.3.3. The statistical analysis identifies optimum exposure conditions for the CCDs.

3.3.1 The Electron Beam

The source of the electron beam for diffraction is a modified Phillips EM300 Transmission Electron Microscope (TEM). The column of the TEM has been truncated below the condenser lens and mounted on top of the diffraction chamber (see Fig. 3.1). This modification has not changed the original operating parameters and specifications concerning the electron beam. The beam energy is selectable in 20 kV steps up to a maximum of 100 kV, and beam currents up to 20 μA are attainable.

Normal operating settings for diffraction experiments are 80 kV and $\sim$2 μA for beam energy and current respectively. Higher beam energies increase the diffraction signal from clusters relative to the signal from the background gas [48], however higher beam energies also reduce the diameter of the diffraction rings at the CCDs. For Pb, a beam energy of 100 kV means the first diffraction ring is not completely visible on the CCDs.

The operation of the CCDs (see section 3.3.2) requires the ability to control the exposure of the CCDs to the diffracted electrons. The Phillips EM300 does not provide a feature to pulse the beam and instead an electrostatic beam stop is used to deflect the beam above the diffraction point. Near the top of the diffraction chamber (see Fig. 3.1) two parallel metal plates are positioned either side of the electron beam path. When the beam is 'on' the plates are uncharged and the beam passes through a small ($\sim$0.5 mm diameter) hole in a graphite plate. Charging one of the plates to 400 V creates an electric field in the path of the electron beam deflecting it onto a graphite plate and effectively switching the beam 'off'. The charge accumulated on the graphite plate passes to ground via an electrometer allowing the electron beam current to be measured.

To align the electron beam with the cluster beam a needle on a retractable arm in the

diffraction chamber is positioned inline with the nozzle separating the 2nd differential pumping stage from the diffraction chamber (nozzle 3 in Fig. 3.2). Positioned ~0.1 m above the CCDs is a movable phosphorescent screen (labeled 'Mobile Viewing Screen' in Fig. 3.1), the shadow cast on the screen by the needle is used to align the electron beam.

3.3.2 The CCD Detectors

The CCD detectors are Texas Instruments VID–283 chips with the protective window, which is opaque to electrons, removed. Each chip has 2048 individual pixels measuring 12.5 μm square and 10 μm deep. Details of the electronic clock settings used for the CCD detectors can be found in ref. [48].

Diffraction patterns are measured as a function of the scattering parameter: s (see section 4.2 for definition). As the energy of the electron beam determines the diameter of the diffraction rings, the range of s detected by the CCDs is dependent on the electron beam energy. The ranges of s detected for electron beam energies from 40 to 100 kV are given in Table 3.2.

Table 3.2: Detection range of CCDs for a given electron beam energy. Note shadowing of the CCD at low s reduces the range from the theoretical maximum.

Beam energy (kV)	s_{min} (Å^{-1})	s_{max} (Å^{-1})
40	0.19	0.87
60	0.24	1.08
80	0.28	1.25
100	0.32	1.42

Electrons incident on the CCD chip generate secondary charge as they pass through the device. Each pixel contains a potential well that accumulates the secondary charge created by electrons incident on or near the pixel.

To measure a diffraction pattern the CCDs operate in a counting mode. This entails repeatedly exposing the CCD for a time, τ. The result of each exposure is to record either that no incident electrons contributed charge to a pixel (null), or that one or more electrons contributed charge to a pixel (count). The charge accumulated in a pixel is not entirely due to secondary charge, during an exposure a significant amount of thermal charge (dark current) is also accumulated. To estimate the amount of thermal charge (dark current) the CCD is repeatedly allowed to accumulate thermal charge for a time, τ, without exposure to electrons. The average thermal charge is called a reference value. The width of the thermal charge distribution is also estimated, half the width is used as a threshold value. After each exposure to electrons the charge accumulated in each pixel

is compared to the sum of the reference and threshold value, for a larger value a count is recorded, for an smaller value a null is recorded. This process does not distinguish between single and multiple incident electrons causing the secondary charge, however section 3.3.3 describes how this can be corrected for when multiple exposures are made.

Calibration of the CCDs uses diffraction patterns from thin polycrystalline films of Au and ThCl. The films of Au and ThCl are held on the arm that is used in alignment of the electron beam. In turn, each film is positioned at the diffraction point and a diffraction pattern obtained. The calculation of a calibration curve for the CCDs is described in section 5.2.1.

Typical exposure periods are $\sim 20\,\mu s$ for calibration patterns and from 100 to $5000\,\mu s$ for diffraction from clusters. The minimum time between exposures is 12.05 ms. For the diffraction patterns displayed in chapter 6 the CCDs have typically been exposed 4000 times, taking about one minute.

3.3.3 The Poisson Correction

If, for a single pixel, counts are recorded in a high proportion of exposures it is likely that there are many exposures where multiple electrons hit the pixel. Conversely, if counts are only recorded for a few exposures it is less likely that there are exposures where multiple electrons hit the pixel. Assuming Poisson statistics, the electron counting can be modeled as follows [105]: the probability of x electrons contributing charge to a pixel (each electron is an event) during a interval τ is given by

$$P(X = x) = \frac{\lambda^x e^{-\lambda}}{x!}, \tag{3.10}$$

where $\lambda = \rho\tau$, the average number of events per interval, and ρ is the event rate. The CCD only distinguishes between a null ($X = 0$) and a count ($X \geq 1$). The corresponding probabilities are then

$$P(X = 0) = e^{-\lambda}, \tag{3.11}$$

$$P(X \geq 1) = 1 - e^{-\lambda}. \tag{3.12}$$

Taking multiple exposures allows an estimate of λ to be made. In N exposures, C will have recorded a count. The ratio C/N is an estimate of the probability of obtaining a count, and is related to λ by Eqn. 3.12, giving

$$\lambda_{estimate} = -\ln\left(1 - \frac{C}{N}\right). \tag{3.13}$$

Eqn. 3.13 is referred to as the Poisson correction and is used to estimate the event rate from the observed C/N ratio. All experimental diffraction profiles are corrected by applying Eqn. 3.13. The effect of applying Eqn. 3.13 to C/N is shown is Fig. 3.9.

Of interest for analysis is the variance of the estimated λ, this is calculated as follows: for a given λ the probability of getting C from N counts is given by the binomial equation

$$P(C \text{ counts from } N \text{ trials }) = \binom{N}{C} p^C q^{N-C}, \tag{3.14}$$

where the probabilities p and q are given by Eqns. 3.12 & 3.11 respectively. The mean, μ of the estimated λ is then

$$\mu = -\sum_{C=0}^{N} \binom{N}{C} p^C q^{N-C} \ln\left(1 - \frac{C}{N}\right), \tag{3.15}$$

and hence the variance, σ^2, is

$$\sigma^2 = \sum_{C=0}^{N} \binom{N}{C} p^C q^{N-C} \left(-\ln\left(1 - \frac{C}{N}\right) - \mu\right)^2. \tag{3.16}$$

The relative uncertainty in λ_{est}, calculated from Eqn. 3.16, is shown in Fig. 3.10. The minimum in the relative uncertainty occurs for $\lambda \approx 1.6$ and in general Fig. 3.10 shows that high event rates ($1 < \lambda < 4$) are preferable to low event rates ($\lambda < 0.5$).

3.4 Beam Sampling

Positioned towards the rear of the diffraction chamber are a quartz deposition rate meter and a TEM grid holder. These devices provide information about the clusters independent of the diffraction experiment. Only one device can be used at a time as to expose TEM grids the grid holder is moved in front of the deposition rate meter. Both devices use the same shutter.

3.4.1 Sampling of Clusters for TEM Observation

The arm that the shutter and TEM grid holder are mounted on is shown in Fig. 3.11. The wheel is capable of holding up to 8 TEM grids that are fixed in place by small circlips. The TEM grids have the standard copper mesh support and are covered by a very thin ($\sim$50 Å) amorphous carbon film. These grids are produced at the Institute de Physique Expérimentale in Lausanne, Switzerland and supplied by Prof. R. Monot. During an experiment the grid holder is generally positioned out of the beam and the clusters land

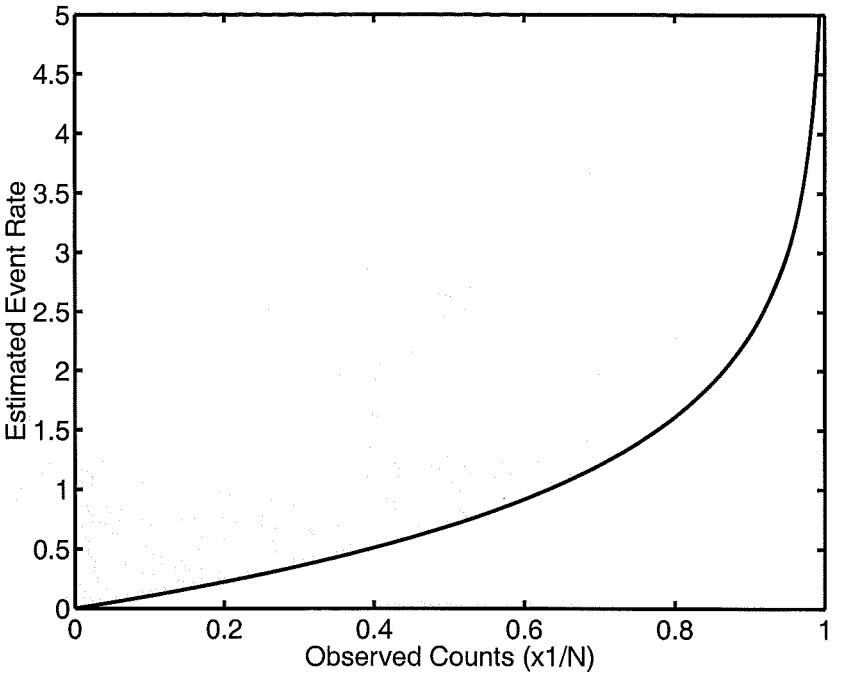

Figure 3.9: The effect of the Poisson correction, the observed C/N ratio is corrected for multiple events. For small values of C/N the correction is small and close to linear, however as C/N approaches 1 the correction has a large non–linear effect.

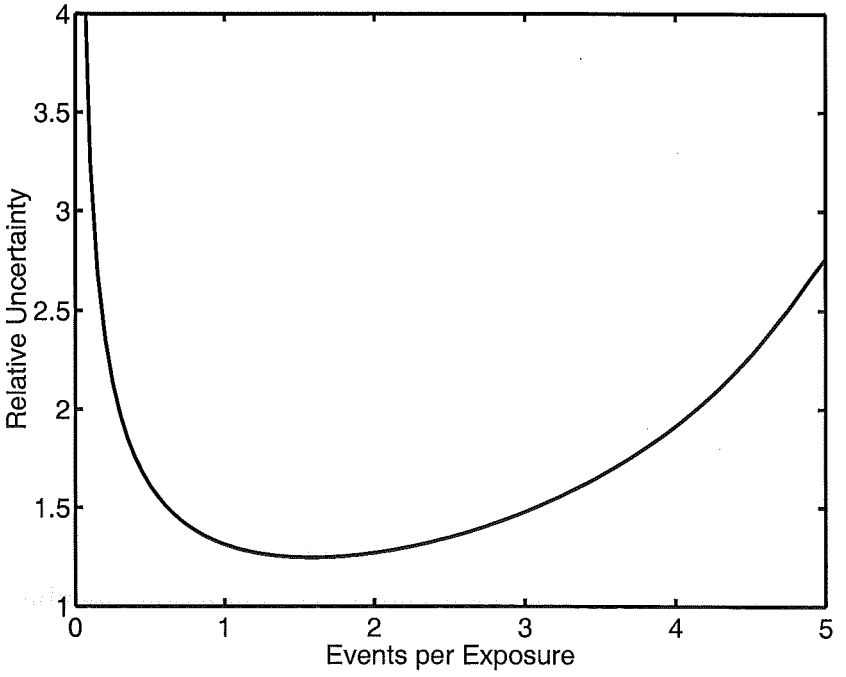

Figure 3.10: The relative uncertainty in the estimated event rate. The uncertainty is a minimum at ~1.6 counts per exposure. The vertical axis represents the quantity $\sqrt{N}\sigma/\rho$, where N, σ & ρ have the same values as in the text. After Hall [105].

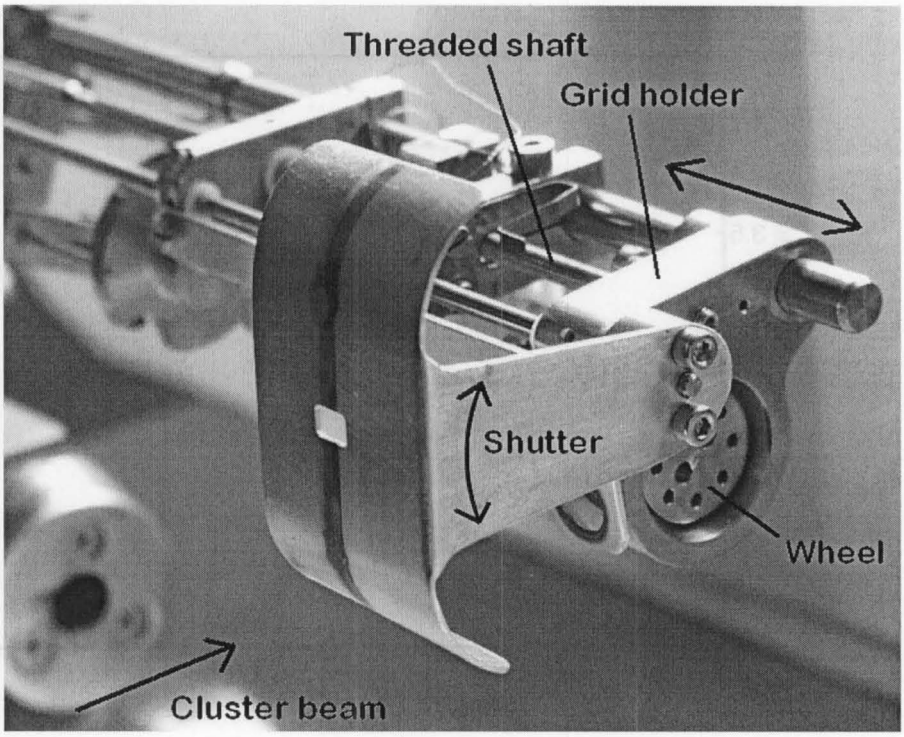

Figure 3.11: The grid holder and shutter arrangement, as shown it is set to expose TEM grids to the cluster beam.

either on the deposition rate meter or on the shutter. When a grid is to be exposed the grid holder is moved into the path of the cluster beam by rotation of the threaded shaft.

For the TEM grids only a brief (~50 ms) exposure to the beam is required (see section 5.3). This is accomplished by passing the rectangular hole in the shutter across the path of the beam.

After an experiment the exposed grids are removed and viewed with a JEOL 1200EX TEM. Unfortunately, the clusters are inevitably exposed to the atmosphere between removal from the vacuum and observation in the TEM. The analysis of the images obtained from the grids is described in section 5.2.3.

3.4.2 Deposition Rate Meter

A Sycon Instruments STM–100/MF deposition rate meter is positioned ~15 cm downstream from where the cluster beam enters the diffraction chamber. At this point the diameter of the cluster beam is similar to the diameter of the sensor in the deposition rate meter and therefore the majority of the clusters land on the sensor. For the deposition rate meter the shutter is either open, so the clusters continually land on the sensor, or closed.

Additional material on the sensor changes its oscillating frequency, and the rate of

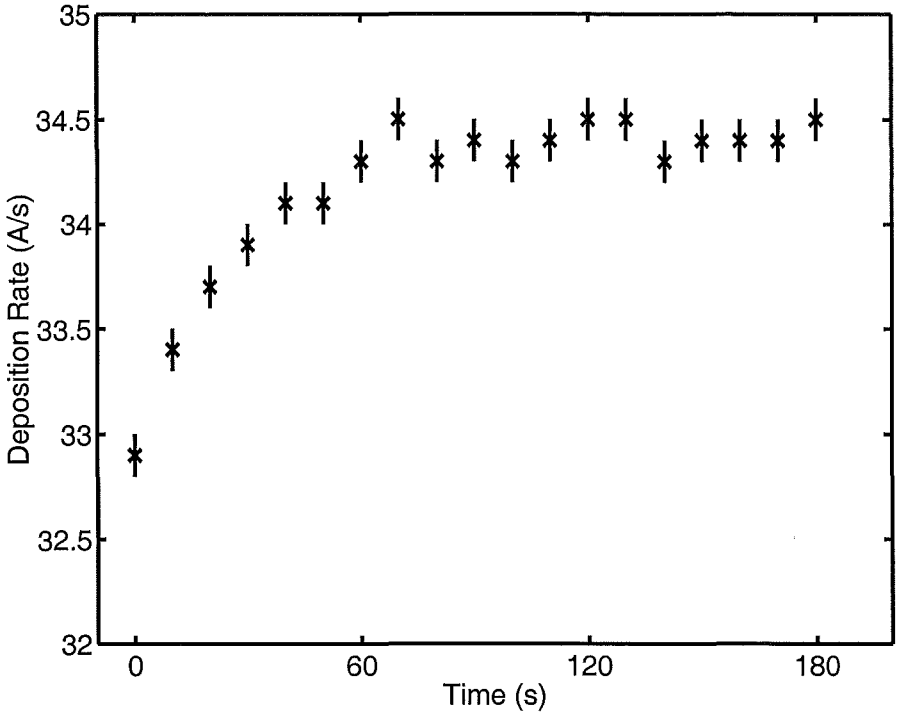

Figure 3.12: Variation of deposition rate over a period of three minutes.

change of frequency is used to determine the rate material is landing on the sensor. Deposition rates are measurable to 0.1 Å/s and the total thickness deposited is recorded in Å units.

Fig. 3.12 shows the variation of deposition rate over a three minute period. Throughout the measurement the deposition rate varies by ~5%. The initial rise in deposition is probably due to the response of the deposition meter rather than a change in cluster flux, as a slow rise in deposition rate is normally observed upon opening the shutter. Taking only the rates between 60 and 180 seconds reduces the variation to ~1%.

The deposition rate meter is most useful in identifying source conditions that produce clusters; the sensitivity and real time display of material flux are advantages over taking repeated diffraction patterns. Other uses for the deposition rate meter are estimating the cluster flux and exposure time for TEM grids (see section 5.3).

Chapter 4

Electron Diffraction

Electron diffraction is a powerful tool in determining the structure of a material. To calculate diffraction patterns for clusters the assumption that the atoms are arranged in a repetitive structure (unit cell) that is generally made when calculating diffraction patterns for bulk materials is not valid. The majority of this chapter is based on the use of the Debye equation to calculate diffraction patterns for model clusters, although some preliminary considerations are initially discussed.

4.1 The Wavelength of Electrons

The wavelength of an electron is given by the de Broglie relationship

$$\lambda = \frac{h}{p}, \tag{4.1}$$

where p is the momentum of the electron, and h is Planck's constant. The momentum of the electron depends on the accelerating voltage. The accelerating voltage used to obtain diffraction patterns is 80 kV, meaning the electrons have an energy that is ~15% of their rest mass, hence the electron's momentum must be treated relativistically. The total energy, E, of the electron is given by

$$E = \sqrt{p^2c^2 + m^2c^4}, \tag{4.2}$$

where m is the mass of the electron and c is the speed of light. The total energy is also the sum of the rest mass and kinetic energy, i.e.

$$E = E_\circ + K, \tag{4.3}$$

where $E_\circ = mc^2$ is the rest mass, and K is the kinetic energy. Combining Eqns. 4.1, 4.2 and 4.3 and solving for the wavelength gives

$$\lambda = \frac{hc}{\sqrt{K(K + 2E_\circ)}}. \tag{4.4}$$

For 80 kV accelerating potential the resulting wavelength for the electron is 4.2×10^{-12}m.

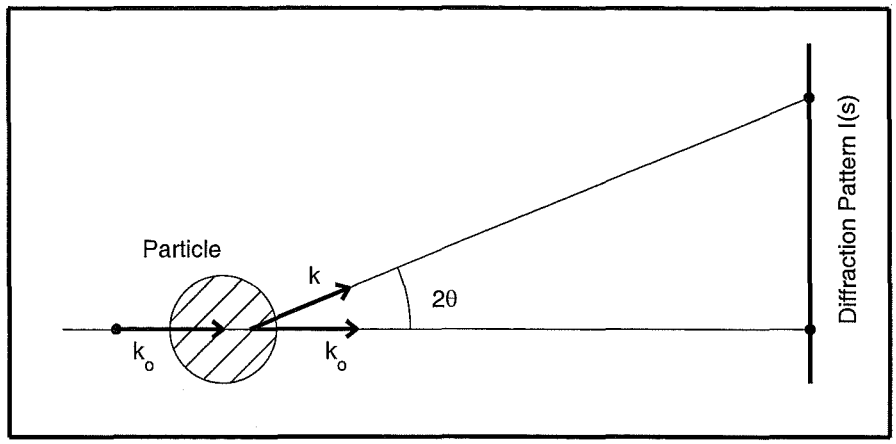

Figure 4.1: Definition of the vectors $\mathbf{k}_o$ and $\mathbf{k}$. After Vainshtein [106].

4.2 The Scattering Parameter

Fig. 4.1 shows the case where an incident wave is scattered by an angle 2θ. The vectors $\mathbf{k_o}$ and $\mathbf{k}$ define the directions of the incident and scattered waves respectively. For a wavelength, λ, the vector, $\mathbf{s}$ is defined by

$$\mathbf{s} = \frac{(\mathbf{k} - \mathbf{k}_o)}{\lambda}. \tag{4.5}$$

The magnitude of $\mathbf{s}$, from here on labeled s, is given by

$$s = \frac{2\sin\theta}{\lambda}. \tag{4.6}$$

The parameter s is referred to as the scattering parameter, and the variation in the intensity of scattered electrons over a range of θ or s creates the diffraction pattern.

4.3 Diffraction from Clusters

The diffraction patterns from clusters can be determined using the dynamic theory or the kinematic approximation. The kinematic approximation assumes the incident beam intensity is unchanged while propagating through the cluster and leads to the Debye equation [107]. A general method using the dynamic theory has been developed by Hall *et al.* [108] but is computationally intensive. Fortunately the error in the kinematic approximation is, to first order, an overestimate by a constant factor across the diffraction profile and means that diffraction patterns calculated using the kinematic approximation are satisfactory for analysis [109].

The Debye equation requires no assumptions regarding the structure of the cluster and can be used to calculate the diffraction pattern for an arbitrary arrangement of atoms. In the derivation of the Debye equation it is assumed that the observed diffraction pattern is created by many clusters each randomly oriented with respect to each other, hence the diffraction pattern produced is similar in appearance to a Debye–Scherrer (powder) diffraction pattern. The Debye equation gives the intensity profile along a radial section of the diffraction pattern. For a cluster with N atoms of a single element, the Debye equation is

$$I_N(s) = I_0 N f^2(s) \left(1 + \frac{D(s)}{N} \sum_{n \neq m} \frac{\sin(2\pi s r_{mn})}{2\pi s r_{mn}} \right), \tag{4.7}$$

where I_0 is the incident intensity, s is the scattering parameter, $f(s)$ is the atomic scattering factor, r_{mn} is the distance between atoms m and n and $D(s)$ is the Debye–Waller factor given by

$$D(s) = exp\left(-\frac{(2\pi s \Delta X)^2}{3} \right), \tag{4.8}$$

where ΔX is the rms displacement of atoms from their equilibrium position due to thermal motion. The effect of the Debye–Waller factor is an increasing attenuation of the diffraction pattern as s is increased.

4.4 Calculation of the Debye Equation

Calculation of the diffraction pattern begins by creating a model cluster with the desired size, shape and structure. The model clusters used were created by two different means: the first method used bulk and symmetry properties to define atomic positions; the models created this way are called geometric models. The second method used MD simulation to determine the atomic positions, and, unless stated otherwise, the model clusters were relaxed to 0 K. These models are called relaxed models. From a model cluster the inter–atomic distances, r_{mn} are calculated. In general many of the distances are approximately the same and can be binned together provided a modification to the Debye equation is made. The modified Debye equation is

$$I_N(S) = I_0 N f^2(s) \left(1 + \frac{D(s)}{N} \sum_{n} h(n) \frac{\sin(2\pi s r_n)}{2\pi s r_n} \right), \tag{4.9}$$

where $h(n)$ is the number of times the inter–atomic distance r_n occurs. The effect of bin size on the diffraction pattern has been considered by Hall [48] who found that

for a bin size of 0.001 nm the effect on the diffraction pattern is negligible. Thus for all the calculation performed during this study a bin size of 0.001 nm was used. Binning the inter–atomic distances significantly increases the speed at which the Debye equation can be calculated. Calculation speed can also be increased by using a Fast Fourier Transform (FFT) to calculate sinc terms [110]. The improvement in speed is impressive, especially when the diffraction pattern for large clusters or across a wide range of scattering angles is required. For this study the FFT routine was not extensively used as binning alone is sufficient to reduce calculation time to, at most, a few seconds.

4.4.1 Changing the Lattice Parameter

The value of the lattice parameter used in a model cluster may differ from the lattice parameter of clusters produced during experiments because the cluster temperature and effects of surface tension are generally not well known. To recalculate the Debye equation for each change in the lattice parameter would be laborious even using the FFT routine. Fortunately the computationally intensive part of the Debye equation is the multiple sinc terms and the effect of changing the lattice parameter on the sinc terms is equivalent to a simple rescaling of the s axis. In the Debye equation the sinc terms appear as

$$\sum_n h(n)\frac{\sin(2\pi s r_n)}{2\pi s r_n}. \tag{4.10}$$

Each term in the summation corresponds to an interatomic distance within the cluster. For one interatomic distance, r, the sin term has a period $1/r$. If the lattice parameter is changed by a factor l, the interatomic distance is also changed by a factor l. The new period for the sin term is then $1/lr$, indicating that the s axis needs to be scaled by $1/l$, i.e. for

$$r \longrightarrow lr, \tag{4.11}$$

$$s \longrightarrow \frac{1}{l}s. \tag{4.12}$$

This process is used in the analysis of diffraction patterns from Pb clusters (see chapter 5) to optimize the match between the experimental pattern and the combination of patterns from model clusters.

4.5 Examples of Cluster Diffraction

This section displays diffraction patterns from model clusters of various sizes and structures. Each diffraction pattern displayed is calculated using the Debye equation and assuming a Debye–Waller factor of 1 (i.e. T=0 K, no thermal motion). The section is split into several parts, the first part displays diffraction patterns from Pb clusters, this is followed by an examination of the effect of twinning in FCC clusters. Then the diffraction patterns from various shapes of Zn clusters are shown. The section finishes with discussions on the effect of size, shape and structure and the effect of domains within the cluster on the diffraction pattern.

For display purposes the intensity of each diffraction pattern is scaled so the intensity of the highest peak in each diffraction pattern is equal. The true ratio of intensity between patterns is, to first order, the ratio of the number of atoms in the clusters.

4.5.1 Diffraction Patterns from Pb Clusters

The analysis of experimental diffraction patterns from Pb clusters, described in chapter 5, relies on the ability to reproduce the experimental pattern using a combination of diffraction patterns from model clusters with different sizes and structures. For each structure considered in analysis, diffraction patterns from several different sized model clusters are shown.

The set of structures includes: FCC, decahedral, icosahedral, anti–Mackay icosahedral, shaved icosahedral and liquid. For FCC, decahedral and icosahedral structures both geometric and relaxed cluster models were created. For anti–Mackay icosahedra, shaved icosahedra and liquid structures only the MD models were available. In all cases Dr. S. Hendy performed the required MD simulations.

- Cuboctahedra (FCC)
  Geometric cuboctahedra (triangular facets) were created using the bulk lattice parameter for Pb. Fig. 4.2 shows diffraction patterns from clusters with (a) 147, (b) 923 and (c) 6525 atoms. Fig. 4.3 shows the diffraction patterns from relaxed clusters, with (a) 147, (b) 923 and (c) 6525 atoms. Increasing the size significantly sharpens the diffraction peaks from both the geometric and relaxed clusters. The slight attenuation of the diffraction peaks at higher s values in the patterns from relaxed clusters compared to the patterns from geometric clusters is caused by the deformation of the perfect FCC lattice in the relaxation process. Diffraction patterns from cuboctahedra with hexagonal facets could also be considered, however as both shapes are very similar there is little difference between the diffraction patterns.

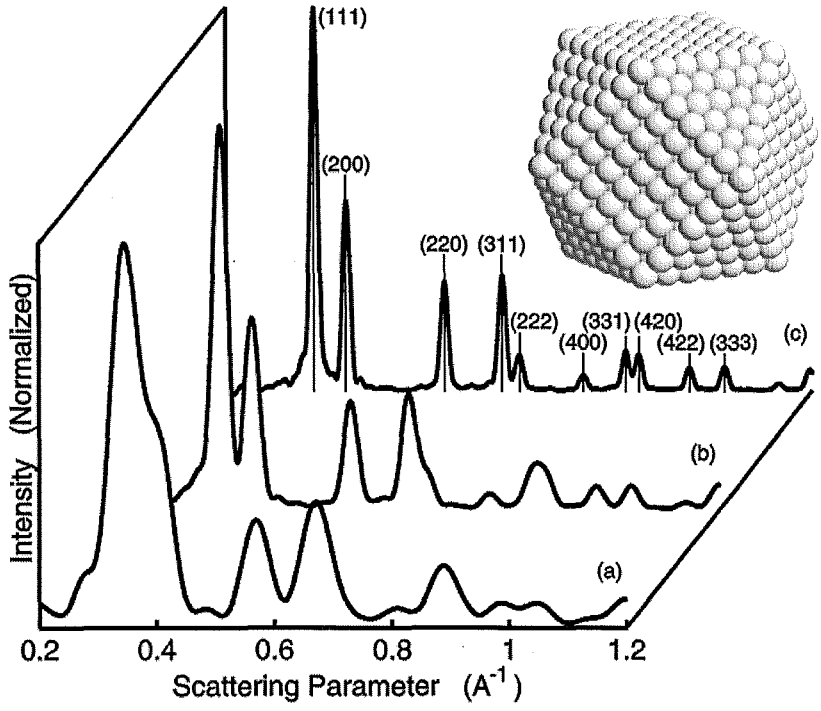

Figure 4.2: Diffraction patterns from geometric cuboctahedral (FCC) clusters: (a) 147, (b) 923 and (c) 6525 atoms. Inset shows the cluster corresponding to diffraction pattern (b). The vertical lines in diffraction pattern (c) indicate the position of bulk (FCC) peaks for Pb.

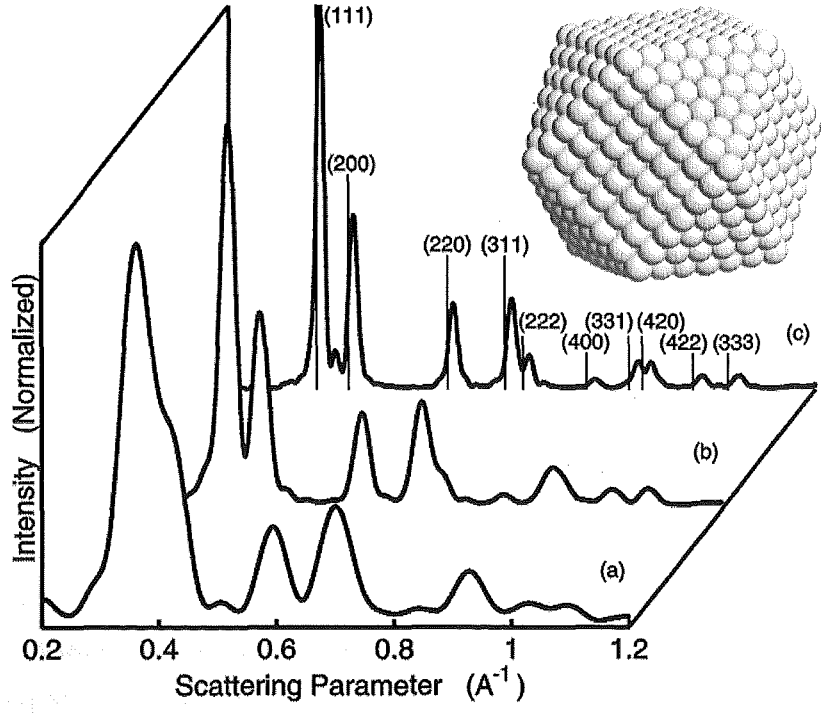

Figure 4.3: Diffraction patterns from relaxed cuboctahedral (FCC) clusters: (a) 147, (b) 923 and (c) 6525 atoms. The cluster shown corresponds to diffraction pattern (b). The vertical lines in diffraction pattern (c) indicate the position of bulk (FCC) peaks for Pb. The displacement of the peaks in diffraction pattern (c) from the bulk peaks is due to a contraction of the lattice parameter in the cluster.

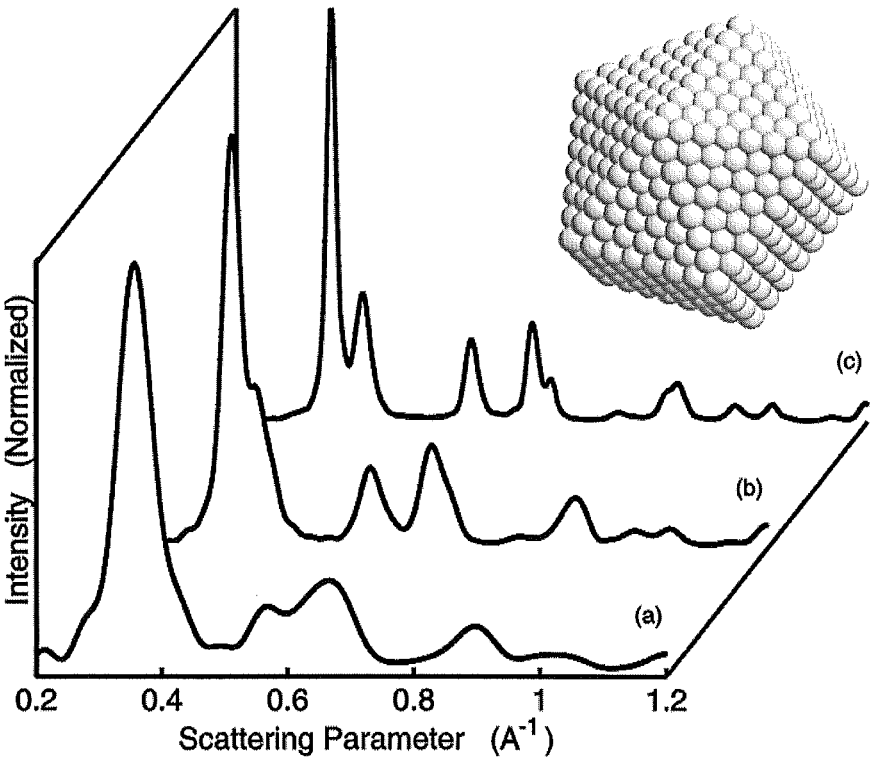

Figure 4.4: Diffraction patterns from geometric decahedral clusters: (a) 116, (b) 992 and (c) 6497 atoms. Inset shows the cluster corresponding to diffraction pattern (b).

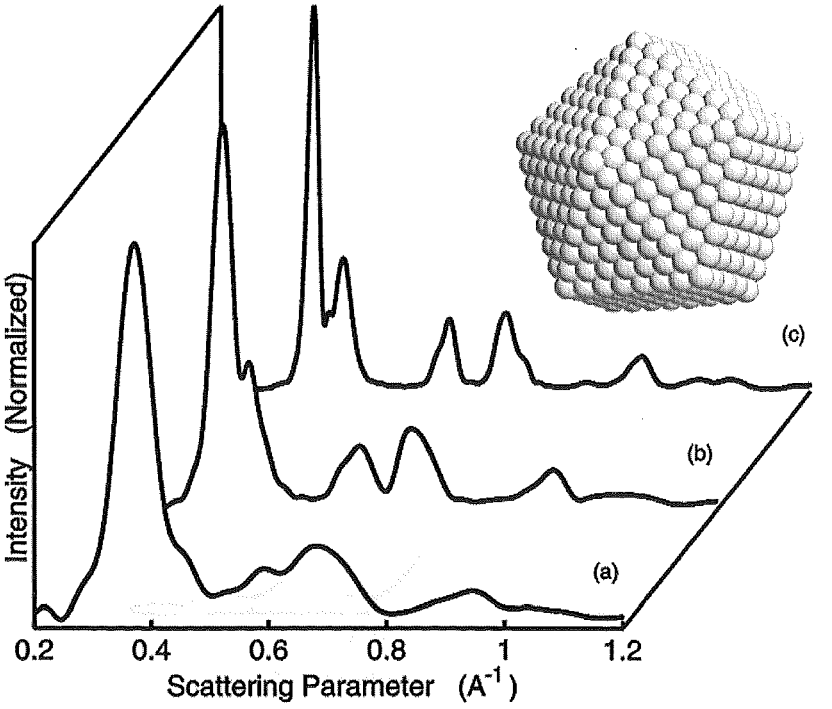

Figure 4.5: Diffraction patterns from relaxed decahedral clusters: (a) 116, (b) 992 and (c) 6497 atoms. Inset shows the cluster corresponding to diffraction pattern (b).

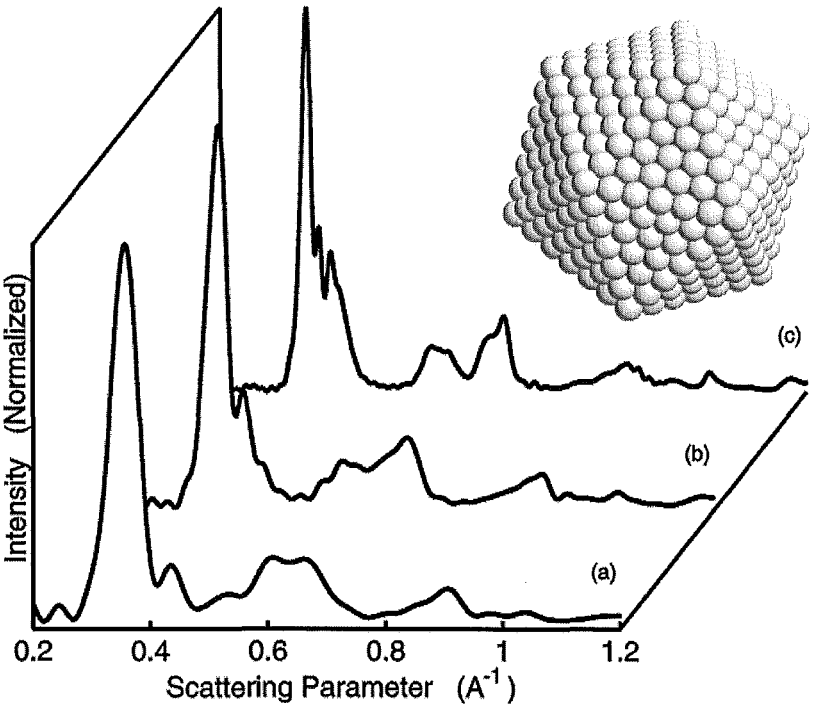

Figure 4.6: Diffraction patterns from geometric icosahedral clusters: (a) 147, (b) 923 and (c) 6525 atoms. Inset shows the cluster corresponding to diffraction pattern (b).

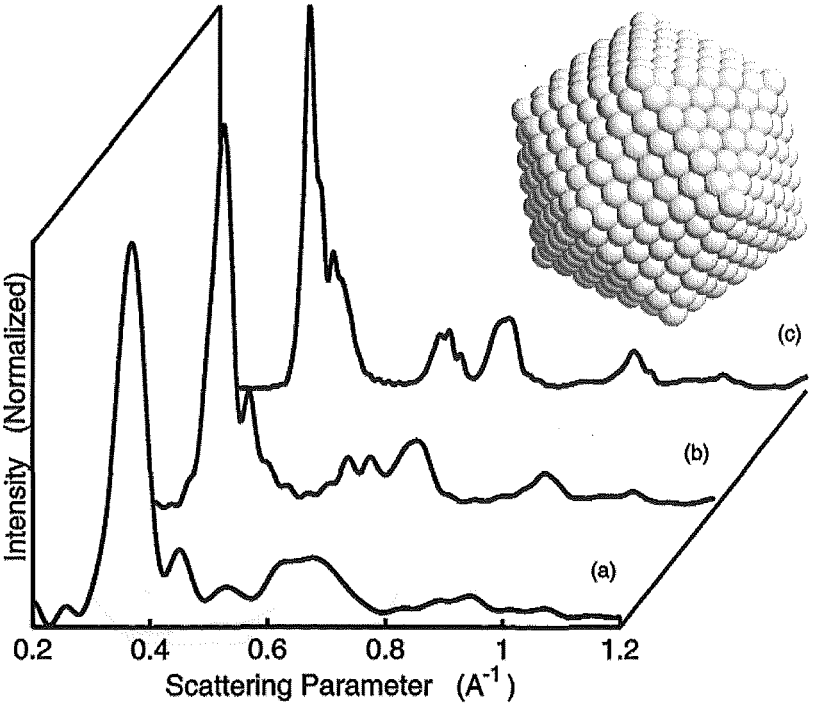

Figure 4.7: Diffraction patterns from relaxed icosahedral clusters: (a) 147, (b) 923 and (c) 6525 atoms. Inset shows the cluster corresponding to diffraction pattern (b).

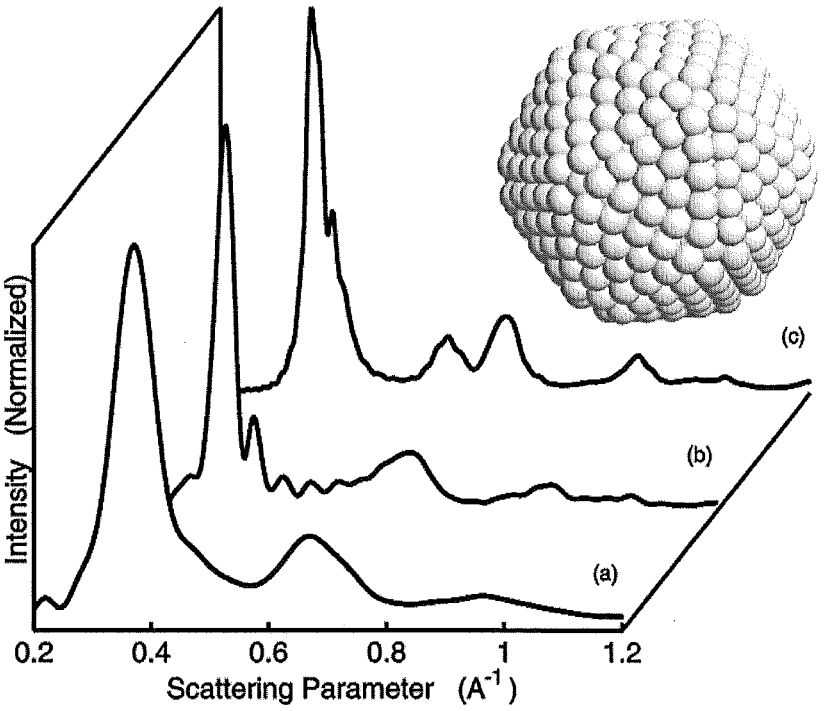

Figure 4.8: Diffraction patterns from MD relaxed anti–Mackay icosahedra: (a) 115, (b) 861 and (c) 6403 atoms. Inset shows the cluster corresponding to diffraction pattern (b).

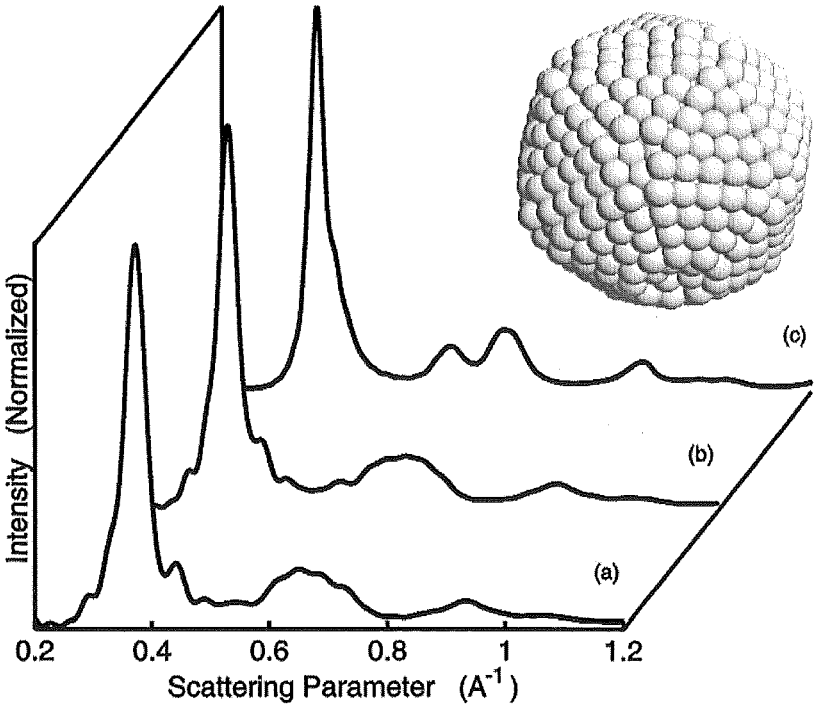

Figure 4.9: Diffraction patterns from shaved icosahedra: (a) 561, (b) 923 and (c) 5083 atoms. Inset shows the cluster corresponding to diffraction pattern (b).

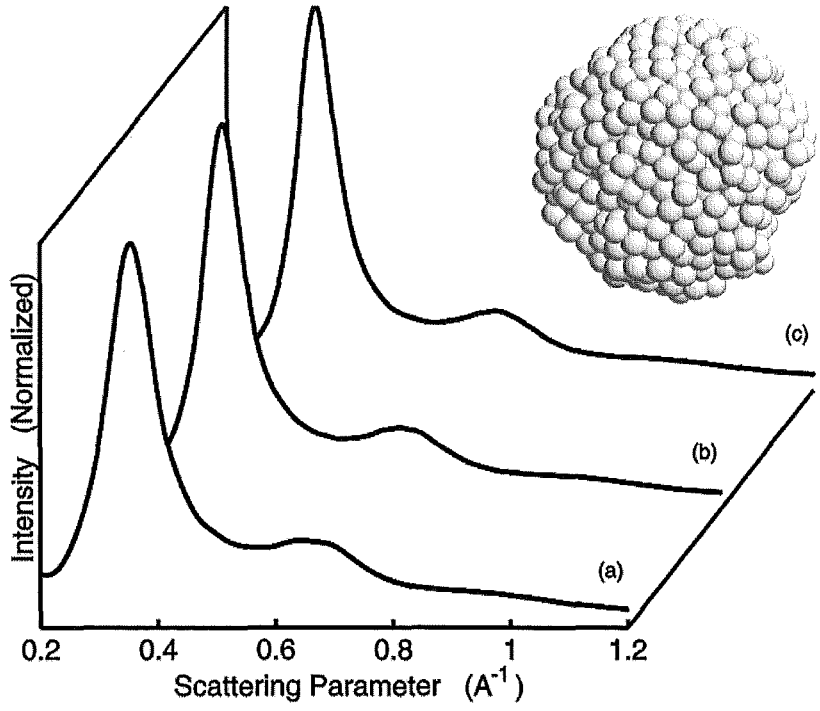

Figure 4.10: Diffraction patterns from MD generated liquid drops at 900K: (a) 147, (b) 923 and (c) 2057 atoms. Inset shows one of the clusters used in calculating diffraction pattern (b).

- Truncated Decahedra

  Geometric truncated decahedra were created using the description given by Ino [57]. The constituent (truncated) tetrahedra are deformed by homogeneous elastic strain to make the truncated decahedra space filling. Fig. 4.4 shows diffraction patterns from clusters with (a) 116, (b) 992 and (c) 6497 atoms. Fig. 4.5 shows the diffraction patterns from clusters that have been relaxed using MD, with (a) 116, (b) 992 and (c) 6497 atoms. A noticeable difference between the diffraction patterns from the two larger geometric and the relaxed clusters is the shape of the diffraction peaks at 0.57 & 0.67 Å^{-1}. For the geometric clusters the deformation of the FCC lattice in each tetrahedra is small resulting peak shapes similar to those from cuboctahedra in Fig. 4.2. For the relaxed clusters the deformation of the tetrahedra caused by relaxation changes the peak shapes. As for the cuboctahedra, increasing the cluster size sharpens the diffraction peaks.

- Icosahedra

  Geometric icosahedra were created using the description given by Ino [57]. As in the decahedra, the tetrahedra are deformed by homogeneous elastic strain to make the icosahedra space filling. Fig. 4.6 shows diffraction patterns from clusters with (a) 147, (b) 923 and (c) 6525 atoms. Fig. 4.7 shows the diffraction patterns from

clusters that have been relaxed using MD, with (a) 147, (b) 923 and (c) 6525 atoms. The diffraction patterns from geometric and relaxed clusters are similar, but are distinctly different to the diffraction patterns from cuboctahedra. For the icosahedra an increase in cluster size sharpens only the main diffraction peak. Another size dependent feature of diffraction patterns from icosahedra is the shoulder on the main peak, for the 147 atom cluster the shoulder appears at $s \approx 0.44\,\text{Å}^{-1}$, for larger icosahedra this feature shifts to lower s values.

- Anti–Mackay Icosahedra

  Anti–Mackay icosahedra are made by adding a new shell to the normal icosahedral structure. The new layer has HCP stacking with respect to the internal FCC stacking. Fig. 4.8 shows the diffraction patterns from relaxed anti–Mackay icosahedra with (a) 115, (b) 861 and (c) 6403 atoms. As the difference between icosahedra and anti–Mackay icosahedra is only the outer layer, the greatest differences between diffraction patterns from these structures is seen at small sizes (where the fraction of surface atoms is higher). The diffraction patterns in Fig. 4.7 and Fig. 4.8 from the smallest clusters are quite different, whereas diffraction patterns from the larger clusters are similar.

- Shaved Icosahedra

  Like the anti–Mackay icosahedra the external layer of the shaved icosahedra has HCP stacking with respect to the underlying layers, however shaved icosahedra also contain internal stacking faults. Fig. 4.9 shows diffraction patterns from shaved icosahedra with (a) 561, (b) 923 and (c) 5083 atoms. The diffraction patterns from the shaved icosahedral structures tend to have a smoother profile than the other types of icosahedra. Also, for the 5083 atom cluster, the shoulder on the main peak is much less pronounced than in diffraction patterns from other types of icosahedra with a similar size.

- Liquid Drops

  Three sizes of liquid drop, 147, 923 and 2057 atoms, were simulated by MD at a temperature of 900 K. For each size 10 different liquid drops were obtained. For a given size the diffraction patterns from each drop are similar, but not identical. To obtain a characteristic diffraction pattern for each size the 10 diffraction patterns were averaged. The resulting patterns for each size are show in Fig. 4.10. For liquid drops the size has very little effect on the diffraction pattern.

4.5.2 Twinning in FCC Clusters

In a perfect FCC lattice (111) planes are stacked in a repetitive pattern where each layer can be labeled either A, B or C. The stacking proceeds as ...ABCABCABC..., however if one of the planes is a twin plane the stacking becomes ...ABCA<u>B</u>ACBA.... This section examines the effect of twinning on the diffraction patterns of spherical geometric FCC models.

In the clusters created each (111) plane along one [111] axis has a probability of being a twin plane. Both the position and number of twin planes in a cluster affect the resulting diffraction pattern. For each size and probability of twinning 100 individual clusters were created and the resulting diffraction patterns averaged to obtain a characteristic diffraction pattern.

The averaged diffraction patterns from clusters with ~470, ~1100 & ~5900 atoms are shown in Figs. 4.11, 4.12 & 4.13 respectively. Comparing the diffraction patterns from twinned clusters and FCC cuboctahedra (Fig. 4.2) shows that twinning has the greatest effect on the peak at $s \approx 0.4\,\text{Å}^{-1}$. Increasing the probability of twinning broadens this peak and shifts it to lower s. The overall effect is that the diffraction patterns tend to look more like those from decahedra. Shown in Fig. 4.14 is a comparison between a 2491 atom decahedra and the average of 100 twinned (20%) FCC clusters with ~2200 atoms. The similarity of the diffraction patterns of these two structures makes unambiguously determining the presence of decahedra from diffraction data difficult.

For a higher probability of twin planes the effect on the diffraction pattern is more extreme. Fig. 4.15 shows the effect of 20%, 50% and 80% twinning in ~2200 atom clusters. Increasing the probability of twinning to high values means the structure becomes more characteristic of HCP than FCC, naturally if the probability of twinning is 100% a perfect HCP structure is obtained.

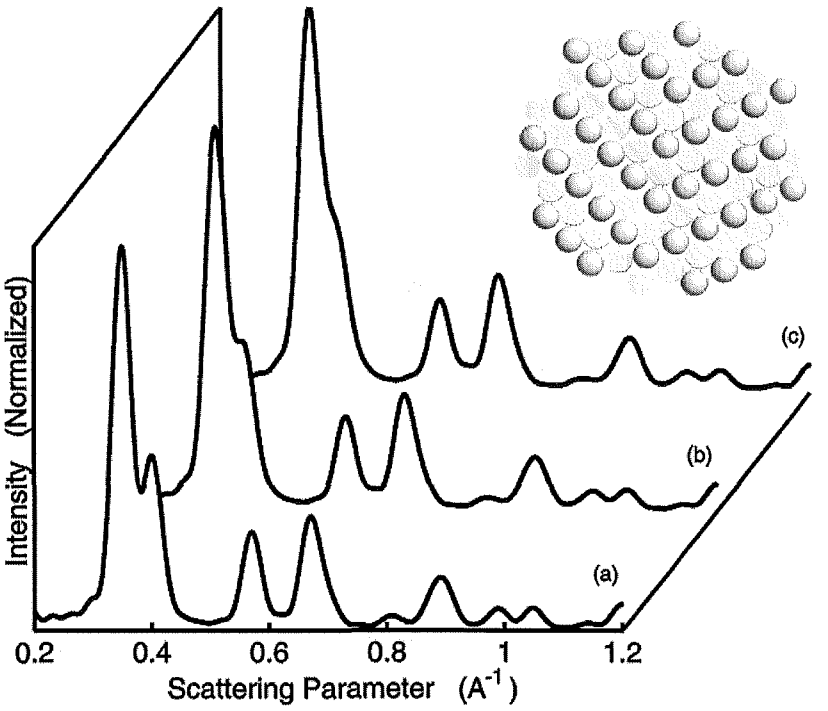

Figure 4.11: The average of diffraction patterns from 100 spherical FCC Pb clusters. Each cluster contains ~470 atoms and a random number of parallel twin planes in random positions along one [111] axis. The probability of a given plane being a twin plane is (a) 10%, (b) 20% and (c) 30%. The inset shows a cross section of a cluster containing a single twin plane.

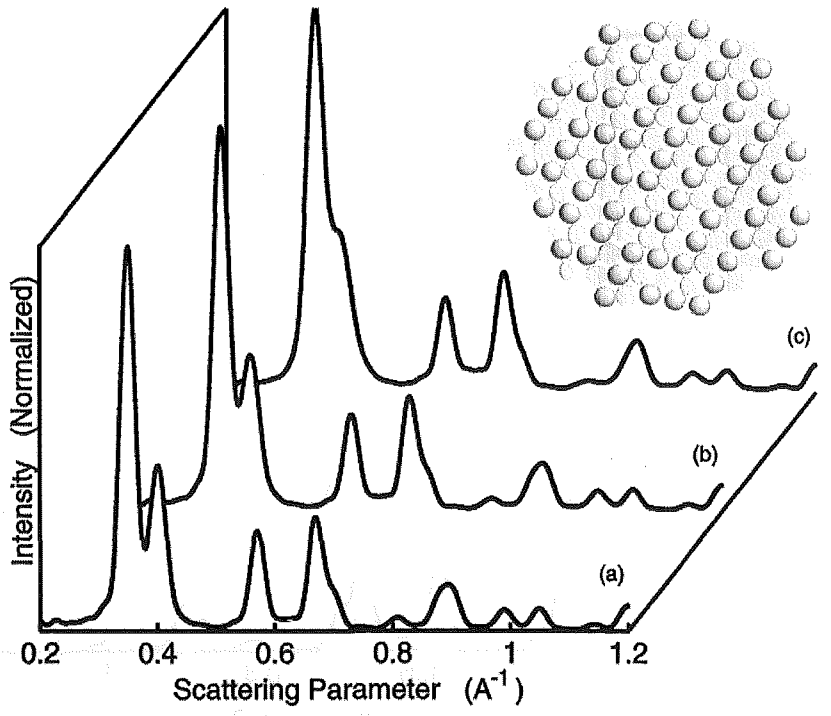

Figure 4.12: The average of diffraction patterns from 100 spherical FCC Pb clusters. Each cluster contains ~1100 atoms and a random number of parallel twin planes in random positions along one [111] axis. The probability of a given plane being a twin plane is (a) 10%, (b) 20% and (c) 30%. The inset shows a cross section of a cluster containing three twin planes.

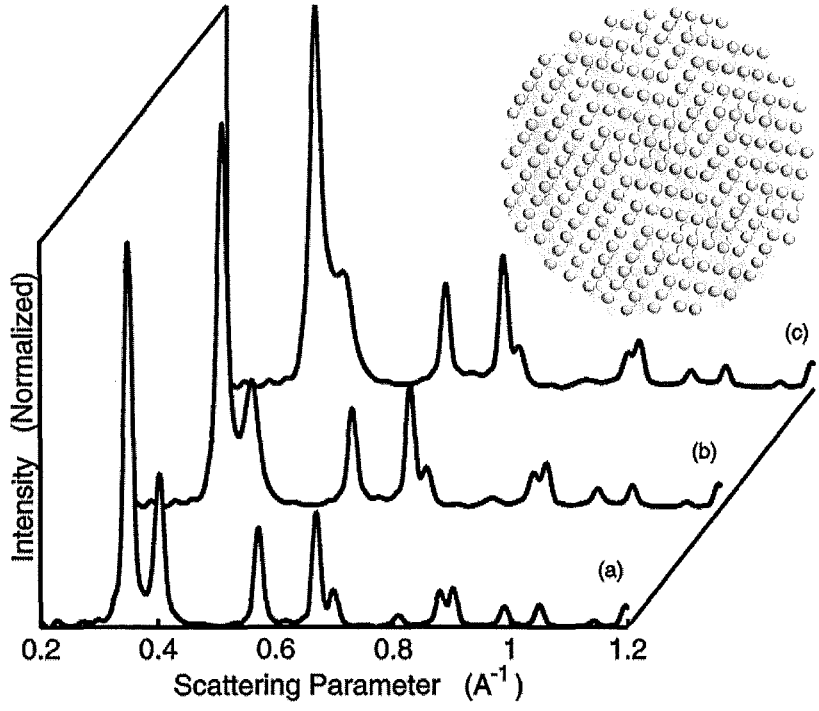

Figure 4.13: The average of diffraction patterns from 100 spherical FCC Pb clusters. Each cluster contains ~5900 atoms and a random number of parallel twin planes in random positions along one [111] axis. The probability of a given plane being a twin plane is (a) 10%, (b) 20% and (c) 30%. The inset shows a cross section of a cluster containing three twin planes.

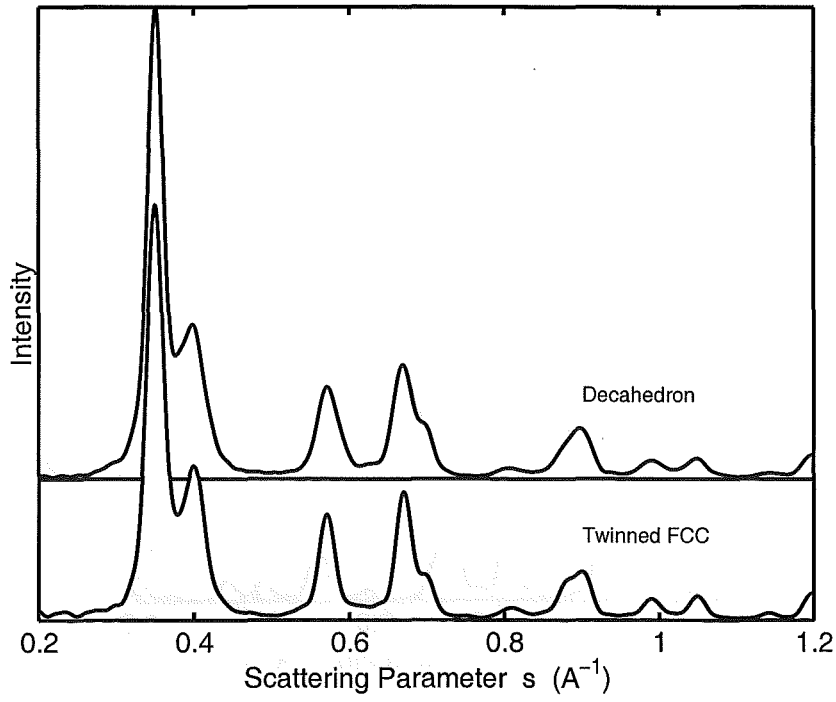

Figure 4.14: Comparison of 2491 atom decahedron (top) with the average of 100 twinned (20%) FCC clusters containing ~2200 atoms (bottom). The diffraction patterns have been scaled so the minor peaks have approximately equal intensity between the two structures.

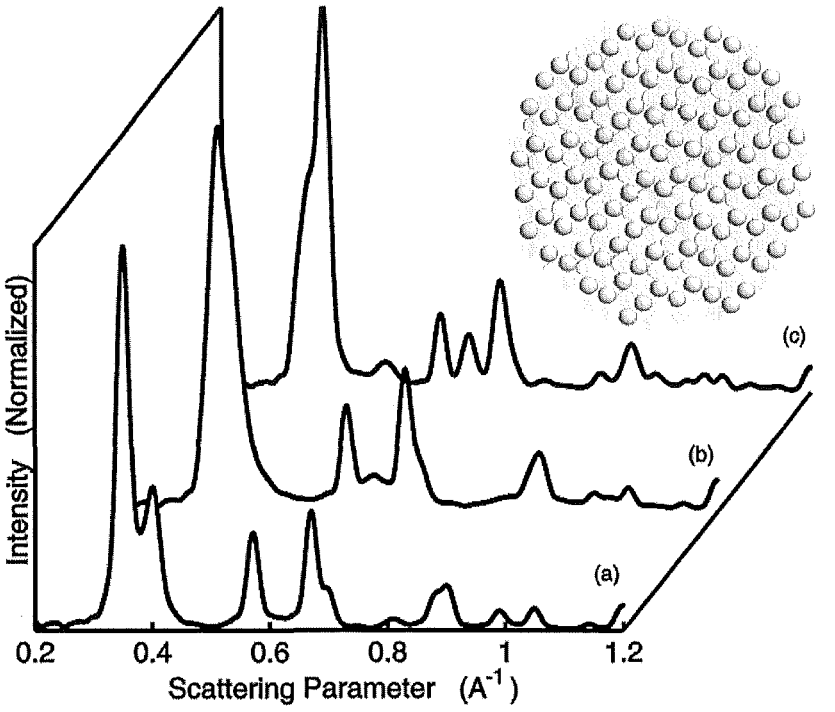

Figure 4.15: The average of diffraction patterns from 100 spherical FCC Pb clusters. Each model cluster contains ~2200 atoms and a random number of parallel twin planes. The probability of a given plane being a twin plane is (a) 20%, (b) 50% and (c) 80%. The inset shows a cross section of a cluster containing 12 twin planes.

4.5.3 Diffraction Patterns from Zn Clusters

The inability to obtain diffraction patterns from Zn clusters means it is unknown whether structures other than the bulk structure (HCP) would have been required for analysis. However, in a TEM examination of Zn clusters by Eversole and Broida [52] a variety of cluster shapes were observed. The dominant shapes observed were plate, column and hourglass. Although electron diffraction is relatively insensitive to the shape of the cluster, the significant difference between the shapes observed may mean some shape related information would have been available from the diffraction patterns. Below diffraction patterns from Zn clusters (based on bulk Zn lattice parameters) with spherical, plate, column and hourglass shapes are shown.

Also shown are the diffraction patterns from several low energy structures found by Michaelian *et al.* [111] during an extensive search for the optimum structure of small Zn clusters.

- Spherical clusters

  Although Eversole and Broida did not report spherical zinc clusters, spherical clusters are included here for comparison. Spherical HCP clusters were created by cutting a spherical section out of a large HCP lattice that had the bulk Zn lattice

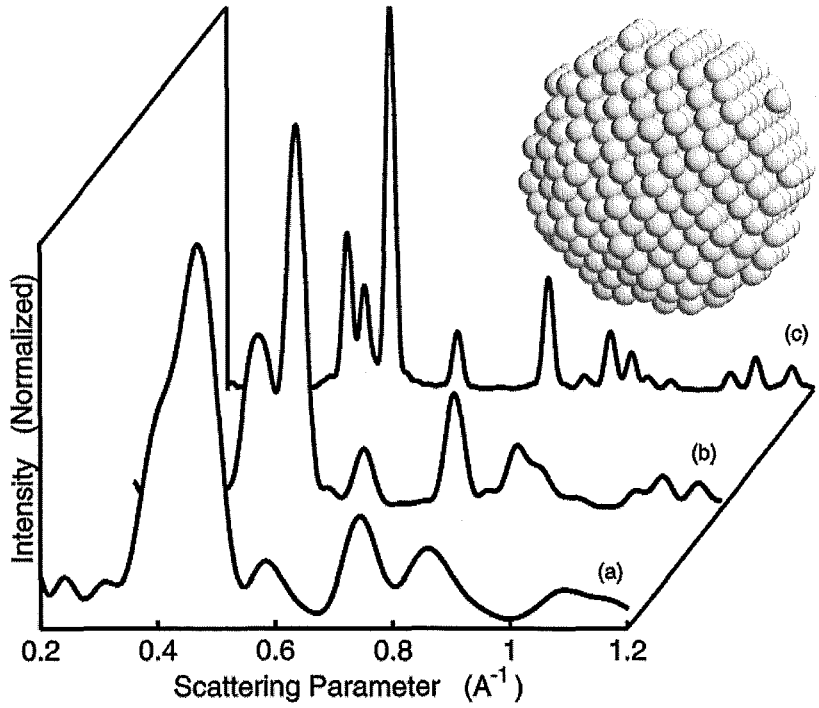

Figure 4.16: Diffraction patterns from spherical shaped zinc clusters: (a) 147 atoms, (b) 931 atoms and (c) 6533 atoms. The inset shows the cluster corresponding to diffraction pattern (b).

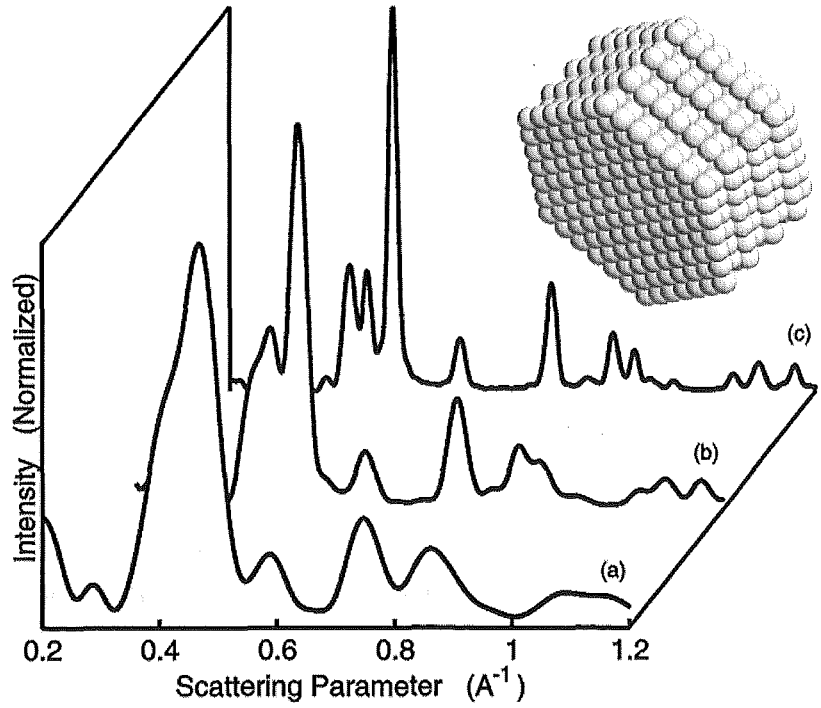

Figure 4.17: Diffraction patterns from plate shaped zinc clusters: (a) 165 atoms, (b) 940 atoms and (c) 6307 atoms. The inset shows the cluster corresponding to diffraction pattern (b).

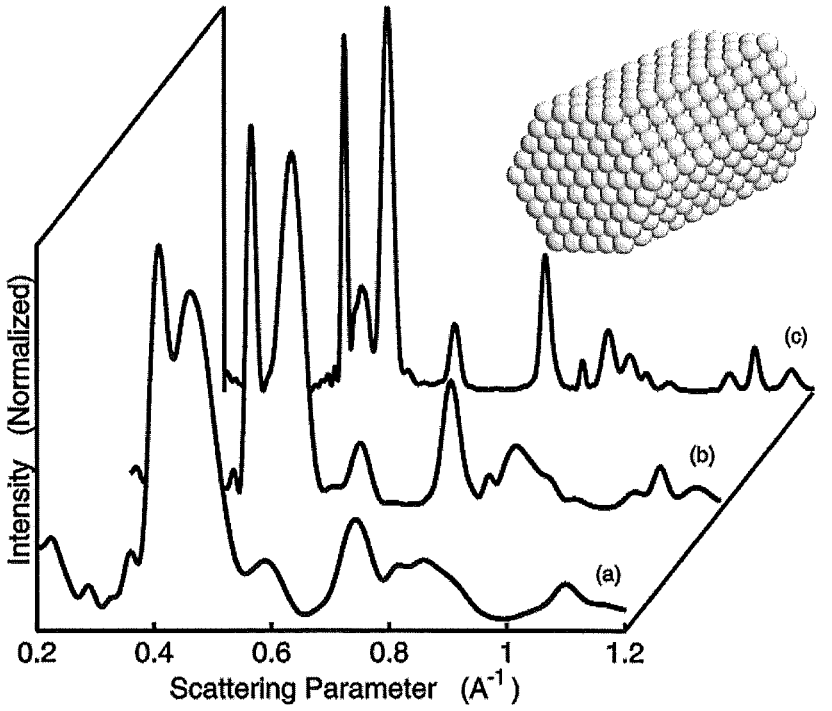

Figure 4.18: Diffraction patterns from column shaped zinc clusters: (a) 186 atoms, (b) 1090 atoms and (c) 7362 atoms. The inset shows the cluster corresponding to diffraction pattern (b).

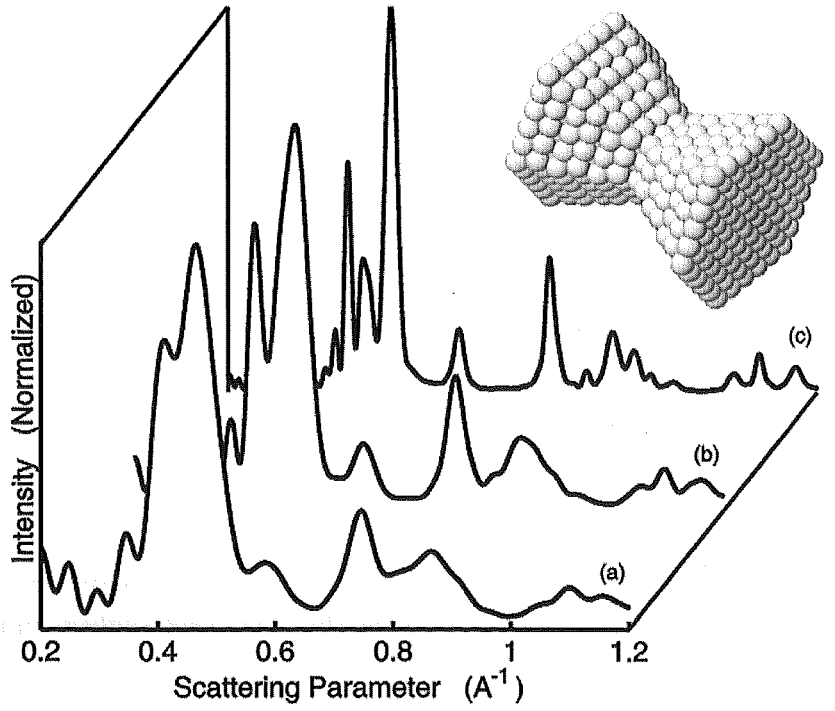

Figure 4.19: Diffraction patterns from hourglass shaped zinc clusters: (a) 197 atoms, (b) 697 atoms and (c) 5821 atoms. The inset shows the cluster corresponding to diffraction pattern (b).

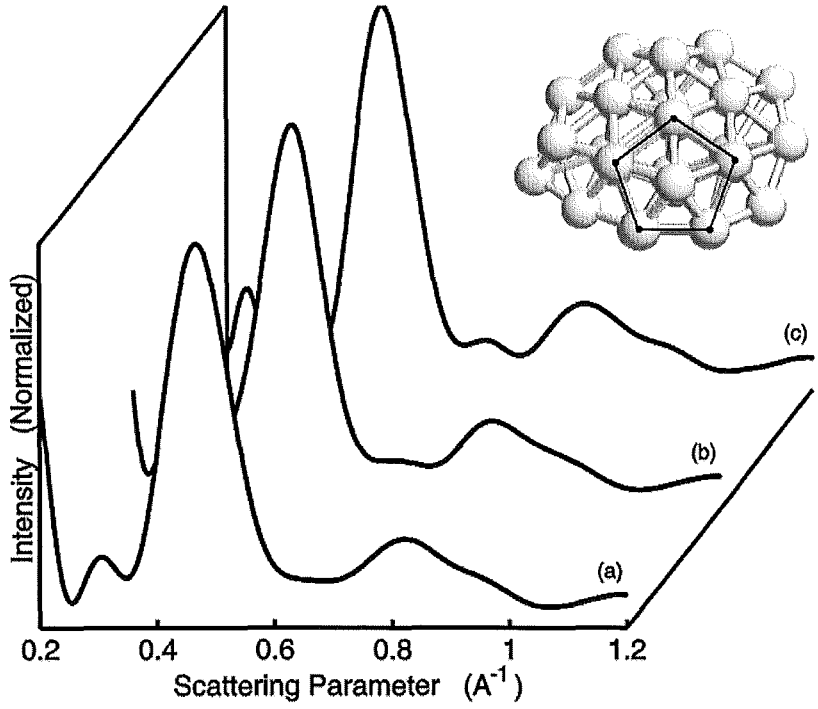

Figure 4.20: Diffraction patterns from small zinc clusters with optimized structures: (a) 38 atoms, (b) 55 atoms and (c) 75 atoms. The insets show the 38 atom cluster with the off centre fivefold axis of symmetry highlighted.

parameters. Fig. 4.16 shows diffraction patterns for clusters with (a) 147, (b) 931 and (c) 6533 atoms. The diffraction patterns produced by the HCP structure are significantly different to any of the diffraction patterns shown in section 4.5.1.

- Plate clusters

  These clusters have the shape of a hexagonal plate. The hexagonal base is the basal plane of the HCP structure and has a width approximately twice the thickness of the plate. Fig. 4.17 shows the diffraction patterns for clusters with (a) 165, (b) 940 and (c) 6307 atoms. Comparing the diffraction patterns from the 6307 atom plate cluster (Fig. 4.17(c)) and the 6533 atom spherical cluster (Fig. 4.16(c)) shows there is a small attenuation of the first diffraction peak for the plate cluster. The intensity of the first peak is related to the thickness (number of close packed planes) of the cluster. For a given number of atoms the spherical shaped cluster is slightly thicker than the plate shaped cluster making the first peak slightly more intense, however the two shapes produce very similar diffraction patterns overall.

- Column clusters

  These clusters are similar to the plate clusters, except that the ratio of edge lengths is different. The width of the base is now approximately half the thickness of the

cluster. Fig. 4.18 shows the diffraction patterns for clusters with (a) 186, (b) 1090 and (c) 7362 atoms. The increased thickness of these clusters means the first peak in the diffraction patterns is now very intense compared to the same peak in diffraction patterns from spherical and plate shaped clusters.

- Hourglass clusters

  The hourglass shape is effectively two truncated hexagonal pyramids joined at the apex. The width at the join is approximately half the width of the base. As for the plate and column clusters the base is the basal plane of the HCP structure. Fig. 4.19 shows the diffraction patterns for clusters with (a) 197, (b) 697 and (c) 5821 atoms. Again the first peak in the diffraction patterns is more intense than the same peak in the patterns from spherical and plate shaped clusters.

- Michaelian's clusters

  Clusters with 13, 38, 55, 75 and 147 atoms have been modeled by Michaelian *et al.* [111] using a combination of the Gupta potential [76, 112] and a symbiotic algorithm[1] [113]. Atomic co–ordinates for the lowest energy cluster with 38 atoms and co–ordinates for low energy clusters with 55 and 75 atoms were provided by Michaelian. The diffraction patterns from the 38, 55 and 75 atom clusters are shown in Fig. 4.20. Michaelian *et al.* describe the clusters as disordered, however the 38 atom cluster, shown in Fig. 4.20, resembles a decahedron with an off centre fivefold axis of symmetry. One side of the 55 atom cluster also has fivefold symmetry and appears almost icosahedral, while the remainder is disordered. The 75 atom cluster appears mostly disordered.

4.5.4 The Effect of Size, Shape and Structure

Examining the range of diffraction patterns shown in Figs. 4.2 to 4.20 allows several general features related to the size, shape and structure of the clusters to be identified.

The effect of increasing the cluster size tends to be a sharpening of the diffraction peaks. The effect is strongest for FCC and HCP structures, weaker in twinned structures and almost non–existent for liquid drops. This means that peak widths are related to structure as well as size. Hence, when interpreting experimental diffraction patterns a sharpening of diffraction features cannot immediately be associated with an increase in cluster size, a possible change in structure must be considered.

Changing the shape of the cluster tends to change only the relative peak heights in the diffraction pattern. This is seen by comparing diffraction patterns from the four different

[1] An alternative method to MD for finding the lowest energy structure of a cluster.

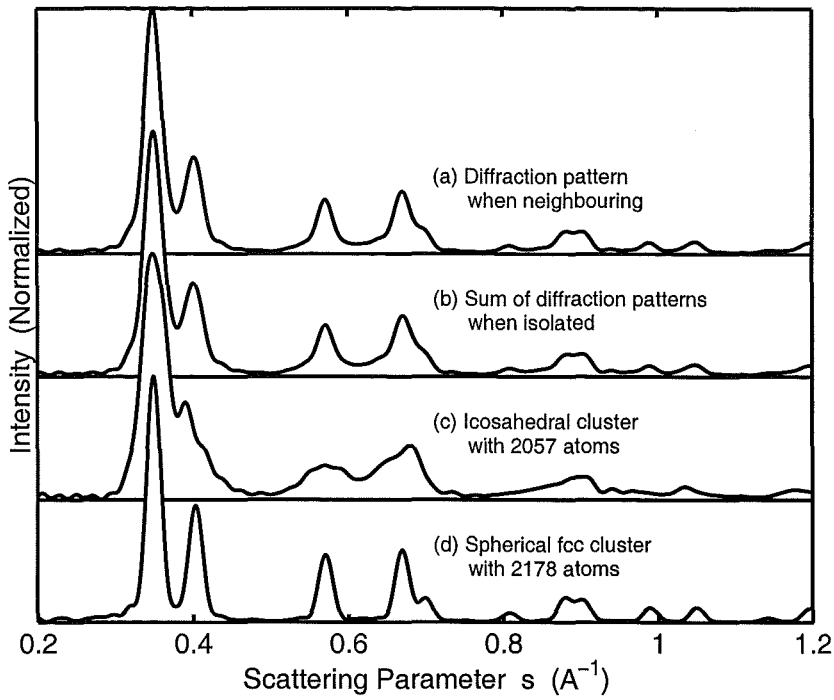

Figure 4.21: The diffraction patterns from several clusters to show the effect of domains on the diffraction pattern. Pattern (a) shows the diffraction pattern obtained when a 2178 atom spherical FCC cluster and a 2057 atom icosahedral cluster are positioned next to each other. (b) shows the diffraction pattern obtained by adding the diffraction patterns from an isolated 2178 atom spherical FCC cluster and an isolated 2057 atom icosahedron together. (c) and (d) show the diffraction patterns from an isolated 2178 atom spherical FCC cluster and an isolated 2057 atom icosahedral cluster respectively.

shapes of Zn cluster that have HCP structure (Figs. 4.16 to 4.19).

The structure of the cluster obviously has the largest influence on the diffraction pattern, diffraction patterns from FCC, HCP, decahedral and icosahedral clusters are clearly different. However, a diffraction pattern is not necessarily unique to a structure, the diffraction patterns from decahedral and parallel twinned FCC clusters are very similar.

4.5.5 The Effect of Domains

The previous sections of this chapter have only considered clusters with a single domain[2], however clusters containing multiple domains are often observed during HRTEM observations [114]. Considering that the primary analysis of the experimental diffraction patterns is by comparison with patterns from mono–domain model clusters any effect multiple domains has on the experimental pattern is important.

One method to approximate the effect of multiple domains is to calculate the contribution to the diffraction pattern from the intercluster interference. Betts and Bi-

[2]i.e. none of the clusters have contained multiple regions with different structure or multiple regions with the same structure but in random orientations with respect to each other.

enenstock [115] have calculated the interatomic interference for two neighbouring, but randomly oriented, Si clusters of the same size and structure. Two cluster sizes were examined, 17 and 29 atoms, and in both cases for $s \lesssim 0.16\text{Å}^{-1}$ the intercluster interference was negligible.[3]

Using a variety of the clusters described in section 4.5.1 the diffraction pattern produced by two neighbouring but randomly oriented Pb clusters has been compared to the sum of the individual diffraction patterns from the clusters. Shown in Fig. 4.21 is the result from one case using a 2178 atom spherical FCC cluster and a 2057 atom icosahedral cluster. Fig. 4.21(a) shows the diffraction pattern obtained when the FCC and icosahedral cluster are positioned next to each other, while (b) shows the pattern obtained by merely adding the diffraction patterns from an isolated 2178 atom spherical FCC cluster and an isolated 2057 atom icosahedron. This pattern is very similar to the pattern in (a) indicating that diffraction is sensitive to the domains of the cluster rather than the cluster as a whole. Similar results were observed in all other cases examined. Fig. 4.21(c) and (d) show the diffraction patterns from an isolated 2178 atom spherical FCC cluster and an isolated 2057 atom icosahedral cluster respectively.

That diffraction is only sensitive to the domains within the cluster is an important feature. It means that analysis based on the diffraction pattern will be indicative only of the domains within the clusters.

4.6 Summary

This chapter has concentrated on the use of the Debye equation to calculate diffraction patterns from clusters. Diffraction patterns from a variety of clusters with different sizes, shapes and structures have been examined. Clearly the structure has a major influence on the diffraction pattern. The structures examined for Pb clusters will be used in chapter 5 in the analysis of experimental diffraction patterns. For Zn the model clusters used to calculate diffraction patterns were mostly based on the HCP structure and, as a range of shapes were considered, allowed the effect of shape on the diffraction pattern to be examined. The final section considered the effect of multiple domains within a cluster and showed that results obtained from diffraction patterns are indicative of the individual domains not the whole cluster.

[3]This value of s differs from the value quoted by Betts and Beinenstock due to the different definition of s (factor 2π larger) used by them. The value quoted in the text above is correct for the definition of s used in this thesis.

Chapter 5

Experimental and Data Analysis Procedures

This chapter provides a summary of how the experiments were performed and how the data obtained were analysed. A description of the experimental procedure, beginning with the preparation of the source chamber and ending with an outline of the procedure during an experiment, is given. The description of the analysis is divided into the separate tasks.

5.1 Experimental Procedure

This section outlines the procedure followed in preparation for and during experiments. It deals specifically with the case of Pb experiments, however it is representative of the procedure followed during experiments using Zn.

5.1.1 Initial Preparation

In general, experiments were performed in groups over a period of about a week. To begin a new group of experiments the entire source (see section 3.2.1) is thoroughly cleaned. Most surfaces are scrubbed with a 3M Scotch Bright Pad to remove deposits from previous experiments before being wiped with acetone or methanol and a low lint cloth. The process produces a large amount of fine metallic dust and is performed in a fume cupboard whilst wearing protective overalls, gloves, goggles and breathing filters. The heat shields in the crucible arrangement, being delicate, are cleaned by immersion in dilute nitric acid. Pb deposits are slowly removed by the nitric acid whereas the tantalum metal is unaffected. Pb remaining in the crucible could not easily be removed and a new crucible is used for each group of experiments. A new crucible is initially $\sim$1 cm too long and is cut to size with a diamond saw. The crucible is then cleaned by boiling in distilled water to remove any residue from the cooling fluid used while being cut. The crucible arrangement and source are then reassembled and inserted into the main system (see section 3.2). The equipment is evacuated to a pressure of $\sim 10^{-6}$ Torr before a flow of Ar (99.99%) or He (99.99%) is introduced and the crucible baked at 900°C for several hours. The crucible is left to cool before the source is removed from the system and

opened so that fresh Pb (99.95+%) can be added to the crucible. The source is then inserted back into the system and the system left to evacuate overnight.

Between experiments within a group the only cleaning performed is the removal of deposits from the nozzles. The deposits on the nozzles can become quite substantial and often cause a nozzle to block. The blocking affects the gas flow through the nozzles and reduces the cluster flux into the diffraction chamber, causing the experiment to be terminated.

5.1.2 Procedure during an Experiment

An experiment typically proceeds as follows:

- A flow of inert gas through the source is initiated and heating of the crucible begins.
- The electron beam is switched on and brought to operating conditions (80 kV energy, filament saturated giving $\sim$2 μA current). The beam is allowed to stabilize ($\sim$1 hr).
- The electron beam is aligned (see section 3.3.1) and the CCD detectors are positioned across the diameter of the diffraction rings. To position the CCDs a diffraction peak from either the Au or ThCl film is observed on both CCDs. When the CCDs are positioned across the diameter of the diffraction rings the separation between the peak in the left CCD and right CCD is a maximum.
- Calibration patterns are obtained by taking diffraction patterns from the thin films of Au and ThCl.
- Background (gas) patterns are obtained by taking diffraction patterns from the residual gas in the diffraction chamber. Both the pressure and composition of the inert gas in the source chamber affect the background pattern and therefore patterns are obtained for a range[1] of inert gas pressures and compositions.
- The crucible is heated to experimental temperatures and diffraction patterns from clusters are obtained. In general, patterns are taken as sequences, during which one of crucible temperature (T_C), inert gas pressure (P_G) or Ar/He ratio is varied. A pleasing reproducibility of the diffraction patterns is observed when returning to source conditions observed in a previous sequence or experiment. TEM grids are exposed during the sequence, however due to the limited number of grids available a grid is not exposed for every pattern taken.

[1]The range depends on what source conditions are to be examined during the experiment.

- A second set of calibration patterns is obtained.
- The electron beam is turned off and the crucible left to cool.
- Once the crucible has cooled the vacuum pumps are switched off and the system flooded with N_2 to atmospheric pressure.
- Any exposed TEM grids are removed and replaced.

5.2 Analysis

The primary analysis examines the experimental diffraction patterns to determine size and structure of the domains within the clusters, however the experimental data must first be Poisson corrected and calibrated. A measurement of the cluster size distribution, independent of the diffraction pattern, is obtained by TEM observation of the clusters deposited on the TEM grids (section 5.2.3). Size estimates are also made by applying either Fourier inversion (section 5.2.4.1) or the Scherrer formula (section 5.2.4.2) to the experimental diffraction pattern (after the background is subtracted).

5.2.1 Data Preparation

Due to the counting procedure (see section 3.3) used to obtain an experimental diffraction pattern the data must be corrected for multiple events during each exposure of the CCD using the Poisson correction (Eqn. 3.13). Fig. 5.1 shows the effect of applying the Poisson correction to a typical diffraction pattern.

To be able to compare experimental and model diffraction patterns the scattering parameter, s, for each CCD pixel must be determined so patterns from model clusters can be calculated at the same values of s. The positions of peaks in the calibration patterns are determined by fitting a parabola over the data points that contribute to the peak. The peak positions are estimated to about ± 0.5 pixel widths. The Au diffraction sample provides 8 peaks spread across the s range of the experiment and the ThCl sample provides 12 peaks mostly in the low to mid s range. Peak positions in calibration patterns taken before and after the experiment tend to show an offset of ~ 2 pixels ($\sim 0.001\,\text{Å}^{-1}$) indicating that the electron beam shifted slightly during the experiment. To create a calibration curve, which determines the value of s for each pixel, peak positions measured before and after the experiment are averaged, there being no reason for choosing one set over the other.

Although careful attempts are made to position the CCDs across the diameter of the diffraction rings, when the CCDs are close to the diameter the separation of peaks is

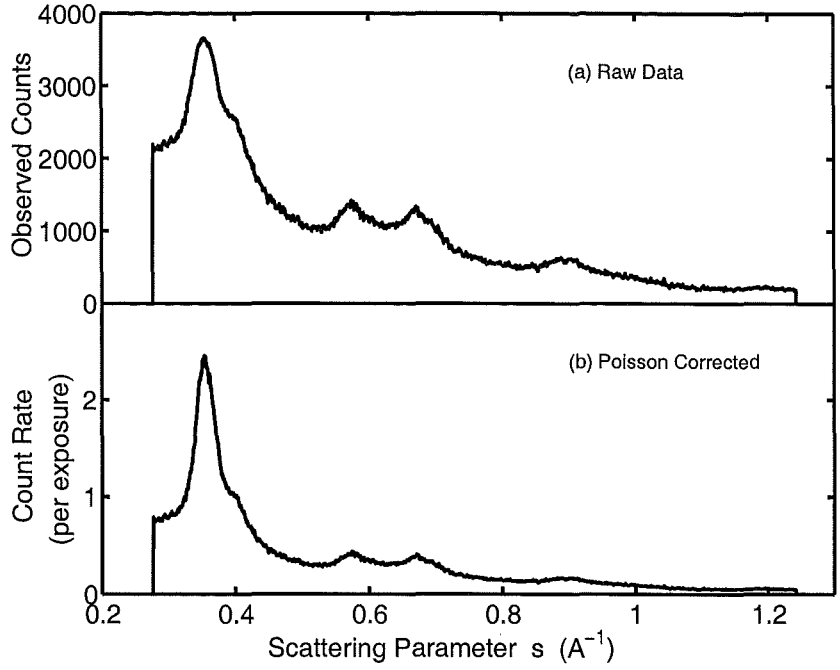

Figure 5.1: The application of the Poisson correction to experimental data. (a) shows the original number of counts observed during 4000 exposures and (b) shows the same data after the application of the Poisson correction to produce the true diffraction pattern.

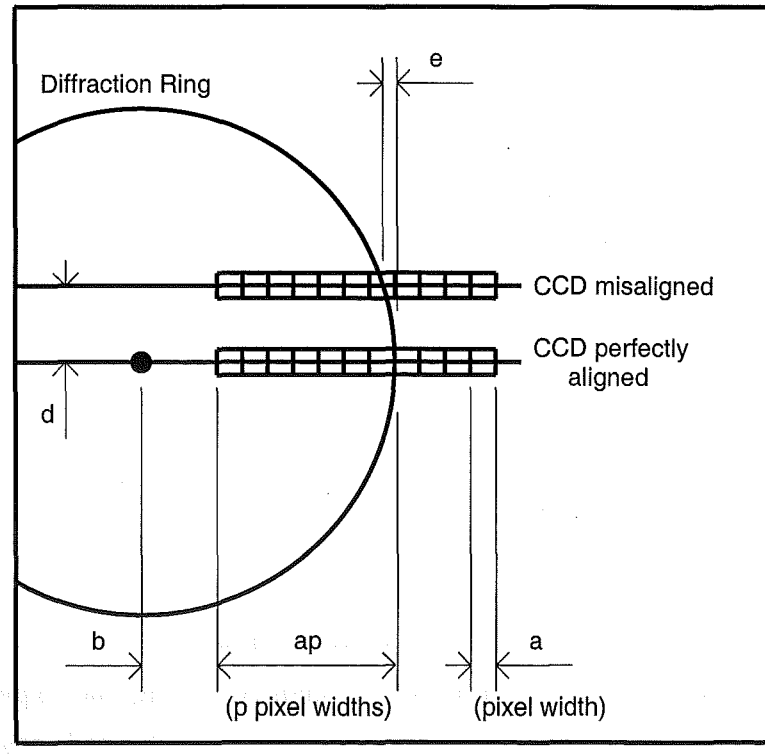

Figure 5.2: Alignment of the CCD detectors. b is the distance from the central spot to the start of the pixels, a is the width of the pixels, p is the distance, in pixel widths, from the start of the pixels to the diffraction ring and d is the offset of the pixels from the diameter of the diffraction ring. e shows the difficulty in aligning the CCD along the diameter, a large change in d only makes a small change in e.

insensitive to the movement of the CCDs (see Fig. 5.2). Thus, accurate positioning of the CCDs is difficult. In the ideal case, with CCDs positioned along the diameter of the diffraction rings, the calibration curve is linear, however the calibration curve becomes parabolic when the CCDs are offset from the diameter of the diffraction rings. Using the definitions from Fig. 5.2 the equations for linear and parabolic calibration curves are

Linear :

$$s = ap + b, \tag{5.1}$$

Parabolic :

$$s^2 = a^2p^2 + 2abp + (b^2 + d^2). \tag{5.2}$$

In practice there is little difference in the calibration curves from each of these equations, the maximum being about 0.1% at the minimum of the s range. The parabolic calibration curve is used in the analysis of experimental diffraction patterns.

5.2.2 Fitting

The cluster source produces clusters with a variety of shapes, sizes and structures that all contribute to experimental diffraction patterns. To determine the characteristic sizes and structures of the domains that contribute to an experimental diffraction pattern an automated routine based on Simulated Annealing is used to fit diffraction patterns from model clusters, a background pattern[2] and a constant to the experimental pattern. The background pattern is included in fitting instead of being subtracted first as, in general, the source conditions and exposure settings of the CCDs for the background pattern and the experimental pattern are different. The differences mean the background pattern requires scaling for it to be subtracted from the experimental data, the different source conditions mean it is difficult to calculate the appropriate scaling factor. The constant allows for a signal from the dark current in the CCDs that is assumed to be constant across the CCDs. Note that the diffraction patterns are usually displayed with the background and constant subtracted.

In essence the fitting procedure is similar to the Debye Functional Analysis (DFA) technique described by Vogel *et al.* [116] and Hall [117]. The models used in analysis are based on icosahedral, decahedral and FCC structures. For bulk FCC metals, these structures are commonly observed in HRTEM studies of small particles and have been used successfully in the analysis of previous cluster diffraction experiments [48, 50, 118].

For each of the icosahedral, decahedral and FCC structures closed shell geometrical

[2]From the range of background patterns available, the background pattern used in fitting is the pattern that was obtained using source conditions most similar to the experimental pattern.

model clusters with up to ~6500 atoms have been created. The shape of the FCC model clusters is cuboctahedral (triangular facets, Fig. 2.2(c)), which provides 11 closed shell models in the size range 55 to 6525 atoms. The icosahedral model clusters share the same closed shell sizes as the cuboctahedra. The decahedral model clusters are truncated according to Ino's [57] calculations for the approximate Wulff form, which gives 10 closed shell models in the range 39 to 6497 atoms. Lists of the exact closed shell sizes for each structure are given in section 2.4. For each geometric model cluster the corresponding MD relaxed model cluster has been calculated. In addition, several other MD generated model clusters are available, the structures of these models are: liquid drops, anti–Mackay icosahedra and shaved icosahedra. In all cases Dr. S. Hendy performed the required MD simulations.

The experimental diffraction pattern is generally analysed twice, once using the geometric icosahedra, decahedra and FCC cluster models (geometric models) and once using the relaxed icosahedra, decahedra and FCC cluster models (relaxed models).

5.2.2.1 Simulated Annealing

The optimization routine Simulated Annealing (SA) mimics the processes occurring during the annealing of a metal. To obtain the lowest energy structure for a metal it is slowly cooled. Random fluctuations in energy allow the structure to escape local minima and proceed towards the global minimum. SA was originally used in combinatorial type problems such as the 'traveling salesman' [119], however SA has been shown to be very effective for continuous type problems as well [120]. The problem of fitting diffraction patterns from models to the experimental pattern is continuous and the SA algorithm described by Corana *et al.* [121] has been followed.

Given a function of n variables SA attempts to find the minimum of the function by considering random steps in parameter space and accepting them under certain conditions. For the purpose of fitting diffraction patterns from models to the experimental diffraction pattern the function χ^2 is defined as

$$\chi^2 = \sum_i \left(\frac{\exp_i - \mathrm{fit}_i}{\sigma_i} \right)^2, \tag{5.3}$$

i.e. the standard sum of the difference squared, where $\exp_i$ and fit_i are the value of the experimental and fitted pattern at pixel i respectively. Here $1/\sigma_i$ is a weighting value used to reduce some of the bias the main diffraction peak has on the fit. The weighting values used are shown in Fig. 5.3, overlaid on the experimental pattern shown in Fig. 5.1(b).

In turn each variable has a step generated by randomly selecting a value between -S_j

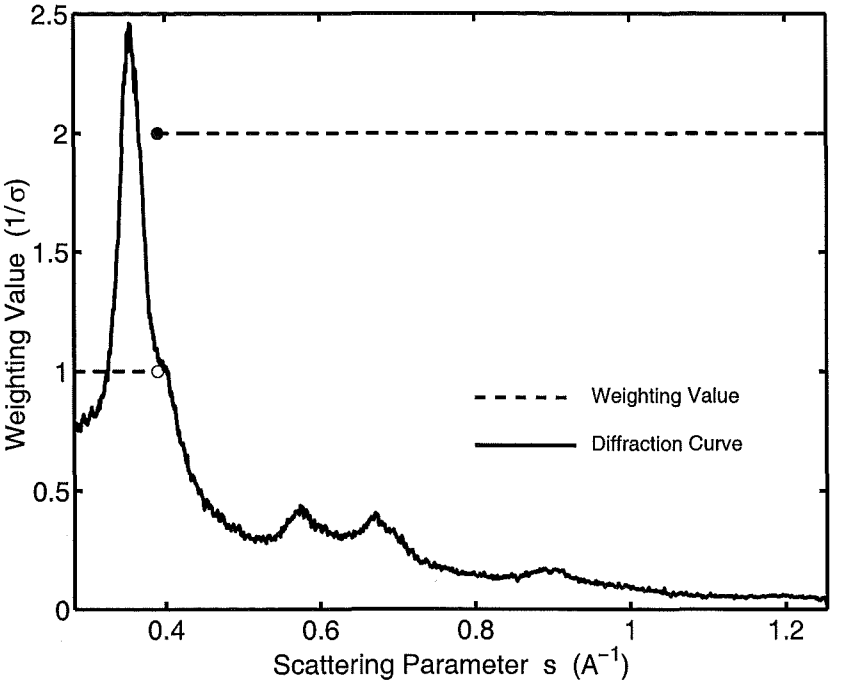

Figure 5.3: The weighting values used in fitting. Shown overlaid on the Poisson corrected diffraction pattern from Fig. 5.1(b).

and S_j, where S_j is the maximum step size for variable j (of n). The step is added to the present value of the variable and χ^2 is recalculated. The step results in a $\Delta\chi^2$ defined by $\Delta\chi^2 = \chi^2_{new} - \chi^2_{old}$ and the step is either accepted or rejected according to the following criteria: if $\Delta\chi^2$ is negative ($\chi^2_{new} < \chi^2_{old}$) then the step is always accepted, if $\Delta\chi^2$ is positive then the step is accepted with a probability given by

$$P_{accept} = \exp\left(\frac{-\Delta\chi^2}{T}\right), \tag{5.4}$$

where T is a parameter analogous to temperature in annealing. Hence, for a given T, a small increase in χ^2 is more likely to be accepted than a large increase. The initial value of T is high and the system can explore parameter space by being able to take steps to unfavourable (high χ^2) states. T is reduced slowly during fitting and high χ^2 states become less accessible, guiding the system towards the minimum of χ^2. Taking steps that increase χ^2 allows the system to escape local minima and more freely explore parameter space than a purely downhill (always reduce χ^2) type minimization routine.

In order to keep the routine efficient the step size is actively controlled so that there is approximately a ratio of 1:1 between accepted and rejected steps. To control the step size the ratio of accepted to rejected steps, c_j, is calculated periodically. The step size, S_j is then adjusted by

$$S'_j = 5S_j(c_j - 0.4) \quad \text{if } c_j > 0.6, \tag{5.5}$$

$$S'_j = \frac{S_j}{5(0.6 - c_j)} \quad \text{if } c_j < 0.4, \tag{5.6}$$

$$S'_j = S_j \quad \text{otherwise.} \tag{5.7}$$

At high T the step size is large (so that large $\Delta\chi^2$ are obtained and sufficient steps are rejected) and SA is only sensitive to the large scale behaviour of the system. At lower T the step size reduces and fine details become important.

5.2.2.2 Application of Simulated Annealing to Experimental Patterns

To optimize the match between experimental and model diffraction patterns the SA routine has variables for: a Debye–Waller (DW) factor, the lattice parameter (LC), each of the diffraction patterns from model clusters, the background pattern and the constant. All the variables, except LC, have a lower bound of zero. The variable LC represents a lattice contraction (positive value for LC) for the model clusters, however in some cases (see section 5.2.2.5) a lattice expansion can be expected resulting in a negative value for LC.

For each model cluster the term

$$\sum_n h(n)\frac{\sin(2\pi s r_n)}{2\pi s r_n} \tag{5.8}$$

of the Debye equation (Eqn. 4.9) is calculated. Values for DW and LC are randomly chosen and the calculation of the Debye equation for each model cluster is completed.

Initial weightings for the diffraction patterns from model clusters, background pattern and constant are randomly chosen in the range 0 to 1 to produce an initial fit pattern. The weightings are then scaled to give the fit and experimental patterns similar intensities. To obtain a starting value for T a random walk is performed and the χ^2 value for each state visited is recorded. The range of χ^2 values is used to calculate a value for T from Eqn. 5.4 assuming a P_{change} of 99%. This process is used to chose a starting T that should allow SA to freely explore parameter space.

The iteration section now commences. In turn, each variable has a trial step generated. Steps that take a variable out of bounds are recalculated. $\Delta\chi^2$ for the step is calculated and then the step is tested for acceptance or rejection. After every 100th trial step for each variable is made the ratio of accepted to rejected steps is calculated and used to adjust the step size. After completing 20 adjustments of the step size the temperature is

multiplied by 0.85.

The iterations continue until the temperature drops below a threshold value. The minimum value for T was chosen by observing when the step size reached $\sim 10^{-4}$ during initial testing of the routine. The SA routine typically gives only a few of the model clusters significant weightings ($\sim$1), the weightings of the other model clusters are generally very small ($\lesssim 10^{-4}$).

For each experimental pattern the fitting process is repeated several times using a random starting state to check the reproducibility of the fit results. Comparing the results from each fit shows that there are very small differences in the fitted parameters. These differences can be attributed to the non–zero value of T when the fitting routine is terminated.

A general concern with SA is that if the temperature is reduced too fast the system may not have time to escape local minima. To address the concern fits have been performed on several patterns using a starting temperature 10$\times$ higher and a temperature reduction rate of 0.95. This significantly increases the time required to complete a fit but should reduce the possibility of becoming stuck in local minima. Results from these fits are within the range of results from the standard fits described above.

The SA results have also been compared with results from the 'lsqcurvefit' routine (based on the interior trust minimization method [122,123]) in the MATLAB® optimization toolbox. The 'lsqcurvefit' routine is significantly faster than SA but is unable to optimize the DW and LC variables. Due to this restriction on 'lsqcurvefit' the DW and LC values obtained from the SA fit were used when calculating the diffraction patterns from model clusters for the 'lsqcurvefit' routine. The results from 'lsqcurvefit' and SA were in good agreement.

5.2.2.3 Presentation of SA results

The upper panel in Fig. 5.4 shows (after background and constant subtraction) the fitted curve obtained from one fit to the experimental pattern in Fig. 5.1(b) using diffraction patterns from geometric models. The lower panel shows the difference between the experimental and fitted curve ($\times$5). The values for the fitted parameters obtained are shown in Fig. 5.5. Similarly the fitted curve and fitted parameters obtained from a fit using the diffraction patterns from relaxed models are shown in Figs. 5.6 & 5.7 respectively

In the histograms the bars for each model cluster do not show the relative number of clusters, but rather the relative volume weighting of the model.[3] This weighting by the volume associated with a particular size and structure is necessary because this is

[3]The relative volume weighting is essentially the relative number of atoms associated with the model.

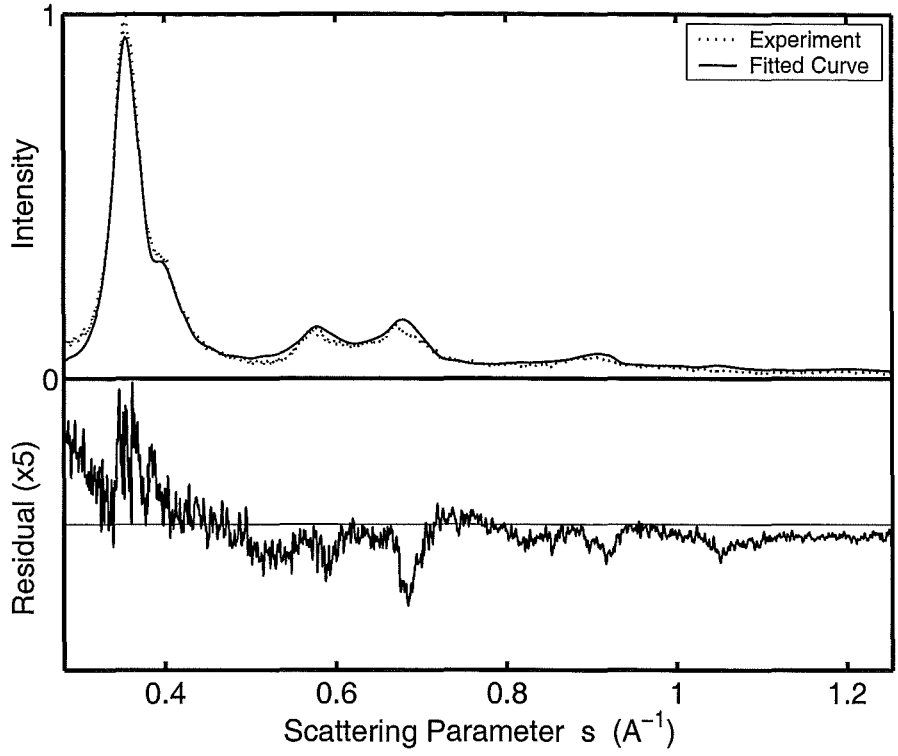

Figure 5.4: The upper panel shows the fitted curve, obtained using diffraction patterns from geometric models, for one fit to the experimental diffraction pattern in Fig. 5.1(b). The lower panel shows the difference between the experimental and fitted curves (×5).

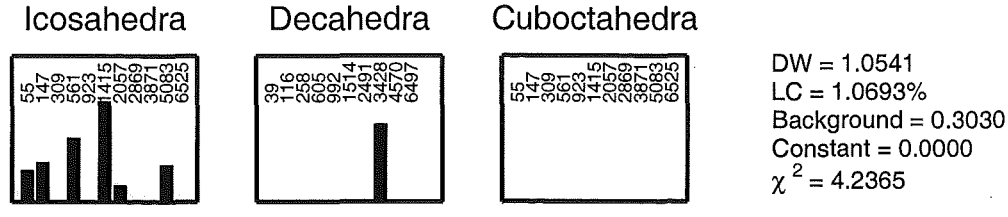

Figure 5.5: The fitted parameters obtained from one fit to the diffraction pattern shown in Fig. 5.1(b) using diffraction patterns from geometric models. Each histogram bar represents the volume weighting of the indicated model cluster. The corresponding fit curve is shown in Fig. 5.4.

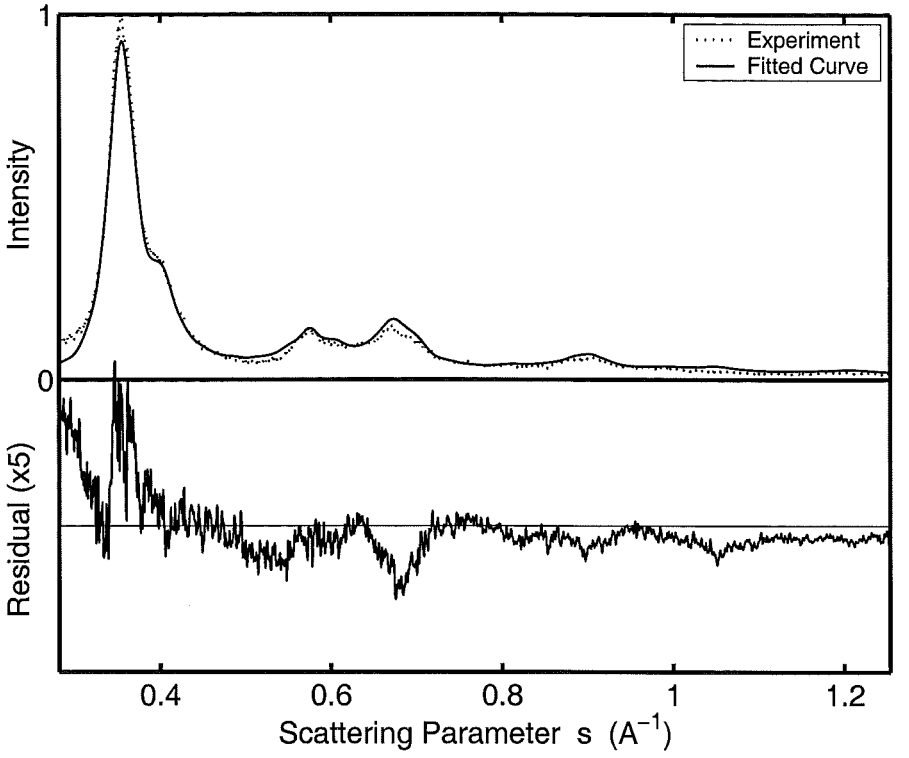

Figure 5.6: The top panel shows the fitted curve, obtained using diffraction patterns from relaxed models, for one fit to the experimental diffraction pattern in Fig. 5.1(b). The lower panel shows the difference between the experimental and fitted curves (×5).

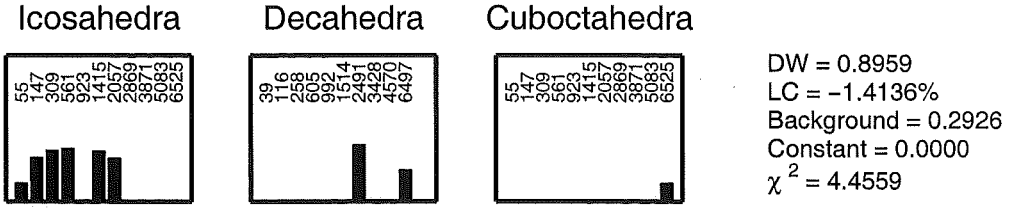

Figure 5.7: The fitted parameters obtained from one fit to the diffraction pattern shown in Fig. 5.1(b) using diffraction patterns from relaxed models. Each histogram bar represents the volume weighting of the indicated model cluster. The corresponding fit curve is shown in Fig. 5.6. Note the negative lattice contraction, indicating that the real clusters had lattice parameter greater than the model clusters.

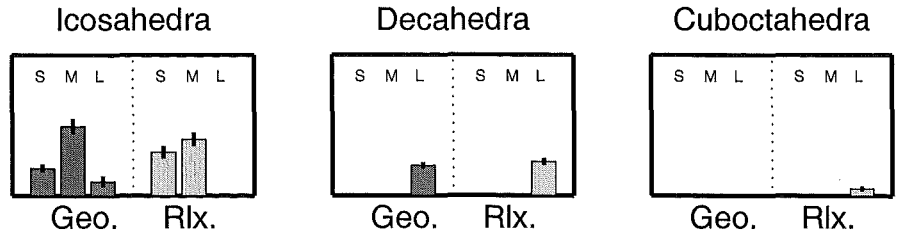

Figure 5.8: Fitting results displayed to reduce misleading interpretation. Note the results from fits using geometric models and fits using relaxed models have been combined. Dark gray bars are results from fits using geometric models; light gray bars are results from fits using relaxed models. S, M & L indicate model size ranges: S, small (<3.0 nm); M, medium (>3.0 & <5.5 nm); L, large (>5.5 nm). The height of each bar gives the relative volume weighting for the structure type in the indicated size range. The small line at the top of each bar is the uncertainty (see section 5.2.2.4) in the height of the bar.

what the diffraction pattern is sensitive to – not the number of domains. For example, in Fig. 5.5 the bars for 147 and 5083 atom icosahedra have similar heights indicating that there is a similar number of atoms associated with each structure. Hence there are many more 147 atom icosahedra than 5083 atom icosahedra, but the contribution to the diffraction pattern is similar. It would, though, be misleading to interpret the results so literally, i.e. that a significant fraction of the beam is icosahedra with exactly 147 atoms. The results of fitting can only indicate the size–structure distribution on a broader scale. Calculating the mean and variance of the cluster diameter for each structure can also be misleading in cases where fitting produces a bimodal distribution for a structure or when only one size is selected for a given structure (e.g. the decahedra in Fig. 5.5). To avoid these problems the fitting results are presented as in Fig. 5.8, here the fitted parameters for the model clusters are binned into 3 groups, small (S), medium (M) and large (L), for each structure depending on the size of the model cluster. The bins used are shown in Table 5.1.

Table 5.1: The binning of cluster models used in the presentation of fitting results. Note ϕ is the cluster diameter, other sizes are in atoms.

Structure	Bin S (ϕ <3.0 nm)	M (3.0< ϕ <5.5 nm)	L (ϕ >5.5 nm)
Decahedral	39, 116, 258	605, 992, 1514	2491, 3428, 4570, 6497
Icosahedral	55, 147, 309	561, 923, 1415, 2057	2869, 3871, 5083, 6525
Cuboctahedral	55, 147, 309	561, 923, 1415, 2057	2869, 3871, 5083, 6525

From the fitted parameters the number and volume weighted average domain size and relative contribution from each type of structure to the diffraction pattern are calculated. The calculation of the average domain size requires a diameter to be assigned to each model cluster. However, as the model clusters are, in general, non-spherical there are a variety of possible definitions for the diameter (see Ref. [124]). In this thesis the average projected area diameter (in random orientation) [124] is used. To calculate the projected area diameter the model cluster is positioned with a random orientation in space and then projected on to a plane. The area, A, defined by the projection is calculated and a diameter, d, is calculated using

$$d = \sqrt{\frac{4A}{\pi}} \tag{5.9}$$

(i.e. assuming the shape of the area is circular). This process is repeated for 40 random orientations and the average of all the diameters calculated is used as the diameter of the model cluster in the calculations of the average domain size.

For the fitted parameters in Figs. 5.5 & 5.7 the number and volume weighted domain sizes and the relative contribution from each structure to the diffraction pattern are given in Table 5.2.

Table 5.2: The average size and relative contribution from each type of structure to the diffraction pattern. 'Number' and 'Volume' indicate whether number or volume weighting was used when calculating the value.

	Geometric Structures		Relaxed Structures	
Parameter	Number	Volume	Number	Volume
Average Diameter (nm)	2.20±0.04	4.35±0.04	2.35±0.04	4.22±0.01
Decahedral contribution (%)	2.0±0.1	21.2±1.6	2.6±0.7	24.1±4.0
Icosahedral contribution (%)	98.0±0.1	78.8±1.5	97.1±0.6	71.1±3.3
Cuboctahedral contribution (%)	0.0±0.1	0.0±0.1	0.3±0.1	4.8±0.6

5.2.2.4 Estimation of Uncertainties in the Fitted Parameters

The method used to estimate uncertainties in the fitted parameters is similar to that suggested by Hall [117]. For an experimental pattern twenty additional (simulated) diffraction patterns are produced using the procedure described in the next paragraph. The simulated patterns are also fitted and the variation in the fitted parameters obtained used to estimate uncertainties.

To produce a simulated diffraction pattern the experimental process is reproduced numerically. From the Poisson corrected diffraction pattern an estimate of λ for each pixel is obtained. Using the estimate for λ and Eqn. 3.12 the probability for a count in

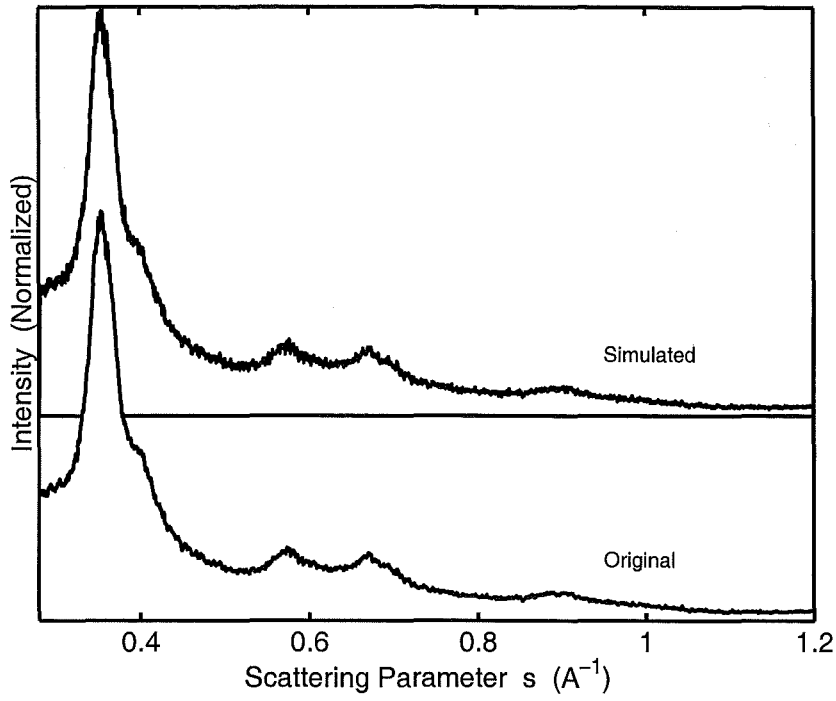

Figure 5.9: An example of the simulated diffraction patterns used in uncertainty estimation. The upper curve shows the simulated pattern, and the lower curve shows the original pattern.

each pixel during an exposure is calculated. Then N (where N is the number of exposures in the original diffraction pattern) random numbers between 0 and 1 are generated for each pixel. For each pixel the number of counts, C, is determined by counting how many of the random numbers have a value less than the probability for a count. A C/N ratio is calculated for all the pixels and, as in the experimental case, the C/N ratios must be Poisson corrected to obtain a diffraction pattern.

The upper panel in Fig. 5.9 shows a simulated diffraction pattern obtained from the experimental pattern in Fig. 5.1(b). The experimental pattern is reproduced in the lower panel for comparison. The simulated diffraction pattern is noisier than the original as the above process is essentially adding noise to the original diffraction pattern.

Each of the twenty simulated diffraction patterns is fitted using the MATLAB® 'lsqcurvefit' routine and the values of DW and LC obtained from the SA fit to the original diffraction pattern. The use of the 'lsqcurvefit' routine instead of SA is because the optimization of DW and LC parameters is computationally intensive. However, to estimate the uncertainties in DW and LC the SA routine was used to optimize one set of simulated patterns, the uncertainties obtained for DW and LC were 2% and 5% respectively.

The results from fitting multiple simulated diffraction patterns indicate the variation in the fitted parameters. To calculate the uncertainty in the binned histogram (Fig. 5.8) the fitted parameters for each simulated pattern are binned (summed) as they would be

for the histogram. The bin values from the SA fit to the original diffraction pattern are assumed to be the mean values and the bin values from the fits to the simulated diffraction patterns are used to calculate a standard deviation. The assumption regarding the mean values will typically cause a bias towards a larger standard deviation, however the bias is generally small compared to the standard deviation.

A significant amount of the variation in the fitted parameters for the model clusters is caused by the fitted parameter for one model increasing and the fitted parameter for the next smaller or larger sized model (with the same structure) decreasing. Provided the variation is between models within the size range of a bar, the variation should not contribute to the uncertainty for the bar. This type of variation means the uncertainties are calculated as in the previous paragraph instead of by adding the uncertainty for each model cluster within a histogram bar.

5.2.2.5 The Lattice Contraction and Debye–Waller Variables

An interesting feature is observed in the predicted values for LC. Using diffraction patterns from geometric models in the fit always results in a positive value for LC, indicating the lattice parameter in the real clusters is less than in the models. Using patterns from relaxed models in the fit always results in a negative value for LC, indicating the lattice parameter in the real clusters is larger than in the models. The difference in the sign of LC is a result of how surface tension and cluster temperature were considered when creating the model clusters.

Decreasing the cluster size is expected to increase the lattice contraction due to the surface tension, while increasing the temperature of the clusters will cause a thermal expansion of the lattice. The geometric models were created using the bulk lattice parameter at room temperature and it was assumed there was no contraction due to the surface tension. The lattice contraction reported is therefore the net effect of a lattice contraction due to surface tension and a thermal expansion (assuming the cluster temperature is greater than room temperature). In comparison, the MD relaxed models have a simulated temperature of 0 K and there is a lattice contraction compared to the bulk, presumably due to the surface tension. Thus the lattice expansion reported in the fits using relaxed models could be expected to originate from thermal expansion.

An estimate of cluster temperature can be made if it is assumed that the fitted lattice parameter is solely due to thermal expansion of the 0 K MD structure. For the pattern in Fig. 5.1(b) the fit using diffraction patterns from relaxed models gives a lattice expansion of 1.41% (Fig. 5.7). Using the thermal expansion of bulk Pb [125, 126] results in an estimated cluster temperature of ~500 K. This value is clearly an overestimate since

measurements of Pb cluster melting temperature (see Ref. [127] & section 6.2) show that only clusters larger than ~10 nm are solid at ~500 K (TEM size estimates, discussed in section 5.2.3, show the average cluster size for the diffraction pattern in Fig. 5.1(b) is only 6.7 nm). There are several sources of error in the temperature estimated from the lattice expansion:

- An isolated cluster will have a greater lattice contraction relative to the bulk than a similar domain within a larger cluster because the contraction is dependent on cluster size. The model clusters are isolated domains, while a comparison of size estimates from fitting (4.22 nm) and TEM (6.7 nm) shows the domains observed by diffraction are part of larger clusters.
- A temperature dependence of the surface tension: for metals surface tension typically decreases with increasing temperature. Therefore the lattice contraction in a cluster with finite temperature is less than the same cluster at 0 K.
- It is not obviously valid to apply bulk thermal expansion coefficients to clusters.

The Debye–Waller factor in the Debye equation (Eqn. 4.7) is related to the rms displacement of the atoms from their equilibrium positions. The rms displacement of the atoms can also be related to the temperature of the atoms and thus an estimate of the cluster temperature can be made. In the Debye equation the Debye–Waller factor is given by

$$D(s) = \exp\left(-\frac{(2\pi s \Delta X)^2}{3}\right), \tag{5.10}$$

where ΔX is the rms displacement of the atoms from their equilibrium position due to thermal motion. In the SA fitting routine the DW variable represents the term

$$\mathrm{DW} = \frac{(2\pi \Delta X)^2}{3}, \tag{5.11}$$

hence

$$\Delta X^2 = \frac{3\,\mathrm{DW}}{4\pi^2}. \tag{5.12}$$

The value of ΔX^2 is also given by [107]

$$\Delta X^2 = \frac{9\hbar^2 T}{mk\Theta^2}\Phi\left(\frac{\Theta}{T}\right), \tag{5.13}$$

where $\hbar = h/2\pi$, T is the temperature, m is the atomic mass, k is Boltzmann's constant, Θ is the Debye temperature and the function $\Phi\left(\frac{\Theta}{T}\right)$ is given by

$$\Phi\left(\frac{\Theta}{T}\right) = \frac{\Theta}{4T} + \frac{T}{\Theta}\int_0^{\frac{\Theta}{T}} \frac{y\,dy}{\exp(y)-1}. \tag{5.14}$$

The value of $\Phi\left(\frac{\Theta}{T}\right)$ is within 3% of unity for $T > \Theta$ [107], given that Θ is 89 K for Pb this term is assumed to be unity. Equating Eqns. 5.12 & 5.13 and solving for T gives

$$T = \frac{\mathrm{DW}\, mk\Theta^2}{12\pi^2\hbar^2}. \tag{5.15}$$

Figs. 5.5 & 5.7 give the value of DW parameter for the fit using geometric models and the fit using relaxed models as 1.0541 and 0.8967 respectively. Substituting these values into Eqn. 5.15 gives 301 K for the fit using geometric models and 256 K for the fit using relaxed models.

The two DW parameter values above are typical values obtained from fitting. For the patterns presented in chapter 6 the mean and standard deviation of DW parameters obtained from fitting with geometric models are 1.0724 and 0.0673 respectively, similarly the mean and standard deviation of DW parameters obtained from fitting with relaxed models are 0.8588 and 0.0562 respectively. No apparent relationship between source parameters and the DW value obtained from fitting is observed.

The DW values from fits using relaxed models are slightly lower than the DW values from fits using geometric models due to the distortion in the relaxed model clusters introduced by the relaxation process. The distortion produces an attenuation of the diffraction pattern similar to the effect of the Debye–Waller factor.

5.2.3 Analysis of TEM Grids

Clusters are deposited on the TEM grids to provide an estimate of the cluster size that is independent of the diffraction patterns. The size estimates obtained from TEM observation are of the actual cluster size whereas size estimates obtained from fitting indicate the size of the coherent domains within the clusters.

The grids exposed to the cluster beam were observed in a JEOL 1200EX TEM, typically at a magnification of 100,000×. While viewing each TEM grid several negatives were exposed. However, there was generally little contrast between the edge of the Pb clusters and the amorphous carbon grid making observation (and analysis) difficult. The low contrast, despite the high atomic weight (and thus electron scattering factor), suggests the clusters had probably become amorphous or oxidized. To reduce the possibility that the effect was due to oxidation of the clusters after removal from the vacuum, the grids exposed during one experiment were immediately transported to the TEM and observed, however no improvement in contrast was obtained.

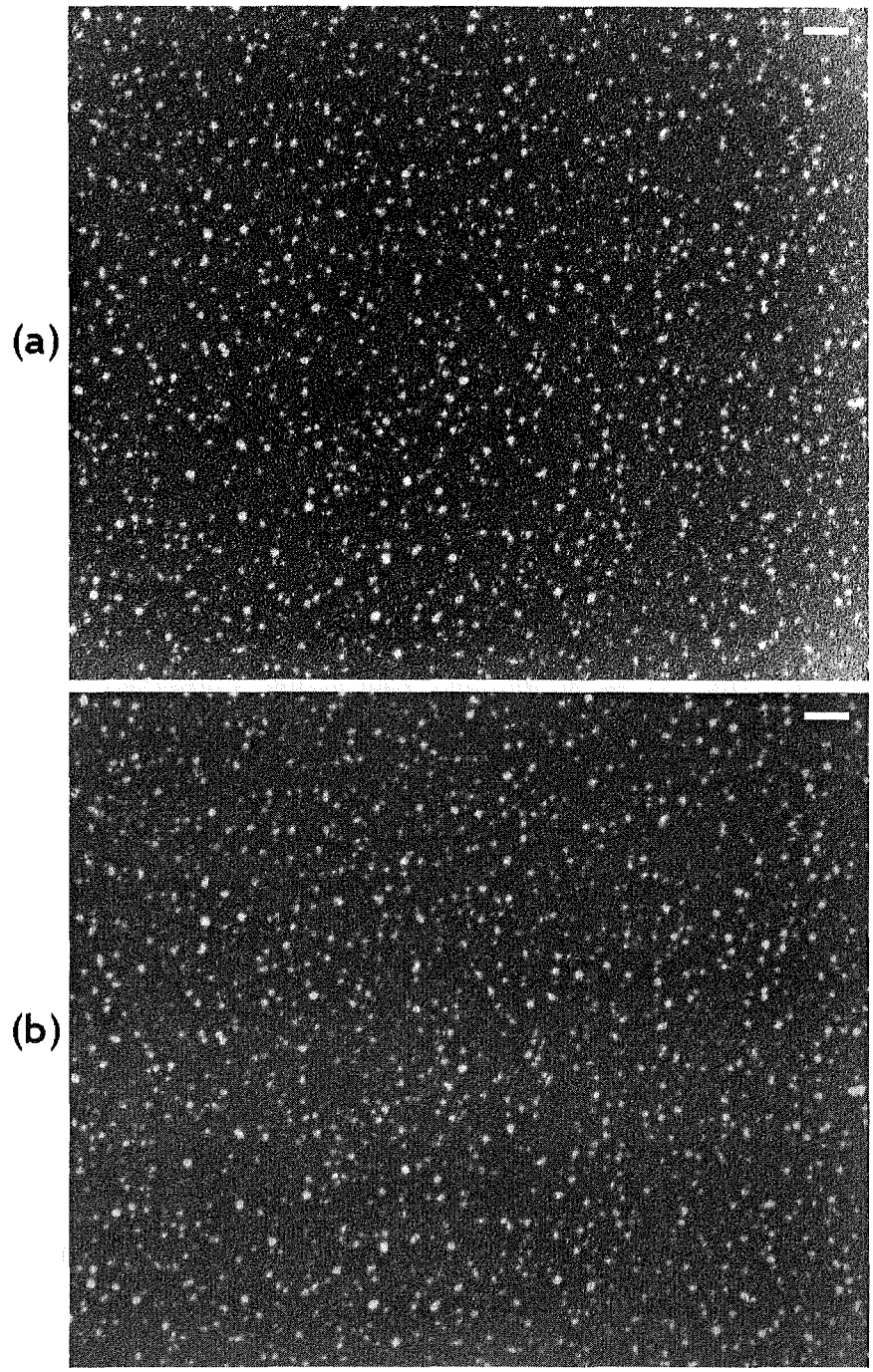

Figure 5.10: A sample TEM image (a) before and (b) after filtering and background equalization. In both images the scale bar is 50 nm.

The negatives obtained were digitized using an Epsom 1200U desktop scanner with slide adapter. The negatives were digitized in grayscale at 1200 dpi, the maximum optical resolution of the scanner. The scanner has 12 bit internal grayscales, with 8 bit grayscale externally available.

In the digitized images the clusters appear as bright spots (see Fig. 5.10). A method for measuring the cluster size from the TEM images has been developed by Hall [48] and is used in the present study to analyse the TEM images of Pb clusters.

Shown in Fig. 5.10(a) is the digitized image of one slide taken from a TEM grid exposed to the cluster beam under the same source conditions as the diffraction pattern in Fig. 5.1. The initial processing attempts to remove noise and equalize the background across the image so a threshold value can be applied to the entire image. Firstly, mean and median filters are applied to the image, the mean filter size is 3×3 pixels and the median filter size is 7×7 pixels. The filters help to remove noise and have been shown by Hall [48] to aid image reconstruction. The image is then sub–divided into smaller sections and the position of the peak in the grayscale histogram for each section is determined. The process for determining the position of the peak differs from that used by Hall: here a Gaussian function is fitted over the grayscale histogram of each section. Fitting a Gaussian function was found to produce similar results, but be more reliable (for the images processed during this study) than Hall's method of detecting a change in sign of the gradient at the peak of the histogram, which could produce erroneous results if the peak was not reasonably smooth. The background levels are 3×3 median filtered then interpolated to create a background surface that is subtracted from the filtered image. The result of applying the above process to the image in Fig. 5.10(a) is shown in Fig. 5.10(b), note the variation of the background in the original image is significantly reduced.

The next step in processing is to determine a suitable threshold level. Shown in Fig. 5.11 is the grayscale histogram for the image in Fig. 5.10(b). Due to the lack of contrast between clusters and the background, the grayscale histogram does not contain separate peaks corresponding to background and clusters making the choice of threshold difficult. A low threshold value introduces more background noise and distorts the outline of the clusters, while a high threshold value causes the edges of clusters to be eroded, resulting in an underestimate of cluster size.

The procedure for choosing a threshold value is similar to that of Hall. Inspection of the thresholded images identifies the threshold value that removes the background influence on the clusters. For the TEM images analysed, this value was found to be consistently ~60 grayscale levels higher than the peak in the grayscale histogram and roughly corresponded to the start of the tail in the grayscale histogram. A threshold

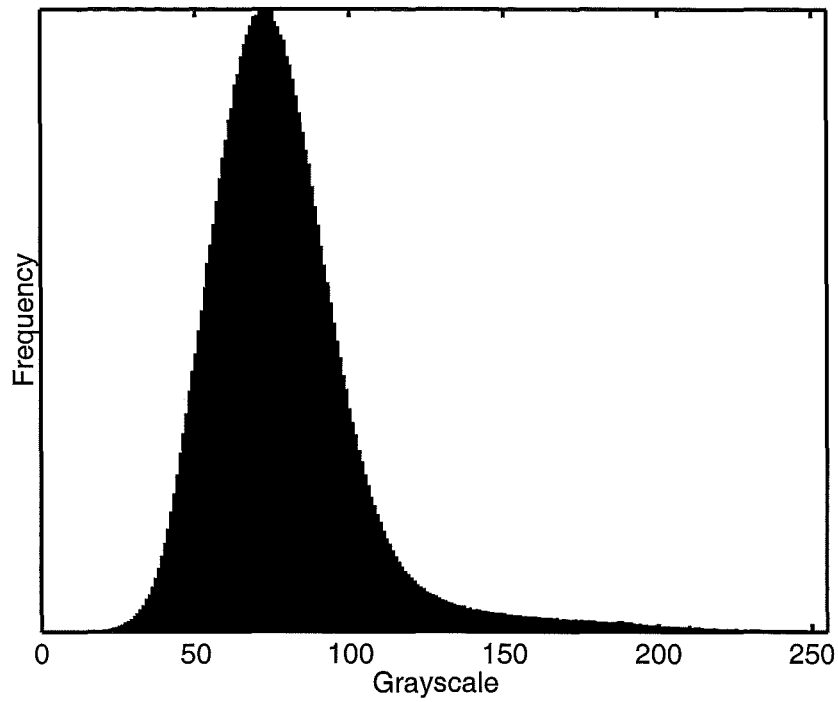

Figure 5.11: Grayscale histogram for the image shown in Fig. 5.10(b).

value of 60 grayscales above the peak in the grayscale histogram was applied to all images to calculate the cluster size distribution. For Fig. 5.10(b) the result of thresholding is shown in Fig. 5.12.

Threshold images are one bit images containing zeros for the background and regions of ones indicating the clusters. A line by line scan of the image is performed, when the scan encounters a 1 the perimeter of the region of 1's is traced out and perimeter length calculated. The area of the region is calculated by counting the number of 1's within the perimeter. The values of perimeter length and area for each region encountered are stored.

During exposure of the TEM grid (to the cluster beam) it is possible that some clusters landed in close proximity and have subsequently joined together. In the threshold image this will result in a single region which should be removed from the analysis. To identify cases where clusters have joined together the compactness,

$$C = \frac{4\pi A}{P^2}, \tag{5.16}$$

where A is the area and P is the perimeter, of each region is calculated. The compactness is effectively a measure of the roundness of a shape: a circle has a compactness of 1, other shapes have a compactness less than 1. It is assumed that when clusters join together the

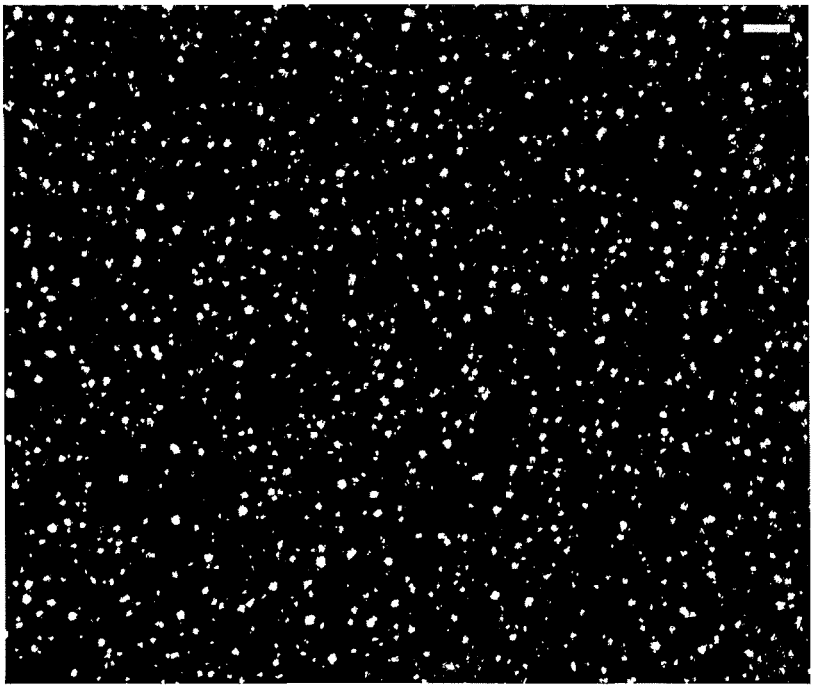

Figure 5.12: The result of thresholding the image in Fig. 5.10(b) with a threshold of 132. The scale bar is 50 nm.

resulting region in the threshold image will be elongated giving it a low compactness value. To remove clusters that have joined together Hall discarded regions with a compactness less than 0.7, the same value is used to discard these regions in the TEM images analysed in the present study.

After discarding regions with a compactness less than 0.7 the remaining regions are approximately circular. A diameter is now assigned to each region, this diameter is equal to the diameter of a circle with the same area as the region. The diameter values are used to create number and volume weighted diameter distributions. Histograms of the number and volume weighted diameter distribution for the image in Fig. 5.12 are shown in Fig. 5.13. The number distribution is also plotted as a linear–probability plot, in which the abscissa is the diameter and the ordinate is the percentage smaller or equal to the diameter. For the image in Fig. 5.12 the linear–probability plot is shown in Fig. 5.14.

The mean of the volume weighted distribution (or 3 rd moment) is considered the best choice for characterizing the cluster size in diffraction experiments [117]. The volume weighted histogram could now be used to calculate the mean size, however even with the best possible choice of threshold value there is a contribution to the histogram from background noise and its effect must be considered.

- The background noise creates an artificial increase in the histogram bins corresponding to small cluster sizes. This increase can be exaggerated by artificially

lowering the threshold value (see Fig. 5.15). However, the contribution to the volume weighted diameter distribution is minor and has little effect on the mean size, which is the key parameter extracted from TEM images.

- The lack of contrast in the TEM images causes an increase in the apparent size of the clusters if the threshold value is set too low. Figs. 5.15 & 5.16 show the number and volume weighted diameter distributions, and the linear–probability plot, obtained by applying a threshold value of 50 grayscale levels above the peak in the grayscale histogram (i.e. 10 grayscale levels less than the optimum threshold value) to the image in Fig. 5.10(b). The means of the volume weighted diameter distributions in Figs. 5.13 & 5.15 are 6.9 nm (optimum threshold) and 7.2 nm (reduced threshold) respectively showing that the mean size is only weakly dependent on the choice of threshold value.

Combining the volume weighted distribution from Fig. 5.13 with the results of analysing other TEM negatives for the same TEM grid gives a mean size of 6.7 nm for the clusters being produced when the diffraction pattern in Fig. 5.1 was obtained. A conservative uncertainty of ± 0.5 nm is assigned to this estimate to account for an uncertainty in the threshold value and the poor contrast during the TEM observation.

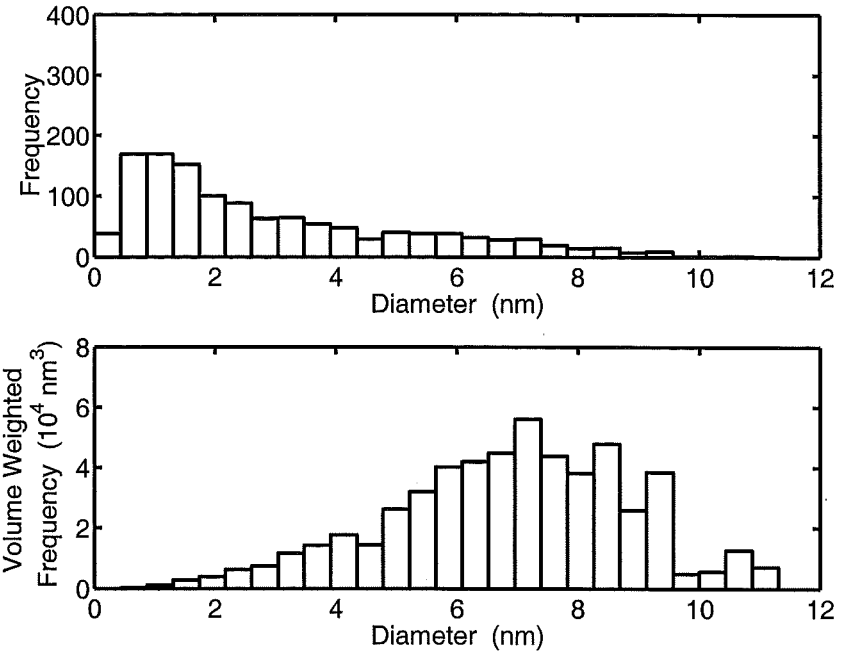

Figure 5.13: The number (top) and volume (bottom) weighted diameter distributions for the image shown in Fig. 5.12(a) (threshold 132).

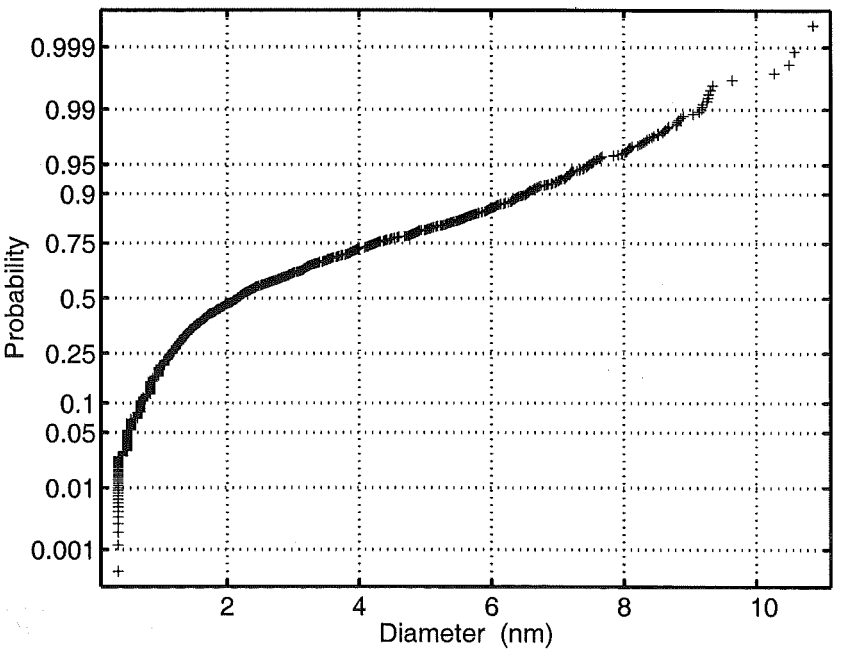

Figure 5.14: The linear–probability plot for the number distribution in Fig. 5.13 (threshold 132).

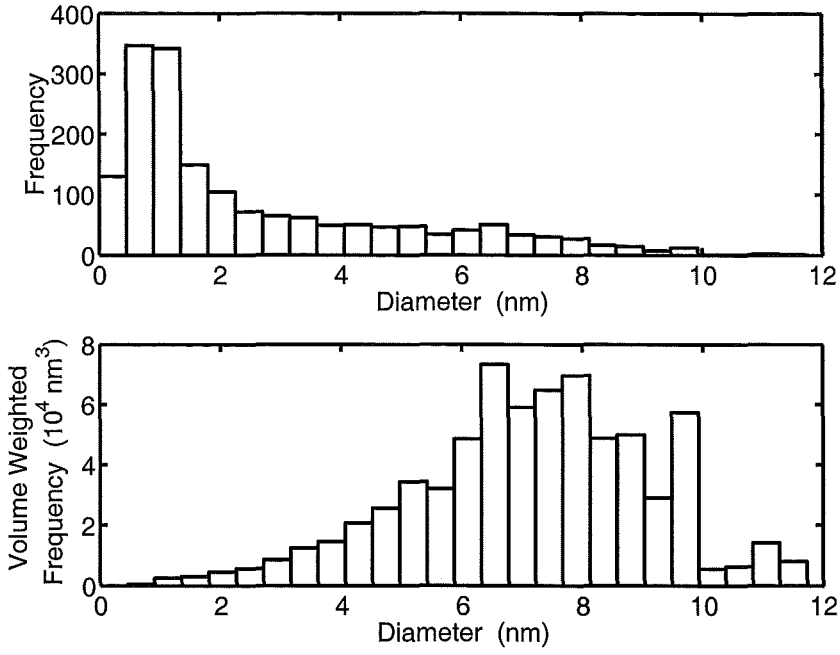

Figure 5.15: The number (top) and volume (bottom) weighted diameter distributions for the image shown in Fig. 5.12(b) (threshold 122). Note the volume weighted distribution appears different to the volume weighted distribution in Fig. 5.13 because the heights of the frequency bars are weighted by volume. The increase in cluster size, due to lowering the threshold value, means an overall increase in volume and hence area in the histogram.

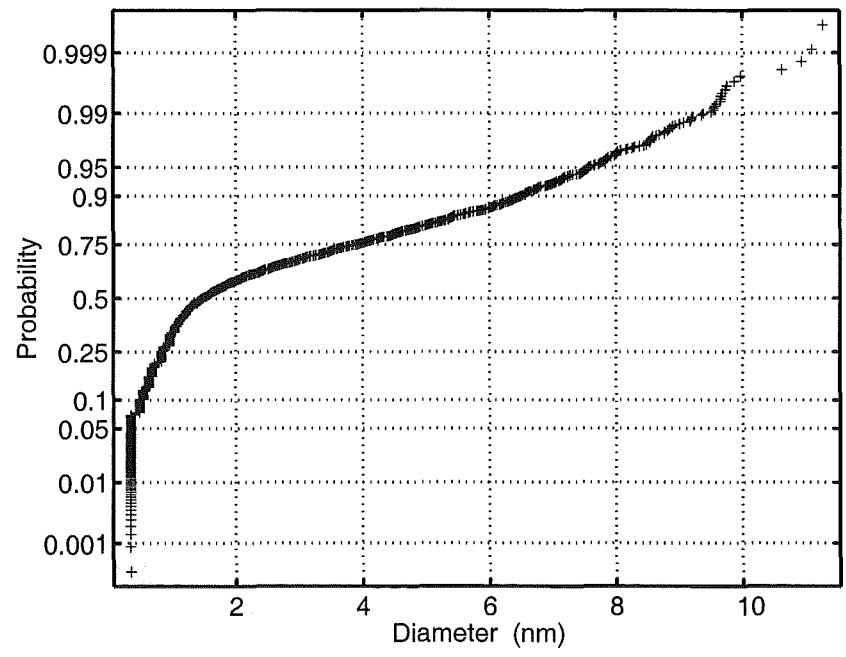

Figure 5.16: The linear–probability plot for the number distribution in Fig. 5.15 (threshold 122).

5.2.4 Alternative Methods of Size Estimation

In addition to cluster size estimations gained from fitting and TEM analysis, size estimates are also obtained using Fourier inversion and the Scherrer formula.

5.2.4.1 Fourier Inversion

The Debye equation (Eqn. 4.7) is essentially a Fourier transform of the distribution of interatomic distances within a cluster. Thus, in principle, the diffraction pattern can be inverted to regain the interatomic distances and then, from the upper bound to the interatomic distances observed, an estimate of the sample diameter can be made. Experimental diffraction patterns are only recorded over a limited range of scattering angles meaning the function obtained from inversion is only an approximation of the original distribution. This section outlines a procedure, developed by Hall *et al.* [128], that still allows a good size estimate to be made from the experimental data.

In an experimental situation, a sample is characterized by its radial distribution function[4] (rdf), $4\pi r^2\rho(r)$, defined such that $4\pi r^2\rho(r)\,dr$ is the average number of atom centers with interatomic distances between r and $r+dr$. The Debye equation can then be rewritten as [128]

$$I_N(s) = I_0 f^2(s)\left(N + \int_0^\infty 4\pi r^2(\rho(r)-\rho_a)\frac{\sin(2\pi sr)}{2\pi sr}\,dr\right) \tag{5.17}$$

where N is the total number of atoms and ρ_a is the sample average atom density. Cluster samples are usually so dilute that ρ_a is negligible. The result of inversion, $P(r)$, is given by

$$P(r) = \beta r \int_{s_{min}}^{s_{max}} s\left(\frac{I^{\exp}(s)}{\alpha f^2(s)} - 1\right)\sin(2\pi sr)\,ds. \tag{5.18}$$

where $I^{\exp}$ is the observed intensity and, α and β are parameters that must be estimated. Fig. 5.17(a) shows the rdf of a cuboctahedral cluster with 561 atoms (diameter 2.8 nm), (b) shows $P(r)$ calculated by applying Eqn. 5.18 to the diffraction pattern from the cuboctahedral cluster assuming s_{min}=0.3 Å^{-1} and s_{max}=1.3 Å^{-1}. The envelope of decreasing oscillations in $P(r)$ can be used to identify an upper limit for the interatomic distances and hence cluster size. However, estimation of the upper limit to the rdf is made difficult by the spurious oscillations in $P(r)$, these oscillations are caused by the truncation of the diffraction pattern at S_{max}. To attenuate the oscillations Hall *et al.* weight the diffraction data with a Lanczos modification function given by

[4]Instead of the distribution of interatomic distances.

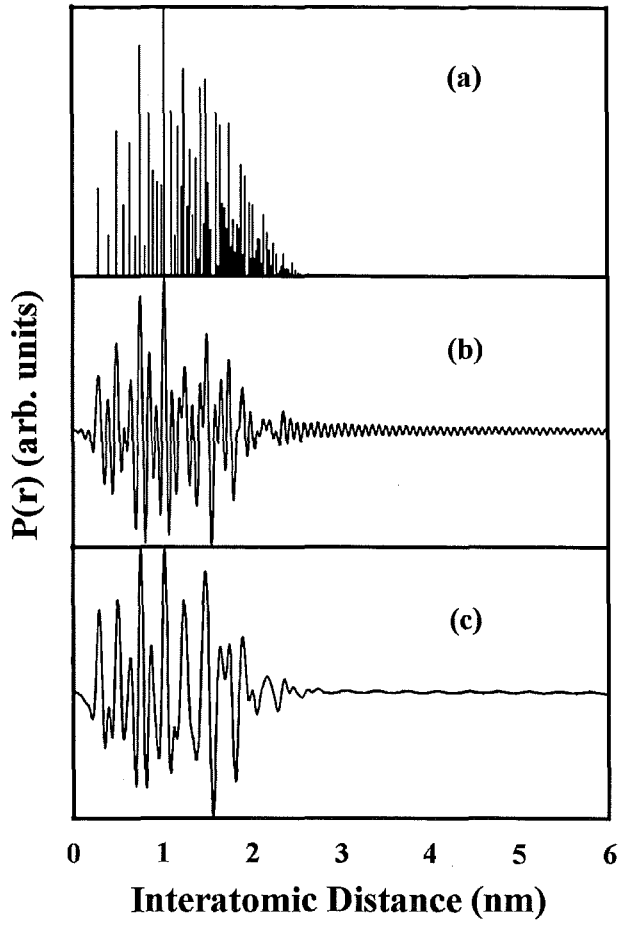

Figure 5.17: The rdf obtained from the inversion of a diffraction pattern. (a) shows the original rdf for the cuboctahedral cluster (diameter 2.8 nm), (b) shows the rdf calculated using Eqn. 5.18 and (c) shows the rdf calculated using Eqn. 5.20, which incorporates the Lanczos modification. After Hall *et al.* [128]

$$M(s) = \frac{\sin(2\pi sa)}{2\pi sa}, \tag{5.19}$$

where $1/a = 2s_{max}$. Eqn. 5.18 then becomes

$$P(r) = \beta r \int_{s_{min}}^{s_{max}} sM(s) \left(\frac{I^{\exp}(s)}{\alpha f^2(s)} - 1 \right) \sin(2\pi sr)\, ds. \tag{5.20}$$

Fig. 5.17(c) shows the improvement the Lanczos modification function produces: the spurious oscillations in $P(r)$ have essentially been eliminated and the cluster size (2.8 nm) is now easily estimated.[5]

Another source of oscillations in $P(r)$ is experimental noise. To assist in estimating the cluster size from noisy data Hall *et al.* create several additional diffraction patterns by adding more noise to the original pattern, these patterns are also inverted. The deviations

[5]Software implementing Eqn. 5.20 has been provided by B. Hall for use in this study.

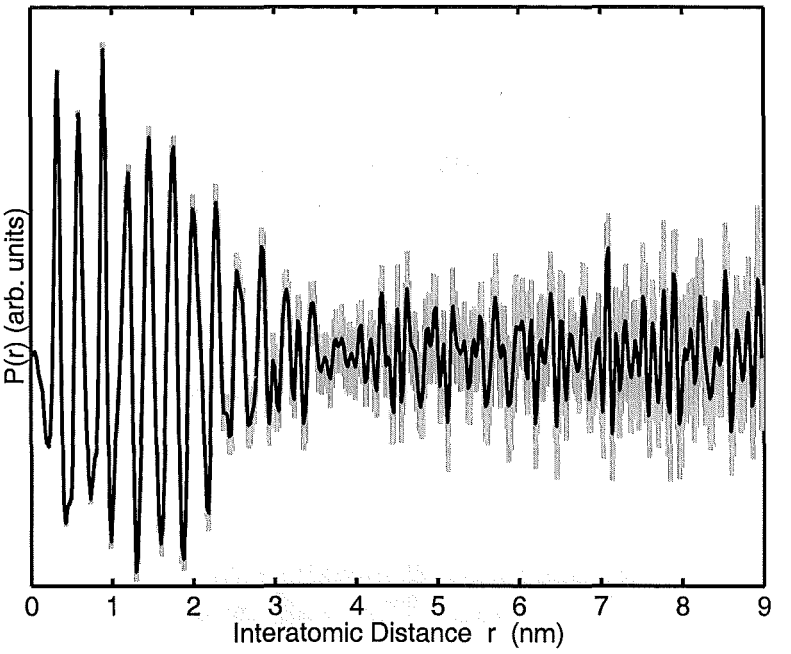

Figure 5.18: Inversion of the diffraction pattern in Fig. 5.1. The gray bands extend two standard deviations from the black line, the standard deviation is calculated using the $P(r)$ values from the simulated diffraction patterns.

between the $P(r)$ values obtained from the original data and the $P(r)$ values obtained from the added–noise data can be used to identify features in $P(r)$, from the original data, that are caused by noise.

To apply Fourier inversion to experimental data obtained in the present study the experimental pattern and the twenty simulated patterns, generated to calculate uncertainties in the fit results (see section 5.2.2.4), are used. For each pattern the fit results are used to subtract the contribution from background to the diffraction pattern. Then Eqn. 5.20 is applied to each pattern. As an example, the result of inverting the diffraction pattern in Fig. 5.1(b) is shown in Fig. 5.18. Inversion of the original diffraction data (after subtracting the background) generates the black line. Inversion of the simulated diffraction patterns provides a distribution of $P(r)$ values for each value of r. For each distribution the standard deviation is calculated, the gray bands in Fig. 5.18 extend either side of the black line by twice the standard deviation. Estimation of the upper limit of the envelope of oscillations in the black line, with help from the gray bands, gives a cluster size of 4.0 ± 0.5 nm.

Hall *et al.* interpret the size obtained from Fourier inversion as an estimate of the actual cluster size rather than the domain size. A comparison between TEM, fitting and Fourier inversion estimates for thiol–passivated Au clusters [118] appears to support this interpretation. The TEM and Fourier inversion estimate are in good agreement while the

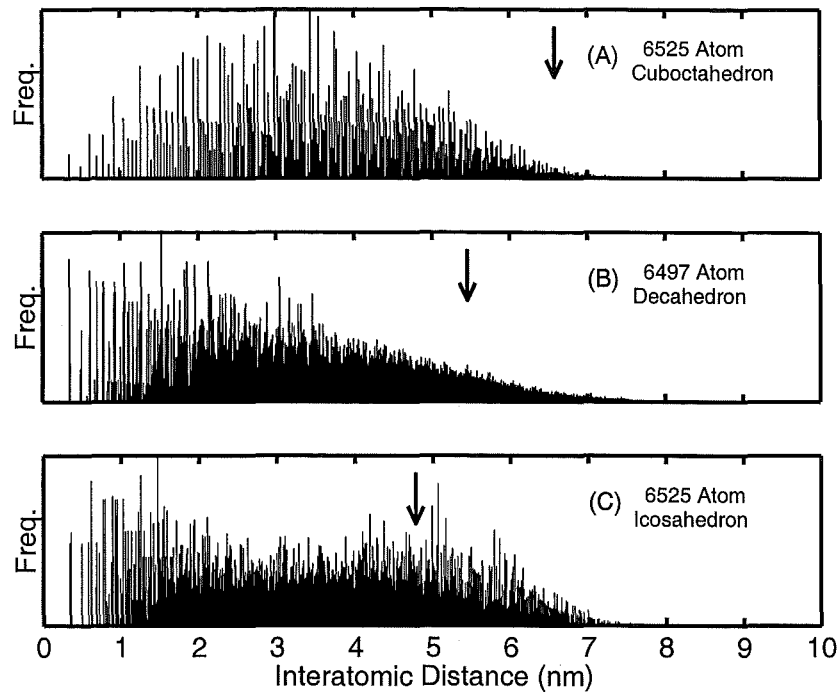

Figure 5.19: Examples of applying the Scherrer formula. The three panels, from top to bottom, show the interatomic distances for a 6525 atom cuboctahedron, a 6497 atom decahedron and a 6525 atom icosahedra. For each panel the arrow indicates the size estimate obtained by applying the Scherrer formula to the diffraction pattern calculated from each set of interatomic distances.

size estimate from fitting is significantly smaller. For the Pb clusters in the present study, a comparison between the fit size estimates in Table 5.2 (4.35 & 4.22 nm), the TEM size estimate in section 5.2.3 (6.7 nm) and the estimate using Fourier inversion above (4.0 nm) suggests that the Fourier inversion estimate is more characteristic of the domain size.

5.2.4.2 The Scherrer Formula

In powder diffraction experiments, as the size of the diffracting particle is reduced the diffraction peaks are observed to broaden. By assuming that the peak broadening is purely due to the limited number of atomic planes and there is a continuous planar structure throughout the particle an estimate of the particle size can be made. The general form of the Scherrer formula is [129]

$$2\delta\theta = \frac{\lambda}{t\cos\theta} \tag{5.21}$$

where $\delta\theta$ is the broadening of the peak (FWHM), which appears at angle 2θ from the central beam, λ is the wavelength (X–ray or electron), and t is the crystal thickness. For experiments in this study the equation is more usable in the form

$$t = \frac{1}{\delta s} \tag{5.22}$$

where δs is the broadening of the peak in Å^{-1} at FWHM. This simplification is possible as the angles involved are small, and hence only applies for electron diffraction. For application to clusters the Scherrer formula has some limitations: the assumption that the diffracting particle has a continuous planar structure may not be true (eg. MTPs), and defects and disorder will also contribute to peak broadening. In such cases application of the Scherrer formula will result in an underestimate of the cluster size.

Panels (A), (B) and (C) of Fig. 5.19 show the distribution of interatomic distances within a 6525 atom cuboctahedra, a 6497 atom decahedron and a 6525 atom icosahedron respectively. For each panel the arrows indicate the cluster size estimated by applying the Scherrer formula to the main peak of the corresponding diffraction pattern. The Scherrer formula is only accurate for the cuboctahedra, which contains a continuous planar structure, for the MTPs the result is an underestimate. Applying the Scherrer formula to the main peak of the diffraction pattern in Fig. 5.1(b) (after subtracting the background) gives a size estimate of 2.6±0.1 nm.

5.3 Deposition Rate Meter

In addition to the total material flux, several interesting parameters can be estimated using the deposition rate meter, these are: the cluster flux (number of clusters entering the diffraction chamber per second), the TEM grid exposure time and the source efficiency. The calculations below have been made assuming that the deposition rate meter samples all the clusters in the beam. In the case of Pb experiments this is a reasonable assumption because the cluster beam diameter at the deposition rate meter is similar to the sensor size (of the deposition rate meter).

The cluster flux can be estimated using

$$\begin{aligned} \text{Cluster flux} &= \frac{\text{Volume deposited per second}}{\text{Average volume per cluster}} \\ &= \frac{\text{Deposition rate} \times \text{Sensor area}}{\text{Average volume per cluster}}. \end{aligned} \tag{5.23}$$

Eqn. 5.23 uses the average volume per cluster. The diameter corresponding to the average volume ($d_{av.\ vol.}$) can be calculated from the number weighted diameter distribution

obtained from TEM measurements using

$$d_{av.\ vol.} = \sqrt[3]{\frac{\sum_i (d_i)^3}{n}}, \tag{5.24}$$

where d_i is the diameter of cluster i and n is the total number of clusters. For the diffraction pattern in Fig. 5.1, $d_{av.\ vol.}$ and the deposition rate are 5.1 nm and 40 Å/s respectively giving a cluster flux of $\sim 5 \times 10^{12}$ clusters per second.

Assuming there is no overlap of clusters on the grid an exposure time for the TEM grids can be estimated using

$$\text{Exposure time} = \frac{\text{Coverage}}{\text{Deposition rate}} \times \frac{\text{Average volume per cluster}}{\text{Average area per cluster}}, \tag{5.25}$$

where coverage is the fraction of the grid covered by clusters and the average area per cluster is the average area a cluster covers on the grid (i.e. the area measured in section 5.2.3). The diameter corresponding to the average area ($d_{av.\ area}$) can be calculated from the number weighted diameter distribution obtained from TEM measurements using

$$d_{av.\ area} = \sqrt{\frac{\sum_i (d_i)^2}{n}}, \tag{5.26}$$

where d_i is the diameter of cluster i and n is the total number of clusters. In an experimental situation $d_{av.\ vol.}$ and $d_{av.\ area}$ are unlikely to be known and estimates would have to be made. If, for convenience during an experiment, the estimates for $d_{av.\ vol.}$ and $d_{av.\ area}$ are both assumed to equal d_{est} (an estimate of the average cluster diameter made from the diffraction patterns) then Eqn. 5.25 reduces to

$$\text{Exposure time} = \frac{\text{Coverage}}{\text{Deposition rate}} \times \frac{2}{3} d_{est.} \tag{5.27}$$

For the diffraction pattern in Fig. 5.1 (deposition rate 40 Å/s), assuming $d_{est.}$= 4 nm and a desired coverage of 0.05 (i.e. 5%), the exposure time given by Eqn. 5.27 is 33 ms. For this example the exposure time can be calculated using the actual values of for $d_{av.\ vol.}$ and $d_{av.\ area}$ determined from the TEM measurements in section 5.2.3. Using the actual values for $d_{av.\ vol.}$ (5.1 nm) and $d_{av.\ area}$ (4.6 nm) in Eqn. 5.25 gives an exposure time of 52 ms for a coverage of 0.05. Hence the value of 4 nm for $d_{est.}$ would result in a coverage lower than desired, fortunately the coverage of the grid is not critical to obtaining a cluster size estimate from TEM observations.

To estimate the source efficiency, i.e. the % of atoms evaporated that become clusters and enter the diffraction chamber, the mass of Pb evaporated from the crucible during

two experiments was measured and an estimate of the average deposition rate for each experiment was made (first experiment: ~1 hour, estimated average rate 50 Å/s; second experiment: ~1 hour, estimated average rate 75 Å/s.). The efficiency can then be calculated as follows:

$$\begin{aligned}
\text{Mass of Pb evaporated} &= \text{(Mass of Pb + crucible before experiments)} \\
&\quad - \text{(Mass of Pb + crucible after experiments)} \\
&= 1.0\text{g}
\end{aligned}$$

$$\begin{aligned}
\text{Mass of Pb deposited} &= \text{Mass deposited in } 1^{st} \text{ experiment} \\
&\quad + \text{Mass deposited in } 2^{nd} \text{ experiment} \\
&= \rho_{\text{Pb}} \times \text{Volume}_1 + \rho_{\text{Pb}} \times \text{Volume}_2 \\
&= \rho_{\text{Pb}} \times \text{Area} \times \text{Rate}_1 \times \text{Time}_1 + \rho_{\text{Pb}} \times \text{Area} \times \text{Rate}_2 \times \text{Time}_2 \\
&= 0.04\text{g}
\end{aligned}$$

$$\begin{aligned}
\text{Efficiency} &= \frac{\text{Mass deposited}}{\text{Mass evaporated}} \times \frac{100}{1} \\
&= 4\%.
\end{aligned}$$

5.4 Summary

This chapter began by describing the procedure used during Pb experiments, then reviewed the preparation and subsequent analysis of data obtained. The primary method of analysis is the fitting of diffraction patterns from model clusters to the experimental diffraction pattern. Fitting allows the size and structure of domains within the clusters to be determined. An estimate of the cluster size, independent of the diffraction pattern, was made by viewing a sample of clusters collected from the beam in a TEM. This estimate is characteristic of the actual cluster size rather than the domain size. Fourier Inversion and the Scherrer formula were also used to obtain size estimates from the diffraction pattern. The final section showed several interesting and useful pieces of information can be derived from the mass deposition rate meter.

Chapter 6

Diffraction from Lead Clusters

This chapter describes diffraction experiments performed on Pb clusters. The opening sections review prior research related to the growth and structure of Pb clusters. Mass spectra of Pb clusters provide insights into the structure of clusters smaller than those observed in this diffraction experiment, while the melting temperature of Pb clusters is found to have implications for the growth of clusters in the inert gas aggregation source used in the present study. HRTEM studies provide direct measurement of the structure of Pb clusters, but influences from the electron beam are observed. Theoretical predictions of the structure of Pb clusters based on bulk Pb parameters and MD simulation are made before beginning the examination of Pb diffraction patterns. The experimental diffraction patterns are obtained as a function of several source parameters: in general a sequence of diffraction patterns is obtained by varying only one source parameter. The chapter closes with a discussion on the results from several other diffraction experiments, prior Pb cluster diffraction experiments and a final discussion of the diffraction patterns presented in this study.

6.1 Mass Spectra of Pb Clusters

Although mass spectra of Pb ions have generally been obtained for sizes smaller than the typical size of clusters observed in this study, reviewing the observations made from mass spectra helps to complete an overview of the structure of Pb from the atom to the bulk. In addition, mass spectra can provide valuable insights into the early stages of cluster growth. Many authors have observed the mass spectrum of Pb clusters. For cations the magic numbers 7, 10, 13, 15, 17, and 19 are commonly observed [96, 130–134], while for anions the magic numbers are 7, 10 and possibly 15 [135, 136]. The magic numbers appear insensitive to the type of source used to produce the clusters, with inert gas aggregation [96, 130, 131, 133, 134] and laser vaporization [132] used in cation experiments and laser vaporization [136] and PACIS [135] both used in anion experiments. Farley *et al.* [131] observe the mass spectrum is sensitive to the laser wavelength and fluence used in ionization, too high fluence causes multiple charging and fragmentation

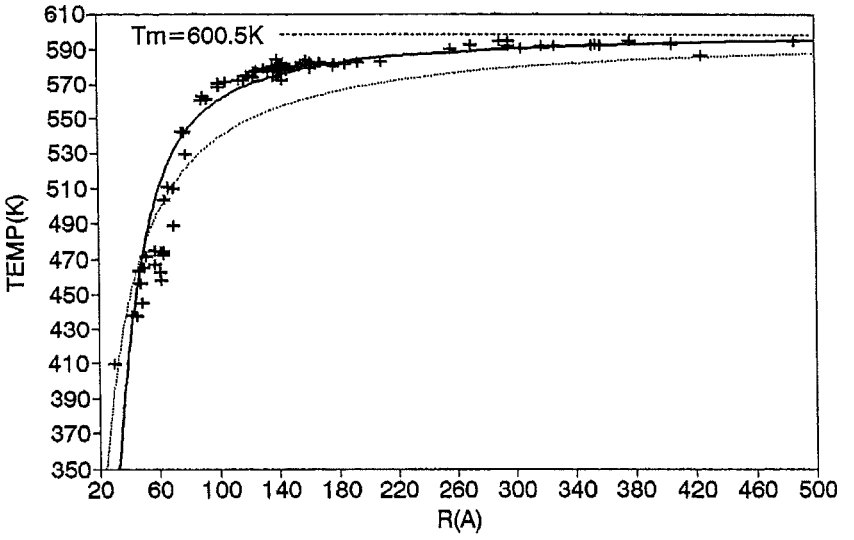

Figure 6.1: The melting temperature of Pb clusters with size measured by Ben David *et al.* [127]. Dashed curve is the standard Pawlow model [2] for cluster melting and the solid line is a model proposed by Ben David *et al.* The dashed horizontal line is the bulk melting temperature.

of the clusters, changing the observed mass spectra and making identification of magic numbers difficult. The magic numbers 7, 13 and 19 are generally attributed to pentagonal bipyramid, icosahedral and capped icosahedral structures respectively [134, 137]. The magic numbers 10 and 17 are less well explained, Rabin *et al.* [130] proposed that they are due to electronic shell closing, though calculations by Iniguez *et al.* [138] suggest that the atomic arrangement is still important in the stability of these clusters.

Above ~20 atoms little structure is seen in the mass spectra. Mühlbach *et al.* [134] speculate that this is because the larger clusters are liquid.

6.2 Pb Cluster Melting

The reduction of the melting temperature of clusters as the cluster size is decreased has been studied extensively [7, 127, 139–143]. Pb is often chosen for study due to the low melting point of the bulk reducing technical requirements for the experiments. In studies by Ben David *et al.* [127], Pb clusters were encased between two layers of SiO_x and observed in a TEM. During observation the clusters were slowly heated and melting temperatures determined by a change in contrast of the cluster image. Fig. 6.1 reproduces the size *vs* melting temperature results obtained by Ben David *et al.*. The rapid decrease in melting temperature for diameters below ~10 nm is typical for clusters (see chapter 1).

Extrapolation of the solid line in Fig. 6.1 suggests that at room temperature clusters less than ~5±1 nm in diameter will be liquid. Clusters with diameters of ~3 nm have

been reported to be liquid in HRTEM observations [7], but the effect of the electron beam must be considered. Assuming that Pb clusters with diameters up to several nanometres are liquid at room temperature has some implications on the cluster growth in the source used in the present study (see section 3.2). The inert gas injected into the source and the source chamber walls are at room temperature, thus the minimum temperature within the source is room temperature. The cluster temperature during growth will be higher than room temperature due to heating from the crucible, hence the clusters are expected to initially grow as liquid drops.

Note that some of the results presented later in this chapter indicate that clusters only several nanometres in size are solid, this apparent contradiction is resolved by considering that (i) electron diffraction is sensitive to the domain size rather than to the cluster size and (ii) prior to the diffraction measurement the cluster/inert gas mixture undergoes two adiabatic expansions which may cool the clusters sufficiently.

6.3 HRTEM of Pb Clusters

HRTEM studies of Pb clusters reveal that the majority of Pb clusters contain twin planes. Ben David *et al.* [144] studied Pb clusters of 4 to 10 nm in diameter embedded in an amorphous SiO matrix and found that their structure fluctuated. The lifetime of any given structure was dependent on the diameter of the cluster. Clusters of 4 nm diameter had a lifetime of ~0.04 s at room temperature, while clusters >10 nm had long term stability. The nature of the fluctuations were different to the fluctuations observed by Iijima and Ichihashi [43] in Au clusters where complete rearrangement of the shape and structure occurred. For the Pb clusters the fluctuations involved the creation and annihilation of twin planes with the cluster retaining a memory of its original crystalline orientation. The twin planes within a cluster were not necessarily parallel; one cluster shown by Ben David *et al.* contained 5 twin planes meeting to create a decahedral cluster with an off centre five–fold axis. In studies by Wu *et al.* [145] Pb clusters were grown on a Si (110) substrate and observed without encasing in a matrix. The clusters shown by Wu contained twin planes and other defects, and were also reported to fluctuate during observation. Fluctuations shown for one cluster, originally FCC with parallel twin planes, resulted in imperfect decahedral and icosahedral structures. However, in both studies no indication is given of whether MTPs were observed prior to fluctuation or their frequency of occurrence during fluctuations.

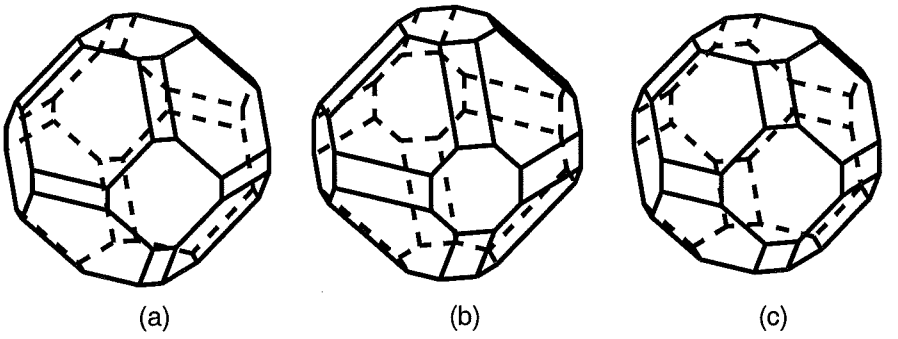

Figure 6.2: Wulff shape for FCC Pb clusters. The shapes were calculated using the surface energies from (a) Sun *et al.* [146], (b) Wan *et al.* [147] and (c) Lim *et al.* [69].

6.4 Wulff Shape for Pb Clusters

Calculation of the Wulff shape requires the surface energies for the low index facets. Several authors have calculated values for the (111), (110) and (100) surfaces from interatomic potentials for Pb. Values for surface energies and surface energy ratios at 0 K are listed in Table 6.1, and the resulting Wulff shapes for FCC clusters are shown in Fig. 6.2.

Table 6.1: Surface energies for Pb.

	Surface Energy (meV/Å^2)			Surface Energy Ratio	
Author	γ_{111}	γ_{110}	γ_{100}	$\gamma_{100}/\gamma_{111}$	$\gamma_{110}/\gamma_{111}$
Sun *et al.* [146]	31.0	35.6	34.0	1.097	1.148
Wan *et al.* [147]	22.3	24.6	25.5	1.143	1.103
Lim *et al.* [69]	37.5	41.8	38.0	1.013	1.115

The ratio $\gamma_{110}/\gamma_{111}$ determines the presence of the rectangular (110) faces: only for ratios $< \sqrt{\frac{3}{2}}$ ($\sim$1.22) will the (110) faces appear. The $\gamma_{100}/\gamma_{111}$ ratio determines the relative size of the octagonal (square if (110) faces are not present) (100) faces. This ratio is also influential in determining at what cluster size the icosahedral structure becomes preferable to cuboctahedral (FCC) structure, because it determines the energy reduction icosahedra obtain from exposing only (111) faces.

6.5 Predictions of Pb Cluster Structure

From the calculations made by Ino [57] (see section 2.3) based on bulk properties of Pb, Pb clusters are predicted to favour icosahedral structure below a diameter of 9.8 nm. This calculation assumed $\gamma_{100}/\gamma_{111}$=1.155, which, compared to the above values for γ_{100} and γ_{111}, could be too high. If the true value is lower it means that the benefit of

exposing (111) faces instead of (100) faces is reduced. Re–evaluating Ino's calculation with the values from Table 6.1 gives the maximum diameter for icosahedral clusters as 3.7 nm (Sun), 5.2 nm (Wan) and 4.3 nm (Lim). These sizes predict that a structural change for Pb clusters occurs in the range of ~1000 to ~2000 atoms.

In contrast, MD simulations of Pb clusters performed by Lim *et al.* [69] predicted that cuboctahedral clusters are more favourable than icosahedral clusters for all sizes. Lim *et al.* attribute this result to the low surface energy anisotropy and high tensile surface stress. To investigate the effect of surface stress Lim *et al.* examined the variation of the in–plane lattice parameter for atoms within the faces of relaxed 309 atom cuboctahedral and icosahedral clusters. For the cuboctahedron, the (100) faces contracted and the (111) faces expanded. Overall, this gave the cuboctahedron an average surface contraction of ~2%. For the icosahedron the (111) faces (and therefore the whole surface) were expanded because of the need to distort the tetrahedra when building an icosahedron. The high tensile surface stress makes the expansion of surface faces energetically costly.

Although Lim *et al.* predicted FCC clusters were preferable to icosahedral clusters for all sizes a later simulation by them [148] in which an 8217 atom liquid drop was quenched did produce an icosahedral–like structure. This structure was thought to form due to (111) facets nucleating at the surface of the liquid drop and nucleation proceeding inwards. It was expected that, given sufficient simulation time, the cluster would transform into the preferred FCC structure.

Recent MD simulations of Pb clusters by Hendy and Hall [70] have expanded on the work by Lim *et al.* and also found a structure that has lower energy than the FCC structure for Pb clusters. The potential used by Hendy and Hall is the same as used by Lim *et al.* in the earlier simulations and hence when comparing cuboctahedral and icosahedral clusters it is unsurprising that Hendy and Hall also report that cuboctahedra are preferred for all sizes. Hendy and Hall also include decahedra and incomplete shell cuboctahedra in the comparison. The decahedra were found to have slightly higher energy than cuboctahedra and the energies of incomplete shell cuboctahedra were found to lie between the decahedra and icosahedra. In subsequent work Hendy [71] has added anti–Mackay icosahedra to the comparison. The stability of this form of icosahedra is in close competition with the cuboctahedral and decahedral structures.

During the simulated melting and freezing of spherical FCC clusters Hendy and Hall observed the expected increase in melting temperature with size and an undercooling of the liquid drop during freezing. As described in chapter 2 the re–solidification of the clusters did not result in the original FCC structure, but the shaved icosahedral structure. The shaved icosahedral structure is predicted to be the preferred structure within the size

range ~500 to ~5000 atoms. Clusters outside this size range are still expected to be cuboctahedral. Diffraction patterns and an example of a shaved icosahedra are shown in Fig. 4.9.

By simulating the melting and re–solidification of a 6525 atom icosahedron Hendy and Hall produced a FCC structure containing parallel stacking faults. The shape of the cluster was the hexagonal faced cuboctahedra (Fig. 2.2(b)), which is interesting because 6525 is a magic number for triangular faced cuboctahedra (Fig. 2.2(c)). The cluster was expected to change shape given sufficient simulation time, however.

In summary, MD simulations suggest that Pb clusters are expected to be cuboctahedral up to about ~500 atoms. From ~500 to ~5000 atoms the shaved icosahedral structure is preferred. Above ~5000 atoms the cuboctahedral structure is expected to be favoured. This sequence of structures is significantly different to the general expectation of icosahedral → (decahedra →) cuboctahedra predicted for other FCC metals [64–68].

6.6 Pb Experimental Results

This section begins with some general observations on Pb experiments. Then experiments covering the range of diffraction patterns observed are examined. These experiments study the response of cluster size and structure to changes in the crucible temperature, T_C, the inert gas pressure, P_G, and the composition of the inert gas (ratio of Ar to He). In general, the experimental diffraction patterns have been analysed twice, once using diffraction patterns from geometric decahedra, icosahedra and cuboctahedra (geometric models) and then using diffraction patterns from relaxed decahedra, icosahedra and cuboctahedra (relaxed models). The results from each analysis are compared and discussed with reference to the predictions of MD simulations and previous observations of cluster production (see section 3.2.3). In addition, several experimental diffraction patterns have been analysed using diffraction patterns from relaxed decahedra, icosahedra and cuboctahedra as well as patterns from anti–Mackay and shaved icosahedra.

6.6.1 General Observations

Overall, for the same source conditions, the diffraction patterns were very reproducible between experiments. Fig. 6.3 shows diffraction patterns from 4 different experiments. In each case the values of T_C and P_G are between 800 and 810°C and 2 and 3 mbar of Ar respectively; the resulting diffraction patterns are almost identical.

Experiments with Pb were conducted for a range of T_C, P_G, inert gas composition and size of first nozzle in the source chamber. In general, variation of T_C and P_G produced a

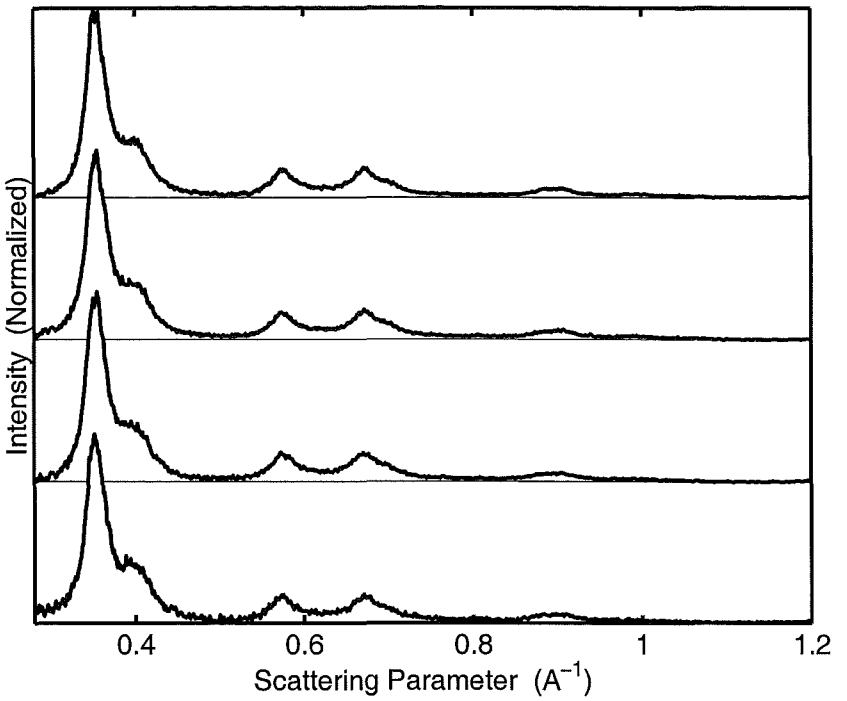

Figure 6.3: The reproducibility of diffraction patterns obtained in different experiments. The diffraction curves have all been obtained with T_C between 800 and 810°C, P_G between 2 and 3 mbar, a 6 mm diameter nozzle and using Ar as the inert gas.

slow evolution in the diffraction patterns observed. Lower limits for observing diffraction patterns for both T_C and P_G were determined during experiments. The exact values depended on experimental settings, such as the first nozzle size, however $P_{G_{min}}$ was ~0.5–1 mbar using Ar or He and $T_{C_{min}}$ was ~750°C using Ar or ~800°C using He. Increasing T_C or P_G through the threshold value first produced a measurable deposition rate, then an observable diffraction pattern. Diffraction patterns were generally observable for deposition rates above ~5 Å/s, however the deposition rate was not always a good indicator of when diffraction patterns would be observable; in some cases diffraction patterns were not observed for rates above 10 Å/s. Cluster size and low background pressures in the diffraction chamber were also important factors in the observability of diffraction patterns. Further increases of T_C increased the intensity of the diffraction pattern when using both He and Ar. With He the value of P_G had little effect on the diffraction intensity once the threshold region was passed unless very high pressures were used. Using Ar an upper threshold for P_G was encountered, values of P_G above ~5 mbar prevented the formation of a detectable cluster beam.

Air in the source was also found to be detrimental to the formation of a cluster beam. During one experiment a vacuum leak in the source prevented the formation of the cluster beam.

6.6.2 Pressure – Temperature Experiments

The results for experiments using either He or Ar as the inert gas are discussed first. In these experiments the effects of changing T_C or P_G are examined. The changes in the diffraction patterns during each experiment are rather subtle but establish a series of baselines from which to compare patterns obtained under varying the He/Ar ratios, where the patterns evolve quickly.

To aid in interpreting the results in the following sections previous observations of cluster production (see section 3.2.3) are summarized:

1) increasing P_G produces larger clusters.

2) increasing T_C produces larger clusters.

3) increasing inert gas flow rate produces smaller clusters.

4) decreasing inert gas temperature produces larger clusters.

Note that, with the source used in this study, conditions (1) and (2) cannot be changed independently of (3) and (4) during an experiment. An increase of P_G requires an increase in the gas flow rate and an increase of T_C will tend to heat the inert gas more. Thus the results from experiments varying P_G and T_C must be interpreted with these effects in mind.

6.6.2.1 Effect of varying He pressure while T_C is constant

Fig. 6.4 shows the evolution of diffraction patterns as P_G is increased from 1 and 20 mbar while using He as the inert gas, a T_C of 975°C and a first nozzle diameter of 2 mm. The change between pattern 1 and 2 shows the evolution over the threshold region of P_G. The narrowing of the main peak and splitting of the broad peak at $s \approx 0.6$ Å^{-1} from pattern 1 to 2 suggests an increase in cluster size. Diffraction patterns 2 to 5 appear almost identical, despite P_G increasing from 2 to 7.5 mbar. From patterns 5 to 6 the splitting of the peaks at s=0.57 and 0.67 Å^{-1} becomes more distinct. Also the asymmetry of the main peak in pattern 5 develops into a shoulder in pattern 6.

Table 6.2: Size estimates and main peak intensity for the diffraction patterns displayed in Fig. 6.4. Diffraction patterns were obtained with T_C=975°C, P_G between 1 and 20 mbar (He) and a nozzle diameter of 2 mm.

Pattern	P_G (mbar)	Size (Diameter) Estimates (nm) Scherrer	Inversion	Fit (geo)	Fit (rlx)	TEM	Intensity ×10^{8}cnts/As
1	1.0	1.5	2.3	2.62	2.29	–	1.5
2	2.0	2.2	3.5	4.03	3.78	–	4.8
3	2.5	2.1	3.7	3.89	3.65	–	5.3
4	5.0	2.0	3.7	3.86	3.59	4.2	5.1
5	7.5	2.0	3.7	3.87	3.59	–	5.2
6	20	2.6	4.5	4.98	4.43	–	10.1

The results of fitting the diffraction patterns are shown in Fig. 6.5. A detailed explanation of this presentation is given in chapter 5.2.2, briefly the dark gray bars are the results of fits performed with diffraction patterns calculated from geometric models, while the lighter gray bars are for fits with diffraction patterns calculated from MD relaxed models. Small (S) models are <3.0 nm in diameter, medium (M) models are between 3.0 and 5.5 nm in diameter and large (L) models have diameters >5.5 nm. Each bar gives the relative volume weighted contribution to the fitted diffraction curve from model clusters with the indicated structure and in the indicated size range. The small line at the top of the bar is the uncertainty in the height of the bar.

Table 6.2 summarizes the results from the different methods of domain or cluster size estimation. The Scherrer estimate is derived from the width of the main peak using the Scherrer formula (see section 5.2.4.2). The Inversion estimate uses Fourier inversion to obtain an estimate of the distribution of interatomic distances. The upper bound on the interatomic distances provides a characteristic size for the clusters (see section 5.2.4.1). The two estimates from fitting are the volume weighted average domain sizes obtained from the fitted parameters (see section 5.2.2.3). The TEM estimate is the volume weighted

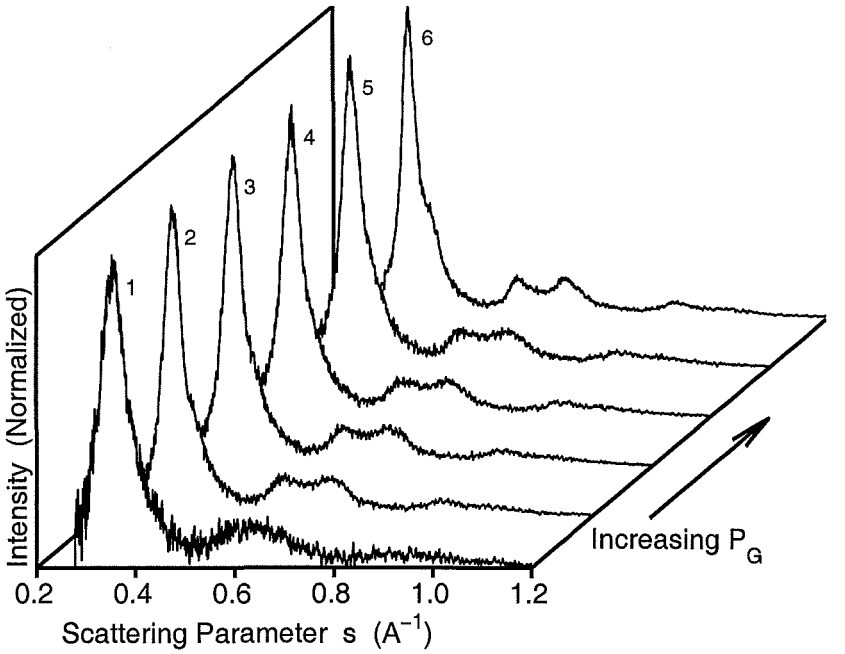

Figure 6.4: Diffraction patterns obtained by varying He pressure. The patterns were obtained with T_C=975°C, P_G between 1 and 20 mbar and a nozzle diameter of 2 mm.

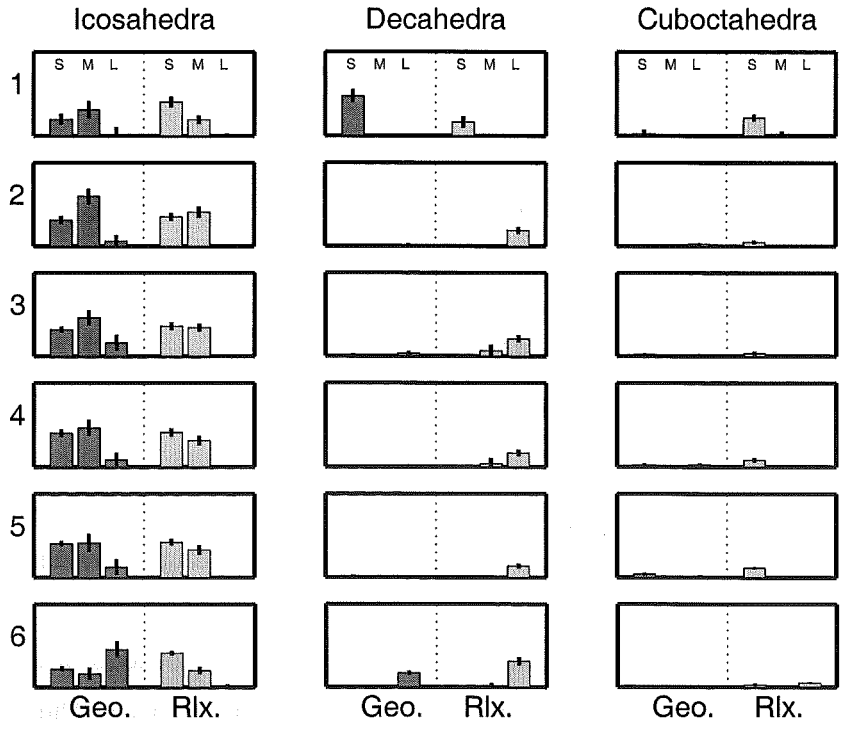

Figure 6.5: Fitting results for the diffraction patterns shown in Fig. 6.4. Dark gray bars are results from fits using geometric models; light gray bars are results from fits using relaxed models. S, M & L indicate model size ranges: S, small (<3.0 nm); M, medium (>3.0 & <5.5 nm); L, large (>5.5 nm). Height of each bar gives the relative volume weighting for the structure type in the indicated range. Diffraction patterns were obtained with T_C=975°C, P_G between 1 and 20 mbar (He) and a nozzle diameter of 2 mm.

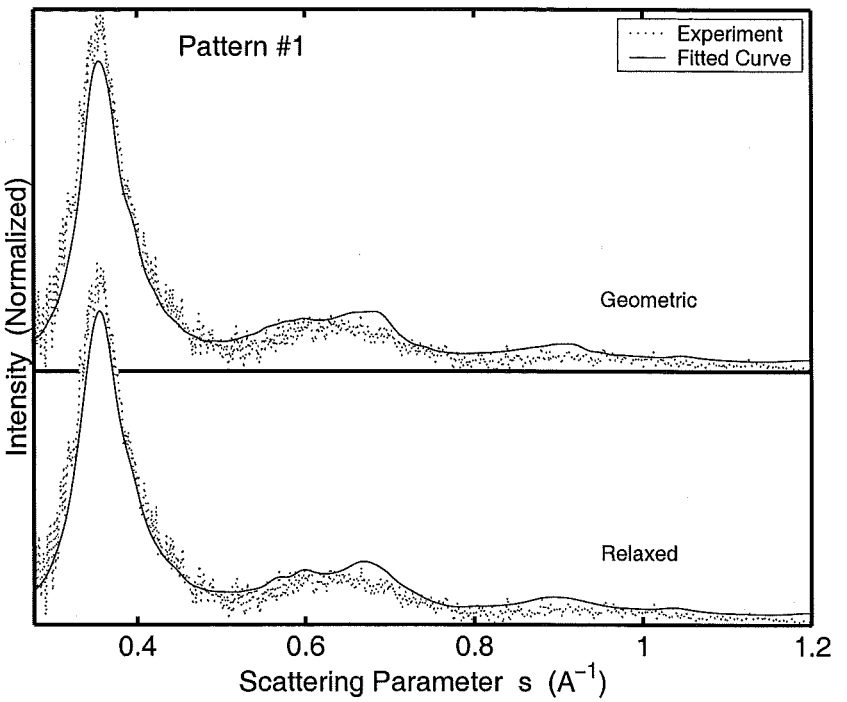

Figure 6.6: Fitted diffraction curves for pattern 1 shown in Fig. 6.4. Source conditions: T_G=975°C, P_G=1 mbar (He).

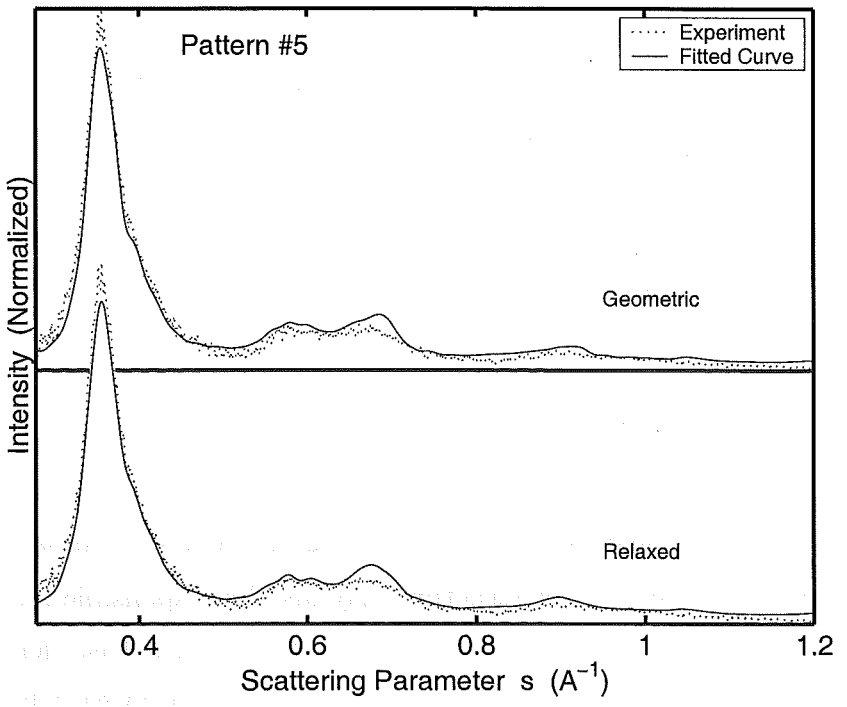

Figure 6.7: Fitted diffraction curves for pattern 5 shown in Fig. 6.4. Source conditions: T_G=975°C, P_G=7.5 mbar (He).

average diameter of the clusters collected from the beam and observed in a TEM (see section 5.2.3). The final column in the table is the intensity of the main peak (after background subtraction). The count rate (per exposure) obtained from the Poisson correction has been divided by exposure time and electron beam current giving an intensity with the units counts/ampere.second.

The results for pattern 1 indicate a variety of small particles are present in the beam, though the fitted curves, shown in Fig. 6.6, do not reproduce the shape of the experimental pattern between 0.5 & 0.75 Å^{-1} well and underestimate the height of the main peak. From Table 6.2 the size estimates for pattern 2 indicate the domains produced are roughly 50% larger than those in pattern 1, this is probably due to a significant increase in cluster size as P_G passes through the threshold region.

As could be expected from the similarity of the diffraction curves, the fits and size estimates for patterns 2 to 5 are all similar. The fit results indicate that most of the domains are either small or medium sized icosahedra. The fitted curves for these patterns suffer from an overestimate of the experimental curve at $s \approx 0.67\ \text{Å}^{-1}$ as shown for pattern 5 in Fig. 6.7. The consistency from pattern 2 to 5 suggests that the effects of increased gas flow rate and increased P_G essentially cancel.

Pattern 6 shows that increasing P_G does eventually cause an increase in size, however the P_G used to obtain pattern 6 creates a pressure in the 2nd stage turbo pump close to the operating limit meaning further increases of P_G were not explored. For this pattern the fit results using relaxed models are not greatly different to those from patterns 2 to 5, the main change being an increase in the contribution from large decahedral domains. When using geometric models the changes are more substantial, the results now include large decahedra and a much greater contribution from large icosahedra.

The TEM size estimate for pattern 4 shows the actual cluster size is slightly larger than the domain size calculated from the fit results. Such a result is typically expected when comparing size estimates from the diffraction data with TEM data. This is due to the fact that diffraction is only characteristic of the coherent domains within the cluster. In general, imperfections, such as multiple domains, disorder or defects, in the structure of many clusters will mean that they appear smaller in analysis based on diffraction data.

Imperfections in the cluster structure may also be responsible for the inability of the fit curves to completely reproduce the experimental pattern. Disorder will tend to smooth out the diffraction pattern with increasing s. It is observed in section 6.6.3 that including shaved icosahedra, which contain stacking faults, in the fits does improve the ability of the fitting routine to reproduce similar diffraction patterns.

The size estimates from inversion are closer to those obtained from fitting than the

TEM size estimate. The similarity is observed in nearly all of the patterns presented in this chapter and supports the suggestion made in section 5.2.4.1 that this method of estimation gives approximately the volume weighted average domain size. The size estimates using the Scherrer formula are always, as expected, less than the other methods.

Overall, fits using either geometric or relaxed structures show that a large contribution to the diffraction pattern is made by domains with icosahedral structure. The fits differ though on the predicted structure for large domains, fits using geometric models tend to show large domains as mostly icosahedral, whereas the fits with relaxed models report them as decahedral.

6.6.2.2 Effect of varying T_C using low He pressure

The diffraction patterns in Fig. 6.8 show the effect of varying T_C while keeping P_G constant. The patterns were obtained with P_G=4.5 mbar, He as the inert gas and a 6 mm diameter first nozzle. From pattern 1 to 6 the main peak narrows slightly and the broad peak at $s \approx 0.6$ Å^{-1} flattens. The broad peak in pattern 1 appears more triangular than the same peak in pattern 1 of Fig. 6.4, however the overall evolution of the patterns suggests that they will eventually look similar to patterns 2 to 5 in Fig. 6.4. The greatest effect that increasing T_C has on this sequence of diffraction patterns is the increase in intensity, Table 6.3 shows that from pattern 1 to 5 the intensity increases by factor of $\sim$25. A similar increase was observed in the deposition rate, in pattern 1 the deposition rate was $\sim$5 Å/s while for pattern 5 the deposition rate was $\sim$120 Å/s. A reduction in the deposition rate was observed while obtaining pattern 6 due to the second nozzle beginning to block.

Table 6.3: Size estimates and main peak intensity for the diffraction patterns displayed in Fig. 6.8. Diffraction patterns were obtained with T_C between 790 and 890°C, P_G=4.5 mbar (He) and a nozzle diameter of 6 mm.

	T_C	Size (Diameter) Estimates (nm)					Intensity
Pattern	(°C)	Scherrer	Inversion	Fit (geo)	Fit (rlx)	TEM	$\times 10^8$cnts/As
1	790	1.2	2.2	1.86	1.96	–	1.8
2	800	1.5	2.5	2.14	2.14	–	4.5
3	830	1.8	3.5	3.02	2.76	–	22.7
4	850	2.0	3.7	3.25	2.99	–	37.7
5	870	2.0	3.5	3.35	3.08	–	49.7
6	890	2.1	3.5	3.65	3.38	–	29.3

Fig. 6.9 and Table 6.3 show the results of fitting and the size estimates respectively. The fitted parameters for pattern 1 and 2 are dominated by small domains, but the fit (for pattern 1 the fitted curves are shown in Fig. 6.10) has difficulty in reproducing the broad peak at $s \approx 0.6$ Å^{-1}. When fitting pattern 1 with diffraction patterns from relaxed models the triangular shape of the broad peak favours small icosahedra, however the main peak in the experimental pattern has a broad base, while the main peak in diffraction patterns from small icosahedra is quite narrow.

The fitted parameters for patterns 3 to 6 show that most of the clusters in the beam have icosahedral domains. A small amount of large decahedral domains are also included in the fits using relaxed models. The flatter broad peak for these experimental patterns is better reproduced by the fitted curves, as shown in Fig. 6.11 for pattern 6.

Overall, the fit results suggest that these patterns show a transition corresponding to

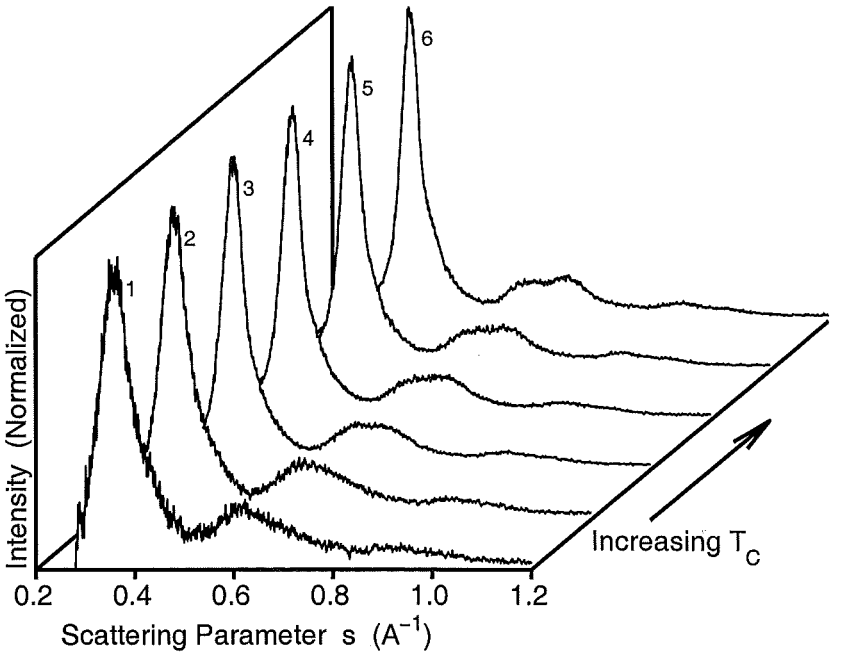

Figure 6.8: Diffraction patterns obtained by varying T_C while using He as the inert gas at low pressure. The patterns were obtained with T_C between 790 and 890°C, P_G=4.5 mbar (He) and a nozzle diameter of 6 mm.

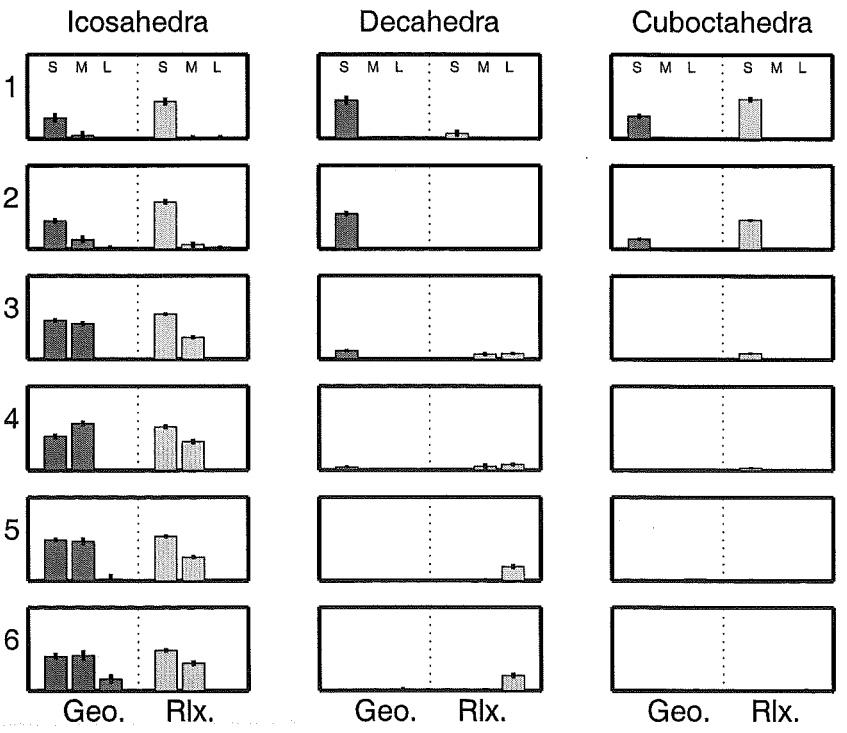

Figure 6.9: Fitting results for the diffraction patterns shown in Fig. 6.8. Dark gray bars are results from fits using geometric models; light gray bars are results from fits using relaxed models. S, M & L indicate model size ranges: S, small (<3.0 nm); M, medium (>3.0 & <5.5 nm); L, large (>5.5 nm). Height of each bar gives the relative volume weighting for the structure type in the indicated range. Diffraction patterns were obtained with T_C between 790 and 890°C, P_G=4.5 mbar (He) and a nozzle diameter of 6 mm.

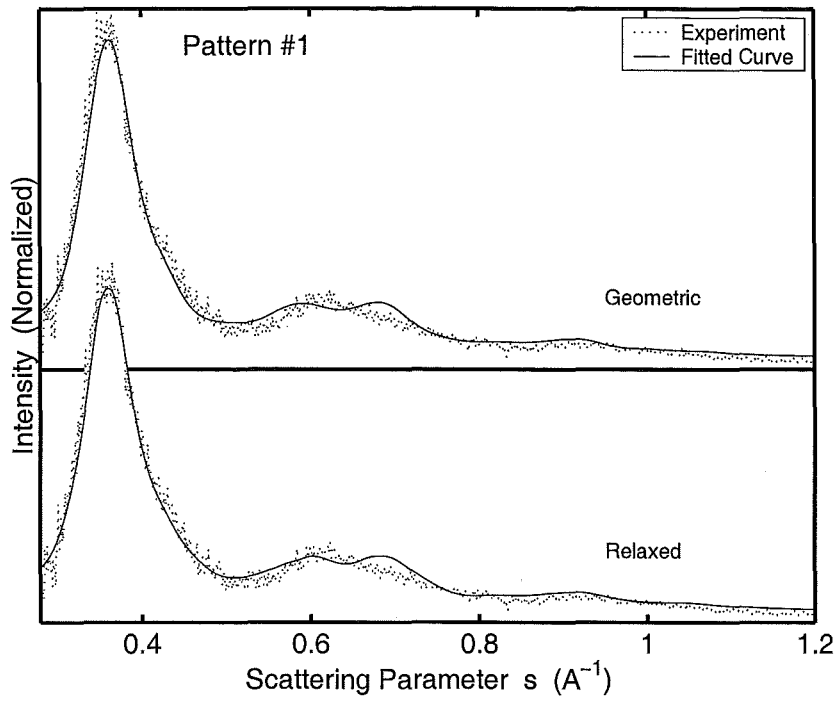

Figure 6.10: Fitted diffraction curves for pattern 1 shown in Fig. 6.8. Source conditions: T_C=790°C, P_G=4.5 mbar (He).

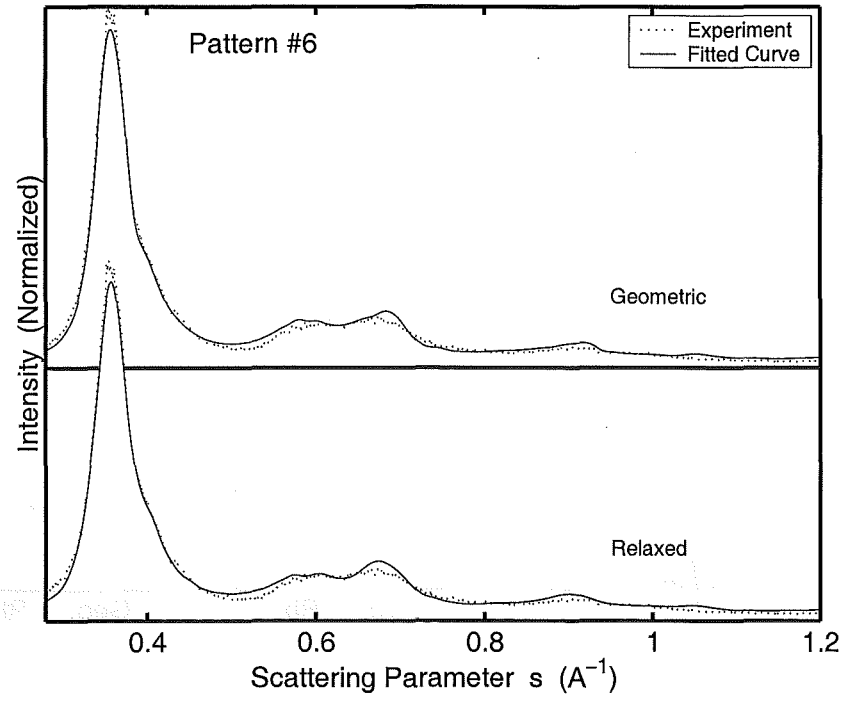

Figure 6.11: Fitted diffraction curves for pattern 6 shown in Fig. 6.8. Source conditions: T_C=890°C, P_G=4.5 mbar (He).

the transition between patterns 1 and 2 in the previous experiment (section 6.6.2.1). The results for pattern 2 and 6 in Fig. 6.8 are similar to results for pattern 1 and 2 respectively in Fig. 6.4.

The size estimates show the domain size increases from pattern 1 to 6. Assuming there is a corresponding increase in cluster size indicates that the size increase due to a higher T_C is greater than any reduction due to additional heating of the inert gas (from a higher T_C).

6.6.2.3 Effect of varying T_C using high He pressure

From previous observations of cluster production, reviewed at the start of section 6.6.2, using higher T_C and P_G and a smaller nozzle size (lowers the flow rate required to obtain P_G), could be expected to combine to produce larger clusters than in the previous experiment (section 6.6.2.2). Fig. 6.12 shows the diffraction patterns obtained with P_G=15 mbar, He as the inert gas, a 1.5 mm first nozzle and a T_C between 900 and 1050°C. Initial comparisons between the patterns in Fig. 6.12 and the patterns in Fig. 6.8 suggest that there is a definite difference between the clusters in the two sets of patterns, however a general increase in size is not clear. The evolution of the patterns in Fig. 6.12 is more complicated than for Fig. 6.8. Here the main peak narrows from pattern 1 to 4, but then broadens in the last two patterns. The peaks at $s \approx 0.57\,\text{Å}^{-1}$ and $0.67\,\text{Å}^{-1}$ initially split apart to become two rounded peaks between patterns 1 and 3, however from pattern 5 to 6 the intensity of these two peaks increases relative the main peak.

Table 6.4: Size estimates and main peak intensity for the diffraction patterns displayed in Fig. 6.12. Diffraction patterns were obtained with T_C between 900 and 1050°C, P_G=15 mbar (He) and a nozzle diameter of 1.5 mm.

	T_C	Size (Diameter) Estimates (nm)					Intensity
Pattern	(°C)	Scherrer	Inversion	Fit (geo)	Fit (rlx)	TEM	$\times 10^8$cnts/As
1	900	1.8	3.0	3.17	3.38	6.5	5.4
2	950	1.9	3.5	3.34	3.54	–	8.1
3	975	1.9	3.5	3.54	3.76	–	9.9
4	1000	2.0	3.5	3.61	3.89	–	12.1
5	1025	2.0	3.5	3.60	3.85	–	13.3
6	1050	1.8	3.0	2.97	3.42	–	12.2

A summary of the fitting results and size estimates are shown in Fig. 6.13 and Table 6.4 respectively. The results of fitting for all the patterns are similar. Using geometric models the results typically include small decahedral and a range of icosahedral domains. When using relaxed models the results include a range of both decahedral and icosahedral domains. In the two previous experiments (sections 6.6.2.1 & 6.6.2.2) the fits using relaxed models indicated a general preference for small and medium sized domains to be icosahedral and large domains to be decahedra, however for these source conditions the fit results show no relationship between size and structure.

The fitted curves for pattern 1 and 5 are shown in Figs. 6.14 & 6.15 respectively. For both patterns and both types of fit the fitting routine is able to produce a good reproduction of the experimental curve. An overestimate at $s \approx 0.67\,\text{Å}^{-1}$ is still observed, but is generally less than in the previous experiments.

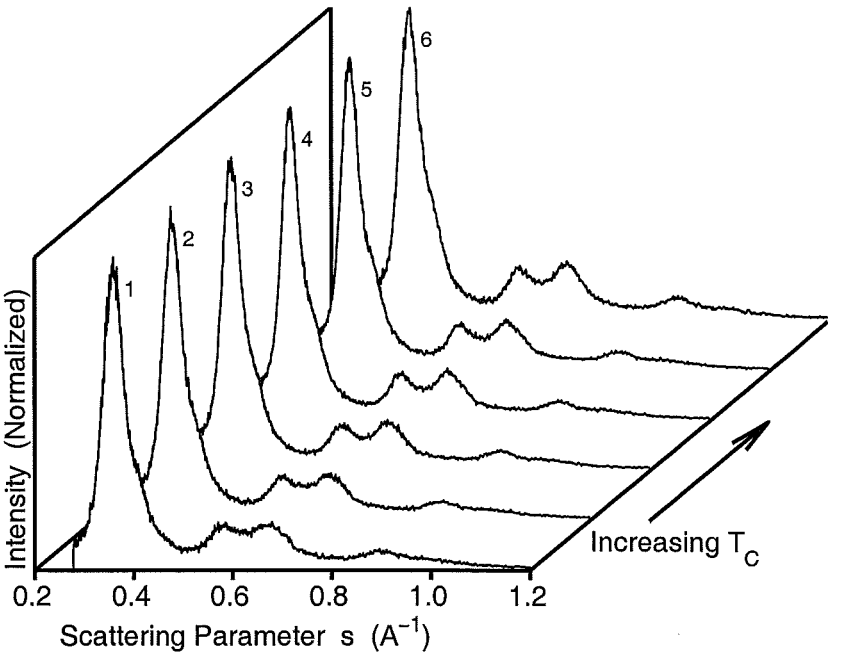

Figure 6.12: Diffraction patterns obtained by varying T_C while using He as the inert gas at high pressure. The patterns were obtained with T_C between 900 and 1050°C, P_G=15 mbar (He) and a nozzle diameter of 1.5 mm.

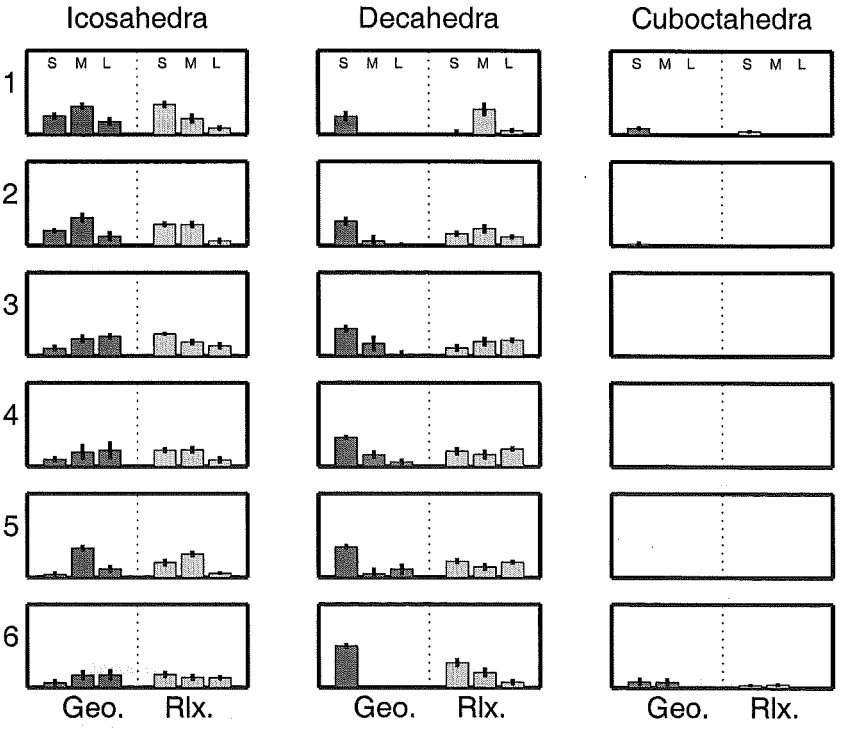

Figure 6.13: Fitting results for the diffraction patterns shown in Fig. 6.12. Diffraction patterns were obtained with T_C between 900 and 1050°C, P_G=15 mbar (He) and a nozzle diameter of 1.5 mm. Dark gray bars are results from fits using geometric models; light gray bars are results from fits using relaxed models. S, M & L indicate model size ranges: S, small (<3.0 nm); M, medium (>3.0 & <5.5 nm); L, large (>5.5 nm). Height of each bar gives the relative volume weighting for the structure type in the indicated range.

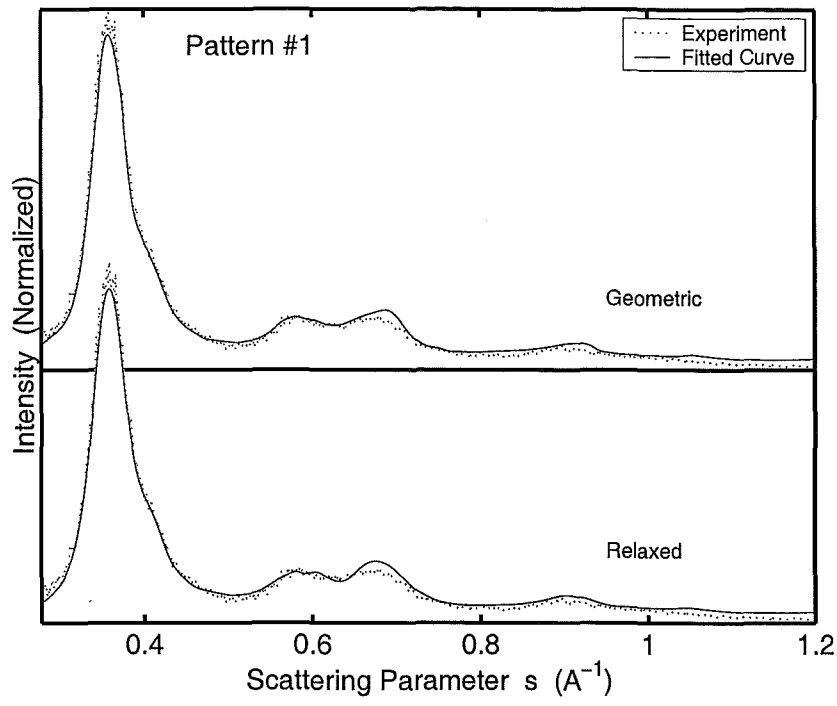

Figure 6.14: Fitted diffraction curves for pattern 1 shown in Fig. 6.12. Source conditions: T_C=900°C, P_G=15 mbar (He).

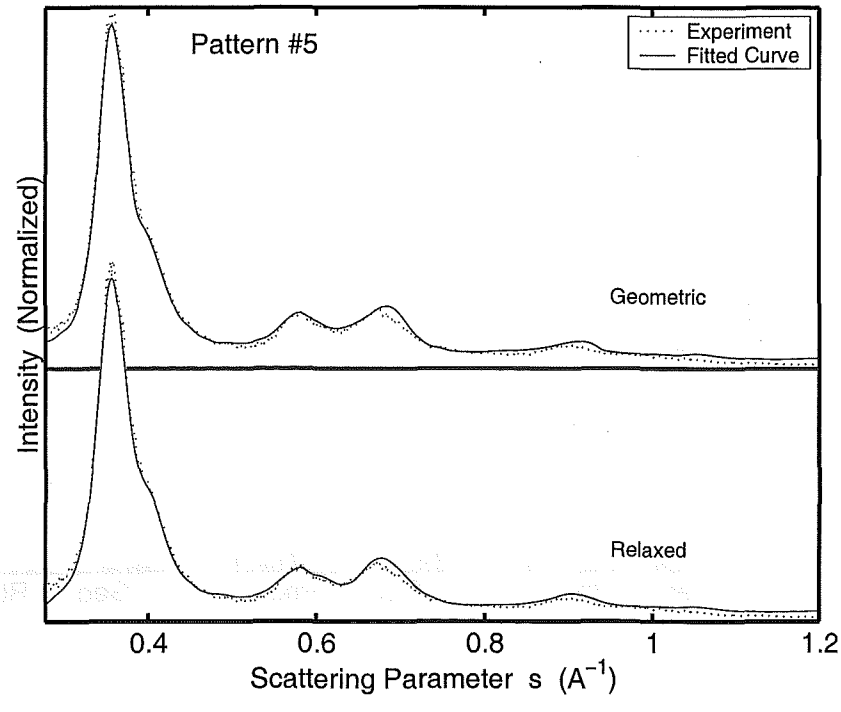

Figure 6.15: Fitted diffraction curves for pattern 5 shown in Fig. 6.12. Source conditions: T_C=1025°C, P_G=15 mbar (He).

A comparison between the size estimates from fitting and the TEM size estimate for pattern 1 in Table 6.4 show that there is a large difference between domain and cluster size for these experimental conditions. The large difference suggests that the clusters are comprised of multiple domains and possibly that a significant amount of coalescence, which is expected to become more frequent at higher P_G, has occurred.

6.6.2.4 Effect of varying T_C while Ar pressure is constant

Fig. 6.16 shows diffraction patterns obtained using a constant P_G of 1.7 mbar, Ar as the inert gas, a 6 mm first nozzle and a T_C between 750 and 810°C. In general, these patterns are distinctly different to the typical patterns obtained using He. Only pattern 6 of Fig. 6.4, which has a prominent shoulder on the main peak and two small peaks at s=0.57 Å^{-1} and 0.67 Å^{-1}, shows similarities to the patterns in Fig. 6.16. However, when using Ar the two small peaks are more distinct and less rounded.

Examination of the diffraction patterns in Fig. 6.16 shows that increasing T_C causes the main peak to narrow slightly and the shoulder on the main peak to become more pronounced, suggesting a small increase in size. As in section 6.6.2.2, a higher T_C increases the deposition rate, in pattern 1 the rate is ~20 Å/s compared to ~60 Å/s in pattern 7.

Table 6.5: Size estimates and main peak intensity for the diffraction patterns displayed in Fig. 6.16. Diffraction patterns were obtained with T_C between 750 and 810°C, P_G=1.7 mbar (Ar) and a nozzle diameter of 6 mm.

	T_C	Size (Diameter) Estimates (nm)					Intensity
Pattern	(°C)	Scherrer	Inversion	Fit (geo)	Fit (rlx)	TEM	$\times 10^8$cnts/As
1	750	2.7	3.7	4.36	4.81	–	5.4
2	760	2.7	4.0	4.73	4.90	7.8	7.1
3	770	2.7	4.0	4.65	5.23	–	9.4
4	780	2.9	4.0	4.90	5.05	–	12.6
5	790	3.2	4.5	5.10	5.11	–	15.3
6	800	3.3	4.5	5.14	5.14	–	16.4
7	810	3.3	4.5	5.24	5.23	–	18.8

The fitted parameters for the experimental patterns are shown in Fig. 6.17. For all the patterns the fitting routine is able to reproduce the experimental curve well. Figs. 6.18 & 6.19 show the fitted curves for patterns 2 and 7 respectively.

The fit results are all quite similar. The fits using geometric models show a significant contribution from medium and large decahedra, in the experiments using He the amount of medium and large decahedra reported by fitting (using geometric models) was generally small. The fits using relaxed models also have a significant contribution from decahedra, but in this case it is almost entirely from large decahedra. It is also important to note a small contribution from large cuboctahedra in patterns 4 to 7. In addition, both types of fit show that a range of icosahedral domains is present.

The fit size estimates in Table 6.5 show that the domains in this experiment are typically larger than the domains observed in experiments using He. The TEM size estimate in Table 6.5 is also larger than the TEM size estimates made in experiments

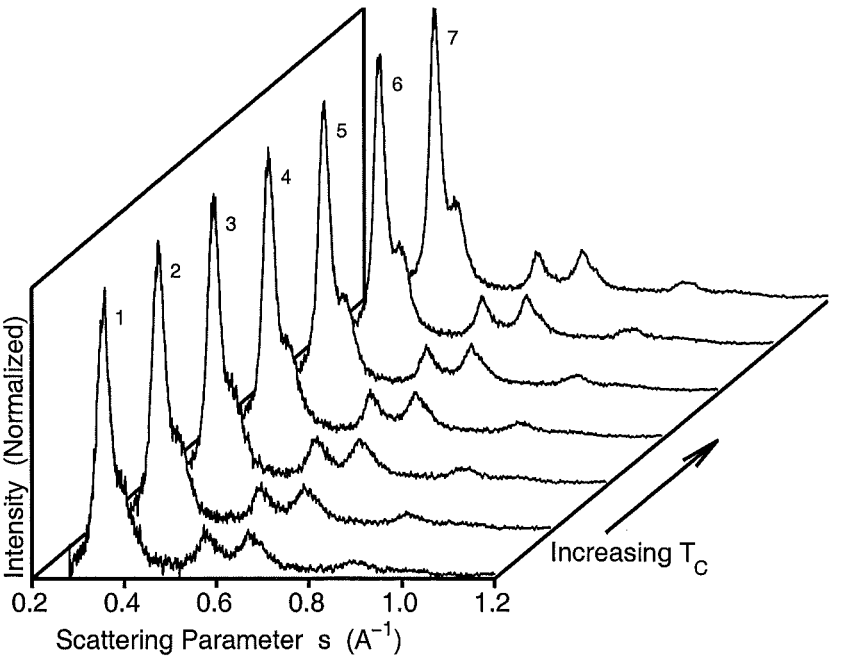

Figure 6.16: Diffraction patterns obtained by varying T_C while using Ar as the inert gas. The patterns were obtained with T_C between 750 and 810°C, P_G=1.7 mbar and a nozzle diameter of 6 mm.

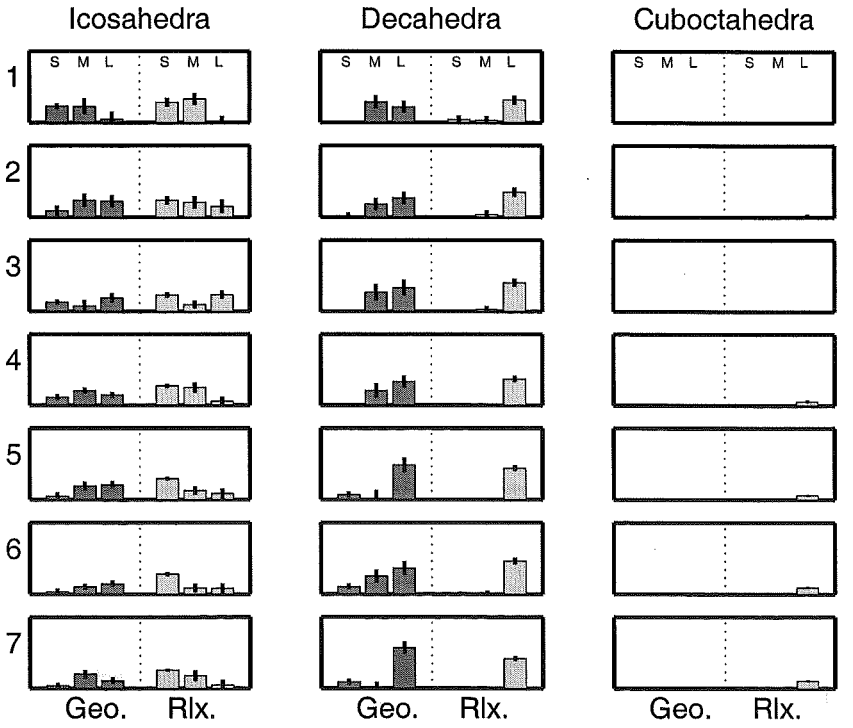

Figure 6.17: Fitting results for the diffraction patterns shown in Fig. 6.16. Dark gray bars are results from fits using geometric models; light gray bars are results from fits using relaxed models. S, M & L indicate model size ranges: S, small (<3.0 nm); M, medium (>3.0 & <5.5 nm); L, large (>5.5 nm). Height of each bar gives the relative volume weighting for the structure type in the indicated range. Diffraction patterns were obtained with T_C between 750 and 810°C, P_G=1.7 mbar (Ar) and a nozzle diameter of 6 mm.

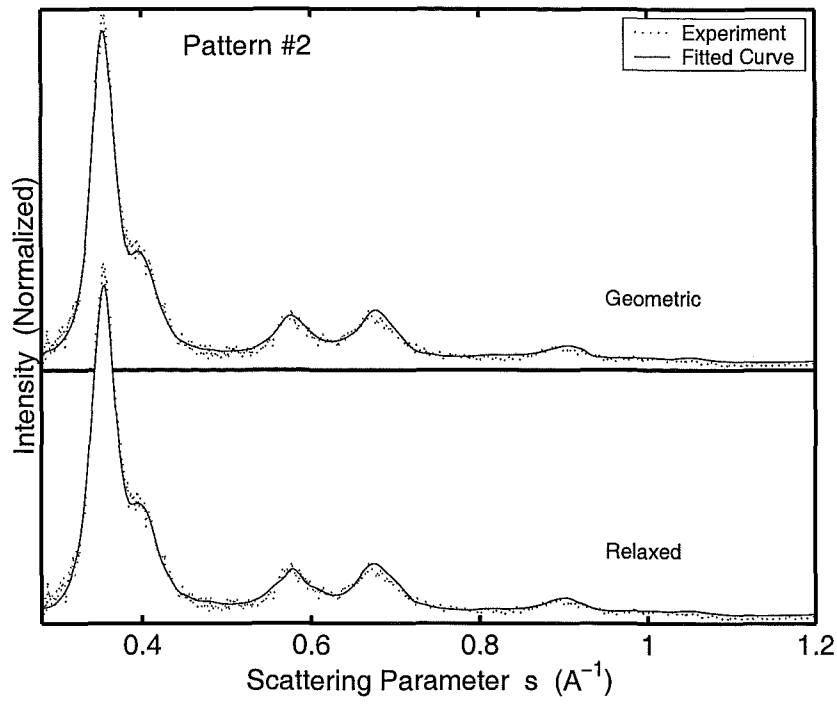

Figure 6.18: Fitted diffraction curves for pattern 2 shown in Fig. 6.16. Source conditions: T_C=760°C, P_G=1.7 mbar (Ar).

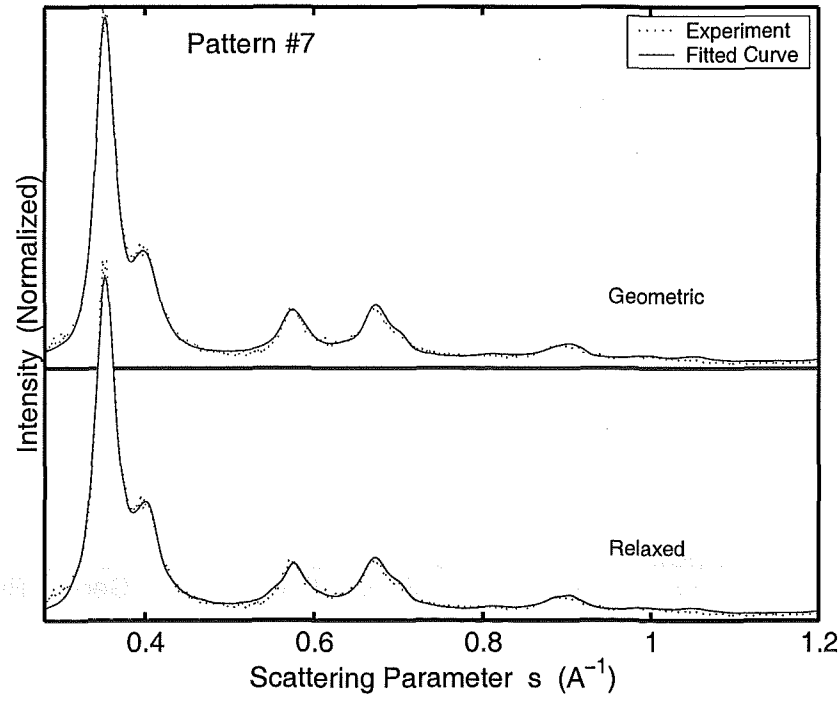

Figure 6.19: Fitted diffraction curves for pattern 7 shown in Fig. 6.16. Source conditions: T_C=810°C, P_G=1.7 mbar (Ar).

using He. It is expected, and typically observed, that Ar will produce larger clusters than He. This is attributed to Ar being better at cooling the metal vapour and thus promoting more nucleation (see section 3.2.3).

Overall, using Ar produced larger clusters and promoted the growth of structures that appear to be decahedral, however, as shown in chapter 4, it is difficult to distinguish between decahedra and faulted FCC clusters on the basis of diffraction patterns. This problem is discussed further in the next section.

6.6.3 Ar – He Mixing Experiments

In the previous section it was observed that the typical diffraction patterns obtained using Ar were substantially different to those obtained with He. Here an examination of diffraction patterns obtained by varying the composition of the inert gas from mostly He to mostly Ar while holding T_C and P_G constant is made. Figs. 6.20 & 6.21 show diffraction patterns obtained with T_C=840°C, P_G=1.5 mbar and a 6 mm first nozzle. Overall, the evolution of diffraction patterns shows a smooth transition between the typical diffraction patterns obtained with He to the typical diffraction patterns obtained with Ar. Pattern 1 looks like pattern 3 in Fig. 6.8 and Pattern 11 is very similar to pattern 7 in Fig. 6.16.

Table 6.6: Size estimates and main peak intensity for the diffraction patterns displayed in Fig. 6.20 & 6.21. Diffraction patterns were obtained by varying the composition of the inert gas from mostly He to mostly Ar, keeping T_C=840°C and P_G=1.5 mbar, and using a 6 mm nozzle diameter.

		Size (Diameter) Estimates (nm)						
Pattern	Ar (%)	Scherrer	Inversion	Fit (geo)	Fit (rlx)	Fit (ext)	TEM	Intensity $\times 10^8$cnts/As
1	8	1.9	3.2	3.04	2.68	3.10	–	7.6
2	10	1.9	3.5	3.07	2.79	3.40	–	9.0
3	20	2.1	3.8	3.43	3.24	3.87	–	18.3
4	30	2.2	3.8	3.41	3.36	4.13	–	23.3
5	40	2.1	3.8	3.38	3.26	3.89	4.8	17.9
6	50	2.2	3.8	3.89	3.76	4.37	–	14.9
7	60	2.6	4.0	4.35	4.22	4.89	6.7	13.9
8	70	2.8	4.2	4.74	4.50	5.18	–	12.6
9	80	3.0	4.5	4.96	5.02	5.61	–	11.2
10	90	3.4	5.2	5.43	5.19	6.01	–	12.0
11	98	3.7	5.5	5.56	5.45	6.22	8.2	13.3

The results for fitting the patterns in Figs. 6.20 & 6.21 are shown in Fig. 6.22, size estimations and the intensity of the main peak are shown in Table 6.6. For patterns 1 & 11 the fit results are essentially the same as for pattern 3 in Fig. 6.8 & pattern 7 in Fig. 6.16 respectively. The patterns in Figs. 6.20 & 6.21 have also been refitted using diffraction patterns from relaxed decahedra, icosahedra and cuboctahedra as well as anti–Mackay and shaved icosahedra. These fits are labeled as 'Extra Structures'. The size estimates and the fitted parameters for the 'Extra Structures' fits are given in Table 6.6 and Fig. 6.23 respectively. The results for patterns 1, 5, 7 & 11 are discussed in more detail below.

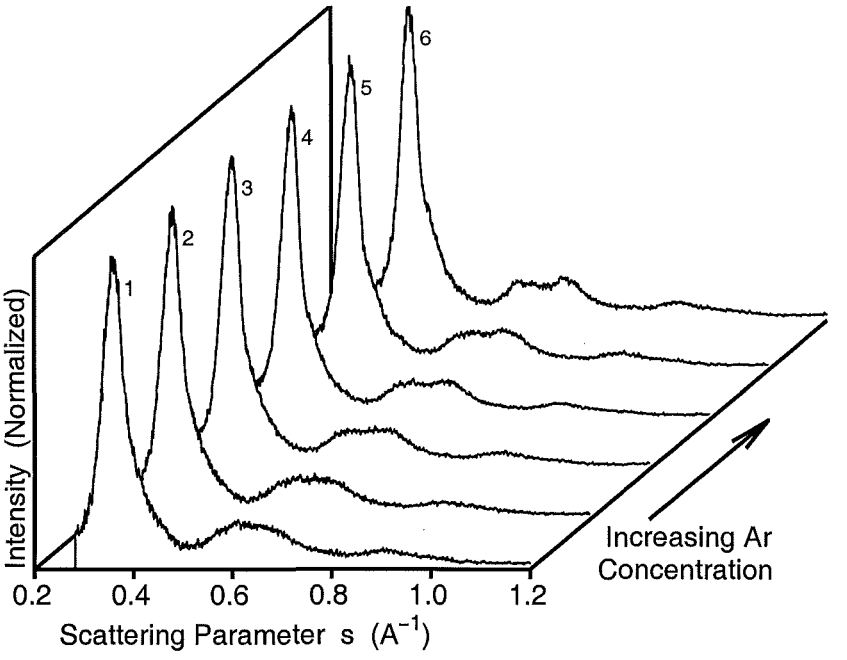

Figure 6.20: Diffraction patterns obtained by increasing the ratio of Ar to He in the inert gas from 8% to 50%. The patterns were obtained with T_G=840°C, P_G=1.5 mbar and a nozzle diameter of 6 mm.

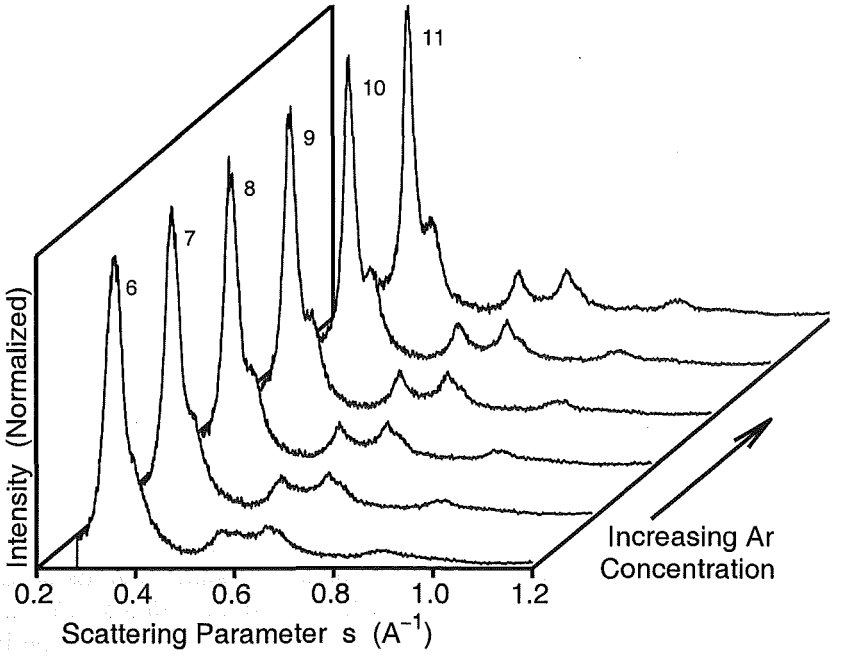

Figure 6.21: Diffraction patterns obtained by increasing the ratio of Ar to He in the inert gas from 50% to 98%. The patterns were obtained with T_G=840°C, P_G=1.5 mbar and a nozzle diameter of 6 mm. Note pattern 6 is included both here and in Fig. 6.20 to provide continuity between the figures.

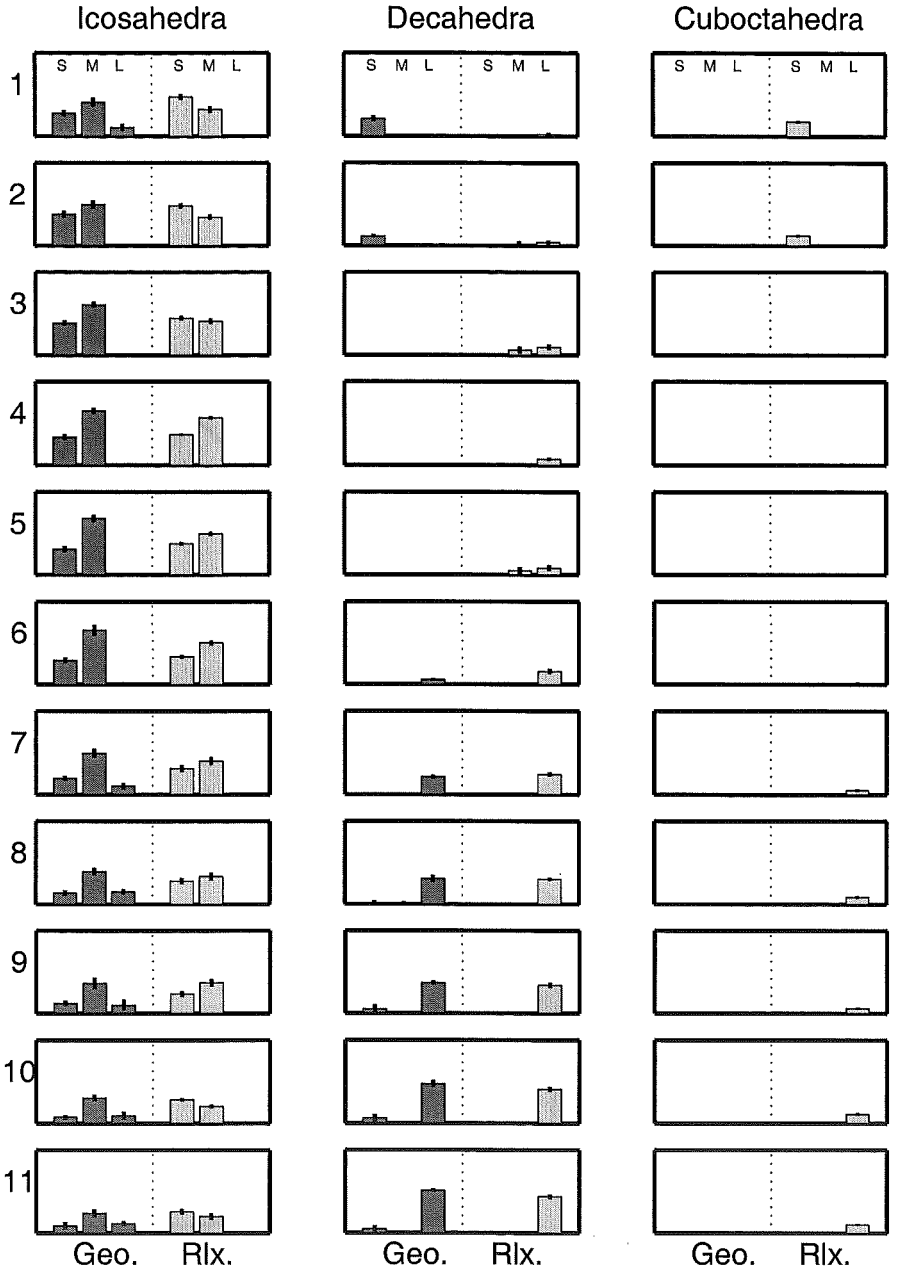

Figure 6.22: Fitting results for the diffraction patterns shown in Fig. 6.20 & 6.21. Dark gray bars are results from fits using geometric models; light gray bars are results from fits using relaxed models. S, M & L indicate model size ranges: S, small (<3.0 nm); M, medium (>3.0 & <5.5 nm); L, large (>5.5 nm). Height of each bar gives the relative volume weighting for the structure type in the indicated range. Diffraction patterns were obtained by varying the composition of the inert gas from mostly He to mostly Ar, keeping T_C=840°C and P_G=1.5 mbar and, using a 6 mm nozzle diameter.

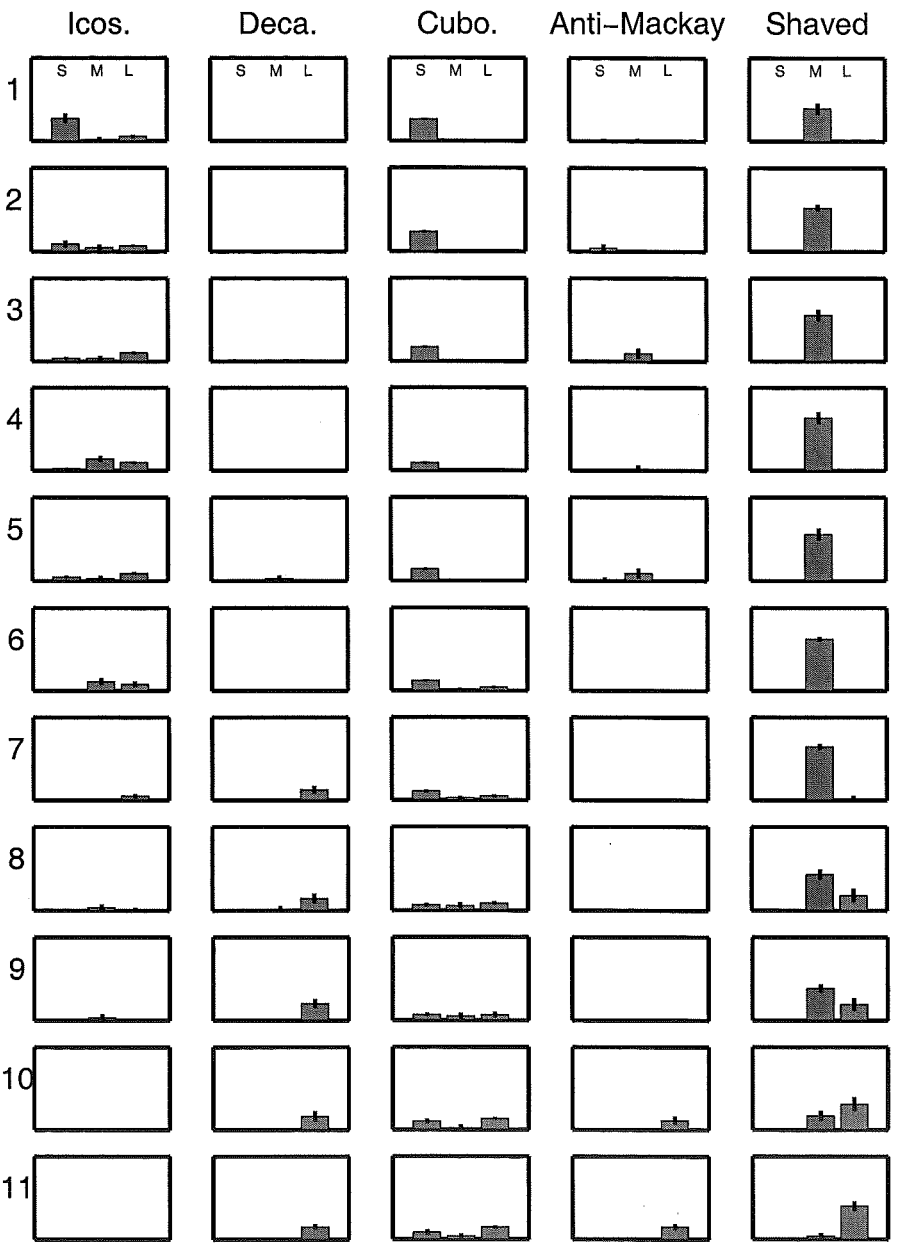

Figure 6.23: Fitting results for the diffraction patterns shown in Fig. 6.20 and Fig. 6.21 using the 'Extra Structures'. S, M & L indicate model size ranges: S, small (<3.0 nm); M, medium (>3.0 & <5.5 nm); L, large (>5.5 nm). Height of each bar gives the relative volume weighting for the structure type in the indicated range. Diffraction patterns were obtained by varying the composition of the inert gas from mostly He to mostly Ar, keeping T_C=840°C and P_G=1.5 mbar and, using a 6 mm nozzle diameter.

6.6.3.1 Pattern 1.

Pattern 1 has a broad rounded peak from s=0.5 to 0.8 Å^{-1} that is difficult to fit (see Fig. 6.24). Fig. 6.25 shows the fitted parameters for this pattern, the first two rows are for fits using geometric and relaxed models (decahedra, icosahedra and cuboctahedra) respectively. Both fits include mostly small and medium sized icosahedra. Examining the fitted curves in Fig. 6.24 shows that with geometric models the fitting routine produces a flattish curve across the broad peak, while with relaxed models the fitted curve contains a ripple. In neither case is the shape of the broad peak reproduced properly, especially for $s\approx$0.67 Å^{-1}.

Refitting with the relaxed models, but this time including extra structures (anti–Mackay and shaved icosahedra), results in the medium sized icosahedra being replaced by the medium sized shaved icosahedra (compare rows two and three in Fig. 6.25). The inclusion of the shaved icosahedra clearly improves the fit curve, however the fit still overestimates at $s\approx$0.67 Å^{-1}. In an attempt to further improve the fitted curve diffraction patterns from liquid models were also included in fitting, however these diffraction patterns were rejected by the fitting routine.

Overall, the use of the extra structures changes the interpretation of pattern 1 very little from the interpretation obtained from the original fits using geometric and relaxed models, except to note that the medium sized shaved icosahedra replace the normal icosahedra.

6.6.3.2 Pattern 5.

This pattern, shown in Fig. 6.26, is better reproduced by the fitting routine, using either geometric or relaxed models, than pattern 1. The fit using geometric models, except for an overestimate at $s\approx$0.67 Å^{-1}, reproduces the general shape of the experimental curve well. The fitted curve obtained using relaxed models contains a ripple at $s\approx$0.6 Å^{-1}, but is otherwise similar to the fitted curve obtained using geometric models. In both types of fit the majority of the domains are reported to have icosahedral structure (see Fig. 6.27).

The inclusion of the extra structures results in an improved fitted curve, most notable is a reduction of the overestimate at $s\approx$0.67 Å^{-1}. The results for this fit are also shown in Fig. 6.27. As for pattern 1, there is a strong contribution from medium sized shaved icosahedra, the contribution from other domains is spread across a variety of sizes and structures. Again the major change over the original fits using geometric and relaxed models is to replace normal icosahedra with shaved icosahedra.

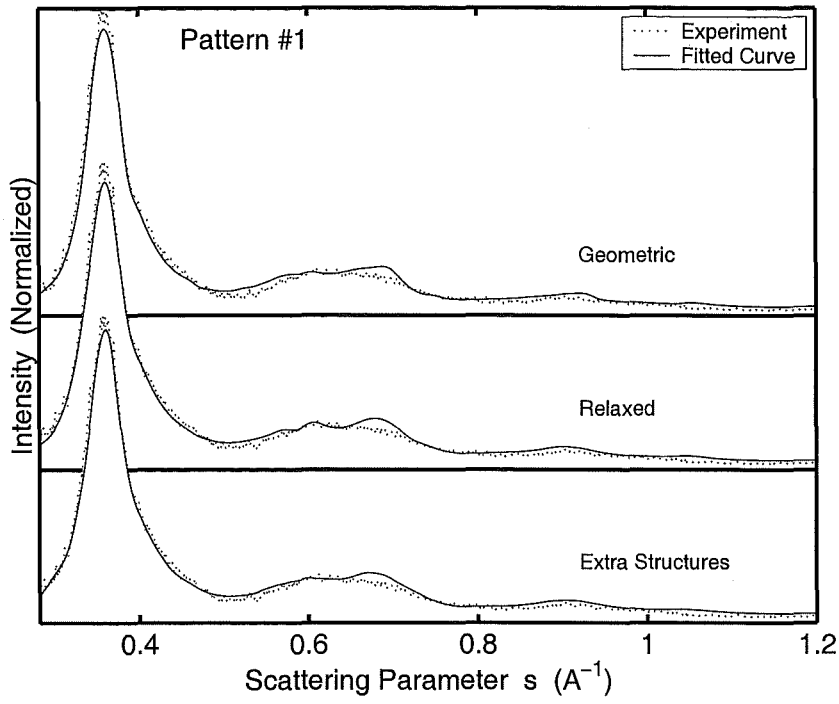

Figure 6.24: Fitted diffraction curves for pattern 1 shown in Fig. 6.20. Source conditions: T_C=840°C, P_G=1.5 mbar (8% Ar).

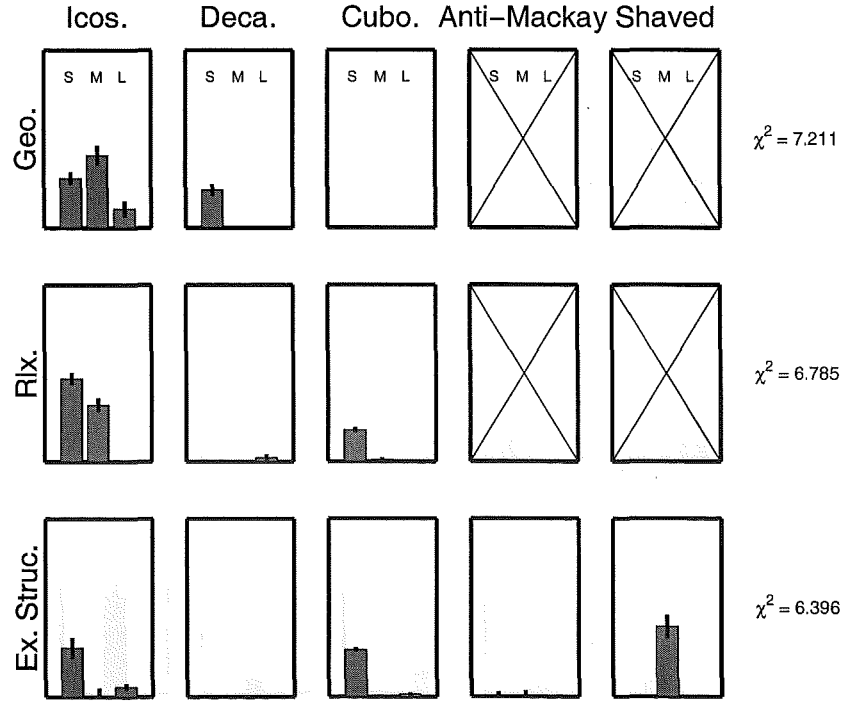

Figure 6.25: Fit results for curves fitted to pattern 1 shown in Fig. 6.24. S, M & L indicate model size ranges: S, small (<3.0 nm); M, medium (>3.0 & <5.5 nm); L, large (>5.5 nm). Height of each bar gives the relative volume weighting for the structure type in the indicated range. Source conditions: T_C=840°C, P_G=1.5 mbar (8% Ar).

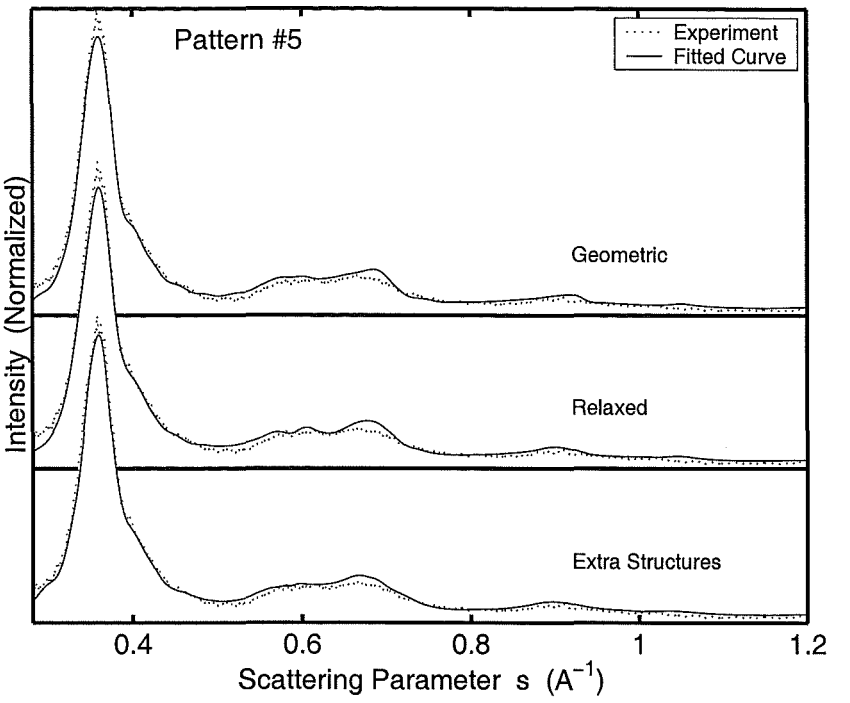

Figure 6.26: Fitted diffraction curves for pattern 5 shown in Fig. 6.20. Source conditions: T_G=840°C, P_G=1.5 mbar (40% Ar).

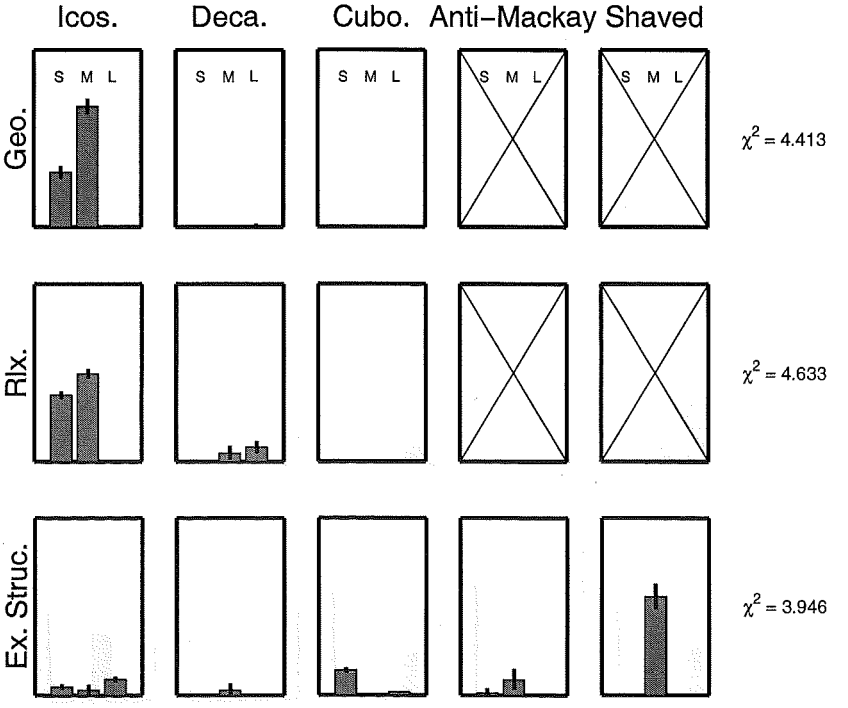

Figure 6.27: Fit results for curves fitted to pattern 5 shown in Fig. 6.26. S, M & L indicate model size ranges: S, small (<3.0 nm); M, medium (>3.0 & <5.5 nm); L, large (>5.5 nm). Height of each bar gives the relative volume weighting for the structure type in the indicated range. Source conditions: T_G=840°C, P_G=1.5 mbar (40% Ar).

6.6.3.3 Pattern 7.

In pattern 7 the asymmetry of the main peak in patterns 1 & 5 has developed into a shoulder and the broad peak from s=0.5 to 0.8 $Å^{-1}$ has split into two distinct peaks. The fitted curves for pattern 7 obtained using geometric and relaxed models are shown in Fig. 6.28. Both fitted curves reproduce the experimental pattern well, except for $s\approx$0.67 $Å^{-1}$. For $s\approx$0.67 $Å^{-1}$ the experimental patterns has a pointed peak with a shoulder while both fitted curves have a rounded peak. The fitted parameters for each curve are shown in Fig. 6.29 and indicate that the clusters consist of icosahedral or large decahedral domains.

When including the extra structures in the fit for pattern 7 the shape of the peak at $s\approx$0.67 $Å^{-1}$ is correctly reproduced, although the intensity is still overestimated. The results for this fit indicate that the contribution from shaved icosahedra is even greater than for pattern 5. Shaved icosahedra now account for $\sim$2/3 of all the domains. As for pattern 5, the contribution from other domains is spread over a variety of sizes and structures, including cuboctahedra and large decahedra.

Comparing the results from the fits using the geometric and relaxed models with the fit including the extra structures shows general agreement in that the majority of domains are icosahedral. However, it should be noted that the contribution from large decahedra is less in the fit including the extra structures than in either of the fits using geometric or relaxed models.

6.6.3.4 Pattern 11.

Fig. 6.30 shows that, for pattern 11, both the fit using geometric models and the fit using relaxed models produce an excellent representation of the experimental curve. The results for both fits, shown in Fig. 6.31, indicate a strong contribution from large decahedra and, when using relaxed models, a contribution from large cuboctahedra.

The fitted curve obtained by including the extra structures does improve on the fitted curve obtained using only relaxed decahedra, icosahedra and cuboctahedra, however the fitted results change substantially (compare rows two and three in Fig. 6.31). Including the extra structures indicates a strong contribution from large shaved icosahedra and, compared to the fits using geometric or relaxed models, the contribution from large decahedra is significantly reduced and the contribution from small and medium icosahedra vanishes.

In patterns 1 & 5, when the extra structures were included in fitting the results were readily accepted because the fitted curve was improved and the new interpretation was

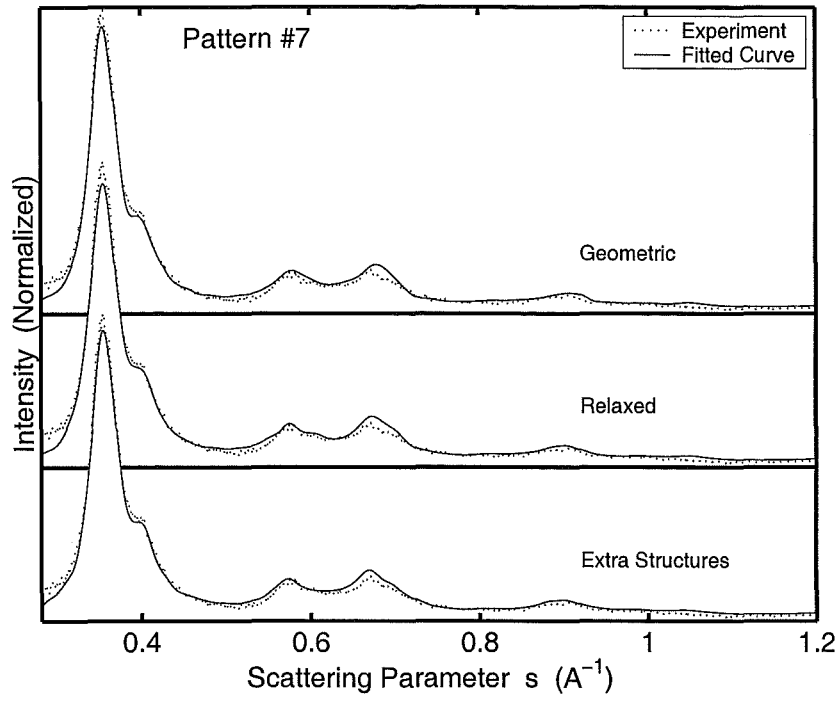

Figure 6.28: Fitted diffraction curves for pattern 7 shown in Fig. 6.21. Source conditions: T_G=840°C, P_G=1.5 mbar (60% Ar).

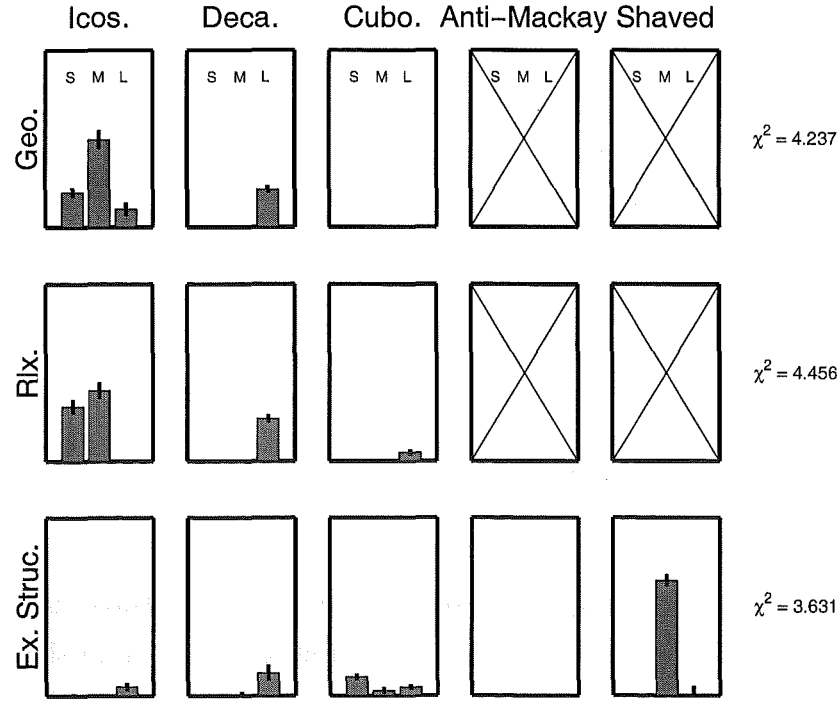

Figure 6.29: Fit results for curves fitted to pattern 7 shown in Fig. 6.28. S, M & L indicate model size ranges: S, small (<3.0 nm); M, medium (>3.0 & <5.5 nm); L, large (>5.5 nm). Height of each bar gives the relative volume weighting for the structure type in the indicated range. Source conditions: T_G=840°C, P_G=1.5 mbar 60% Ar.

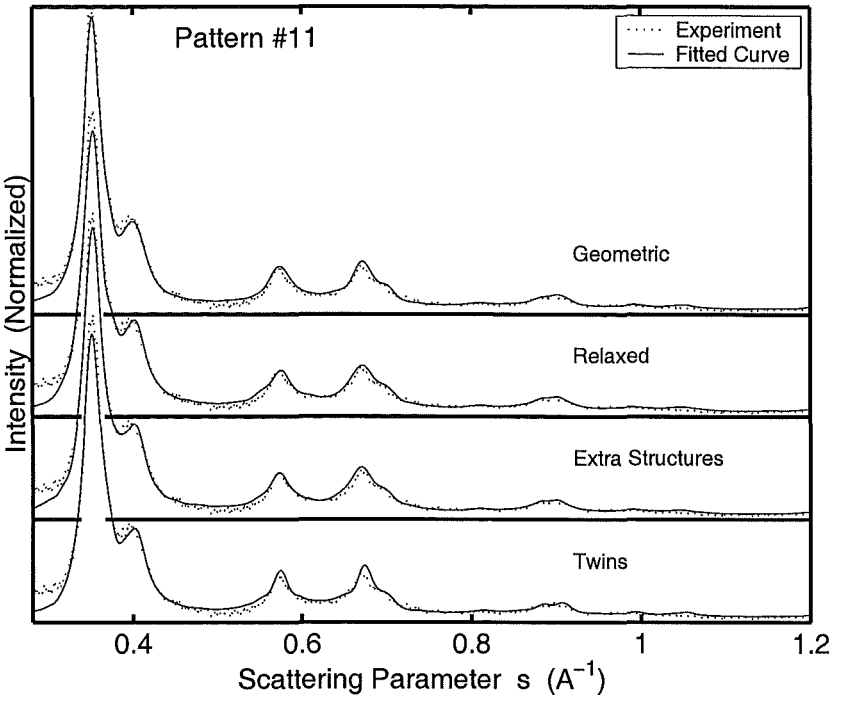

Figure 6.30: Fitted diffraction curves for pattern 11 shown in Fig. 6.21. Source conditions: T_C=840°C, P_G=1.5 mbar (98% Ar).

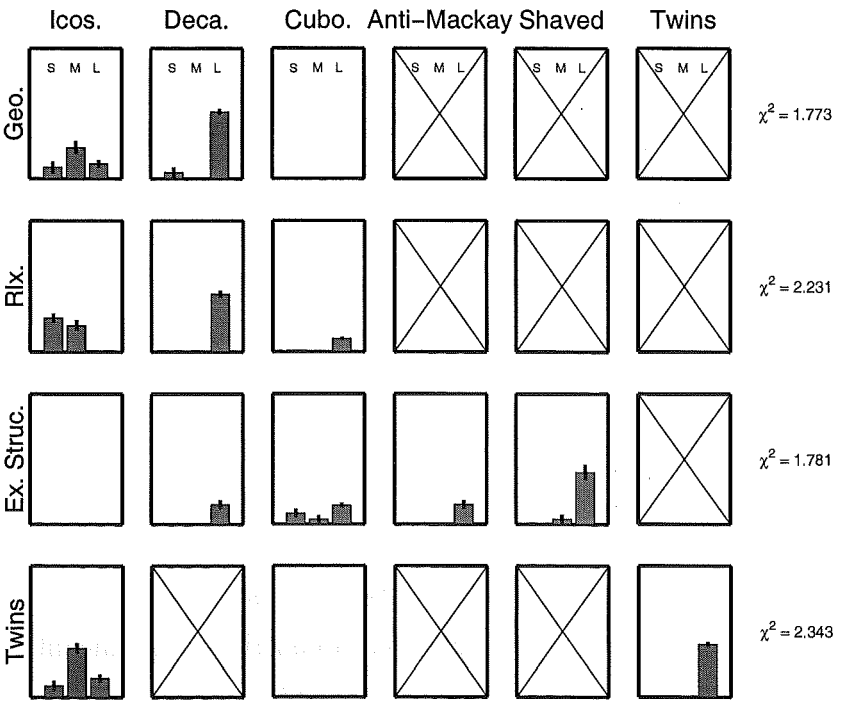

Figure 6.31: Fit results for curves fitted to pattern 11 shown in Fig. 6.30. S, M & L indicate model size ranges: S, small (<3.0 nm); M, medium (>3.0 & <5.5 nm); L, large (>5.5 nm). Height of each bar gives the relative volume weighting for the structure type in the indicated range. Source conditions: T_C=840°C, P_G=1.5 mbar (98% Ar).

only a refinement on the previous result. In pattern 7 the fitted curve was again improved, and although there was some change in the interpretation it did not greatly conflict with the previous results. Here the inclusion of the extra structures not only produces results that conflict with the original interpretation, but does not significantly improve the fitted curve either.

The conflicting interpretations for pattern 11 require further examination. As the fitted curves provide no reason for choosing one interpretation over the other, other details must be considered.

The fit using geometric models creates an excellent reproduction of the experimental pattern and indicates that the domains have decahedral structure. However, in section 4.5.2 it was shown that diffraction patterns from geometric decahedra are very similar to diffraction patterns from FCC clusters with parallel twin planes. Fitting pattern 11 using geometric decahedra, icosahedra, cuboctahedra and a selection of twinned FCC models resulted in the fitting routine rejecting the twinned FCC models. Another fit was performed where the decahedra were replaced by the selection of twinned FCC models. The results from this fit, labeled 'Twins', are shown in Fig. 6.31 and indicate a large contribution from the twinned FCC models. The fitted curve is shown in Fig. 6.30 and demonstrates that a satisfactory fit can be obtained using twinned FCC models. Comparing the 'Geometric' and 'Twins' curves in Fig. 6.30 suggests that, although twinned FCC models can reproduce the general shape of the experimental pattern, the geometric decahedra are preferred because they match the relative peak heights in the experimental curve better than the twinned FCC clusters.

It is also interesting to note that combining all the diffraction patterns used in fitting with random weightings[1] will tend to produce a diffraction pattern similar to that from large decahedral structures and thus pattern 11. The upper and lower panels in Fig. 6.32 show a randomly weighted combination of diffraction patterns from geometric and relaxed models respectively. Both curves are overlaid on pattern 11.

The fit including the extra structures indicates that a significant proportion of the domains are large shaved icosahedra and also that a range of other large structures are present. However, examining how the fitted curves are assembled reveals an interesting feature; although the large shaved icosahedra contribute significantly to the fitted curve, by themselves they do not match the experimental curve well. The other structures are required to create the shoulder on the main peak and the 'pointyness' of the small peaks at s=0.57 & 0.67 Å^{-1}. The top 4 panels in Fig. 6.33 show the contribution to the fitted

[1] i.e. each diffraction pattern is multiplied by a random number between zero and one, the resulting diffraction patterns are then added together.

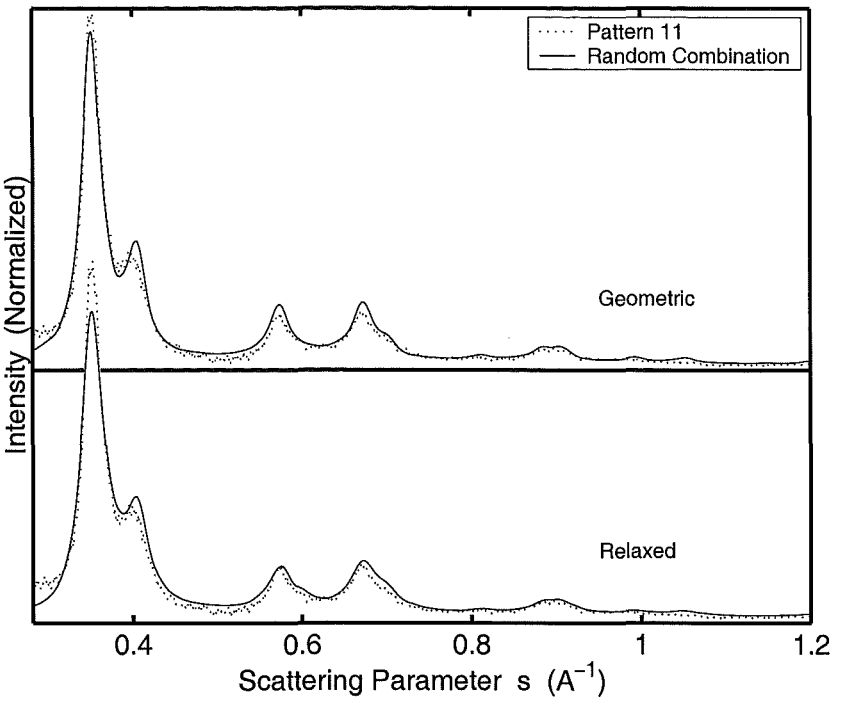

Figure 6.32: The similarity between pattern 11 and a random combination of the diffraction patterns from the decahedral, icosahedral and cuboctahedral models used in fitting. Top using geometric models, bottom using relaxed models.

curve from decahedra, cuboctahedra, anti–Mackay icosahedra and shaved icosahedra. The bottom panel shows the combination of the upper 4 panels, weighted as they are in the fitted curve, indicating that all the structures are important to produce the correct shape for the fitted curve.

Although the requirement of using multiple structures to fit the experimental curve is, in some ways, similar to the random combination seen above, this interpretation is supported by MD simulations: a transition from shaved icosahedra to cuboctahedra is predicted for clusters ~6.5 nm in diameter, i.e. within the large (L) size range. Hence, MD is indicating that clusters larger than those in pattern 11 is should adopt the FCC structure.

To produce very large clusters and observe if they adopt a FCC structure would require different source conditions to those used to obtain the diffraction patterns shown in Figs. 6.20 & 6.21. From source conditions similar to pattern 11 a large increase in T_C is needed to produce bigger clusters. The top panel in Fig. 6.34 shows a diffraction pattern obtained with T_C=840°C and P_G=1.5 mbar using Ar as the inert gas and a 3 mm nozzle, this diffraction pattern is very similar to pattern 11. The middle panel in Fig. 6.34 shows the diffraction pattern obtained when T_C is increased to 1000°C and P_G is held constant. The diffraction pattern obtained at high T_C is clearly not from icosahedral clusters. To

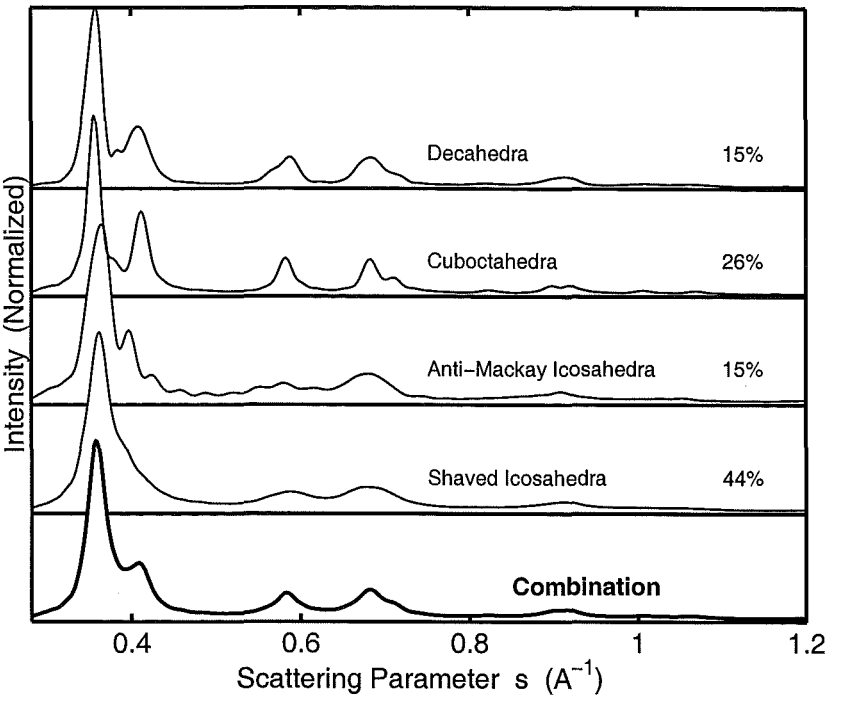

Figure 6.33: Top 4 panels: contribution from decahedra, cuboctahedra, anti–Mackay icosahedra and shaved icosahedra to the fitted curve. Bottom panel: combination of the top 4 panels weighted as they are in the fitted curve (decahedra: 15%, cuboctahedra: 26%, anti–Mackay Icosahedra: 15% and shaved icosahedra: 44%).

fit this pattern requires larger models than the other diffraction patterns presented in this chapter and an extra size range has been added to the fit results in Fig. 6.35. The 'VL' size range contains models with diameters between 8.0 & 9.5 nm. The fit curve obtained using the geometric models plus a range of parallel twinned FCC clusters, shown in the lower panel of Fig. 6.34, is a good reproduction of the experimental pattern. The fit results in Fig. 6.35 indicate a significant contribution from very large decahedra. Very large cuboctahedra and twinned FCC also make some contribution. However, the fit reports that small and medium sized domains account for about half the diffracted intensity, the inclusion of these domains by the fitting routine is possibly due to imperfections in the larger domains. It should be noted that the fit does not report any icosahedral domains.

Overall, there are three possible interpretations for pattern 11: 1) that large decahedra are being produced, 2) that defected (multiple parallel twins) FCC clusters are being produced and 3) that a mixture of shaved icosahedra and FCC clusters are being produced. With the information available none of the possibilities can be dismissed. However, taking a broader view the clusters in pattern 11 appear to be in a transitionary region, smaller clusters have icosahedral structures while larger clusters have a structure that is more characteristic of FCC. Although the structure of the larger clusters contributing to pattern

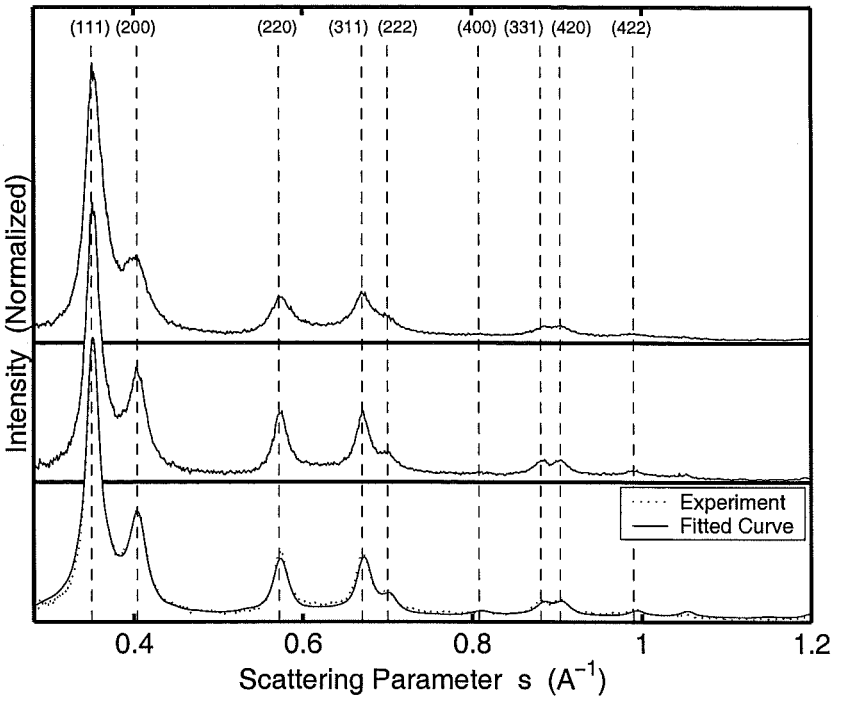

Figure 6.34: The top panel shows a diffraction pattern obtained with T_C=840°C and P_G=1.5 mbar using Ar as the inert gas and a 3 mm nozzle. This diffraction pattern is similar to pattern 11 in Fig. 6.21. The middle panel shows the diffraction pattern obtained when T_C is increased to 1000°C and P_G is held constant. The lower panel shows the fit curve obtained for the diffraction pattern in the middle panel. The vertical lines indicate the position of bulk (FCC) peaks for Pb.

11 cannot be fully identified it is clear the structure contains faults (probably including stacking faults and twins); to prevent ambiguity the structure is labelled as 'multiply faulted structure' (MFS). The presence of MFS is associated with medium and large decahedra appearing in the fit results for diffraction patterns from clusters produced using Ar.

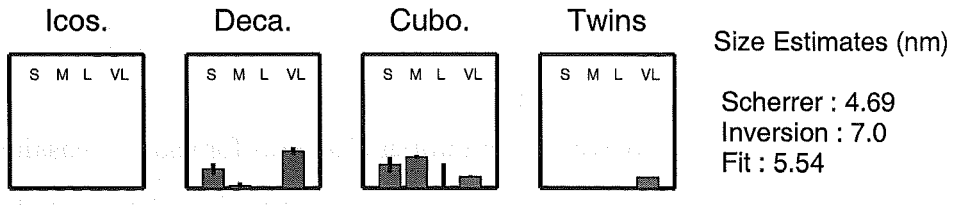

Figure 6.35: Fit results for the diffraction pattern in Fig. 6.35. S, M, L & VL indicate model size ranges: S, small (<3.0 nm); M, medium (>3.0 & <5.5 nm); L, large (>5.5 & < 8.0 nm); VL, very large (>8.0 nm). Height of each bar gives the relative volume weighting for the structure type in the indicated range. 'Twins' are parallel twinned FCC models. The diffraction pattern was obtained with T_C=1000°C, P_G=1.5 mbar (Ar) and a nozzle diameter of 3 mm.

6.6.3.5 Overview

Returning now to Fig. 6.22, which contains the fitted results for all the experimental patterns shown in Figs. 6.20 & 6.21, it can be seen that the composition of the cluster beam varies continuously while increasing the concentration of Ar in the inert gas. Fig. 6.36 shows how the relative contribution from each type of structure changes with Ar concentration in a more graphical form. In Fig. 6.22 both types of fit show low Ar / high He concentrations produce mostly small and medium sized icosahedral domains, and that increasing the Ar concentration produces more large decahedral domains. The fit using relaxed models also includes large cuboctahedra for high Ar concentrations. The transition from icosahedra at small and medium sizes to decahedra (and cuboctahedra) at larger sizes can be used to estimate a size for the transition to the MFS. The best estimate of this size comes directly from the fit results in Fig. 6.22, the fit results show that small and medium domains are almost entirely icosahedral while large domains are mostly decahedral or cuboctahedral, hence the transition size is approximately the transition size between medium and large bins, i.e. at a diameter of ~5.5 nm.

Alternative size estimates can be made from Table 6.6 and Fig. 6.36, arguably the increase in the number of decahedral domains reported by fitting starts in pattern 7 where the average domain size is ~4.3 nm. However, in pattern 7 the majority of domains are still icosahedral domains so the average size is not a good estimate of the transition size. In patterns 9 to 11 the contribution from icosahedral and non–icosahedral domains is approximately equal and the average domain size is ~5.0 to ~5.5 nm.

Fig. 6.23 shows the results from fits including the extra structures. Clearly, there is a strong preference for shaved icosahedra in all the patterns. In addition, the shaved icosahedra are not limited to the medium size range, from pattern 8 onwards large shaved icosahedra are reported. In pattern 7 the presence of large decahedra is reported for the first time. Observed from pattern 6 onwards is a growing contribution from large cuboctahedra. In Table 6.6 the size estimates from the fits including the extra structures are consistently larger than those from the fits using geometric or relaxed models. The disorder within the shaved icosahedra means that larger models are usually required to fit the experimental patterns compared to the fits using geometric or relaxed models.

Using this set of results to estimate an upper size limit for shaved icosahedra is difficult, even in pattern 11 the majority of the domains are still shaved icosahedral meaning the average domain size for pattern 11 is not a good estimate of the upper limit. However, fitting assigns a variety of structures to large domains indicating that the transition occurs over a size range: an estimate for the lower end of this range is given as ~5.5 nm, i.e. the lower size limit for the large bin.

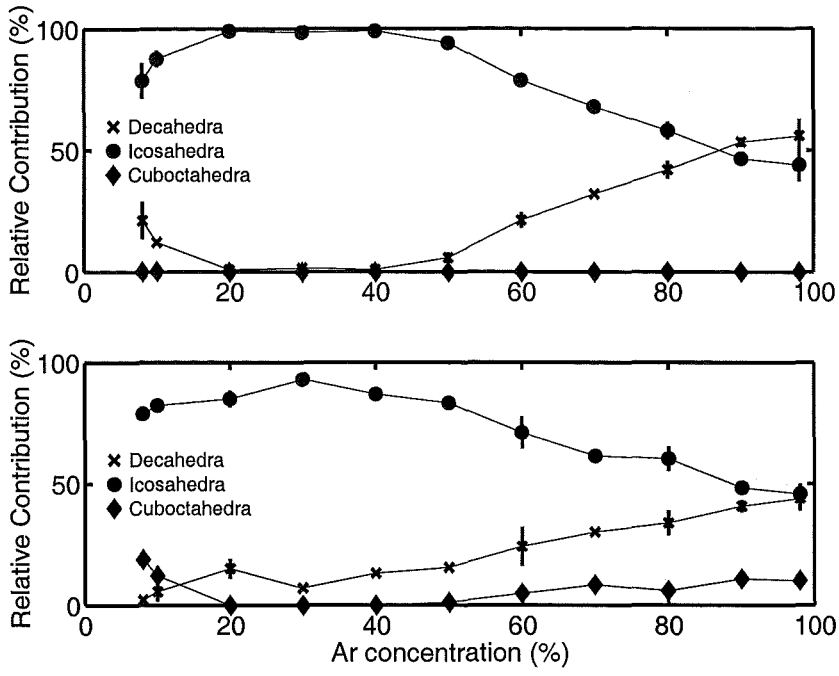

Figure 6.36: Relative contribution to the fitted curve from each type of structure. The top panel shows the results obtained using geometric models, and the bottom panel shows results obtained using relaxed models.

6.7 Discussion

Throughout this chapter emphasis has been placed on the results of fits performed using diffraction patterns from geometric and relaxed decahedral, icosahedral and cuboctahedral models. In general, previous studies [35, 40, 48], which used the method of optimized pattern fitting, used only geometric models, but expected that relaxed models would provide more accurate results and a better fit. For the experimental patterns analysed during this study the results from fits using either geometric or relaxed models tended to be in agreement and the use of relaxed models did not allow fits to be obtained to patterns which could not be fitted using geometric models.

That the geometric models produced equal or in some cases better fits to the experimental curves was surprising. However, this cannot be immediately taken to mean the clusters actually have the geometrically defined structures, but rather only that the diffraction patterns from geometrical models are more similar to the diffraction patterns from the unknown experimental structure (note the similarity between diffraction patterns from geometric decahedra and faulted FCC shown in section 4.5.2). In addition, it must be remembered that the relaxed models still represents an idealized situation for the cluster: the cluster is considered to have an ideal structure with the correct number of atoms and to be free, i.e. not a domain within a larger cluster. Experimentally clusters

are often observed to have defects and multiple domains, and are unlikely to have a magic number of atoms. These effects presumably influence the relaxation of the atoms within the cluster.

Reviewing the analysis of all the diffraction patterns presented in this chapter allows several observations to be made. The source parameters T_C and P_G had only a weak effect on the diffraction patterns produced. This is contrary to behaviour observed in other experiments [31, 101, 149]. The fit results indicate that icosahedral domains were typically produced when using He. Using Ar increased the cluster (and domain) size and the fit results indicated that decahedral domains were being formed. However, the experimental diffraction patterns could also be fitted using other structures: a mixture of shaved icosahedra, anti–Mackay icosahedra, cuboctahedra and decahedra produced a good fit, and, although decahedra produce a better fit, a satisfactory fit could be obtained using parallel twinned FCC clusters. Due to this ambiguity the structure produced using Ar has been described as a multiply faulted structure.

Comparing results from the different methods used in size estimates shows that estimates obtained from TEM observations were systematically larger than the estimates obtained from fitting. Such a result is typically expected: in general HRTEM observations of clusters show that the structure of many clusters is imperfect, however the size estimate from fitting is characteristic of the domain size within the clusters. Also observed was a general agreement between the size estimate from fitting and the estimate from Fourier inversion. It was initially unclear what the size from the Fourier inversion method would represent, but for the diffraction data from Pb clusters it appears to be a good estimate of the volume weighted domain size.

6.7.1 Previous Diffraction Studies

In this section the literature results from several previous diffraction studies will be related to the observations made on Pb clusters. Section 6.7.1.1 discusses a situation, similar to that for pattern 11 in Fig. 6.21, where two different, but equally satisfactory, interpretations of a diffraction pattern can be made. Sections 6.7.1.2, 6.7.1.3 & 6.7.1.4 discuss series of diffraction patterns which appear very similar to the sequence in Figs. 6.20 & 6.21. In addition, section 6.7.1.4 discusses the causes of structural transitions observed in experiments on Ag and Cu clusters (these experiments on Ag and Cu clusters were performed using the same equipment as the present study on Pb clusters). Section 6.7.1.5 discusses a previous diffraction experiment on Pb clusters, in which larger (than in the present study) clusters were observed and assigned a FCC structure.

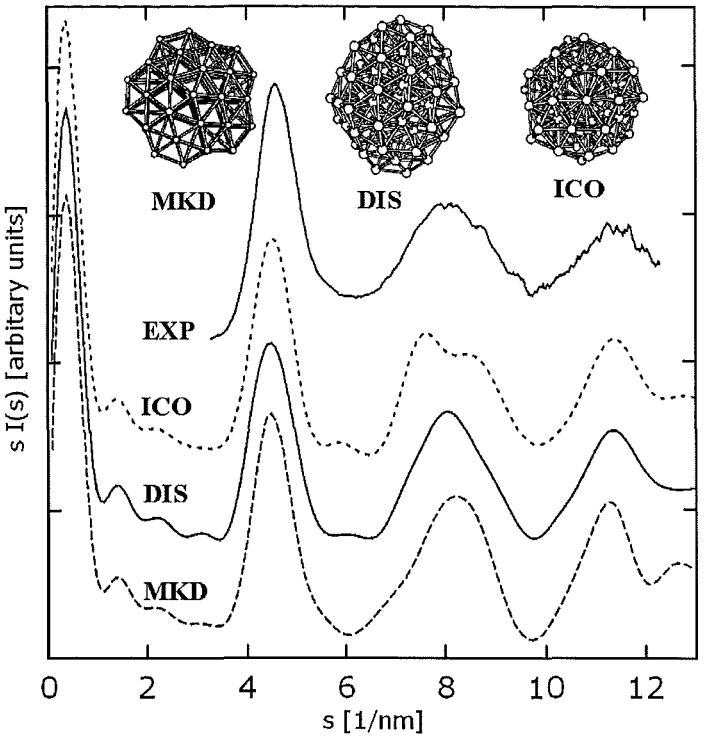

Figure 6.37: Comparison of experimental X–ray diffraction patterns from ~70 atom (~1 nm) Au clusters and diffraction patterns from model structures. The upper curve, labeled 'EXP' is the experimental diffraction pattern, the three lower curves are from model icosahedral (ICO), disordered (DIS) and Mark's decahedral (MKD) clusters respectively. After Michaelian *et al.* [150].

6.7.1.1 Structure of Small Au Clusters

Fig. 6.37 shows an experimental X–ray diffraction pattern obtained from Au clusters with ~70 atoms. The clusters were prepared by chemical synthesis method that allows a very narrow size range to be produced, hence there is no need to consider a size distribution in analysis. Cleveland *et al.* [73] initially searched for the theoretical minimum energy structure for the clusters. A large variety of structures, including partially disordered ones, were considered and the truncated decahedron was found to be the minimum energy structure. Comparison between the diffraction patterns from the various model clusters and the experimental pattern also favoured the decahedral clusters (in Fig. 6.37 compare the lines labeled 'EXP' and 'MKD'). This evidence would appear to put beyond doubt the structure of the Au clusters. However, subsequent studies by Michaelian *et al.* [150] have indicated that completely disordered structures are close in energy to the decahedral structure. Fig. 6.37 shows there is a strong similarity between the diffraction patterns from the disordered ('DIS') and MKD structures, and that they are both a good fit to the experimental data. Hence, it is impossible to determine which of the disordered and decahedral structures is present in the experiment.

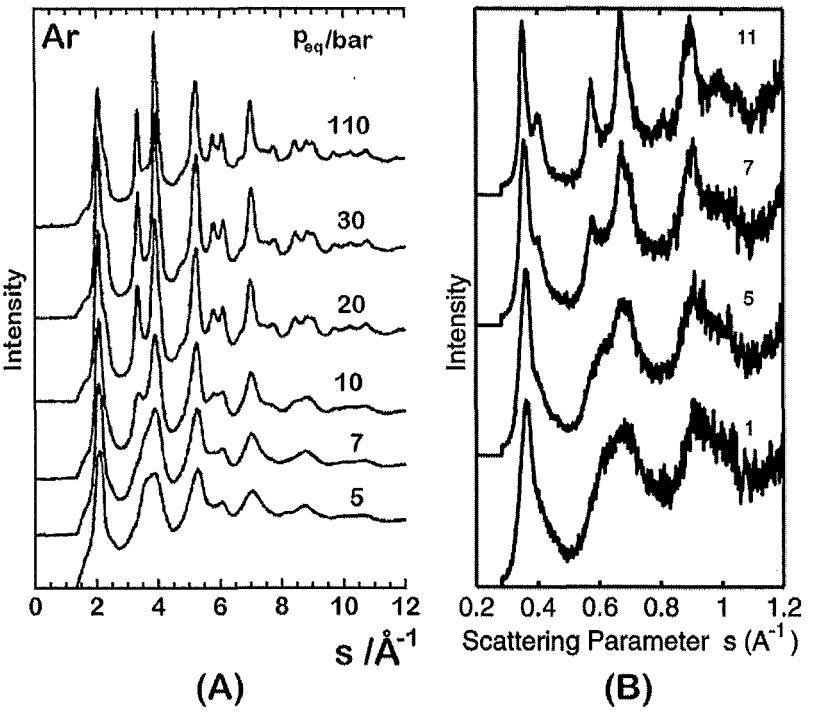

Figure 6.38: (A) Electron diffraction patterns obtained by the Orsay group from Ar clusters. After de Feraudy *et al.* [151]. Size estimates (calculated from Fig. 1 in Ref. [151]) for the patterns from top to bottom are 80000, 7500, 3500, 1000, 500 & 300 atoms. (B) For comparison, patterns 1, 5, 7 & 11 from Figs. 6.20 & 6.21 have been scaled by s^3 and replotted. The s^3 scaling gives the same enhancement to high s values as the experimental equipment used by de Feraudy *et al.*. Size estimates (calculated from the fits using geometric models) for the patterns from top to bottom are 4000, 2000, 900 and 500 atoms.

The studies by Cleveland *et al.* and Michaelian *et al.* highlight a case similar to that encountered with pattern 11 in Fig. 6.21 where different, but equally satisfactory interpretations of the experimental diffraction pattern can be made. That similar diffraction patterns can be obtained from different structures is a problem with diffraction studies. In such cases complementary analysis, such as HRTEM observations (if the cluster size is large enough), could resolve the problem.

6.7.1.2 Size – Structure Relationship in Ar Clusters

Perhaps some of the most extensively studied cluster diffraction patterns are those from Ar clusters produced by the Orsay group in France. Over the past 30 years significant effort has gone into explaining the size–structure relationship of the Ar clusters (see Appendix A for a review). A series of diffraction patterns from Ar clusters is shown in Fig. 6.38(A), the patterns are arranged in order of increasing cluster size from bottom to top (note the experimental equipment used enhances the diffraction intensity by a factor s^3 as s increases.). The size–structure relationship for small Ar clusters is well established [32,152,

153], icosahedral structures are observed from the minimum observable size (~20 atoms) up to ~1000 atoms. Below ~50 atoms the structure consists of interlinking icosahedral cages, while above ~50 atoms the normal icosahedral structure is observed.

At ~1000 atoms the diffraction patterns from Ar clusters (pattern third from bottom in Fig. 6.38(A)) begin to deviate from the patterns obtained using model icosahedral structures and develop features associated with FCC structure. The nature of this transition is difficult to explain: the diffraction patterns were not consistent with that from a simulated mixture of icosahedral and FCC clusters. This lead van de Waal to propose a structure (see section 2.7 and Ref. [88]) in which FCC structure grew on a MTP core. The diffraction pattern from van de Waal's structure was in good agreement with the experimental patterns for clusters with ~3000 atoms. This model predicted (and the general expectation was) that for larger sizes the FCC structure would dominate, meaning the shoulder on the peak at $s \approx 2\,\text{Å}^{-1}$ would develop into a separate peak, however even in experiments where clusters with ~80,000 atoms (top curve in Fig. 6.38) were produced the peak did not develop, indicating that the model was not satisfactory for larger sizes.

Another important feature of the experimental patterns from large Ar clusters is that the peaks, especially the first peak, are very broad compared to peaks in diffraction patterns from crystalline models with a similar number of atoms.[2] The structure of larger Ar clusters has been considered by de Feraudy and Torchet [151] and by van de Waal *et al.* [154, 155]. Both authors attempt to use structural defects to explain the diffraction patterns and the results appear promising, but both reports were a summary of work in progress. Subsequently, van de Waal *et al.* [155] have considered clusters with a mixture of FCC, HCP and random close–packed regions, the diffraction patterns from such clusters are in good agreement with the experimental diffraction patterns from large Ar clusters (top curve in Fig. 6.38(A)) and, although bulk Ar has FCC structure, this result suggests that the structure of large Ar clusters has no significant preference for FCC.

To allow a comparison between the diffraction patterns from Ar and Pb clusters, patterns 1, 5, 7 & 11 from Figs. 6.20 & 6.21 have been scaled by s^3 and replotted in Fig. 6.38(B). The diffraction patterns from small Ar clusters (lower two curves in Fig. 6.38(A)) are similar to the patterns from small Pb clusters (lower two curves in Fig. 6.38(B)). For Ar and Pb these diffraction patterns have been interpreted as coming from clusters with icosahedral structure. In the case of larger clusters there is a noticeable difference between the diffraction patterns from Ar clusters (top three curves in Fig. 6.38(A)) and Pb clusters (top two curves in Fig. 6.38(B)). The diffraction patterns

[2]The size of the larger clusters observed in the experiment is estimated by extrapolating a size–experimental parameter relationship observed for smaller sizes where the cluster size could be accurately determined from the diffraction pattern and mass spectroscopic measurements.

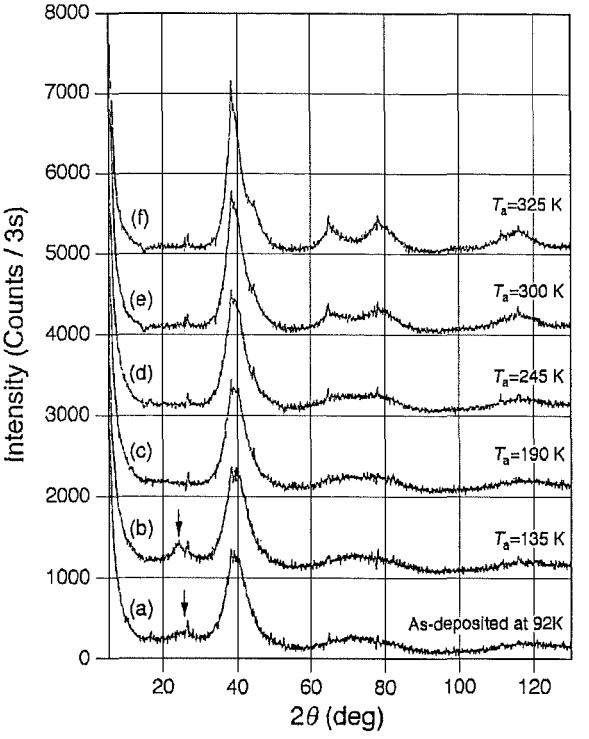

Figure 6.39: X–ray diffraction patterns of Au obtained during an annealing cycle. Pattern (a) is from ~2 nm clusters deposited on a Si substrate. Patterns (b) to (f) are from the sample after annealing at T_a for 0.5 hours. After Koga *et al.* [156].

from large Pb clusters show a definite splitting in the main peak ($s \approx 0.35\,\text{Å}^{-1}$), this splitting does not occur in any of the diffraction patterns from Ar clusters. The splitting suggests that there is a greater preference for, at least faulted or twinned, FCC stacking in Pb clusters than Ar clusters.

6.7.1.3 Au Cluster Coalescence

Grazing incidence X–ray diffraction patterns obtained by Koga *et al.* [156, 157] from Au are shown in Fig. 6.39. Small Au clusters (~2 nm diameter) were initially deposited on a Si substrate and observed by HRTEM. Only the structure of clusters larger than ~2 nm was determinable, the structure of smaller clusters fluctuated and was difficult to resolve against the background. For clusters with diameters between 2 to 3 nm decahedral structures were commonly observed, FCC structures (some containing faults) were also observed, but icosahedral structures were not.

Fig. 6.39(a) shows the diffraction pattern obtained from the deposited clusters, this pattern is very similar to pattern 1 in Fig. 6.20 from Pb clusters. Koga *et al.* attempted to reproduce pattern (a) in Fig. 6.39 using diffraction patterns from model clusters and

claimed decahedra gave the best match[3], however the match is not particularly good. Koga *et al.* suggest that the differences between the experimental diffraction pattern and the diffraction patterns from decahedral models are due to the presence of defects in the clusters, but no evidence is given to show the inclusion of these defects in model clusters would result in a better match to the experimental pattern. In addition, the size distribution shown by Koga *et al.* indicates that a significant contribution to the diffraction pattern could come from the clusters that had undeterminable structure in the HRTEM measurements (i.e. less than 2 nm in diameter). In the case of Pb clusters, the fit for pattern 1 in Fig. 6.20 has a clear preference for icosahedral domains, indicating that icosahedra produce a better fit to this type of pattern.

The deposited sample was then subjected to an annealing cycle. The sample was annealed for 0.5 hours before being cooled to 82 K and another diffraction pattern obtained. This process was repeated, each time increasing the annealing temperature. Annealing at progressively higher temperatures created an increase in the average domain size from one diffraction pattern to the next. The annealing temperatures, T_a, and diffraction patterns obtained are shown in Fig. 6.39(b)–(f). An SEM image of the sample after the final annealing cycle showed the clusters had aggregated to become 'lumpy–type networks' with a typical scale of 100 nm.

The final diffraction pattern, (f) in Fig. 6.39, is similar to pattern 8 in Fig. 6.21. For pattern (f) a comparison with diffraction patterns from model clusters was made. Attempts to match the experimental pattern with diffraction patterns from faulted FCC structures failed, however the diffraction pattern from a 428 atom decahedron matched the experimental pattern well. Despite the agreement between the experimental pattern and the diffraction pattern from the decahedron, Koga *et al.* state that the actual grains should not be represented with one structure model and suggest that "... the initial decahedral clusters coalesce to form nano–grain structures with multiple–twinning relations." This interpretation appears to be similar to the MFS for large Pb clusters (see section 6.6.3.4).

6.7.1.4 Results of Reinhard *et al.*

Reinhard *et al.* used the same experimental equipment as the present study on Pb clusters to examine the structure of Ag and Cu clusters.

Ag clusters up to ~11 nm in diameter were produced and it was found that a kinetic

[3]Koga *et al.* do not numerically optimize a combination of diffraction patterns from model clusters as performed for the diffraction patterns from Pb clusters analysed in the present study. For each structure considered Koga *et al.* combine diffraction patterns from model clusters using the weightings given by the size distribution obtained from HRTEM observations. The structures considered by Koga *et al.* were FCC, twinned FCC, icosahedra and decahedra.

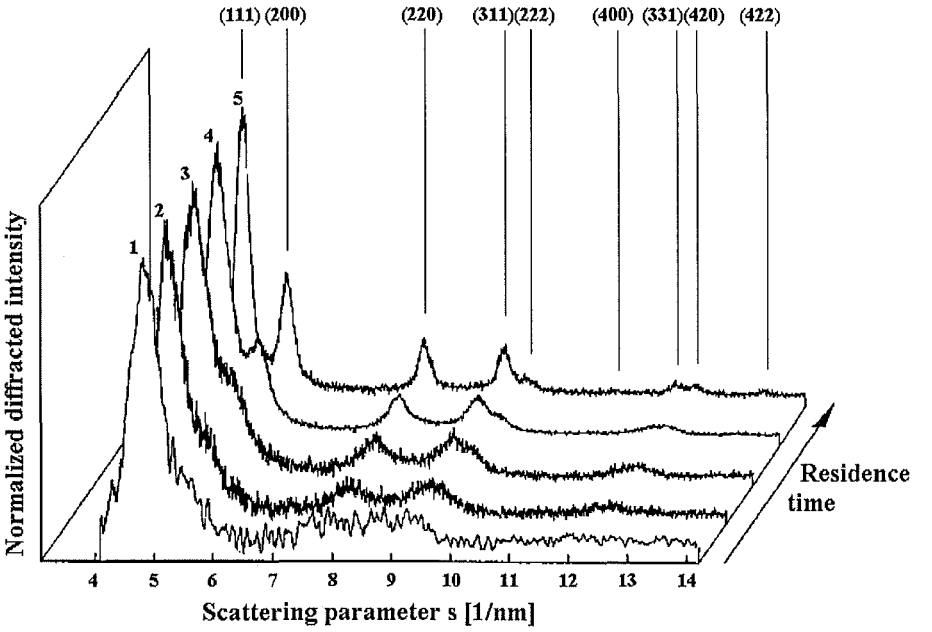

Figure 6.40: Electron diffraction patterns obtained by Reinhard [35] from Cu clusters. The patterns are arranged by residence time of the clusters within the source chamber, which, for Cu, was determined to be proportional to cluster size.

effect determined whether the clusters had icosahedral or FCC structure. The occurrence of the kinetic effect depended on the temperature of the clusters during growth [40–42, 50] (in this case it effectively meant a dependence on T_C). Low temperatures during growth caused the clusters to become trapped with an icosahedral structure, while higher temperatures during growth allowed the clusters to transform to FCC structure once the FCC structure became more favourable. The temperature had a lesser effect on the size of the clusters produced meaning the structure of the clusters could be changed while the size remained roughly the same.

Diffraction patterns obtained by Reinhard *et al.* [35,39,50] from Cu clusters are shown in Fig. 6.40. The diffraction patterns in Fig. 6.40 are arranged in order of residence time in the source chamber, which, for Cu, was determined to be proportional to cluster size. To analyse the diffraction patterns a method of pattern fitting similar to the one described in chapter 5 was used. It was concluded the diffraction patterns showed that Cu clusters had a size dependent structural transition from icosahedral to FCC structure at ~2000 atoms. The first pattern, although noisy, appears to have a broad flat peak between s=7 & 10 nm^{-1} similar to the patterns in Fig. 6.20 and is also determined to be from icosahedral structures. Reinhard's pattern 4 is strikingly similar to pattern 11 in Fig. 6.21

and is determined to have a significant contribution from decahedral structures[4]. For the last pattern in the sequence the fit shows a large proportion of the clusters have FCC structure, however decahedra and very large icosahedra are also reported by the fitting process. Reinhard *et al.* interpret the presence of the decahedra and icosahedra as an indication that the FCC structures contain defects.

The experimental domain size[5]–structure relation determined from this sequence of diffraction patterns is similar to the size–structure relationship predicted by MD simulations of Cu clusters [66], indicating the clusters grew thermodynamically. The observation of thermodynamic growth is in contrast to the kinetic effects observed in Ag clusters. The ability to produce the thermodynamically stable structure for Cu is thought to be linked to the growth rate of the clusters. Reinhard *et al.* believe that as the size of Cu clusters is proportional to the residence time (which is inversely related to the P_G) in the source chamber the Cu clusters grew slowly compared to the Ag clusters that did not have this dependence.

Reinhard's studies of Cu and Ag provide two examples of how the source conditions affected the structure of the clusters produced using the same equipment as the present study on Pb clusters. For Ag the structure was controlled by T_C, which revealed that the cluster temperature during growth was important. For Cu the dependence on flow rate (P_G^{-1}) revealed that the growth rate was slow and thermodynamic growth was possible. In diffraction patterns from Pb clusters obtained in this study there is little dependence of the structure on either T_C or P_G suggesting a mechanism different to those observed in Ag and Cu determines the structure of Pb clusters. However, in section 6.7.2 it is postulated that cluster size and temperature are still important.

6.7.1.5 Previous Pb Cluster Diffraction Experiments

Returning now to diffraction patterns from Pb clusters, previous studies by Yokozeki [158] and Yokozeki and Stein [31] reported that the clusters had FCC structure with some evidence for an amorphous structure at smaller sizes. However, they did not fully consider MTPs. The source used by Yokozeki was an inert gas aggregation source similar to the one used in the present study, except that the source nozzle was much smaller, being 0.75 mm diameter. Values of T_C used by Yokozeki were between 930 and 1040°C, while values of P_G were between 0.55 and 0.83 Torr (Ar was used as the inert gas). Several of the diffraction patterns obtained by Yokozeki are shown in Fig. 6.41. Cluster size estimates, calculated

[4]The values quoted in ref. [35,39] are number weighted, volume weightings in ref. [50] give the decahedral contribution as 32%

[5]As expected TEM size measurements showed the actual cluster size was slightly larger than the size estimated from fitting.

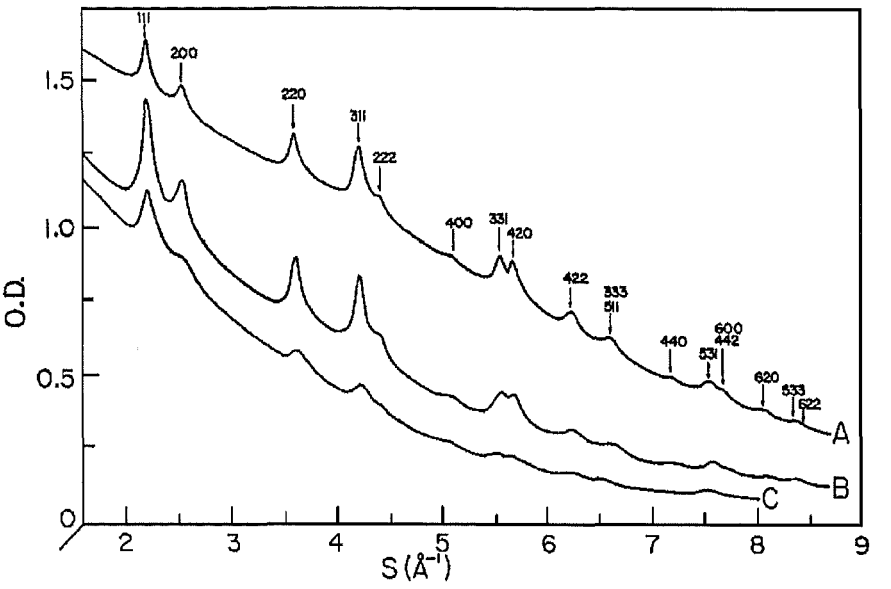

Figure 6.41: Electron diffraction patterns obtained from Pb clusters by Yokozeki and Stein [31]. The diffraction patterns are interpreted as showing the clusters had FCC structure. The typical size of the clusters produced by Yokozeki and Stein was larger than the typical size produced in this study (see text).

by Yokozeki using the Scherrer formula, are A : 82±10 Å, B : 60±5 Å and C : 40±10 Å. Pattern C appears similar to pattern 11 in Fig. 6.21 and B similar to the pattern showed in Fig. 6.34. Pattern C is from the lower end of the size range examined by Yokozeki while Pattern 11 is from the upper end of the size range typically examined in this study suggesting that the clusters observed by Yokozeki were generally larger than the clusters observed in this study. In the case of pattern B it would appear these clusters are not perfect FCC as the dip between (111) and (200) peaks does not reach the background level.

6.7.2 Discussion of Growth Sequences

This section discusses the growth of the Pb clusters and suggests why the composition of the inert gas strongly influences the structure of the clusters. Unfortunately, as the conditions within the source are not well known, this discussion is mostly speculative.

Two factors influenced by the inert gas are the diffusion and temperature of the metal vapour. An increase in the mass of the inert gas is expected to reduce the diffusion of the metal vapour causing clusters to grow in a more concentrated vapour [103, 104]. The cooling ability of the inert gas is expected to depend on the energy transferred during collisions between the inert gas and metal vapour atoms [103]. The energy transferred is maximum when the masses of both atoms are equal. Given that Ar and He atoms are

lighter than Pb atoms and that Ar atoms are heavier than He atoms it is expected that there is less diffusion and better cooling using Ar compared to using He. Both factors are expected to result in Ar producing larger clusters than He. Therefore, it could be simply argued that the larger clusters produced using Ar favour the MFS structure over the icosahedral structure. However, this does not explain the origin of the MFS, i.e. at what point during growth does the MFS form?

If the clusters are assumed to solidify with icosahedral structure a structural transition from icosahedral to MFS must occur during growth. The nature of structural transitions in clusters is generally not well understood, although several possibilities have been proposed. MD simulations by Valkealahti [66], discussed in section 2.5.2, showed magic number cuboctahedral (triangular facets) clusters could transform into icosahedra at all temperatures up to their melting temperature. This suggests that during growth there may be opportunities for structural transitions that have little or no activation barrier. In addition, HRTEM studies indicate clusters are able to enter a quasi–molten state in which rapid changes of structure can occur [43–46]. However, to enter these states stimulus from the electron beam is required. Alternatively, structural transitions could occur as a slow change in the dominant structure of the cluster during growth rather than by a sudden and complete change of the structure. A model for this type of structural transition, proposed by van de Waal [88], is discussed in section 2.7. In van de Waal's model faulted FCC structure grows on a MTP core.

In the case of Pb the initial assumption that the clusters are solid during growth may not be required. As discussed in section 6.2 the clusters are expected to grow to several nanometres in size before solidifying. This expectation suggests that the observed structure may be characteristic of the structure formed during solidification. Hence, the clusters grown in He may condense at a size where shaved icosahedral structures are preferred, while the clusters grown in Ar may condense at larger sizes where the MFS is preferred. Such an origin for the difference in structure appears to contradict the above expectation that Ar is more effective at cooling the vapour than He, however due to the reduced diffusion it could also be expected that once nucleation begins the clusters grow faster in Ar, resulting in less cooling of the clusters during growth and a higher solidification size.

Several results would appear to contradict the simple assumption of a purely size related structural transition. In section 6.6.2.3 small, medium and large sized decahedra and icosahedra were reported by fitting indicating no preferred size range for decahedra or icosahedra. In this case P_G was very high and a large difference was observed between the TEM and fit size estimates. It is suggested that increased coalescence, due to the

high P_G, has produced clusters with complex twinning arrangements that are best fit by the mixture of decahedra and icosahedra.

In section 6.6.2.4 the fit results for the patterns in Fig. 6.16 show that the medium and large domains are a mixture of decahedra and icosahedra. Compared to the clusters in Figs. 6.20 & 6.21, the clusters in Fig. 6.16 are expected to be cooler during growth due to the lower T_C. The cooler growth may result in more kinetic effects. In support of this suggestion note that the fit results (Fig. 6.17) for pattern 7 of Fig. 6.16, which has the highest T_C of the patterns in Fig. 6.16, indicate only a small contribution from large icosahedral domains and essentially no medium sized decahedral domains.

In future experiments it may be possible to be more definitive about conditions within the source chamber, a transition from crystalline to molten structure as T_C was increased has been observed by Wurl *et al.* [159] in Bi clusters.[6] Further studies of this transition may yield a series of data points allowing the effect of source parameters on growth conditions to be better understood.

6.8 Summary

Several series of diffraction patterns from Pb clusters have been presented in this chapter. Each series examined the effect of changing one source parameter, finding that T_C and P_G have only a weak effect on the size and structure of clusters produced. However, the type of inert was found to be more influential and diffraction patterns produced using He were distinctly different from those produced using Ar. Varying the composition of the inert gas from mostly He to mostly Ar produced a smooth transition in the diffraction patterns observed.

From analysis of the diffraction patterns it was found that clusters produced using He favoured icosahedral domains, however it was not possible to reproduce the experimental pattern (especially in the region $s \approx 0.67\,\text{Å}^{-1}$) completely using diffraction patterns from decahedral, icosahedral or FCC clusters. The inclusion of shaved icosahedra in the fits made an improvement but did not completely solve the problem. The diffraction patterns obtained using Ar were well reproduced by fitting and initially appeared to have a strong contribution from large decahedra. However, when shaved icosahedra were also included the contribution from large decahedra decreased and a strong contribution from large shaved icosahedra was reported instead. In addition, the main features of the patterns obtained using Ar could also be reproduced using parallel twinned FCC models. Although none of the interpretations could be dismissed they suggested that there was a

[6] Wurl *et al.* are using the same equipment as this study.

developing preference for FCC structure. The fit to diffraction patterns from larger clusters (Fig. 6.34) still indicated a strong contribution from decahedral domains, however there was significant contributions from perfect and twinned FCC domains.

From MD simulations of Pb clusters the shaved icosahedral structure is predicted to be the lowest energy structure [70]. For diffraction patterns obtained using mostly He the dominance of the shaved icosahedra in fit results is clear and suggests that structures at least similar to the shaved icosahedra are being formed. For diffraction patterns obtained using mostly Ar the shaved icosahedra are still dominant in the fit results, however alternative interpretations of these diffraction patterns exist. It is also noted that, although the fit results (for patterns obtained with mostly Ar) are dominated by shaved icosahedra, the diffraction patterns from shaved icosahedra by themselves do not reproduce the main features of the experimental patterns. This is in contrast to the other interpretations, decahedra and faulted FCC, that do have diffraction patterns very similar to the experimental patterns.

Chapter 7

Zinc Clusters

This chapter discusses the experiments on Zn clusters. The chapter begins by reviewing several theoretical studies on the structure of Zn clusters. These studies show that very small Zn clusters are expected to have non–bulk structures. The following sections review the production of Zn clusters in previous experiments. The remainder of the chapter discusses the attempts to observe diffraction patterns from Zn clusters and suggests reasons for the difficulties encountered using Zn.

7.1 Predictions of Zn Cluster Structure

Several authors have examined the structure of small Zn clusters.

Park *et al.* [160] calculate the energy of many structures for Zn clusters with up to six atoms using the *ab initio* density–functional method. The Zn dimer is predicted to be stable and have a binding energy of 0.153 eV, compared to a dissociation energy of 0.30 eV [161] from experimental measurement, indicating that the Zn dimer is weakly bound. For three atom clusters the equilateral triangle is the most stable, although a linear geometry (three atoms in a line) is metastable. For four, five and six atom clusters several planar structures are metastable, however the most stable structures are the tetrahedra, hexahedra and octahedra respectively.

Ramprasad and Hoagland [162] compare the energy of Zn clusters with different structures using MD simulations. For clusters with four to six atoms the most stable structures found are the same as those predicted by Park *et al.* While for seven atoms the pentagonal bipyramid is predicted to be the most stable. For cluster sizes from eight to 57 atoms (at 0 K) a comparison between FCC, HCP and icosahedral structures shows that icosahedra are the most stable at all sizes except 15 atoms, which is predicted to be HCP. Ramprasad and Hoagland also consider the nucleation and growth of each structure at high temperature (1450 to 1650 K). The seven atom HCP cluster is found to have a formation energy twice that of the icosahedral[1] cluster suggesting that the icosahedral structure will grow more readily than the HCP structure. For cluster sizes up to 13 atoms the most

[1]Ramprasad and Hoagland describe the 7 atom pentagonal bipyramid as icosahedral.

stable structures at high temperature are the same as at 0 K. Above 13 atoms the HCP structure is more stable except for 16 atoms, which remains icosahedral. However, the choice of temperature range considered by Ramprasad and Hoagland is puzzling, as the bulk melting temperature is only 693 K, it would be expected that the clusters are liquid in the range considered.

A more extensive search for the most stable structure for Zn clusters has recently been performed by Michaelian *et al.* [111]. For clusters with 13, 38, 55, 75 or 147 atoms disordered structures are predicted to be the most stable at 0 K. In fact the normally magic 13, 55 and 147 atom icosahedra and the 75 atom Marks' decahedra are predicted as being unstable. The magic 38 atom FCC octahedron is predicted to be metastable, but there are at least 1537 disordered structures that have lower energy. The lowest energy 38 atom cluster found, which resembles a decahedron with an off centre axis of symmetry, is shown in Fig. 4.20, also shown are the corresponding diffraction pattern and the diffraction patterns for low energy (though not lowest energy) 55 and 75 atom clusters. At temperatures up to 300 K the disordered structures are still predicted to be the most stable except for clusters with 38 atoms. The FCC octahedron is expected to become the most stable structure for 38 atom clusters at temperatures slightly over 165 K because of entropy effects.

7.2 Production of Zn Clusters

In this section previous experiments where Zn clusters have been produced are reviewed, focussing on details relevant to the production of the clusters. The three parts to the section concentrate on different methods of producing clusters. Where necessary a short description of each method has been given, though further details can be found in reviews by de Heer [163] and Haberland [164]. Also note that the diffraction experiment attempted in this thesis requires not only that clusters are produced (which was possible for certain conditions), but that the flux of clusters is very high.

7.2.1 Gas Aggregation

The inert gas aggregation (IGA) technique has been used to produce Zn clusters for a variety of experiments. Table 7.1 summarizes the source conditions and the size range of clusters produced. The conditions listed in Table 7.1 are similar to the conditions used in the Zn experiments performed in the present study (see section 7.3).

Although Xu *et al.* [169] were concentrating on the optical properties of the Zn clusters, they also obtained an X–ray diffraction pattern of the clusters that is reproduced in

Table 7.1: Source conditions and cluster sizes produced in IGA sources. T_C is the evaporation (crucible) temperature and P_G is the inert gas pressure.

Author	Source Conditions			Cluster Size
	T_C(°C)	P_G(Torr)	Gas Type	(nm)
Pasche [165, 166]	450–550	1	Xe	1–5
Xu *et al.* [167–169]	527	0.46–9.9	Ar	20–400
Hecht *et al.* [170, 171]	500	6	Ar	20–100
Hogg and Silbernagel [172]	300–480	$\sim 10^{-4}$	Ar	5–100
Eversole and Broida [52]	412	1–35	N_2	up to 500
Daub *et al.* [173]	425–475	1–30	Ar	~40

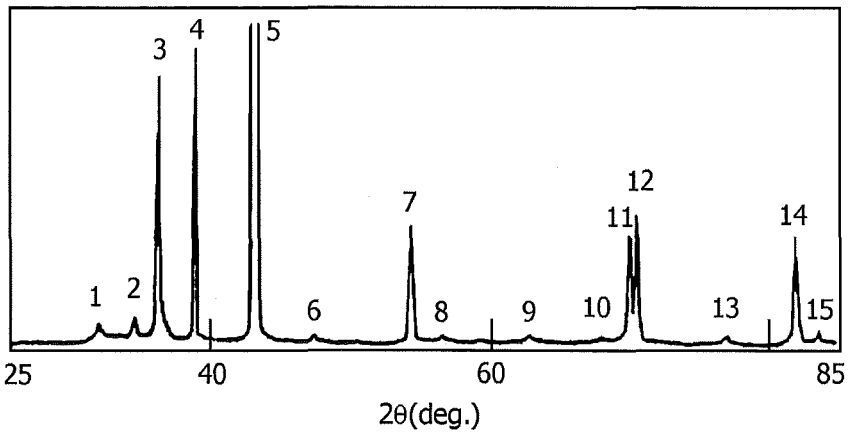

Figure 7.1: X–ray diffraction pattern from large Zn clusters. The peaks 3–5,7 and 11–15 are from the Zn HCP core of the clusters. The peaks 1,2,6 and 8–10 are from a thin oxide layer. After Xu *et al.* [169]

Fig. 7.1. The diffraction pattern shows the Zn clusters had the bulk HCP structure and the sharp diffraction peaks indicate a large cluster size.

In most IGA sources attempts are made to limit the heating of the inert gas, however in several experiments with Zn the inert gas has been heated to a temperature near or above the temperature of the Zn. In these sources the mixture of inert gas and Zn cools downstream from the crucible.

Eversole and Broida [52] produced Zn clusters with sizes up to 500 nm (although agglomerates of clusters up to 5000 nm were also observed) using hot inert gas. The inert gas was used to conduct heat to the crucible and hence had a temperature higher than the crucible temperature, which was usually 412±5°C. N_2 was used in most experiments at pressures between 1–35 Torr. Ar and H_2 were also used but no dramatic differences in particle production were observed. Clusters were collected and observed in a TEM. Observation showed that clusters larger than ~5 nm had clear geometric shapes, while

the shape of smaller clusters was not resolved. The typical cluster shapes observed were hexagonal plates, rods and hourglasses (Models and diffraction patterns for each shape are shown in section 4.5.3). From TEM images shown by Eversole and Broida a crude estimate of the cluster flux can be made: assuming the cluster density shown in the images is representative of the flux across the last nozzle of their equipment and a one minute exposure time (typical exposure times are given as 1–4 minutes) gives a flux of $\sim 10^8$-10^9 clusters per second. In comparison an upper limit for the cluster flux of 5×10^{12} clusters per second was calculated by Eversole and Broida assuming complete conversion of vapour into clusters.

Daub *et al.* [173] also produced clusters using hot inert gas. Bulk Zn was placed in a ceramic boat inside a stainless steel tube. A furnace placed around a section of the tube caused the Zn and a flow of Ar gas to be radiantly heated. The boat was positioned near the start of the furnace and typically had a temperatures between 425 and 475°C. The mixture of inert gas and metal vapour was heated further as it passed through furnace. For boat temperatures around 475°C a black powder was obtained, higher boat temperatures produced a gray or metallic solid. For an Ar pressure of 20 mbar, size estimates of the clusters in the black powder from neutron scattering and X–ray diffraction were 42 and 46 nm respectively. The X–ray diffraction patterns of the clusters were assigned to crystalline Zn. Daub *et al.* claim that the powder can be made at rates of greater than 0.1 g/h indicating a cluster production rate of $\sim 10^{12}$ clusters per second (assuming a cluster size of 44 nm).

7.2.2 Nozzle Expansion

In this type of source metal vapour is expanded into a high vacuum through a nozzle. The vapour cools during the expansion and condenses into clusters.

Experiments using this type of source have shown that the design of the nozzle and the crucible temperature (vapour pressure) are important in determining the size of the clusters produced. Fig. 7.2 shows the source used by Urban *et al.* [174,175] to produce Zn clusters. Urban *et al.* were unable to produce large clusters using a crucible temperature of 520° (2 Torr) and the cylindrical nozzle. However, by switching to the converging–diverging nozzle and increasing the crucible temperature to ~1200°C (thousands of Torr) it was possible to produce large clusters. For crucible temperatures of 1120, 1180 and 1260°C the average cluster sizes were 100, 1000 and 2200 atoms respectively.

Using a similar cluster source to Urban *et al.*, Gspann [176] also produced large Zn clusters. Gspann used a time of flight mass spectrometer to measure an average cluster size of 4570 atoms per elementary charge.

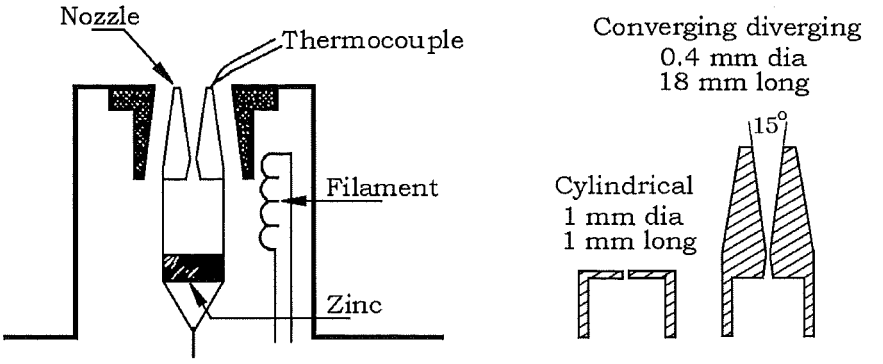

Figure 7.2: (Left) A nozzle expansion cluster source used to produce Zn clusters. (right) The different types of nozzle used in the source. After Urban *et al.* [174,175]

Pruett *et al.* [177] have also used a similar source to Urban *et al.*, however Pruett *et al.*'s source used the cylindrical nozzle and for vapour pressures up to 40 Torr only the monomer was observed. Monomers and dimers were observed using vapour pressures from 40 to 200 Torr. For comparison, it was possible to produce Ag clusters with up to nine atoms using the same source.

7.2.3 Sputtering

The sputtering technique bombards a source metal with high energy inert gas ions that cause the emission of atoms from the surface of the metal. The metal vapour is not condensed in an inert gas and although a considerable amount of metal can be vaporized cluster production is inefficient. The clusters produced tend to be small and ionized.

Yadav *et al.* [178] produced Zn clusters with up to four atoms by bombarding bulk Zn with 3.8 keV Cs^+ ions. The cluster size distribution was measured using mass spectrometry, finding that the dimer was the most numerous.

Larger clusters, containing up to 75 atoms were produced by Katakuse *et al.* [179] using 10 keV Xe^+ ions. Again mass spectrometry was used to measure the cluster size distribution for positively and negatively charged clusters. In both spectra peaks were observed indicating the presence of magic cluster sizes. For positively charged clusters the observed magic cluster sizes were $n = 10, 18, 20, 28, 30, 32, 35, 41, 46, 54, 57, 60$ and 69 and $n = 27, 29, 31, 34, 40, 46, 54, 56, 60$ and 68 for the negatively charged clusters. Katakuse *et al.* compared these sizes with expected magic sizes for electron shell closing in Zn clusters and obtained a good agreement.

7.3 Zn Experiments

The experiments using Zn are now discussed. Section 7.3.1 describes the attempts to produce enough Zn clusters to observe diffraction patterns. Section 7.3.2 discusses TEM images of Zn clusters deposited on TEM grids and several SEM images of large Zn particles collected within the source chamber.

7.3.1 Attempts to Obtain Diffraction Patterns from Zn Clusters

Zn was chosen because of the low temperature (480°C) required to produce a vapour pressure of 1 mbar. In experiments by Hall and Reinhard the filament had been made out of tungsten, however because of the low temperature it appeared that a filament made out of Nichrome (Ni–Cr alloy) would be suitable. This was helpful because Nichrome is more malleable than tungsten making construction of the filament easier.

Apart from the filament, the design of the first crucible arrangement used in Zn experiments was the same as that used in Pb experiments (see section 3.2). Zn (99.995+%) pellets were used as the source material and initially He was used as the inert gas.

For all the experiments discussed below the typical values of P_G and T_C explored during experiments ranged between 0.1 and 10 mbar for P_G and between 400 and 550°C for T_C.

An examination of the crucible after each experiment invariably found that the Zn pellets had become covered in a thick oxide layer. The layer presumably formed below the melting temperature as the individual pellets had not melted together. To reduce the amount of oxide that was on the pellets before an experiment the pellets were etched in 1 mol/l HCl and then repeatedly rinsed in distilled water to remove any residual acid. The pellets were then immediately loaded into the crucible and the system evacuated to limit the reoxidation of the Zn. The etching process reduced the oxide layer that formed during an experiment, but did not completely solve the problem.

Despite the formation of an oxide layer there still appeared to be a significant amount of Zn evaporated: a layer of Zn would form on all surfaces inside the source chamber during an experiment. To promote nucleation of the Zn vapour experiments were also performed using Ar as the inert gas, however no diffraction patterns were observed.

Further examination of the crucible arrangement after each experiment showed that there was some evaporation coming from the Nichrome filament, leaving a black film on surfaces directly exposed to the filament (i.e. the inside of the insulator and the outside of the crucible). Several filaments were then made out of molybdenum, which is also more malleable than tungsten, but these filaments also produced a black film. Tungsten was

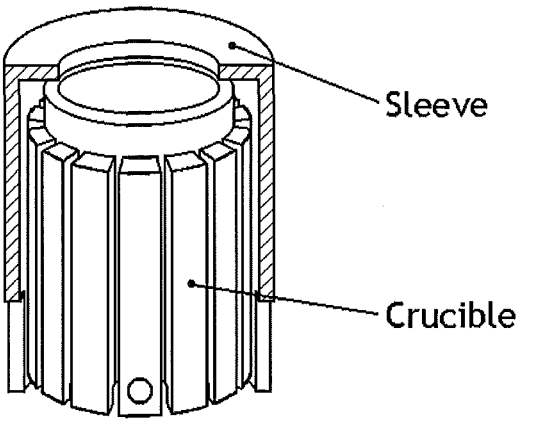

Figure 7.3: Design of the two piece boron nitride crucible. The filament is wound around the groves and across the base.

then used to make filaments and the black film was significantly reduced: only a faint black line would be produced where the filament was in contact with the crucible. Due to the cover sheet on the crucible arrangement, which has a tight fit around the crucible, this problem was effectively isolated to the gap between crucible and insulator and solving it did not make any difference to the Zn oxidation problem or allow diffraction patterns to be observed.

After a subsequent experiment it was measured that ~2/3 of the Zn evaporated had condensed onto the heat shielding. To prevent this condensation and create as dense vapour as possible a new crucible arrangement without heat shields was designed. The new design is shown in Fig. 7.3 and consists of an inner boron nitride (BN) crucible and an outer BN sleeve. A tungsten filament is wound around the groves and across the base of the crucible. The use of a BN crucible also greatly reduced the oxidation problem and the Zn pellets would melt together without forming an oxide layer.

Using the BN crucible the average Zn evaporation rate during experiments was measured to be ~1 g/hr, in comparison the evaporation rate of during Pb experiments was ~0.5 g/h. Although these rates are similar, the mass of Zn atoms is only ~32% that of a Pb atom meaning the evaporation rate of Zn atoms was ~6 times the evaporation rate of Pb atoms.

After several experiments trying different source conditions it was found that small deposition rates (~1 Å/s) could occasionally be attained with high (~10 mbar) Ar pressures and crucible temperatures above ~550°C. The high evaporation rate, but low deposition rate suggests the Zn vapour was not nucleating into clusters efficiently. The deposition would only last for a few minutes before the source nozzle (nozzle 1 in Fig. 3.2) would

block. To increase the deposition rate several experiments were performed with N_2 as the inert gas instead of Ar, but no increase in deposition was observed. During these experiments a 3 mm first nozzle had been used and the high Ar pressure in the source chamber meant the pressure in the 2nd stage chamber (see Fig. 3.2) was close to the operating limit of the turbo pump. To allow higher pressures in the source chamber the diameter of the first nozzle was reduced to 2 mm, however the first nozzle would become blocked before deposition was observed. It was then found that diffraction patterns were observed from Bi clusters only when significantly higher deposition rates ($\sim$20+ Å/s) were measured [51,159]. The inability to produce sustained high deposition rates was the main reason for discontinuing experiments with Zn.

7.3.2 TEM and SEM images

TEM grids were exposed for several minutes during one experiment (source conditions: Ar, P_G=1–10 mbar and T_C=400–480°C) in which deposition was not observed. Inspection of the grids in the TEM showed that only a few clusters had been collected. The diameter of clusters was $\sim$5 nm and the number of clusters observed suggested a flux of $\sim 10^6$ clusters per second (about 6 orders of magnitude less than in Pb experiments).

Unfortunately, during the experiments where deposition was observed the TEM grid holder had been removed for modification, so no TEM examination of the clusters produced was possible.

After one experiment where deposition was observed (i.e. high P_G and T_C values were used) particles deposited in the source chamber were collected and viewed in a SEM. Fig. 7.4 is a low magnification image showing a range of particles collected. Due to the size ($\sim 1\,\mu$m+) the particles are expected to have bulk Zn structure. Many of the particles observed had a rough surface as in Fig. 7.5. Also commonly observed were particles similar to the one in Fig. 7.6. These particles appear to be made from layers of semi–hexagonal plates and overall have an approximately spherical shape.

7.4 Discussion

In the initial experiments the oxide layer that formed on the Zn pellets was thought to be main reason for the inability to produce clusters. The oxide layer was presumably restricting the evaporation of the Zn thus lowering the vapour concentration and inhibiting the production of clusters. Once the oxidation problem was solved the Zn vapour still did not readily form clusters. This was despite the fact that a considerable amount of vapour was produced (in comparison to Pb experiments). Therefore the problem must have been

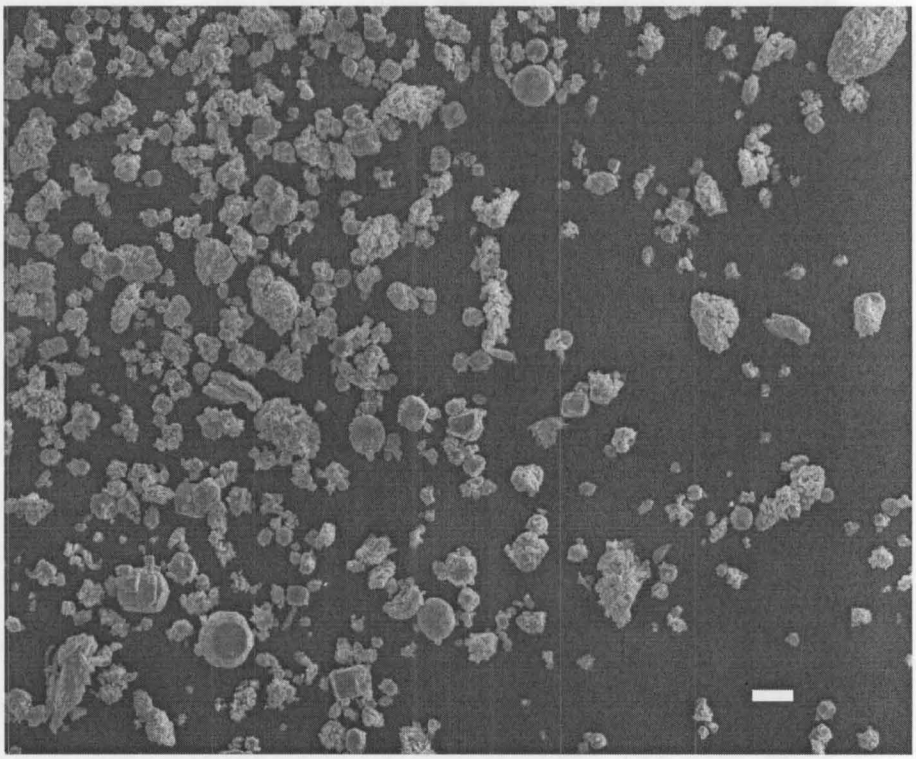

Figure 7.4: Zn particles collected from the source chamber after an experiment in which deposition was observed (i.e. high P_G and T_C were used). Scale bar is $10\,\mu m$.

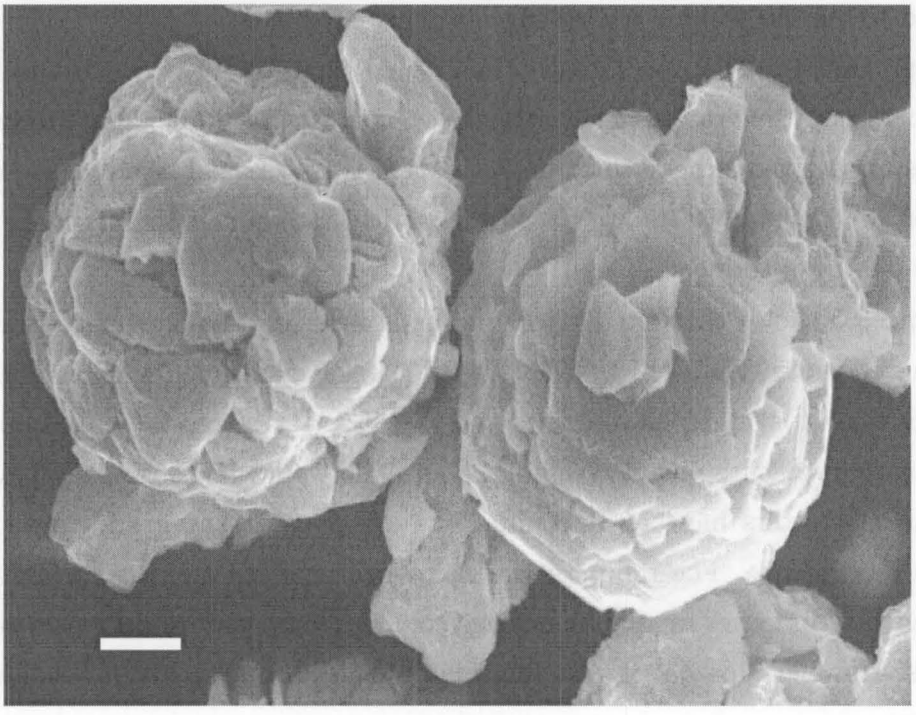

Figure 7.5: Example of the common 'rough' Zn particle observed. Scale bar is $1\,\mu m$.

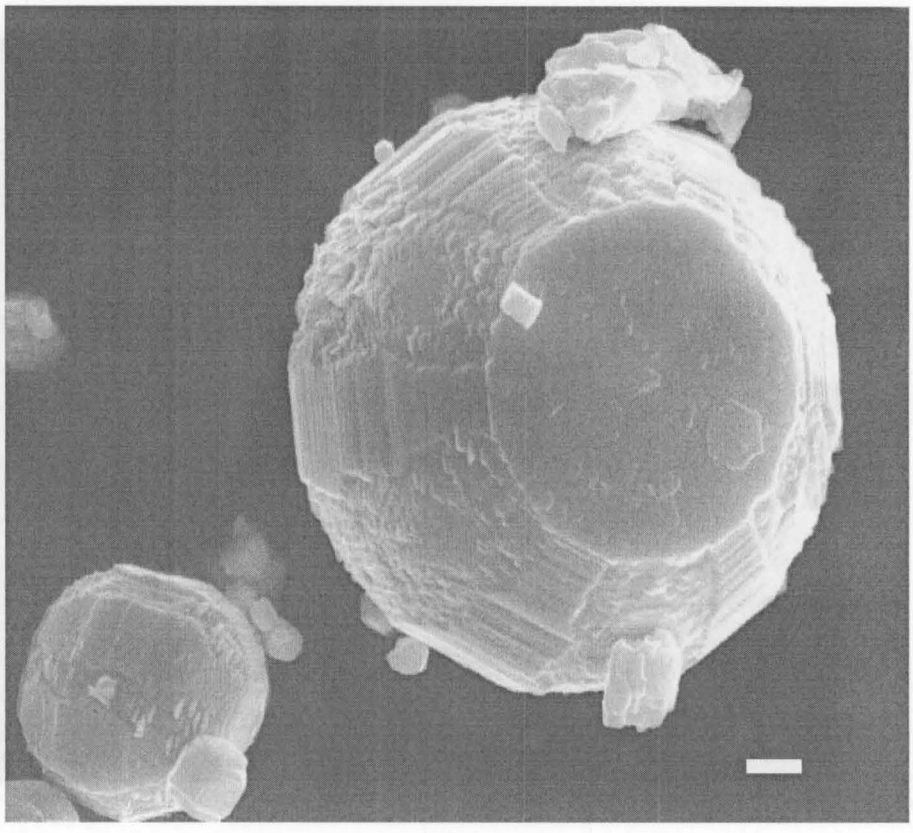

Figure 7.6: Example of the semi–hexagonal Zn particle observed. Scale bar is 1 μm.

related to the Zn vapour nucleating into clusters.

Fig. 3.8(B) in chapter 3 shows the critical sizes for Ag, Cu, Pb and Zn as a function of supersaturation ratio. The critical size for Zn is significantly larger than the other metals for a given supersaturation ratio. The large critical size means fewer of the small randomly formed clusters are above the critical radius and therefore the number of large stable clusters produced is less.

Eqn. 3.5 shows that the critical radius is inversely dependent on the value of $T \ln S$. Compared to Ag, Cu and Pb, the value of T in Zn experiments is low, meaning producing a high value for $T \ln S$ is difficult, and in hindsight suggests that choosing Zn because the low temperature meant designing a crucible would be easier may have actually made producing clusters harder. It could also be expected that producing a high S with Zn would be difficult. The temperature difference between the vapour and inert gas is less for Zn than the other metals, hence the cooling (temperature decrease) of the vapour will be less. However, for Zn, the cooling required to produce a given S is less, offsetting this problem.

In the case of Zn one solution maybe to use high T_C to produce a very high vapour pressure. If the vapour can still be cooled efficiently this should result in a higher S and

promote the nucleation of clusters. Such practices were limited in the source used in the present study by the blocking of the source nozzle. Raising T_C above ~550°C would cause the source nozzle to block rapidly.

It could be argued that the values calculated from homogeneous nucleation are inaccurate given that bulk properties are being applied to clusters. In a more atomistic view of cluster growth, nucleation begins with the formation of a dimer (by a three body stabilizing collision). The stability of the dimer influences whether it grows to become a cluster or dissociates. In the case of Zn and other group II metals the binding energy of the dimer is so weak (van de Waal bonding), and the internuclear distance so large, that these dimers are often considered to be analogous to the weakly bound rare gas dimers [180]. A weak dimer that readily dissociates rather than growing into a larger cluster would clearly be a problem.

That other groups managed to produce apparently large quantities of Zn clusters using hot inert gas is surprising. The reason these experiments were able to produce clusters is possibly related to the physical design of the experiment. In Daub *et al.*'s [173] experiment the 'source chamber' was a tube 22 mm in diameter, while in Eversole and Broida's [52] experiment the 'source chamber' was a tube ~30 mm in diameter. In comparison, the source chamber described in section 3.2 has a diameter of 87 mm. The narrow diameter of Daub *et al.*'s and Eversole and Broida's source chambers suggests the vapour was more confined and, although cooling occurs downstream from the crucible, the vapour was still concentrated when nucleation began.

7.5 Summary

Attempts to observe diffraction patterns from Zn clusters were unsuccessful. Oxidation of the Zn (to be evaporated) in the initial experiments was thought to mean the evaporation rate was too low and thus insufficient vapour was present to produce enough clusters to be detected. However, the oxidation of the Zn problem was solved and evaporation rates ~6× higher than those in Pb experiments were attained. Even in these conditions only a weak cluster beam could be created. The problem appears to be caused by the Zn vapour having difficulty nucleating into clusters. Homogeneous nucleation theory shows that Zn has a significantly larger critical cluster size than Cu, Ag or Pb given similar conditions. The larger critical size will result in a lower nucleation rate for Zn clusters.

Chapter 8

Conclusion and Outlook

This thesis used high energy electron diffraction to study the structure of metal clusters entrained in a molecular beam. Attempts were made to study two different metals: Zn and Pb, however only in the case of Pb were diffraction patterns observed. In the case of Zn the cluster flux produced was insufficient to obtain diffraction patterns.

The analysis of the diffraction patterns from Pb clusters was based on using a combination of diffraction patterns calculated from model clusters to produce a best fit to the experimental pattern. In general, two sets of models were used: the first set (geometric models) contained decahedra, icosahedra and cuboctahedra created using bulk and symmetry properties. The second set (relaxed models) contained MD relaxed versions of the models in the first set. For the experimental patterns analysed in this study the results from fits using either set of models were generally in agreement. The access to results from further MD simulations of Pb clusters provided selections of shaved and anti-Mackay icosahedra that were also used in the analysis of several diffraction patterns.

In the case of Pb the inert gas pressure, P_G, and crucible temperature, T_C, which are typically reported to strongly influence cluster size, were observed to have only a weak effect. A much greater effect was observed as the composition of the inert gas was varied. Clusters produced using He were dominated by icosahedral structure. The diffraction patterns from the icosahedral structures were better fit using shaved icosahedra than the normal (Mackay) structure. The composition of the inert gas was varied by changing the ratio of Ar to He entering the source chamber. As the concentration of Ar was increased the size of the clusters produced also increased and a structural transition was observed. The observation of a structural transition while increasing the cluster size implies the presence of a structural size effect. The estimated transition size is $\sim$5.5 nm, in comparison the MD predicted size for the transition from shaved icosahedral to FCC structure is $\sim$6.5 nm [70].

The diffraction patterns obtained from clusters produced using Ar were very similar to diffraction patterns from decahedra and fits using the geometric or relaxed models indicated a significant contribution from large decahedral domains. However, other structures or combinations of structures produce diffraction patterns that are similar to those

from decahedra. Fits using the relaxed models as well as shaved and anti-Mackay icosahedra showed that the experimental pattern could be fitted using a mixture of shaved icosahedra, cuboctahedra, anti-Mackay icosahedra and decahedra. A fit using icosahedra, cuboctahedra and a selection of twinned FCC clusters showed that the experimental pattern could also be fitted using a mixture of icosahedra and twinned FCC clusters.

In cases where analysis of the diffraction pattern is unable to uniquely identify the structure of the clusters HRTEM observations, where possible, may provide a guide to which structures are actually present. A sample of clusters produced using Ar was sent to Daniel Ugarte at the Laboratório Nacional de Luz Síncrotron in Brazil for HRTEM observation, unfortunately the clusters observed were amorphous indicating that oxidation had occurred.

Further MD simulations may also help to identify the structure of clusters produced using Ar. In the source it is expected that the clusters will grow to several nanometres in size before solidifying. From MD simulations [70] it is expected that liquid drops with less than ~5000 atoms (~6.5 nm) will solidify as shaved icosahedra (the energetically favoured structure); it would be interesting to know the result of further growth for this structure. Is the shaved icosahedral structure preserved? If so is a structural transition observed at ~5000 atoms? Or does the surface reconstruction of the shaved icosahedra provide growth sites that have similar properties to the preferred nucleation sites in van de Waal's model [88] resulting in a faulted structure growing on the shaved icosahedral core?

One problem for detailed MD simulations and a better understanding of the growth process is the lack of knowledge regarding the conditions within the source. For example, it is unknown at what size during growth the Pb clusters solidify and how that size is affected by changes in the source parameters (i.e. T_C, P_G and composition of the inert gas). Although not specific to Pb, a transition from crystalline to liquid structure as T_C is increased has been observed in Bi clusters produced using the same equipment as the present study [51, 159]. Further study of this transition may provide a better understanding of the effect of source parameters on the growth process.

Further understanding of the effect of the source parameters may be facilitated by a time of flight (TOF) mass spectrometer that is being designed for use in conjunction with the diffraction experiment. As the device is still in development it is unclear whether it will be a replacement for or complementary to the existing TEM sampling. Clearly, the mass spectrometer should have distinct advantages over the TEM method, a mass spectrometer would provide real-time measurement of the cluster size distribution allowing the effect of source parameters on the cluster size to be mapped in detail.

Appendix A

Electron Diffraction From Atomic Cluster Beams (book chapter)

B. D. Hall, M. Hyslop, A. Wurl and S. A. Brown,
in *Fundamentals of Gas–Phase Nanotechnology*,
Editors: L. Kish, C. G. Granqvist, W. Marlow and R. W. Siegel,
Kluwers Academic Publishing, 2002.

Chapter 1

ELECTRON DIFFRACTION FROM ATOMIC CLUSTER BEAMS

B. D. Hall
Measurement Standards Laboratory of New Zealand,
Industrial Research Ltd.,
Lower Hutt, New Zealand.

M. Hyslop, A. Wurl, and S. A. Brown*
Nanostructure Engineering Science and Technology Group
and Department of Physics and Astronomy,
University of Canterbury,
Private Bag 4800, Christchurch, New Zealand.
**Corresponding author*

Abstract Electron diffraction is a direct method which can be used to probe *in-situ* the structure of unsupported nanoparticles in molecular beams. The technique is important because it permits a determination of structure, free of the perturbing effects of a substrate, matrix or chemical contamination.

This chapter reviews diffraction experiments with particular emphasis on metal clusters and including some of the work done on rare-gases. These experiments are linked by the observation of multiply twinned (five-fold symmetric) structures for small clusters of materials that have face-centered-cubic bulk structure. As well as describing the historical development of the measurements and the apparatus used, the chapter discusses some of the most recent experimental data for bismuth and lead clusters. Some emphasis is given to the interpretation of diffraction measurements, which is complicated by the fact that nanoparticles cannot usually be described in terms of an underlying crystal lattice.

1. INTRODUCTION

Nanoparticles with sizes ranging from a few atoms through to tens of thousands of atoms can be seen as spanning the critical size range where the properties of single atoms evolve into the very different properties of macroscopic materials. Virtually all physical and chemical properties of nanoparticles are strongly size dependent, and it is believed that the often novel characteristics that are observed and predicted make nanoparticles good candidates for applications ranging from catalysis to single electron transistors to quantum dot lasers.

In the same way that crystal structure determines electronic band structure and, hence, the other properties of bulk materials, the structure of a nanoparticle can be seen as underpinning all its other properties. The development of a detailed understanding of the factors determining nanoparticle structure is, therefore, an important goal.

Experiments have revealed a remarkable variety of structural properties, but perhaps the most striking is the occurrence of stable and symmetric non-crystalline structures characterised by five-fold axes of symmetry (which are forbidden in bulk crystals). These 'Multiply-Twinned Particles' (MTPs) occur in many face-centered-cubic (FCC) materials, both metals and rare-gases, and are actually preferred energetically to the bulk FCC structure at sufficiently small sizes. Curiously, MTPs much bigger than their thermodynamic critical-size are regularly observed. This underlines an important feature of nanoparticle growth: that the observed structure can be influenced by *both* thermodynamic *and* kinetic factors. It also suggests that control can be exerted over nanoparticle structure: an exciting prospect for future nano-scale engineering.

One of the key factors determining the structure of a nanoparticle is the high proportion of surface atoms. In a 40 Å lead particle, for instance, roughly 40% of atoms are at the surface. These atoms experience a quite different environment from those inside, and competition between surface and volume energies determines the intrinsic structure. However, the balance between these energies is delicate and any interaction between a nanoparticle and its surroundings may significantly influence its behaviour.

Isolated in high vacuum, nanoparticles flowing in a molecular beam are in an almost ideal environment for studying their intrinsic physical properties. However, they are not in an environment which allows application of some of the standard structure determination techniques: particles flowing in a beam cannot be viewed individually (for example, by high-resolution transmission electron microscopy (HRTEM)); further-

more, the volume density of the particle beam is low, precluding the use of x-ray diffraction techniques. Electrons have a much higher scattering crossection than x-rays, and so the best technique available is high-energy electron diffraction.

This chapter presents an overview of electron diffraction from atomic cluster beams, with particular emphasis on metal clusters and including some of the work done on rare-gases, which exhibit structural properties that closely resemble those of FCC metal clusters. It traces developments in both types of cluster studies, from the earliest experiments in the 1970's to the present day. Throughout the chapter we use the word 'cluster' to indicate a nanoparticle in a molecular beam.

The chapter begins with an introduction to electron diffraction and the calculation of diffraction patterns. Following this, the chapter traces the development of the electron diffraction technique. The first measurements, on rare gases, are discussed, followed by the development of techniques suitable for metal clusters. After reviewing the results of experiments on metals as diverse as bismuth and copper, the chapter concludes with a section on recent experimental developments. Throughout the discussion, emphasis is given to the difficulties inherent in the interpretation of experimental diffraction patterns.

2. ELECTRON DIFFRACTION FROM ATOMIC CLUSTERS

The diffraction experiments of interest have a simple crossed-beam geometry: a high-energy electron beam impinges on the molecular beam of clusters at right-angles, and a diffraction pattern is observed below the beam crossing (see Section 5. for more details). Clusters have no preferred orientation in the beam so the diffraction pattern produced is a radially symmetric Debye-Scherrer 'powder' pattern.

2.1 KINEMATIC DIFFRACTION

The Debye-Scherrer pattern of a cluster can be calculated using the Debye equation [1]. This describes the radial distribution of intensity and assumes that kinematic scattering conditions apply. For clusters containing only one type of atom, the intensity scattered per unit solid angle is given by

$$I_N(s) = I_0 N f^2(s) \left[1 + \frac{D(s)}{N} \sum_{n \neq m} \frac{\sin(2\pi s r_{mn})}{2\pi s r_{mn}} \right] , \qquad (1.1)$$

where $s = 2\sin(\theta)/\lambda$, with θ equal to half the scattering angle and λ the radiation wavelength. I_0 is the incident intensity, N is the number of atoms in the cluster and r_{mn} is the distance between atom m and atom n. The atomic scattering factor, $f(s)$, represents the single-atom contribution to scattering, and is available in tabulated form [2]. The factor $D(s)$ expresses attenuation of the interference term in the Debye equation, due to thermal vibrations and static imperfections. It commonly takes the form: $D(s) = \exp[-Ms^2]$, with M constant.

Equation (1.1) represents the elastic scattering only. Inelastic scattering can be included by adding the term $4NS(s)/a^2s^4$, where $S(s)$ is the x-ray incoherent scattering factor (also tabulated in [2]), and a is the Bohr radius.

Kinematic scattering assumes that incident beam intensity is unchanged in propagating through the particle [3]. However, this may not be true over even a short path through a metal, due to the relatively large value for the atomic scattering crossections. For heavy atoms, such as gold, departures from the Debye equation can occur in nanoparticles containing only a few hundred atoms [4, 5]. Fortunately, the kinematical calculations tend to overestimate the differential crossection by a roughly constant factor, and so the effects of dynamical scattering may not seriously affect identification of structures [5].

2.2 TYPICAL PROFILES

Fig. 1.1 shows examples of the most commonly observed structures for elements that are FCC in the bulk form. Much of the the recent research into cluster structure, and much of this chapter, is centred on these structures. Calculated diffraction patterns for these structures are shown in Fig. 1.2.

Particles with FCC structures are conveniently modelled with the cuboctahedral form shown in the first column of Fig. 1.1. The models used contain between 147 and 1415 atoms, representing diameters from 16 Å to 39 Å. In this case, the models are actually small pieces of a FCC gold lattice, so diffraction peaks could be expected at the positions of bulk diffraction features. Diffraction patterns for the three small FCC particles (Fig. 1.2 (a)) show that, in fact, some small peak shifts can be discerned and there are clearly 'ripples' in the diffraction pattern that are not related to atomic structure. These are indications of the size-dependent nature of diffraction patterns for nanoparticles. For example, the ripples to the left of the (111) peak change quite noticeably with the cluster size. Also, the 'overlap' of distinct bulk peaks is severe for small

particle sizes. In fact, as equation (1.1) shows, it is more appropriate to think of a cluster's diffraction pattern as a continuous intensity profile.

The icosahedral structure (second column, Fig. 1.1) is non-crystalline and consists of twenty tetrahedral units joined at a common apex. Although individual tetrahedra may be thought of as distorted FCC tetrahedra, they are in fact exact sub-units of a rhombohedral lattice [6]. The translational symmetry is broken, however, because each tetrahedron is twinned with its three immediate neighbors. The basic hard-sphere packing structure for an icosahedron was first described in [7], however Ino introduced physical model structures for some metals that incorporated uniform elastic strain and these have been used here [8].

Fig. 1.2(b) shows three diffraction patterns for model icosahedral particles. The positions of bulk FCC peaks are shown again to emphasize the similarity in the appearance of the MTP and FCC diffraction patterns, although icosahedra are not FCC-based structures. The size effects visible in this panel are stronger than those in the FCC patterns. Apart from the strong peak at $s \sim 0.43$ Å^{-1}, the detail in the patterns changes appreciably at each size. Note, in particular, the small peak on the right flank of the main peak which moves to higher s as the size decreases.

Fig. 1.2(c) shows three diffraction patterns for model decahedral particles. The decahedra are also non-crystalline and can be assembled from five tetrahedra sharing a common edge (which becomes the five-fold axis of symmetry for the particle). However, the distortion of the base FCC structure in these tetrahedral units is less severe than in the icosahedral case, and there are fewer tetrahedral units. The diffraction pattern is similar to that for very small FCC particles, as can be seen in Fig. 1.2(a). This of course makes identification of decahedra by diffraction very difficult. The distorted tetrahedra of a perfect decahedron actually belong to an orthorhombic lattice [6]. In Ino's more physical model, the thin external wedges of the geometric decahedron are truncated by (100) planes, resulting in a more compact structure [8].

2.3 RELATING MEASUREMENTS TO STRUCTURE

The lack of translational symmetry in nanoparticles makes it often inappropriate to apply traditional crystallographic methods of analysis (e.g.: indexing 'peaks'; estimating particle size from peak broadening; estimating strain and disorder; etc) in nanoparticle studies, especially in studies of FCC materials [9, 10, 11, 12, 13, 14]. This has a profound

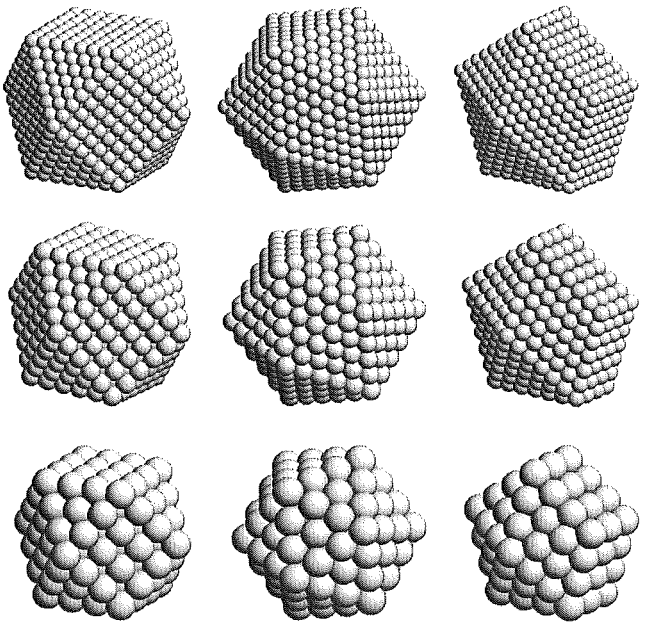

Figure 1.1 Examples of three types of cluster structures: FCC cuboctahedra, icosahedra and decahedra. The cuboctahedra (first column, N=1415; 561, 147 atoms, from top to bottom) have the same FCC arrangement of atoms as the bulk structure, and are typically observed for large particle sizes. The icosahedral (second column; N=1415, 561, 147 atoms also) and decahedral (third column; N=1514, 605, 116 atoms) structures are believed to be energetically favoured only for very small clusters. These models correspond to the structures used to calculate the diffraction patterns of Fig. 1.2.

effect on data analysis[1]. It turns out to be necessary to identify all types of structure that could arise in the experiment *before* beginning quantitative analysis. Hence, theoretical tools, such as molecular dynamics (MD) simulations can be very valuable in identifying low-energy structures. Also, observations using HRTEM have been important in

[1]Our comments about the ineffectiveness of traditional methods apply to clusters in which the size of crystalline domains is of the order of a few tens of Å, or where non-crystalline structures exist. If a sample is known to consist of larger, nearly perfect, crystalline particles, as in Section 6.1 then there is no problem

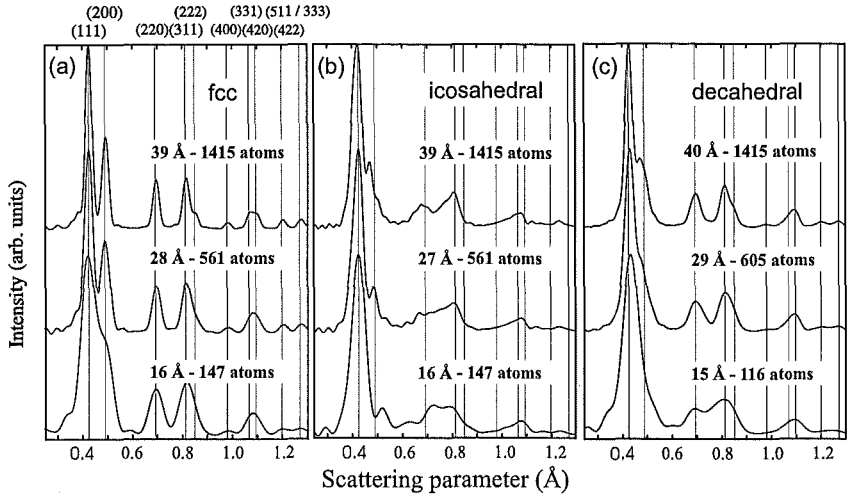

Figure 1.2 Calculated diffraction patterns for three characteristic forms of nanoparticle structure: FCC (a); icosahedral (b); and decahedral (c). Each panel shows diffraction patterns for particles of different sizes. The calculations used equation (1.1) and parameters for gold ($D(s)$ was set to unity, no inelastic scattering, energy 100 kV). The patterns have been offset vertically, and the intensity at the first maximum normalized, for clarity. The position of bulk Bragg diffraction peaks are labeled at the top of panel (a) and are also marked in panels (b) and (c). Note: positions of FCC Bragg peaks are given in (b) and (c) only to ease comparison; the MTP structures are non-crystalline so there is no associated reciprocal lattice.

identifying structures that must be considered in the analysis of experimental diffraction data.

Often, structure determination is best carried out by comparing calculated diffraction patterns, based on realistic models of structure, with a diffraction measurement. A measurement can be interpreted by selecting the calculated pattern, or a combination of patterns, that best matches the observations. This approach is widely accepted and has been particularly successful in studies of rare-gas clusters, discussed in Section 3.. However, it must be borne in mind that similarity of diffraction patterns does not guarantee agreement between underlying structures. More correctly, when diffraction patterns are similar it suggests that the respective sets of inter-atomic distances (rather than atomic coordi-

nates) are also similar[2]. The decahedral particles in Fig. 1.2 are a good example of this: it is difficult to distinguish between FCC particles and decahedra, especially when the molecular beam contains a significant distribution of particle sizes.

In an experiment, where the clusters may not have perfect geometric structures, it is difficult to distinguish between whole-particle structure and the structure of coherent domains. Diffraction measurements on particles in which there is some degree of disorder are dominated by the larger domains of coherent structure: in general, therefore, measurement results should be considered as characteristic of the domain structure rather than of the entire particle. It turns out that inter-domain interference effects can be neglected to a first approximation. These important points have been illustrated in many studies, for example: in experimental studies of argon nanoparticles [15]; in simulations of materials with randomly oriented crystalline domains [16, 17]; and in a simulation of fifty five Au_{55} icosahedra, arranged in a slightly perturbed 'super' icosahedral structure [18].

3. RARE-GAS CLUSTERS - THE ORSAY GROUP

The first electron diffraction measurements of unsupported cluster structure were performed by Philippe Audit in 1969, at the *Laboratoire de Diffraction Eléctronique, Université Paris-Sud*, France [19]. These experiments produced clusters of rare-gases, and CO_2, in supersonic beam expansions. The results were compelling: they showed that a variety of clusters could be produced, ranging from larger particles resembling the bulk crystal structure to smaller unidentified structures and liquid drops. The work demonstrated that electron diffraction could provide unique and valuable information about the structure of unsupported clusters.

The success of this first study prompted the construction of an improved apparatus, by Raoult and Farges [20]. It is this set-up that provided the results discussed in this section; it continues to be used today.

[2]McGreevy gives a more detailed discussion of the relationship between structure models and diffraction measurements [72], in the context of the so-called Reverse Monte Carlo method for structure determination of liquids and amorphous bodies [73].

3.1 EARLY RESULTS AND ANALYSIS

Early results were interpreted by comparing measured diffraction patterns with calculated patterns for geometrical structures. For Ar, the results suggested that clusters had the FCC structure and contained ~500 atoms [21] (later revised upwards to ~ 3000 atoms [22]). However, the experimental pattern (see Fig. 2 in Ref. [21]) could not be explained in detail: the (111) peak is abnormally high and the (200) peak was not distinctly separated from it, as expected. At the time, it was thought that these anomalies were due to atoms in close-packed, but non-FCC, sites – a remnant of non-crystalline precursor structures at smaller sizes. It is interesting that, despite the seemingly obvious FCC component in the diffraction patterns, these early measurements have been difficult to interpret in detail and their interpretation remains an area of active research [12, 15, 23] (see further discussion in Section 3.2).

In an attempt to observe the early stages of the growth sequence, the source was adjusted to produce smaller clusters. The minimum observable size was ~20 atoms. Measurements over the size range 20–50 atoms clearly showed that cluster structure could not be explained by either FCC, icosahedral or liquid structures [22]. In fact, the diffraction patterns appeared very similar to those from amorphous metals [22].

Molecular dynamics simulations (using the Lennard-Jones potential) were used to provide more accurate models for comparison with the data. The MD routine could search for the lowest energy structure by simulating the cooling of a liquid drop, allowing time for rearrangement of the atoms to occur, even after solidification [22, 24]. The routine could also be used to compare the stability of different structures, as well as to observe the dynamics of a system at finite temperature.

MD simulations were performed for Ar cluster sizes up to ~150 atoms, identifying a structural change at approximately 50 atoms. Below 50 atoms, Ar clusters adopted a poly-icosahedral structure containing deformed 13-atom icosahedral cages [22]; this changed to a multi-layer icosahedral structure for the larger clusters [24]. The MD simulations also predicted that multi-layer icosahedra with less than ~82 atoms could have a twinned outer layer. Experiments were in excellent agreement with the MD-model diffraction patterns, and showed both the predicted structural transition, as the cluster size was increased, and evidence of a twin layer on the smaller multi-layer icosahedra.

For cluster sizes greater than ~150 atoms MD was too computationally intensive so unrelaxed geometrical icosahedra were used as the model structures. Nevertheless, excellent agreement was reported between these diffraction patterns and experiments, up to a size of ~750

atoms [24]. Beyond this, the appearance of peaks in FCC positions heralded a further structural transition, which is discussed in the next section.

3.2 ICOSAHEDRAL-TO-FCC TRANSITION

It has generally been assumed that for large enough unsupported Ar clusters the bulk FCC crystal structure will predominate, however, this has not been observed[3]. There are many estimates of the critical size at which the FCC structure will become energetically preferred to the icosahedral structure [25, 26, 27, 28]. These estimates vary widely, with the lowest [27] being N$\sim$2000-3000, close to the transition observed in Refs. [11, 24]. Interesting too is the prediction that decahedra are preferred in an intermediate size range falling between the icosahedron, at smaller sizes, and FCC, at larger sizes [25]. However, decahedra have never been identified in experimental results from Ar, or other rare-gas clusters.

Critical size predictions assume that growing clusters achieve thermodynamic equilibrium. Farges *et al.* [22] argue that the smaller Ar clusters have sufficient time (10^{-4} s time-of-flight after nucleation) and energy (temperature $\sim$27 K, c.f. melting point $\sim$35 K) to adopt the equilibrium structure. However, for larger clusters this may not be the case. The energy required to change structure increases with N, and both growth history [28] and growth rate [29, 30] also influence the structure. These factors may result in the production of meta-stable cluster structures [12].

It would be of considerable interest to resolve the question of how, and when, the five-fold symmetric structures that predominate at small cluster sizes can transform into an FCC structure and continue growing. To allow this transition to take place in a natural way, van de Waal [23] has proposed a complex model structure containing intersecting pairs of twin planes which give rise to local regions of five-fold symmetry. This model provides a plausible growth sequence: in a relatively small cluster, the regions of five-fold symmetry dominate (and hence will be observed in experiments), however, the particular arrangement of twin planes promotes FCC growth at the surface. Hence, although containing several small defects, a large cluster essentially has the FCC structure. Diffraction patterns calculated using this model structure match the experiments very well for clusters with $\sim$3000 atoms.

[3]The preference for FCC structure in the bulk is actually not well understood, see [12, 23] and references therein.

Unfortunately, the van de Waal structure does not describe the features of the experimental diffraction pattern for still larger clusters [11, 15]. Indeed, recently de Feraudy *et al* [11] reported that Ar clusters with $\sim 10^4$ atoms begin to show features characteristic of stacking faults in the diffraction pattern, creating a shoulder on the (111) peak. De Feraudy proposed that these features are created by parallel stacking faults in a FCC cluster, however, diffraction patterns of model structures do not reproduce the peak broadening observed. The most recent study of large Ar clusters ($10^3 < N < 10^5$) now suggests that, in fact, large clusters never adopt a coherent FCC structure [12]! Instead, growth conditions probably lead to formation of inhomogeneous particles with mixed regions of close-packed structure, including FCC, hexagonal close-packed and random stacking of close-packed layers.

4. EARLY METAL PARTICLE STUDIES

The first diffraction measurements on free metal clusters were performed by Gilbert Stein's group at Northwestern University, USA. [31].

4.1 THE NORTHWESTERN SOURCE

Supersonic expansion cluster sources can be used for gases (Ar, CO_2, etc) [19, 21, 32], and seeded supersonic expansions can produce very small metal particles [33]. However, sources for diffraction studies of metals need to provide cooling rates (supersaturation) much higher than those in supersonic expansions, in order to generate intense particle beams. The inert-gas-aggregation (IGA) technique provides suitable conditions and so IGA was readily adapted to provide a particle beam source for diffraction studies [34].

In an IGA source (see Fig. 1.3), clusters are formed in the gas phase by isobaric cooling. Hot metallic vapour, from an evaporation source, is cooled by an inert buffer gas at room temperature. As it cools, the metallic vapour supersaturates in the vicinity of the evaporation source and clusters nucleate and grow as they are carried away by the buffer gas [34]. This is entirely different to the clustering process in supersonic expansion sources, where cooling and growth occur during the expansion of the gas. In an IGA source, the mixture of gas and formed clusters also passes through nozzle apertures, however this is done to provide a well-collimated particle beam and, more importantly, it allows a large proportion of the unwanted buffer gas to be pumped away.

The original Northwestern source was designed to produce clusters of between 500 and 5000 atoms. In operation, it achieved a background gas pressure of about 10^{-5} mbar in the diffraction chamber. Two tech-

niques for evaporating metal were used: a tungsten filament, in which pieces of metal were inserted; and a boron nitride crucible with a coiled filament heater. The capacity of the these was small and was one of the factors limiting beam life-time and stability: diffraction patterns were commonly visible for about 10 s and never for more than 90 s.

4.2 SOURCE CHARACTERISTICS

The technique of IGA has been used extensively for cluster production under static conditions (see, e.g. [35, 36, 37, 38, 39]), as well as with a flowing buffer gas as in Stein's design [34, 40, 41]. The formation of clusters by IGA is understood qualitatively, however the precise conditions prevailing during experiments are not well known. Cluster formation depends on a variety of parameters: the inert gas pressure p_g; the temperature at the surface of the evaporating material T_m; the buffer gas weight and heat capacity, etc. Stein used p_g and T_m to exert control over the mean cluster size [34]. It was found empirically that as the product $p_g \cdot T_m$ was increased clusters of larger diameter were formed, but in smaller numbers.

Stein and co-workers explored the effect of different buffer gases (Ar, He, CO_2 and SF_6) [42] on the production of Ag cluster beams. These experiments were consistent with the $p_g \cdot T_m$ relation, however the heavier gases produced a given cluster size at a lower value of the pressure-temperature product. This implied that heavier gases, especially molecular gases with larger heat capacity, can enhance the production of clusters and lead to significant cluster production at substantially lower evaporation temperatures. Experiments with the two different evaporation methods described above indicated that these details of the source configuration can have a significant effect on the size distribution (i.e., the nucleation and growth processes) [34].

4.3 EXPERIMENTS ON METAL CLUSTERS

Bismuth, lead, indium and silver clusters with sizes from 2500 to 3×10^4 atoms (diameters between 40–110 Å) were investigated by Stein and co-workers [31, 34, 42]. Stein's group analysed their measurements in terms of an underlying crystal structure: peaks were indexed and their positions and widths measured; changes in lattice parameter were used to estimate cluster temperature, using bulk expansion coefficients. They also recognized the limitations of the kinematic scattering approximation and took steps to investigate its validity [42].

Measurements on indium clusters of between 42 Å and 81 Å, revealed a structural change, from the bulk tetragonal structure to FCC, for clus-

ters with sizes smaller than $\sim$ 50 Å ($\sim$ 3000 atoms) [34]. The diffraction patterns clearly show this transition – the indexing of an FCC structure is unambiguous – however, the possibility of deviations from FCC structure at still smaller sizes was not investigated.

On the other hand, diffraction patterns of bismuth clusters, of between 60-95 Å, showed no departure from the rhombohedral structure, nor any significant size-dependent change in lattice parameter [34].

Investigations of lead (30-100 Å [31, 34]) and silver (40-110 Å [42]) were published in more detail. In the case of lead, careful analysis of peak positions and intensity data revealed anomalies. However, simple dynamical scattering corrections could account for some of the discrepancies and a liquid component was postulated to make an oscillatory contribution to the otherwise monotonic gas background signal. In the case of silver, anomalous observations for smaller clusters could not be reconciled with dynamic scattering corrections and various possible explanations were apparently explored, including the liquid background, MTPs, and stacking faults, without success.

5. FURTHER STUDIES OF METALS

Stein's early work on metal particles was important because it showed the potential of the electron diffraction technique to work under the conditions required to produce metal clusters. An improved apparatus was built, in collaboration with Stein, in the laboratory of Jean-Pierre Borel and René Monot at the *Ecole Polytechnique Fédérale de Lausanne* (EPFL), Switzerland [43]. The design improved on the Northwestern source in several ways: it had much greater evaporation source capacity, allowing longer experiments; an extra pumping stage was added to the source, making the background pressure in the diffraction chamber lower and thereby enhancing the sensitivity to weak diffraction signals; it provided on-line, as opposed to photographic plate, diffraction pattern measurements.

5.1 UNSUPPORTED METAL MTPS

Silver was the first material to be studied at EPFL since it was known to form MTPs and could be readily produced using the IGA technique. The experiments were intended to investigate whether or not the occurrence of MTP structures was in some way an artifact of the particle-substrate interaction in conventional TEM studies [44].

The results showed convincingly that MTPs do occur in small isolated clusters [43]. The careful analysis of series of diffraction patterns for different source conditions showed that, although the cluster samples had

roughly comparable size distributions, there were varying proportions of FCC, icosahedral, and decahedral domains present. The icosahedral signature clearly dominated in one pattern, and the FCC structure was identified in another. Intermediate diffraction pattern shapes were found to have a mixture of decahedral and varying amounts of either icosahedral or FCC domains, suggesting that the decahedral domains were most likely to form under conditions in between those favoring FCC or icosahedra, in accord with predictions of the phase diagram for metal nanoparticles [45].

Two factors were important in the success of these experiments [43]. Firstly, the IGA source was tuned to produce much smaller clusters than those observed by Stein. Secondly, the size distribution of clusters in the beam was explicitly considered in the analysis for the first time. If a range of sizes is present, and there are features in the diffraction pattern that are size-related, then a combination of individual cluster diffraction patterns must be used to interpret the data.

5.2 LARGE METASTABLE ICOSAHEDRA

Following this study, further improvements were made to the apparatus [46]. In particular, a 100 kV electron beam illumination system and a new diffraction pattern recording unit were installed (see Fig. 1.3). Measurements were faster and much less sensitive to the inevitable drift of the particle beam intensity.

In this new configuration, an investigation of anomalous structure in large silver clusters was undertaken. While still being tested, the modified apparatus had produced observations of unusually large icosahedra under certain source conditions [46]. The unexpected phenomenon was carefully studied by tracing the changing structures in the particle beam as a function of nucleation conditions [30]. Icosahedral clusters as large as 110 Å in diameter were found and it was observed that their structure could apparently be 'tuned' between icosahedral and FCC, while the overall size of the clusters remained roughly constant. This was achieved by either changing the evaporation source temperature or the molecular weight of the carrier gas. Smooth variation of the latter was achieved by introducing a mixture of argon and helium into the source chamber. MD simulations of the growth of Ag clusters have recently shed more light on the processes which may lead to the formation of larger icosahedra [29].

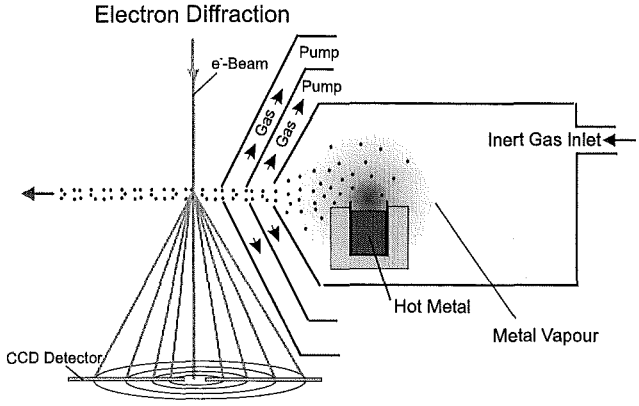

Figure 1.3 A schematic diagram of the EPFL apparatus. On the right, clusters form in an inert-gas-aggregation source. The mixture of clusters and gas is then drawn through two differential pumping stages before entering the diffraction chamber. The electron and clusters beams cross at right-angles, forming a radially symmetric Debye-Scherrer diffraction pattern. The intensity along a diameter of the pattern is recorded by a pair of charge-coupled device (CCD) detectors. This apparatus has since been relocated to the University of Canterbury, New Zealand (see Section 6.).

5.3 STRUCTURAL TRANSITIONS IN COPPER

MD simulations, performed by Valkealahti and Manninen, have investigated the relative stability of different cluster geometries in copper for sizes up to about 10^4 atoms [47]. The study predicted a critical size of about 2500 atoms (about 38 Å diameter): below this limit, icosahedral clusters were the preferred structure; above it, cuboctahedral (FCC) clusters.

The EPFL apparatus was used to investigate this size dependence. A series of diffraction patterns were obtained for a range of source conditions, intended to span the MD-predicted critical cluster size [48, 49]. These patterns showed clear evidence of structural change taking place (Fig. 1.4). Detailed analysis revealed a net preference for icosahedral structure in smaller particles and a dominance of FCC domains at larger sizes. Although the experimental uncertainty was rather large, the results of this study supported the theoretical predictions and the critical size estimated from experiment was very close to the MD predicted value.

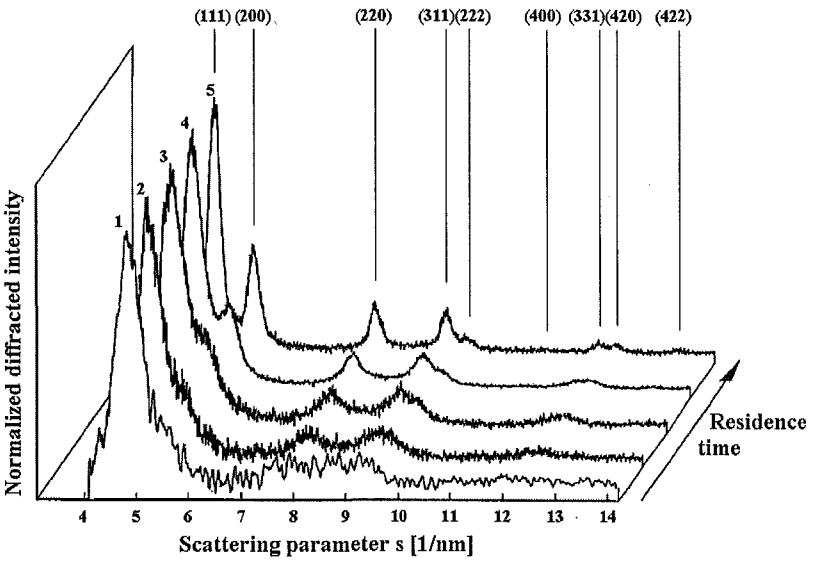

Figure 1.4 A succession of diffraction patterns from copper clusters presented in increasing order of mean cluster size (patterns 1 to 5), from [48].

6. RECENT STUDIES

In 1998 the EPFL apparatus (see Section 5.) was re-established at the University of Canterbury, New Zealand, where again the focus is on the structure of metallic clusters. Work in the last two years on bismuth and lead clusters is discussed in separate subsections below.

6.1 BISMUTH CLUSTERS

The structure of unsupported bismuth particles was first studied by Yokozeki and Stein [34], who reported rhombohedral structures for particles with sizes between 60 and 95 Å (Section 4.).

Besides Stein's work, previous studies of the structure of bismuth clusters have mainly used HRTEM, in which case the clusters are supported on a substrate [50, 51, 52, 53]. These studies have produced a number of conflicting results. Particles with a single-crystalline core (50-100 Å diameter, rhombohedral structure) surrounded by an amorphous or liquid shell, and smaller non-crystalline particles on amorphous carbon films were described in Ref. [52, 53]. Other investigations [50] have found a structural transition at a particle size of 84 Å. Particles larger than $\sim$ 50 Å and smaller than 84 Å had the rhombohedral structure of the bulk material, with the shape of a truncated rhombohedron, while larger particles had a complex structure containing lattice defects.

Due to the variety of observations regarding the structure of Bi particles, a further series of experiments have been performed on unsupported clusters. These experiments have explored a large range of cluster sizes as well as investigating the effects of a range of source parameters (gas type, evaporation temperatures, gas pressures) on cluster structure.

6.1.1 Experiments using argon as the carrier gas. Using argon as a carrier gas, bismuth diffraction patterns were obtained for $770°C < T_m < 950°C$. The crucial parameter for the formation of a high cluster flux was p_g. The optimum pressure for cluster beam intensity shifted from 12 mbar at 770°C to 22 mbar at 893°C.

The diffraction patterns shown in Fig. 1.5 (a)-(d) are characteristic of relatively large clusters and display the rhombohedral structure of the bulk material. Average diameters, determined by the Scherrer formula [1], were 65 Å, 75 Å, 85 Å and 45 Å for patterns (a), (b), (c) and (d), respectively. The uncertainties in these estimates are $\pm$ 10 Å. Relatively small clusters are produced with the original source chamber configuration (Fig. 1.5(d)), whereas larger clusters were produced when the source chamber was modified to improve heat shielding of the carrier gas from the evaporation source (Fig. 1.5 (a)-(c)).

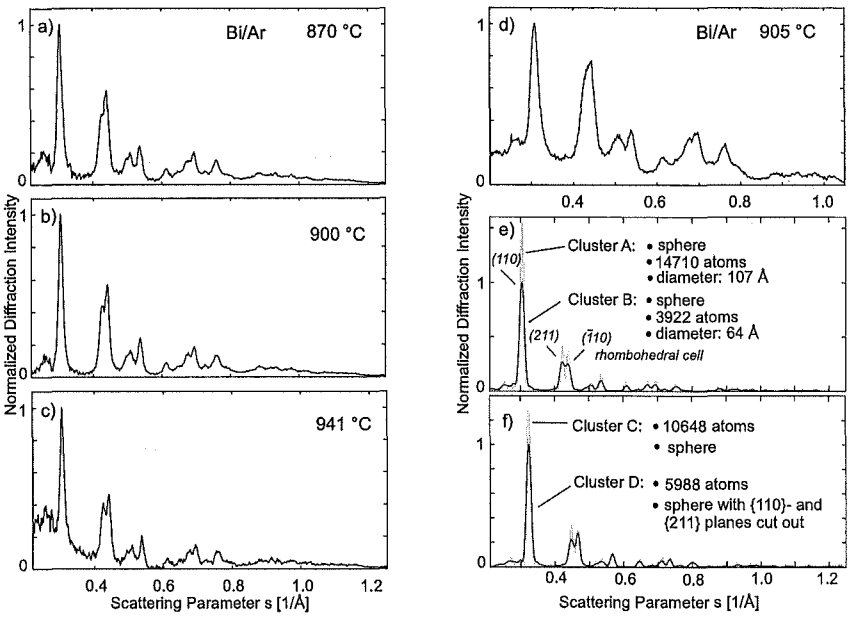

Figure 1.5 (a)-(c): Experimental diffraction patterns of bismuth clusters produced in Ar. Increasing the evaporation temperature leads to an increase in cluster size, shown by the narrowing of the main diffraction peak and by the clearer splitting of the peaks at s $\sim$ 0.43 Å^{-1}. Experiments (a)-(c) were performed in a modified source chamber with improved heat-shielding of the evaporation source, while (d) was performed in the original source chamber and shows smaller clusters. (e) Calculated diffraction patterns for two spherical model structures showing that the (211)/($\bar{1}$10) peak splitting becomes visible for clusters larger than $\sim$ 60 Å. (f) Model structure diffraction patterns showing that the intensity ratio of the (211) and ($\bar{1}$10) peaks can be adjusted by removing some {211} planes from the spherical cluster.

Additional estimates of cluster size can be obtained by comparing the experimental diffraction patterns with calculated patterns of model structures. The splitting of the peak at s $\sim$ 0.43 Å^{-1} is clearly visible in calculated patterns for spherical clusters that have a diameter greater than 60 Å (Fig 1.5(e)). The intensity ratio of the (211) and ($\bar{1}$10) peak in the pattern of the spherical model structures (Fig. 1.5 (e) and (f)) does not agree with the experimental patterns. However, this intensity ratio can be adjusted to match the experimental patterns by changing the shape of the model clusters i.e. by removing some of the {211} planes from the spherical clusters (Fig. 1.5 (e)). The low intensity of the (211) peak, therefore indicates a non-spherical shape for the clusters, suggesting that the clusters have the same, truncated rhombohedron, form reported in Ref. [50]. Fig. 1.5(c) exhibits a residual diffraction background, which may be caused by a high density of atomic bismuth in the cluster beam at higher temperatures.

6.1.2 Experiments using helium as the carrier gas. The production of bismuth clusters using helium required very high gas pressures – beyond the range of our pressure gauge – hence we know only that the pressure was higher than 12 mbar in these experiments. Diffraction patterns of crystalline bismuth clusters were obtained for $T_m > 846°C$ (Fig. 1.6(a)). Additional features begin to appear in the diffraction pattern at $T_m \sim 925°C$ (Fig. 1.6(b)), indicating the formation of a significantly different structure, which becomes dominant for $T_m > 940°C$ (Fig. 1.6(c)). The broad features in these diffraction patterns suggest the presence of amorphous or liquid clusters and are very similar to electron, and x-ray, diffraction patterns from liquid bismuth [54, 55].

During these experiments, a modification was made to the IGA source chamber to improve the heat shielding of the crucible and thereby reduce the transfer of heat from the evaporation source to the inert buffer gas. This effectively enhanced the cooling of the metal vapour by the buffer gas. After this modification, only crystalline diffraction patterns from were observed (Fig. 1.6 (d) and (e)).

The diffraction patterns shown in Figs. 1.6 (a), (d) and (e) are compatible with the rhombohedral structure, with the lattice parameters of the bulk material. The average diameter of the clusters, determined with the Scherrer formula, is 65 Å, 85 Å and 95 Å for Fig. 1.6 (a), (d) and (e), respectively. There is no evidence in these observations to support the claim in Ref. [50] that larger clusters undergo a transition to a new cubic-like structure.

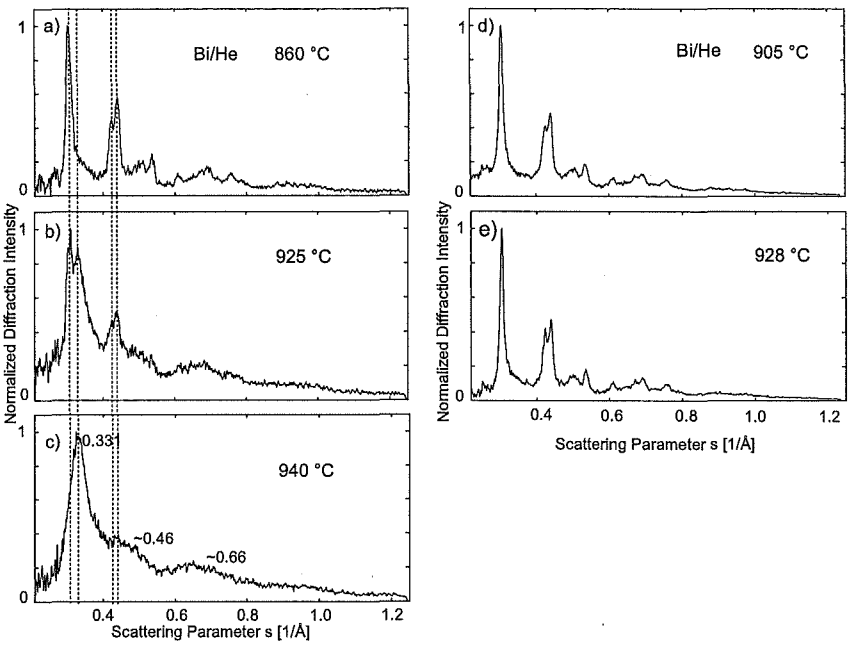

Figure 1.6 (a)-(c): Experimental diffraction patterns from clusters produced in helium at various evaporation temperatures. The diffraction pattern at 860°C is clearly from crystalline clusters. At 925°C additional features can be observed in the diffraction pattern which dominate the diffraction pattern at 940°C. When modified to provide better heat shielding of the crucible, the source chamber produced only crystalline clusters over the whole accessible temperature range, panels (d) and (e).

6.2 LEAD CLUSTERS

The earliest experimental studies of unsupported 80-100 Å Pb clusters identified clusters with the bulk FCC structure, although they were thought possibly to include amorphous regions [34, 56]. The predominance of FCC structure is consistent with early MD simulations [57] which found that cuboctahedra (FCC structure) were energetically favoured in lead at all cluster sizes. However, this behaviour is in contrast to that of many other FCC metals, for which transitions from FCC to icosahedral structures have been predicted [8, 58, 59] and observed [30, 49, 60, 61], and suggests that Pb clusters are in some way different to other more extensively studied FCC metals: Cu [49], Ag [62] and Au [63, 64].

In a subsequent MD study [65], however, a simulated quench was performed on a large, liquid, 8217-atom lead droplet and the resulting structure was characterised as 'icosahedral-like'. It was not the lowest energy structure, but was thought to occur due to initial formation of (111) planes at the droplet's surface allowing crystallisation to proceed inwards.

6.2.1 Results. Diffraction patterns from lead clusters have been observed across a wide range of T_m and p_g. The diffraction patterns are not observed to change considerably with variations in T_m and p_g, and the previously reported increase in size with $p_g \cdot T_m$ (Section 4.) is not observed clearly in this work. However, by varying the molecular weight of the inert gas (changing the He:Ar ratio) very significant changes in particle size and structure can be achieved. Fig. 1.7 shows typical diffraction patterns obtained using only Ar, or He, at similar T_m and p_g.

Fig. 1.8 shows a series of diffraction patterns obtained by varying the He:Ar proportions in the source chamber, while keeping the total inert gas pressure at approximately 4 mbar. A smooth evolution of diffraction patterns was observed between the two extremes shown in Fig. 1.7. The sharpening of features from pattern 1 to pattern 6 suggests an increase in cluster size, and the evolution of the shoulder feature at ~ 0.4 Å^{-1} indicates a change in the structure of the clusters.

6.2.2 Analysis. Lead cluster diffraction patterns have been analysed by comparison with diffraction patterns from geometric model clusters. A fitting routine [66] combines model diffraction patterns from preselected structures to produce a best match to the experimental data. The model structures used are closed-shell geometrical cuboctahedra

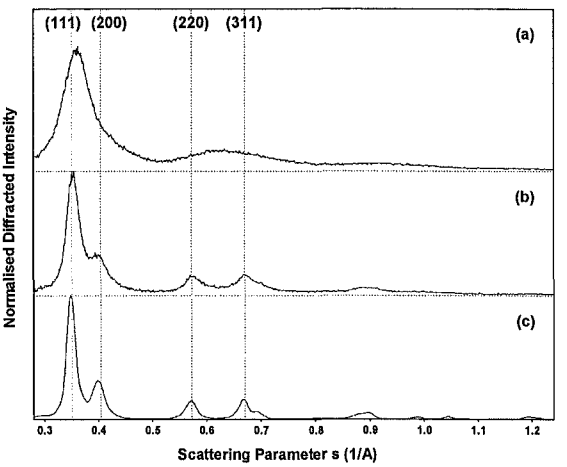

Figure 1.7 Diffraction patterns obtained from Pb clusters with different inert gases: (a) pure He and (b) pure Ar. For both patterns $T_m = 810°C$ with $p_g = 5$ mbar and $p_g = 2$ mbar, for (a) and (b) respectively. Panel (c) shows the diffraction pattern of a large model decahedron cluster, shown for comparison with experimental patterns from large particles. The positions of the bulk (FCC) peaks for Pb are indicated by the dashed lines.

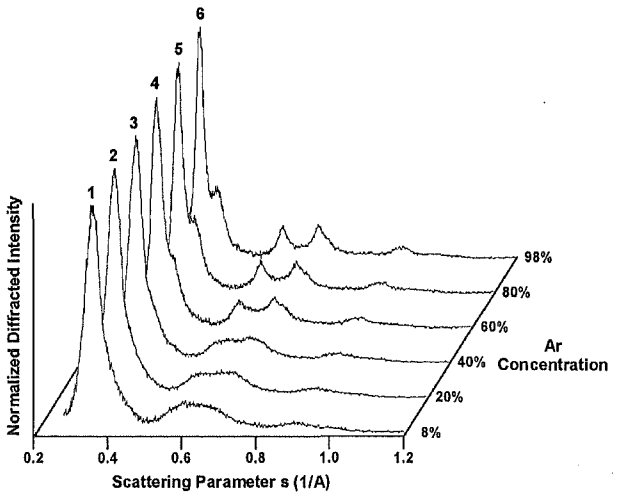

Figure 1.8 Diffraction patterns obtained from Pb clusters by increasing the mixing ratio of Ar to He from profile 1 to 6. $T_m = 840°C$ and the total inert gas pressure is ~4 mbar.

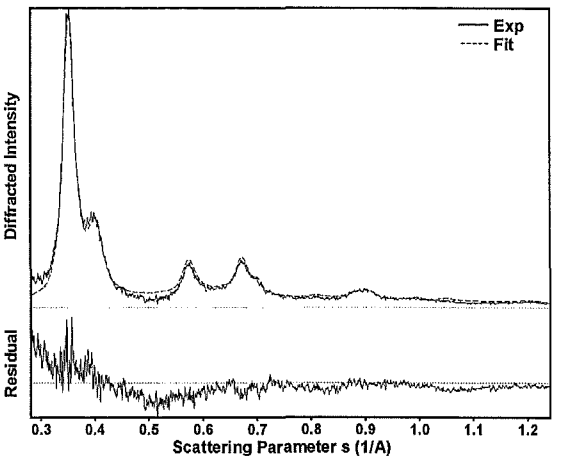

Figure 1.9 Fit for pattern 6 in Fig. 1.8. The experimental curve is well matched by the inclusion of large decahedral domains. The lower panel is the difference between experiment and fit (on an expanded scale).

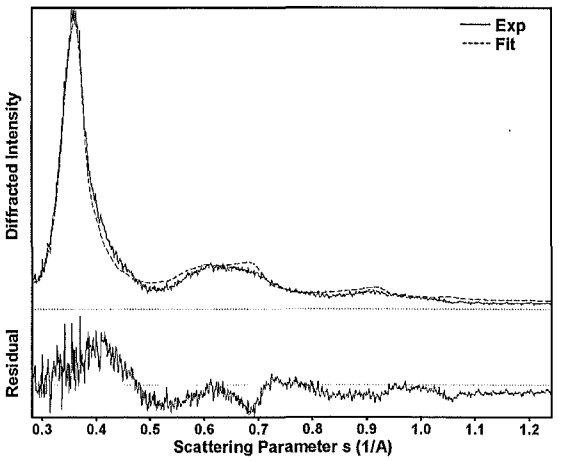

Figure 1.10 Fit for pattern 1 in Fig. 1.8. The fit does not accurately reproduce the shapes of the shoulder at 0.4 $Å^{-1}$ and the broad peak centred on 0.62 $Å^{-1}$, indicating that alternative structures must also be considered. The lower panel is the difference between the experiment and fit (on an expanded scale).

(FCC), truncated decahedra, and icosahedra ranging in size from 55 to 6525 atoms (diameters ~15 to ~80 Å).

Estimates of the mean experimental cluster size are made using several methods: the Scherrer formula [1], Fourier inversion of the diffraction pattern [14], and from results of the fitting analysis (note that, as discussed in Section 2., a size estimate obtained from fitting will be indicative of the domain size, which may be smaller than the particle size).

Table 1.1 summarises the results of the fitting procedure for patterns 1, 3, 4 and 6 from Fig. 1.8, as well as the various size estimates. The rather good agreement between the different size estimates suggests that the fits may be identifying domain structures that fill most of the clusters' volume.

6.2.3 Discussion. The fit for pattern 6 is shown in Fig. 1.9. The results (Table 1.1) suggest that pattern 6 is dominated by large decahedral domains. The resemblance between diffraction patterns, from large decahedral clusters, and the experimental pattern is striking (see Fig. 1.7(c)). However, the decahedron is not the preferred structure at these sizes so its observation is unexpected. The experimental diffraction pattern has also been compared (by fitting) to other candidate structures, such as twinned FCC clusters, however decahedral patterns provide the best fit to the experimental data.

The fit for pattern 1 is shown in Fig. 1.10. Here, the results indicate that domains are predominantly icosahedral. However, in this case, fitting does not satisfactorily reproduce the shapes of the shoulder at 0.4 $Å^{-1}$ and the broad peak centered on 0.62 $Å^{-1}$. This indicates that the basis patterns used for fitting can not completely reproduce the cluster structures in the beam: alternative structural models need to be considered as well.

The results of the fitting procedure (Table 1.1) for patterns 1, 3, 4, and 6 in Fig. 1.8 show that the composition of the cluster beam changes as the proportion of He:Ar is altered. Compared to pattern 1, there is an increase in average domain size for patterns 3 and 4 (note the appearance of a clear splitting between the peaks at 0.57 $Å^{-1}$ and 0.67 $Å^{-1}$) and the continued dominance of icosahedral domains. The fitting analysis of pattern 4 also reports a population of large decahedral domains, which increases for pattern 6. Interestingly none of the patterns in Fig. 1.8 include the bulk FCC structure, in sharp contrast to initial studies [34] which found that slightly larger Pb clusters had exclusively the bulk structure. This may indicate that a transition to bulk structure occurs

Table 1.1 Results of fitting procedure for experimental patterns 1, 3, 4, and 6 from Fig. 1.8. The parameter d is the average (volume weighted) domain size for each structure, δ_d is the standard deviation of d, and v is the proportion of each structure (by volume). The size estimates from three independent methods are also shown.

Structure		Experimental Profile 1	3	4	6
Cuboctahedral	d(Å)	-	-	-	-
	δ_d(Å)	-	-	-	-
	v(%)	0.0	0.0	0.0	0.0
Decahedral	d(Å)	19	42	77	75
	δ_d(Å)	3	6	7	11
	v(%)	3.5	0.2	14.4	58.5
Icosahedral	d(Å)	29	34	43	37
	δ_d(Å)	12	10	14	16
	v(%)	96.5	99.8	85.6	41.4
Size estimates	Fitting ± 1	28	34	48	59
(Å)	Inversion ± 5	30	35	40	60
	Scherrer ± 10	20	25	30	40

at a size larger than 70 Å, however structural analysis in the earlier study did not fully consider the possibility of MTP structures.

Research on lead clusters is ongoing. Other model structures (especially relaxed MD generated structures) need to be compared with our experimental results. Further experiments will also be performed, examining the effects of growth time and enhanced cooling of the metal vapour.

7. ALTERNATIVE ELECTRON DIFFRACTION TECHNIQUES

Inevitably, suitable particle sources generate clusters with a distribution of sizes, so a measured diffraction pattern reflects the ensemble as a whole and is not characteristic of a single particle size. In a continuous beam system, mass filtering has the potential to select particles of a single size but will significantly reduce the diffracted intensity, thus worsening the signal-to-noise in the measurement. In this section we highlight a recently developed alternative technique and discuss some of its advantages and disadvantages.

7.1 DIFFRACTION FROM TRAPPED CLUSTERS

The Trapped Ion Electron Diffraction (TIED) technique [67, 68], developed at the Rowland Institute, Boston, relies on a RF Paul trap to size-select and accumulate clusters. Neutral clusters are produced by either a Knudsen oven [67] or an IGA source [68] and then ionised, so that they can be loaded into the trap. Both the neutral cluster beam and the trapped ions can be probed by a 40 kV electron beam. A carefully designed Faraday cup captures unscattered electrons and a microchannel plate and phosphor screen system, inside the vacuum chamber, is used to image the diffraction pattern in conjunction with an external CCD camera.

The TIED technique works by selecting ions with a certain mass-to-charge ratio. The excellent mass resolution of the system has been demonstrated for $(CsI)_nCs^+$ ions, where the dominant structure (bulk CsI) for $n = 32$ is observed to be different to that for other members of the sequence $n = 30 - 39$ (NaCl structure).

One significant difference between TIED and the molecular beam techniques discussed elsewhere in this chapter is that the clusters are ionised. Electron scattering from a charged body is different from a neutral one. However, the extent of s over which significant differences in the scattering factor occur is roughly from $s = 0$ up to the reciprocal of the particle size [3]. Hence, for metal clusters larger than ~ 10 Å the effect of charging the particle can safely be ignored.

An excellent feature of the TIED technique is that it permits the temperature of the trapped ions to be controlled by brief exposure to low pressure He gas. In contrast, particle temperature in the molecular beam produced by an IGA source is difficult to control. (It can be achieved by allowing the particles to thermalize in drift region separated from the nucleation chamber [40, 41], but it is unlikely that this can still provide an intense particle beam for diffraction).

TIED offers several significant advantages over molecular beam techniques, but it also has some unique difficulties of its own, and in particular the combination of an RF trap with a sensitive electron-beam apparatus is not technically trivial. The Rowland group has carefully characterised their experiment and has shown that many possible problematic effects can be ignored. For example, the perturbing effects of RF fields on the electron probe have been calculated and observed, and are shown to be small.

The TIED technique has yet to be applied to metal clusters, and so the effect of a relatively long exposure period to the electron beam

($\sim$ 45 s per data sequence [67]) have yet to be clarified. It is well-known from HRTEM studies that supported nanoparticles of the order of 30 Å or less undergo rapid structural rearrangements when irradiated with a high-energy electron flux [45, 69, 70]. In contrast to TIED, fast moving clusters from a continuous molecular beam source are individually exposed to a very weak electron flux; so weak in fact that the probability of more than one electron scattering from a single cluster is very low [71].

8. CONCLUSION

Electron diffraction measurements on molecular beams of clusters have been reviewed. Emphasis has been given to studies of beams of metal clusters and the closely related work on inert gas clusters. Improvements in both source design and diffraction techniques over the last 20 years have been discussed alongside the experimental data.

Unsupported silver and copper clusters have been investigated in some detail in the past and deviations from the bulk FCC structure have been clearly observed. For small enough particles icosahedral structures are preferred energetically but much larger meta-stable icosahedral particles have also been observed under rapid growth conditions. The detailed examination of silver and copper clusters contrasts with the scarcity of data for the majority of metal clusters and further investigations are very much needed.

Preliminary new results on bismuth clusters, which exhibit the bulk structure as well as a clear phase transition, and lead clusters, for which the bulk FCC structure is not observed, have been presented. Finally, a new development in the technology of electron diffraction from clusters, the trapped ion electron diffraction technique has been reviewed.

References

[1] A. Guinier, *X-ray diffraction in crystals, imperfect crystals and amorphous bodies*, Dover, New York, 1994.

[2] A. J. C. Wilson, editor, *International tables for crystallography*, volume C, Kluwer, Dordrecht, 1992.

[3] B. K. Vainshtein, *Structure analysis by electron diffraction*, Pergamon Press, Oxford, 1964.

[4] L. S. Bartell, B. Raoult, and G. Torchet, J. Chem. Phys. **66**, 5387 (1977).

[5] B. D. Hall, D. Ugarte, D. Reinhard, and R. Monot, J. Chem. Phys. **103**, 2384 (1995).

[6] C. Y. Yang, J. Cryst. Growth **47**, 274 (1979).

[7] A. L. Mackay, Acta Cryst. **15**, 916 (1962).

[8] S. Ino, J. Phys. Soc. Jpn **27**, 941 (1969).

[9] L. H. Germer and A. H. White, Phys. Rev. **60**, 447 (1941).

[10] C. W. B. Grigson and E. Barton, Brit. J. Appl. Phys. **18**, 175 (1967).

[11] M. de Feraudy and G. Torchet, J. Cryst. Growth **217**, 449 (2000).

[12] B. W. van de Waal, G. Torchet, and M. F. de Feraudy, Chem. Phys. Lett. **331**, 57 (2000).

[13] C. B. Walker, Acta Cryst. A **33**, 342 (1977).

[14] B. D. Hall, D. Zanchet, and D. Ugarte, J. Appl. Cryst. **33**, 1335 (2000).

[15] B. W. van de Waal, J. Mol. Struct. **485-486**, 269 (1999).

[16] F. Betts and A. Bienenstock, J. Appl. Phys. **43**, 4591 (1972).

[17] F. L. Galeener and M. M. Rodoni, Calculation of interparticle contributions to x-ray scattering by a microcrystalline medium, in *Amorphous and liquid semiconductors*, edited by J. Stuke and W. Brenig, pages 101–108, Taylor and Francis, London, 1974.

[18] W. Vogel, B. Rosner, and B. Tesche, J. Phys. Chem. **97**, 11611 (1993).

[19] P. Audit, J. Phys. **30**, 192 (1969).

[20] B. Raoult and J. Farges, Rev. Sci. Instr. **44**, 430 (1973).

[21] J. Farges, B. Raoult, and G. Torchet, J. Chem. Phys. **59**, 3454 (1973).

[22] J. Farges, M. F. de Feraudy, B. Raoult, and G. Torchet, J. Chem. Phys. **78**, 5067 (1983).

[23] B. W. van de Waal, Phys. Rev. Lett. **76**, 1083 (1996).

[24] J. Farges, M. F. de Feraudy, B. Raoult, and G. Torchet, J. Chem. Phys. **84**, 3491 (1986).

[25] B. Raoult, J. Farges, M. F. De Feraudy, and G. Torchet, Phil. Mag. B **60**, 881 (1989).

[26] J. Xie, J. A. Northby, D. L. Freeman, and J. D. Doll, J. Chem. Phys. **91**, 612 (1989).

[27] B. W. van de Waal, J. Chem. Phys. **90**, 3407 (1989).

[28] B. W. van de Waal, J. Chem. Phys. **98**, 4909 (1993).

[29] F. Baletto, C. Mottet, and R. Ferrando, Phys. Rev. Lett. **84**, 5544 (2000).

[30] D. Reinhard, B. D. Hall, D. Ugarte, and R. Monot, Phys. Rev. B **55**, 7868 (1997).

[31] A. Yokozeki, J. Chem. Phys. **68**, 3766 (1978).

[32] G. D. Stein and J. A. Armstrong, J. Appl. Phys **58**, 1999 (1973).

[33] G. D. Stein, Surf. Sci **156**, 44 (1985).

[34] A. Yokozeki and G. D. Stein, J. Appl. Phys. **49**, 2224 (1978).

[35] R. Uyeda, J. Cryts. Growth **24/25**, 69 (1974).

[36] Y. Saito, S. Yatsuya, K. Mihama, and R. Uyeda, J. Cryst. Growth **45**, 501 (1978).

[37] T. Hayashi, T. Ohno, S. Yatsuya, and R. Uyeda, Jpn. J. Appl. Phys. **16**, 705 (1977).

[38] S. Kasukabe, S. Yatsuya, and R. Uyeda, Jpn. J. Appl. Phys. **13**, 705 (1974).

[39] C. G. Granqvist and R. A. Buhrman, J. Appl. Phys. **47**, 2200 (1976).

[40] H. Abe, W. Schulze, and B. Tesche, Chem. Phys. **47**, 95 (1980).

[41] W. Schulze, F. Frank, K. P. Charlé, and B. Tesche, Ber. Bunsenges. Phys. Chem. **88**, 263 (1984).

[42] B. G. D. Boer and G. D. Stein, Surface Science **106**, 84 (1981).

[43] B. D. Hall, M. Flüeli, R. Monot, and J.-P. Borel, Phys. Rev. B **43**, 3906 (1991).

[44] J.-P. Borel, Surf. Sci. **106**, 1 (1981).

[45] P. M. Ajayan and L. D. Marks, Phys. Rev. Lett. **60**, 585 (1988).

[46] B. D. Hall, M. Flüeli, D. Reinhard, R. Monot, and J.-P. Borel, Rev. Sci. Instrum. **62**, 1481 (1991).

[47] S. Valkealahti and M. Manninen, Phys. Rev. B **45**, 9459 (1992).

[48] D. Reinhard, B. D. Hall, P. Bertould, S. Valkealahti, and R. Monot, Phys. Rev. Lett. **79**, 1459 (1997).

[49] D. Reinhard, B. D. Hall, P. Bertould, S. Valkealahti, and R. Monot, Phys. Rev. B **58**, 4917 (1998).

[50] Y. Oshima, K. Takayanagi, and H. Hirayama, Z. Phys. D **40**, 534 (1997).

[51] M. Treilleux, G. Fuchs, F. S. Aires, P. Melinon, and A. Hoareau, Z. Phys. D **20**, 263 (1991).

[52] M. Treilleux et al., Phil. Mag. A **67**, 1071 (1993).

[53] G. Fuchs, M. Treilleux, F. S. Aires, A. H. B. Cabaud, and P. Melinon, Phil. Mag. A **61**, 45 (1990).

[54] M. Takagi, J. Phys. Soc. Japan **11**, 396 (1956).

[55] P. C. Scharrah, J. I. Petz, and R. F. Kruh, J. Chem. Phys. **32**, 241 (1960).

[56] A. Yokozeki and G. D. Stein, J. Appl. Phys. **49**, 2224 (1978).

[57] H. S. Lim, C. K. Ong, and F. Ercolessi, Surf. Sci. **269/270**, 1109 (1992).

[58] J. E. Hearn and R. L. Johnston, J. Chem. Phys. **107**, 4674 (1997).

[59] S. Valkealahti and M. Manninen, Z. Phys. D **26**, 255 (1993).

[60] L. D. Marks, Rep. Prog. Phys. **57**, 603 (1994).

[61] S. Ino, J. Phys. Soc. Jpn **21**, 346 (1966).

[62] S. Giorgio, J. Urban, and W. Kunath, Phil. Mag. A **60**, 553 (1989).

[63] C. L. Cleveland et al., Phys. Rev. Lett. **79**, 1873 (1997).

[64] K. Heinemann, M. J. Yacaman, C. Y. Yang, and H. Poppa, J. Cryst. Growth **47**, 177 (1979).

[65] H. S. Lim, C. K. Ong, and F. Ercolessi, Comp. Mat. Sci. **2**, 495 (1994).

[66] B. D. Hall, J. Appl. Phys. **87**, 1666 (2000).

[67] M. Maier-Borst, D. B. Cameron, M. Rokni, and J. H. Parks, Phys. Rev. A. **59**, 3162 (1999).

[68] S. Kruckeberg, D. Schooss, M. Maier-Borst, and J. H. Parks, Phys. Rev. Lett **85**, 4494 (2000).

[69] S. Iijima and T. Ichihashi, Phys. Rev. Lett. **56**, 616 (1986).

[70] D. Ugarte, Electron Microscopy **2**, 677 (1992).

[71] B. D. Hall, *An installation for the study of unsupported ultrafine particles by electron diffraction with application to silver*, PhD thesis, EPFL, Lausanne, Switzerland, 1991, No. 954.

[72] R. L. McGreevy, J. Non-Crys. Solids **156-158**, 949 (1993).

[73] R. L. McGreevy and L. Pusztai, Mol. Simul. **1**, 359 (1988).

Acknowledgements

I would like to thank my supervisor, Dr. Simon Brown, for making this project available and for his guidance, support and encouragement throughout the course of this thesis.

This thesis has benefited substantially from the experience and expertise of Dr. Blair Hall and Dr. Shaun Hendy at Industrial Research Limited in Lower Hutt. Dr. Hall, who previously used the experimental equipment to study Ag clusters, provided assistance on nearly all aspects of the experiment from the initial reconstruction of the equipment to the analysis of the data. Dr. Hendy performed the molecular dynamics simulations of Pb clusters, the results of his work were used extensively in the analysis of the diffraction patterns from Pb clusters. Their contributions are greatly appreciated.

For the companionship and assistance from fellow students, Andreas Wurl, Juern Schmelzer, Monica Schulze and Martin Kaufmann during my thesis work I am most grateful. I wish you all well for the future.

The enthusiasm and proficiency of the technical staff in the Physics and Astronomy Department were greatly beneficial to this thesis. Nearly all of the technical staff have participated in this thesis and I thank you all for your contributions. In particular, I would like mention Graeme McDonald and Wayne Smith who, amongst other tasks, spent many hours helping with the reconstruction of the equipment, Ron Culley for his willingness to tackle any of the mechanical problems encountered and Geoff Graham who built controllers for the crucible temperature, TEM grid exposure mechanism and the gas flow meters.

The majority of the TEM and SEM work was completed with guidance from Dr. Milo Kral, Jan MacKenzie and Mike Flaws, I greatly appreciate the time they spent helping me in their labs. I would also like to thank Dr. Kral for allowing me to attend his class.

I would like to acknowledge the funding received from the University of Canterbury, the Royal Society of New Zealand, the Royal Society of New Zealand–Canterbury Branch and the Department of Physics and Astronomy that enabled me to attend the ISSPIC conference in Atlanta, USA.

To all the members of 'Club Scott' a special thank you for the many enjoyable times that were had.

Another special thank you must go to Gill Evans, one of the Physics and Astronomy Department's secretaries, for the many efforts she makes to enhance life in the Department.

Finally, I would like to thank my parents for their support during this thesis and for putting up with "I'll be finished soon" for quite some time.

References

[1] G. Stein, *The Physics Teacher* **17** (1979) 503.

[2] P. Pawlow, *Z. Phys. Chem.* **65** (1909) 545.

[3] F. Ercolessi, W. Andreoni and E. Tosatti, *Phys. Rev. Lett.* **66** (1991) 911.

[4] M. Takagi, *J. Phys. Soc. Japan* **9** (1954) 359.

[5] M. Blackman and A. E. Curzon, *Structure and Properties of Thin Films* (Wiley, New York, 1959), pp. 217.

[6] P. Buffat and J.-P. Borel, *Phys. Rev. A* **13** (1976) 2287.

[7] R. Kofman, P. Cheyssac, Y. Lereah and A. Stella, *Eur. Phys. J. D* **9** (1999) 441.

[8] A. A. Shvartsburg and M. F. Jarrold, *Phys. Rev. Lett.* **85** (2000) 2530.

[9] S. L. Lai, J. Y. Guo, V. Petrova, G. Ramanath and L. H. Allen, *Phys. Rev. Lett.* **77** (1996) 99.

[10] C. E. Bottani, A. Li Bassi, B. K. Tanner, A. Stella, P. Tognini, P. Cheyssac and R. Kofman, *Phys. Rev. B* **59** (1999) 15601.

[11] E. A. Flood, editor, *The Solid-Gas Interface* (Marcal Dekker Inc., New York, 1966).

[12] C. W. Mays, J. S. Vermaak and D. Kuhlmann-Wilsdorf, *Surf. Sci.* **12** (1968) 134.

[13] C. R. Berry, *Phys. Rev.* **88** (1952) 596.

[14] T. de Planta, R. Ghez and F. Piuz, *Helv. Phys. Acta.* **37** (1964) 74.

[15] H. J. Wasserman and J. S. Vermaak, *Surf. Sci.* **22** (1970) 164.

[16] G. Apai, J. Hamilton, J. Stohr and A. Thompson, *Phys. Rev. Lett.* **43** (1979) 165.

[17] A. Balerna, E. Bernieri, P. Picozzi, A. Reale and S. Santucci, *Phys. Rev. B* **31** (1985) 5058.

[18] P. Montano, G. Shenoy and E. Alp, *Phys. Rev. B* **56** (1986) 2076.

[19] M. De Crescenzi, M. Diociaiuti, L. Lozzi, P. Picozzi and S. Santucci, *Phys. Rev. B* **35** (1987) 5997.

[20] R. Lamber, S. Wetjen and N. I. Jaeger, *Phys. Rev. B* **51** (1995) 10968.

[21] C. L. Briant and J. J. Burton, *Surf. Sci.* **51** (1975) 345.

[22] L. B. Hansen, P. Stoltze, J. K. Nørskov, B. S. Clausen and W. Neimann, *Phys. Rev. Lett.* **64** (1990) 3155.

[23] J. M. Soler, M. R. Beltrán, K. Michaelian, I. L. Garzón, P. Ordejón, D. Sánchez-Portal and E. Artacho, *Phys. Rev. B* **61** (2000) 5771.

[24] J. M. Soler, I. L. Garzón and J. D. Joannopoulos, *Sol. State. Comm.* **117** (2001) 621.

[25] J. F. Hamilton and R. C. Baetzold, *Science* **205** (1979) 1213.

[26] A. Sanchez, S. Abbet, W.-D. Schneider, H. Häkkinen, R. N. Barnett and U. Landman, *J. Phys. Chem. A* **103** (1999) 9573.

[27] M. Schmidt, R. Kusche, T. Hippler, J. Donges, W. Kronmüller, B. von Issendorff and H. Haberland, *Phys. Rev. Lett.* **86** (2001) 1191.

[28] M. Jarrold, *Phys. World* **14** (2001) 23.

[29] S. Ino, *J. Phys. Soc. Japan* **21** (1966) 346.

[30] J. G. Allpress and J. V. Sanders, *Surf. Sci.* **7** (1967) 1.

[31] A. Yokozeki and G. D. Stein, *J. Appl. Phys.* **49** (1978) 2224.

[32] J. Farges, M. F. de Feraudy, B. Raoult and G. Torchet, *J. Chem. Phys.* **78** (1983) 5067.

[33] H. W. Kroto, J. R. Heath, S. C. O'Brien, R. F. Curl and R. E. Smalley, *Nature* **318** (1985) 162.

[34] J. Farges, M. F. de Feraudy, B. Raoult and G. Torchet, *Ber. Bunsenges. Phys. Chem.* **88** (1988) 211.

[35] D. Reinhard, B. D. Hall, P. Berthoud, S. Valkealahti and R. Monot, *Phys. Rev. B* **58** (1998) 4917.

[36] S. J. Oh, S. H. Huh, H. K. Kim, J. W. Park and G. H. Lee, *J. Chem. Phys.* **111** (1999) 7404.

[37] S. Krückeberg, D. Schooss, M. Maier-Borst and J. H. Parks, *Phys. Rev. Lett.* **85** (2000) 4494.

[38] S. H. Huh, H. K. Kim, J. W. Park and G. H. Lee, *Phys. Rev. B* **62** (2000) 2937.

[39] D. Reinhard, B. D. Hall, P. Berthoud, S. Valkealahti and R. Monot, *Phys. Rev. Lett.* **79** (1997) 1459.

[40] D. Reinhard, B. D. Hall, D. Ugarte and R. Monot, *Phys. Rev. B* **55** (1997) 7868.

[41] F. Baletto, C. Mottet and R. Ferrando, *Phys. Rev. Lett.* **84** (2000) 5544.

[42] F. Baletto, C. Mottet and R. Ferrando, *Phys. Rev. B* **63** (2001) 155408.

[43] S. Iijima and T. Ichihashi, *Phys. Rev. Lett.* **56** (1986) 616.

[44] D. J. Smith, A. K. Petford-Long, L. R. Wallenburg and J. O. Bovin, *Science* **233** (1986) 872.

[45] P. M. Ajayan and L. D. Marks, *Phys. Rev. Lett.* **60** (1988) 585.

[46] N. Doraiswamy and L. D. Marks, *Philos. Mag. B* **71** (1995) 291.

[47] M. Flüeli, *Observation des Structures Anormales de Petites Particules d'Or et d'Argent par Microscopie Electronique à Haute Résolution et Diffraction d'Electrons par un Jet d'Agrégets d'Argent.*, Ph.D. thesis, École Polytechnique Fédérale De Lausanne (1989).

[48] B. D. Hall, *An installation for the study of unsupported ultrafine particles by electron diffraction with application to silver: observation of multiply twinned particle structures.*, Ph.D. thesis, École Polytechnique Fédérale De Lausanne (1991).

[49] B. D. Hall, M. Flüeli, R. Monot and J.-P. Borel, *Phys. Rev. B* **43** (1991) 3906.

[50] D. Reinhard, *Croissance et stabilité d'agrégats d'argent et de cuivre, étudiés en jets moléeculaires par diffraction d'électrons á haute énergie.*, Ph.D. thesis, École Polytechnique Fédérale De Lausanne (1995).

[51] A. Wurl, "Private Communication", (2001).

[52] J. Eversole and H. Broida, *J. Appl. Phys.* **45** (1974) 596.

[53] R. Johnston, *Philos. Trans. R. Soc. Lond. A* **356** (1998) 211.

[54] G. Wulff, *Z. Kristallog.* **34** (1901) 449.

[55] A. L. Mackay, *Acta. Cryst.* **15** (1962) 916.

[56] B. G. Bagley, *Nature* **208** (1965) 674.

[57] S. Ino, *J. Phys. Soc. Japan* **27** (1969) 941.

[58] L. D. Marks, *J. Cryst. Growth* **61** (1983) 556.

[59] L. D. Marks, *Philos. Mag. A* **49** (1984) 81.

[60] L. D. Marks, *J. Microsc.* **130** (1983) 249.

[61] T. P. Martin, *Phys. Rep.* **273** (1996) 199.

[62] W. D. Knight, K. Clemenger, W. A. de Heer, W. A. Saunders, M. Y. Chou and M. L. Cohen, *Phys. Rev. Lett.* **52** (1984) 2141.

[63] T. P. Martin, T. Bergmann, H. Göhlich and T. Lange, *Chem. Phys. Lett.* **172** (1990) 209.

[64] C. L. Cleveland and U. Landman, *J. Chem. Phys.* **94** (1991) 7376.

[65] J. E. Hearn and R. L. Johnston, *J. Chem. Phys.* **107** (1997) 4674.

[66] S. Valkealahti and M. Manninen, *Phys. Rev. B* **45** (1992) 9459.

[67] J. Uppenbrink and D. J. Wales, *J. Chem. Phys.* **96** (1992) 8520.

[68] J. Yi, D. J. Oh, J. Bernholc and R. Car, *Chem. Phys. Lett.* **174** (1990) 461.

[69] H. S. Lim, C. K. Ong and F. Ercolessi, *Surf. Sci.* **269/270** (1992) 1109.

[70] S. Hendy and B. D. Hall, *Phys. Rev. B* **64** (2001) 085425.

[71] S. Hendy, "Private Communication", (2001).

[72] A. N. Patil, D. Y. Paithankar, N. Otsuka and R. P. Andres, *Z. Phys. D* **26** (1993) 135.

[73] C. L. Cleveland, U. Landman, T. G. Schaaff, M. N. Shafigullin, P. W. Stephens and R. L. Whetten, *Phys. Rev. Lett.* **79** (1997) 1873.

[74] Y. Qi, T. Çağin, W. L. Johnson and W. A. Goddard III, *J. Chem. Phys.* **115** (2001) 385.

[75] I. L. Garzón and J. Jellinek, *Z. Phys. D* **26** (1993) 316.

[76] I. L. Garzón and A. Posada-Amarillas, *Phys. Rev. B* **54** (1996) 11796.

[77] I. L. Garzón, K. Michaelian, M. R. Beltrán, A. Posada-Amarillas, P. Ordejón, E. Artacho, D. Sánchez-Portal and J. M. Soler, *Phys. Rev. Lett.* **81** (1998) 1600.

[78] C. L. Cleveland, W. D. Luedtke and U. Landman, *Phys. Rev. Lett.* **81** (1998) 2036.

[79] C. L. Cleveland, W. D. Luedtke and U. Landman, *Phys. Rev. B* **60** (1999) 5065.

[80] Y. G. Chushak and L. S. Bartell, *J. Phys. Chem. B* **105** (2001) 11605.

[81] Y. G. Chushak and L. S. Bartell, *Eur. Phys. J. D* **16** (2001) 43.

[82] S. Valkealahti and M. Manninen, *Z. Phys. D* **26** (1993) 255.

[83] S. Valkealahti and M. Manninen, *J. Phys.: Condens. Matter* **9** (1997) 4041.

[84] S. Valkealahti and M. Manninen, *Phys. Rev. B* **50** (1994) 17564.

[85] S. Valkealahti, U. Näher and M. Manninen, *Phys. Rev. B* **51** (1995) 11039.

[86] S. Valkealahti, *Phys. Rev. B* **57** (1998) 15533.

[87] F. Baletto, C. Mottet and R. Ferrando, *Surf. Sci.* **446** (2000) 31.

[88] B. W. van de Waal, *Phys. Rev. Lett.* **76** (1996) 1083.

[89] B. D. Hall, M. Flüeli, J.-P. Borel and R. Monot, *Rev. Sci. Instrum.* **62** (1991) 1481.

[90] F. W. Sears, M. W. Zemansky and H. D. Young, *University Physics, 6th Edition* (Addison-Wesley, Reading, Massachussetts, 1982).

[91] J. E. McDonald, *Am. J. Phys.* **30** (1962) 870.

[92] J. E. McDonald, *Am. J. Phys.* **31** (1963) 31.

[93] C. J. Smithells, *Metals Reference Book, 5 th Edition* (Butterworths, London, 1976).

[94] J. B. Homer and I. R. Hurle, *Proc. R. Soc. Lond. A* **327** (1972) 61.

[95] I. Nishida and K. Kimoto, *Jap. J. Appl. Phys.* **14** (1975) 1425.

[96] K. Sattler, J. Mühlbach and E. Recknagel, *Phys. Rev. Lett.* **45** (1980) 821.

[97] H. Abe, W. Schulze and B. Tesche, *Chem. Phys.* **47** (1980) 95.

[98] W. Schulze, F. Frank, K. Charlé and B. Tesche, *Ber. Bunsenges. Phys. Chem.* **88** (1984) 263.

[99] K. Kawamura, *Jap. J. Appl. Phys.* **12** (1973) 1685.

[100] S. Kasukabe, S. Yatsuya and R. Uyeda, *Jap. J. Appl. Phys.* **13** (1974) 1714.

[101] C. Granqvist and R. Buhrman, *J. Appl. Phys.* **47** (1976) 2200.

[102] C. Granqvist and R. Buhrman, *Solid State Comm.* **18** (1976) 123.

[103] N. Wada, *Jap. J. App. Phys.* **7** (1968) 1287.

[104] C. Granqvist and R. Buhrman, *Appl. Phys. Lett.* **27** (1975) 693.

[105] B. D. Hall, D. Reinhard and R. Monot, *Rev. Sci. Instrum.* **66** (1995) 2668.

[106] B. K. Vainshtein, *Structure Analysis by Electron Diffraction* (Pergamon Press Ltd., New York, 1964).

[107] A. Guinier, *X-ray diffraction in crystals, imperfect crystals, and amorphous bodies* (W. H. Freeman, San Francisco, 1963).

[108] B. D. Hall, D. Ugarte, D. Reinhard and R. Monot, *J. Chem. Phys.* **103** (1995) 2384.

[109] L. Kish, C. G. Granqvist, W. Marlow and R. W. Siegel, editors, *Fundamentals of Gas-Phase Nanotechnology* (Kluwers Academic Publishing, 2002).

[110] B. D. Hall and R. Monot, *Comp. in Phys.* **5** (1991) 414.

[111] K. Michaelian, M. Beltrán and I. L. Garzón, *Phys. Rev. B* **65** (2002) 041403.

[112] R. P. Gupta, *Phys. Rev. B* **23** (1981) 6265.

[113] K. Michaelian, *Am. J. Phys.* **66** (1998) 231.

[114] L. D. Marks, *Rep. Prog. Phys.* **57** (1994) 603.

[115] F. Betts and A. Bienenstock, *J. Appl. Phys.* **43** (1972) 4591.

[116] W. Vogel, B. Rosner and B. Tesche, *J. Phys. Chem.* **97** (1993) 11611.

[117] B. D. Hall, *J. Appl. Phys.* **87** (2000) 1666.

[118] D. Zanchet, B. D. Hall and D. Ugarte, *J. Phys. Chem. B* **104** (2000) 11013.

[119] S. Kirkpatrick, C. D. Gelatt Jr. and M. P. Vecchi, *Science* **220** (1983) 671.

[120] W. L. Goffe, G. D. Ferrier and J. Rogers, *J. Econometrics* **60** (1994) 65.

[121] A. Corana, M. Marchesi, C. Martini and S. Ridella, *ACM Trans. Math. Soft.* **13** (1987) 262.

[122] T. F. Coleman and Y. Li, *Math. Program.* **67** (1994) 189.

[123] T. F. Coleman and Y. Li, *SIAM J. Optimiz.* **6** (1996) 418.

[124] T. Allen, *Particle Size Measurement, Volume 1* (Chapman & Hall, London, 1997).

[125] V. J. Johnson, editor, *Properties of Materials at Low Temperature (Phase 1) A Compendium* (Pergamon Press, London, 1961).

[126] W. Espe, *Materials of High Vacuum Technology* (Pergamon Press, New York, 1966).

[127] T. Ben David, Y. Lereah, G. Deutscher, R. Kofman and P. Cheyssac, *Philos. Mag A* **71** (1995) 1135.

[128] B. D. Hall, D. Zanchet and D. Ugarte, *J. Appl. Cryst.* **33** (2000) 1335.

[129] C. Hammond, *The Basics of Crystallography and Diffraction* (Oxford University Press Inc., New York, 1997).

[130] I. Rabin, W. Schulze and B. Winter, *Phys. Rev. B* **40** (1989) 10282.

[131] R. W. Farley, P. Ziermann and A. W. Castleman, Jr., *Z. Phys. D* **14** (1989) 353.

[132] K. LaiHing, R. G. Wheeler, W. L. Wilson and M. A. Duncan, *J. Chem. Phys.* **87** (1987) 3401.

[133] W. Schulze, B. Winter and I. Goldenfeld, *Phys. Rev. B* **38** (1988) 12937.

[134] J. Mühlbach, K. Sattler, P. Pfau and E. Recknagel, *Phys. Lett.* **87A** (1982) 415.

[135] C. Lüder and K. H. Meiwes-Broer, *Chem. Phys. Lett.* **294** (1998) 391.

[136] G. Ganeför, M. Gausa, K. H. Meiwes-Broer and H. O. Lutz, *Z. Phys. D* **12** (1989) 405.

[137] J. C. Phillips, *J. Chem. Phys.* **87** (1987) 1712.

[138] M. P. Iñiguez, M. J. Lopez, J. A. Alonso and J. M. Soler, *Z. Phys. D* **11** (1989) 163.

[139] C. J. Coombes, *J. Phys. F* **2** (1972) 441.

[140] S. J. Peppiatt and J. R. Sambles, *Proc. R. Soc. Lond. A* **345** (1975) 387.

[141] R. Kofman, P. Cheyssac, R. Garrigos, Y. Lereah and G. Deutscher, *Z. Phys. D* **20** (1991) 267.

[142] R. Kofman, P. Cheyssac, A. Aouaj, Y. Lereah, G. Deutscher, T. Ben David, J. M. Penisson and A. Bourret, *Surf. Sci.* **303** (1994) 231.

[143] K. F. Peters, J. B. Cohen and Y. W. Chung, *Phys. Rev. B* **21** (1998) 13430.

[144] T. Ben David, Y. Lereah, G. Deutscher, J. M. Penisson, A. Bourret, R. Kofman and P. Cheyssac, *Phys. Rev. Lett.* **78** (1997) 2585.

[145] Y. Wu, M. Takeguchi, Q. Chen and K. Furuya, *Appl. Surf. Sci.* **159-160** (2000) 486.

[146] D. Y. Sun, Y. Xiang and X. G. Gong, *Philos. Mag. A* **79** (1999) 1953.

[147] J. Wan, Y. L. Fan, D. W. Gong, S. G. Shen and X. Q. Fan, *Modelling Simul. Mater. Sci. Eng.* **7** (1999) 189.

[148] H. S. Lim, C. K. Ong and F. Ercolessi, *Comp. Mat. Sci.* **2** (1994) 495.

[149] B. G. de Boer and G. D. Stein, *Surf. Sci.* **106** (1981) 84.

[150] K. Michaelian, N. Rendón and I. L. Garzón, *Phys. Rev. B* **60** (1999) 2000.

[151] M. F. de Feraudy and G. Torchet, *J. Cryst. Growth* **217** (2000) 449.

[152] J. Farges, M. F. de Feraudy, B. Raoult and G. Torchet, *J. Chem. Phys.* **84** (1986) 3491.

[153] J. Farges, M. F. de Feraudy, B. Raoult and G. Torchet, *Adv. Chem. Phys.* **70** (1988) 45.

[154] B. W. van de Waal, *J. Mol. Struct.* **485-486** (1999) 269.

[155] B. W. van de Waal, G. Torchet and M. F. de Feraudy, *Chem. Phys. Lett.* **331** (2000) 57.

[156] K. Koga and H. Takeo, *Eur. Phys. J. D.* **9** (1999) 535.

[157] K. Koga, H. Takeo, T. Ikeda and K. Ohshima, *Phys. Rev. B* **57** (1998) 4053.

[158] A. Yokozeki, *J. Chem. Phys.* **68** (1978) 3766.

[159] A. Wurl, M. Hyslop, S. A. Brown, B. D. Hall and R. Monot, *Euro. Phys. J. D* **16** (2001) 205.

[160] S. Park, K. Lee and C. Lee, *J. Korean Phys. Soc.* **34** (1999) 310.

[161] D. R. Lide, editor, *CRC Handbook of Chemistry and Physics, 81 st Edition* (CRC Press, 2001-2002).

[162] R. Ramprasad and R. Hoagland, *Modelling Simul. Mater. Sci. Eng.* **1** (1993) 189.

[163] W. de Heer, *Rev. Mod. Phys.* **65** (1993) 611.

[164] H. Haberland, editor, *Clusters of Atoms and Molecules* (Springer-Verlag, New York, 1994).

[165] S. Pasche, *Etude de la Susceptibilite Paramagnetique des Amas Metalliques Divalents en Fonction de la Taille.*, Ph.D. thesis, École Polytechnique Fédérale De Lausanne (1989).

[166] S. Pasche and J. Borel, *Z. Phys. D* **12** (1989) 401.

[167] J. Xu, T. Zhou and Y. Du, *Phys. Stat. Sol.* **153** (1996) 313.

[168] J. Xu, J. Zhang, Y. Du, X. Zhang and Y. Li, *Materials Lett.* **29** (1996) 131.

[169] J. Xu, J. Zhang, W. Ding, W. Yang, Y. Du, J. Zuo, C. Xu, Y. Zhang and Z. Du, *Solid State Comm.* **101** (1997) 467.

[170] J. Hecht, W. West and M. Norton, *Surf. Sci.* **106** (1980) 131.

[171] J. Hecht and M. Norton, *J. Appl. Phys.* **52** (1981) 3080.

[172] E. Hogg and B. Silbernagel, *J. Appl. Phys.* **45** (1974) 593.

[173] O. Daub, W. Langel, C. Reiner and L. Kienle, *Ber. Bunsenges. Phys. Chem.* **101** (1997) 1753.

[174] A. Cox, J. Nainaparampil, M. Tabet, A. Hosseini-Tehrani and F. Urban III, *Thin Solid Films* **270** (1995) 637.

[175] S. Feng, J. Nainaparampil, F. Tabet and F. Urban III, *Thin Solid Films* **253** (1994) 402.

[176] J. Gspann, *Z. Phys. D* **26** (1993) S174.

[177] J. Pruett, H. Windischmann, M. Nicholas and P. Lampard, *J. Appl. Phys.* **64** (1988) 2271.

[178] R. Yadav, V. Ramamurthy, D. Mahapatra and G. Raviprasad, *Phys. Rev. A* **49** (1994) 1908.

[179] I. Katakuse, T. Ichihara, M. Morris, T. Matsuo, T. Sakurai and H. Matsuda, *Int. J. Mass Spec. and Ion Proc.* **91** (1989) 85.

[180] K. Rademann, M. Ruppel and B. Kaiser, *Ber. Bunsenges. Phys. Chem.* **96** (1992) 1204.